University of Southampton Research Repository

University of Southampton

Faculty of Engineering and Physical Sciences

Bioengineering Science

A Correlative X-ray and Electron Microscopy Framework for 3D Bone Imaging and its application to Bone Development and Disease in Human and Animal Tissue

by

Patricia Mary Goggin

Thesis for the degree of Doctor of Philosophy

August 2021

University of Southampton
<u>Abstract</u>

Faculty of Engineering and Physical Sciences

Bioengineering Science

<u>Thesis for the degree of Doctor of Philosophy</u>

A Correlative X-ray and Electron Microscopy Framework for 3D Bone Imaging and its application to Bone Development and Disease in Human and Animal Tissue
By Patricia Mary Goggin

Osteocytes are stellate cells which form a network within hard bone matrix and play a key role for bone adaptation during development, ageing and bone diseases including osteoporosis. The mechanisms by which osteocytes sense loading and transmit signals to regulate remodelling are not well understood. Detailed knowledge of the three-dimensional (3D) structure of the osteocyte network and the surrounding lacuno-canalicular network is essential to elucidate these mechanisms. 3D imaging on cellular and sub-cellular scales will allow quantitative hallmarks of health and disease to be derived and will lead to improved computational models of bone mechanotransduction. Until now the location of the cells within calcified bone matrix and the sub-micrometre dimensions of the networks have posed challenges for 3D imaging. Serial block-face scanning electron microscopy (SBF SEM) is a novel imaging technique which produces high-resolution 3D data of the osteocyte and lacuno-canalicular networks (ON&LCN) simultaneously.

The objective of this project is to develop a correlative X-ray and SBF SEM (CXEM) workflow for mammalian bone tissue, providing quantitative data, which will enable realistic computational modelling of bone mechanobiology. This project aims to develop protocols for SBF SEM sample preparation and imaging and to combine SBF SEM with X-ray micro computed tomography in a correlative workflow which allows derivation of established and novel quantitative measures of the ON&LCN across length scales in relevant tissue volumes. CXEM imaging and image analysis workflows are applied to juvenile and adult murine bone tissue and to bone tissue from osteoporotic (OP) and osteoarthritic (OA) human donors.

CXEM applied to juvenile and adult mouse tibia has produced data on osteocyte density, porosity, and cell measures including volume and number of processes. Pericellular space volume and width were quantified in 3D for the first time. The results show that values for pericellular space volume used in previous studies have been overestimated and that the width of the pericellular space is more irregular than values derived from 2D imaging methods and used in computational models, possibly leading to the underestimation of peak strain sensed by osteocytes.

Tissue from OP and OA donors was imaged and analysed using CXEM. Osteocyte number density is 37% of lacunar number density and osteocyte porosity is 30% of lacunar porosity in these samples. These findings illustrate that using lacunar number density and porosity measures to represent osteocyte measures in diseased human bone tissue is misleading. 93% of lacunae contained a cell showing ultrastructural changes indicative of deteriorating health or cell death. This indicates that the cell network, crucial for mechanobiology and bone homeostasis, is compromised in OA and OP tissue, although not in significantly different ways.

CXEM enables imaging of the hard and soft components of bone simultaneously, at high resolution and in 3D, producing unique quantitative measures. CXEM assessment of the ON&LCN in health

and disease paves the way for the study of mechanotransduction mechanisms by computational models based on accurate geometries. This will lead to the identification of relevant features of healthy and diseased bone at the cell level, which could serve as targets for the diagnosis and treatment of bone-related diseases, impacting significantly on public health.

Table of Contents

Table of Tables

Table of Tables

Table of Figures

Table of Figures

Table of Figures

Research Thesis: Declaration of Authorship

Print name: PATRICIA GOGGIN

Title of thesis: **A Correlative X-ray and Electron Microscopy Framework for 3D Bone Imaging and its application to Bone Development and Disease in Human and Animal Tissue**

I declare that this thesis and the work presented in it are my own and has been generated by me as the result of my own original research.

I confirm that:

1. This work was done wholly or mainly while in candidature for a research degree at this University;
2. Where any part of this thesis has previously been submitted for a degree or any other qualification at this University or any other institution, this has been clearly stated;
3. Where I have consulted the published work of others, this is always clearly attributed;
4. Where I have quoted from the work of others, the source is always given. With the exception of such quotations, this thesis is entirely my own work;
5. I have acknowledged all main sources of help;
6. Where the thesis is based on work done by myself jointly with others, I have made clear exactly what was done by others and what I have contributed myself;
7. Parts of this work have been published as:-

A Development of protocols for the first serial block-face scanning electron microscopy (SBF SEM) studies of bone tissue
   Goggin P, Ho ELM, Searle S, Gnaegi H, Oreffo ROC, Schneider P. Bone, 2020. Feb;131:115107
B High-resolution 3D imaging of osteocytes and computational modelling in mechanobiology: Insights on bone development, ageing, health and disease
   Goggin PM, Zygalakis KC, Oreffo ROC, Schneider P. Eur Cell Mater. 2016 May 22;31:264-95

Signature: Date:05/08/21

Acknowledgements

Definitions and Abbreviations

2D	2-dimensional
3D	3-dimensional
AFM	Atomic force microscopy
ATUM	Automatic tape-collecting ultramicrotome
BLC	Bone lining cells
BMD	Bone mineral density
BSE	Back scattered electron(s)
BV	Bone volume
Cn	Canaliculus/Canalicular
CLEM	Correlative light and electron microscopy
CLSM	Confocal laser scanning microscopy
CT	Computed tomography
CXEM	Correlative X-ray and electron microscopy
DM	Digital Micrograph
DMP1	Dentin matrix protein 1
ECM	Extracellular matrix
EM	Electron microscopy
EDTA	Ethylene diamine tetracetic acid
ET	Electron tomography
FA	Formaldehyde
FE	Finite element
FGF	Fibroblast growth factor
FH	Femoral head
FIB	Focussed ion beam
FIB SEM	Focused ion beam scanning electron microscopy
FSI	Fluid structure interaction
GA	Glutaraldehyde
kVp	Kilovoltage peak
Lc	Lacuna/lacunar

LCN	Lacuno-canalicular network
LM	Light microscopy
LSM	Light sheet microscopy
μCT	Micro computed tomography
NHS	National Health Service
NO	Nitric Oxide
OA	Osteoarthritis/Osteoarthritic
ON	Osteocyte network
ON&LCN	Osteocyte and lacuno-canalicular networks
OP	Osteoporosis/Osteoporotic
Ot	Osteocyte
OTO	Osmium-thiocarbohydrazide-osmium
PCM	Pericellular matrix
PCS	Pericellular space
PHEX	Phosphate-regulating neutral endopeptidase on chromosome X
PIPES	Piperazine-N,N'-bis(2-ethanesulfonic acid)
Pr	Process
PTH	Parathyroid hormone
ROTO	Reduced osmium-thiocarbohydrazide-osmium
RT	Room temperature
SBF SEM	Serial block-face scanning electron microscopy
SEM	Scanning electron microscopy
SR CT	Synchrotron radiation (based) computed tomography
TEM	Transmission electron microscopy
THR	Total hip replacement
TV	Total Volume
TXM	Transmission X-ray microscopy
UHVEM	Ultra-high voltage electron microscopy
vEM	volume electron microscopy
Wnt	Wingless-related integration site
WSS	Wall shear stress

Chapter 1 Introduction and Project Summary

1.1 Background

Bone is a complex material, which provides protection, stability and locomotion for the body. Bone is capable of these functions because it is light, stiff, strong and resistant to fracture. At the same time, bone is elastic and flexible, able to absorb energy from deformation and to change shape. The structure and composition of bone are an exquisite design, which contributes to its success as a biomaterial. However if bone structure is compromised, the performance of these functions may be limited, resulting in bone diseases such as osteoporosis (OP) which can be devastating to quality of life.

OP affects the quality (structure, composition and mechanical properties) and quantity (mass) of bone, leading to an increased risk of fracture, particularly in post-menopausal women (WHO, 1994). In the European Union in 2010, 22 million women and 5.5 million men had OP and 3.5 million fragility fractures occurred as a result (Hernlund et al., 2013). The associated economic burden in the EU was estimated at €37 billion in 2010 and is estimated to reach €46.25 billion by 2025 (Hernlund et al., 2013). Aside from the financial cost, the impact on individuals is considerable with chronic pain, deformity and reduction in mobility being typical (Melton III, 2003).

OP is a multifactorial condition affected by genetics, sex, age, inadequate consumption of calcium, inadequate exposure to ultraviolet light coupled with inadequate consumption of Vitamin D, lack of exercise, hormonal deficiency, smoking, alcohol and caffeine consumption (Webster, 1994). It is generally recognised that material properties contribute to changes in bone and the increase in fracture risk; however, the precise biomechanical changes occurring during the disease remain unclear. Better understanding of the

biological mechanisms underlying bone loss in OP and ageing is essential to reduce the number of fractures and the associated financial and social burdens.

Bone is a dynamic tissue which adapts to changed mechanical loading patterns due to development, growth, ageing, disease, disuse or exercise, by removing existing and adding new bone tissue (Parfitt, 1994b). Osteocytes are the key cells which orchestrate bone adaptation (Tatsumi et al., 2007). Osteocytes are ovoid cells approximately 10 μm long, with many cell processes approximately 100 nm in diameter, surrounded by a pericellular matrix (PCM). Osteocytes and their processes form the osteocyte network (ON), which is housed within the lacuno-canalicular network (LCN), a system of voids and channels in the calcified bone matrix (Figure 1).
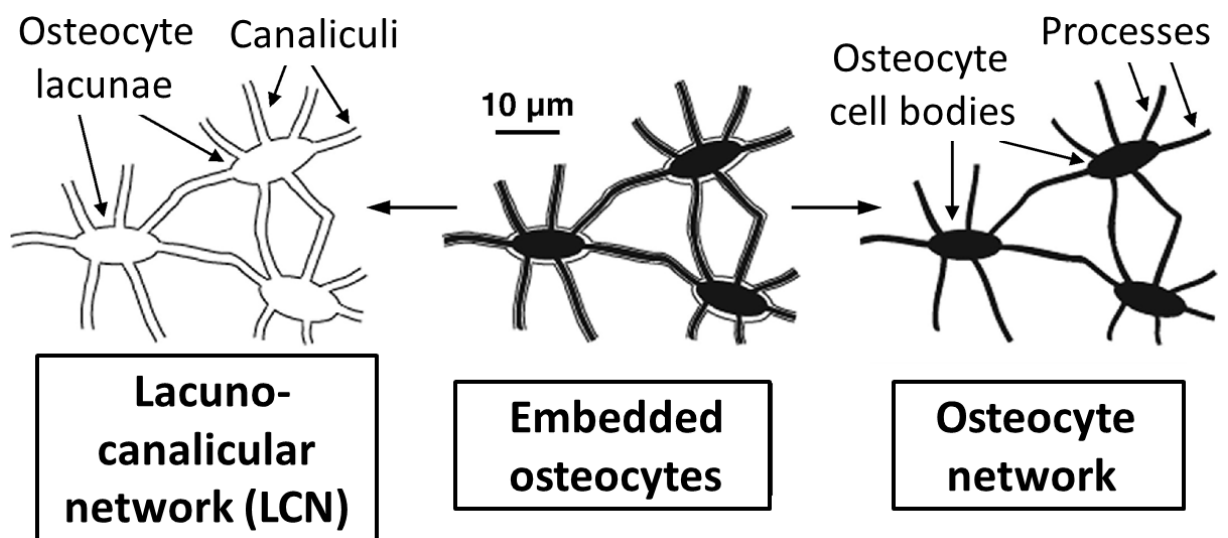
Figure 1   Schematic view of the ON&LCN

The LCN is formed by osteocyte lacunae and interconnecting canaliculi, while the osteocyte network, which resides within, is made up of cells connected to each other by cell processes. Image from (Goggin et al., 2016) adapted from (Schneider et al., 2010).

The presence of osteocytes throughout the bone tissue and their interconnectedness ensures osteocytes are ideally placed to sense changes in mechanical stimuli and to communicate information through the ON. The osteocyte and the lacuno-canalicular networks (ON&LCN) are thought to be a mechanosensitive organ for external mechanical

stimuli, which are translated into biochemical signals that lead to bone resorption and formation by osteoclasts and osteoblasts, respectively (Figure 2) (Bonewald, 2021). As such, the ON&LCN are central in the bone remodelling process. Thus, changes in the local bone microstructure, including the ON&LCN, can alter and disrupt mechanotransduction and mechanosensory mechanisms, which are implicated in bone diseases such as OP, osteomalacia/rickets and osteopetrosis (McCreadie et al., 2004, Neve et al., 2012). The mechanisms of this mechanosensation and subsequent mechanotransduction are not fully understood (Bonewald, 2021).
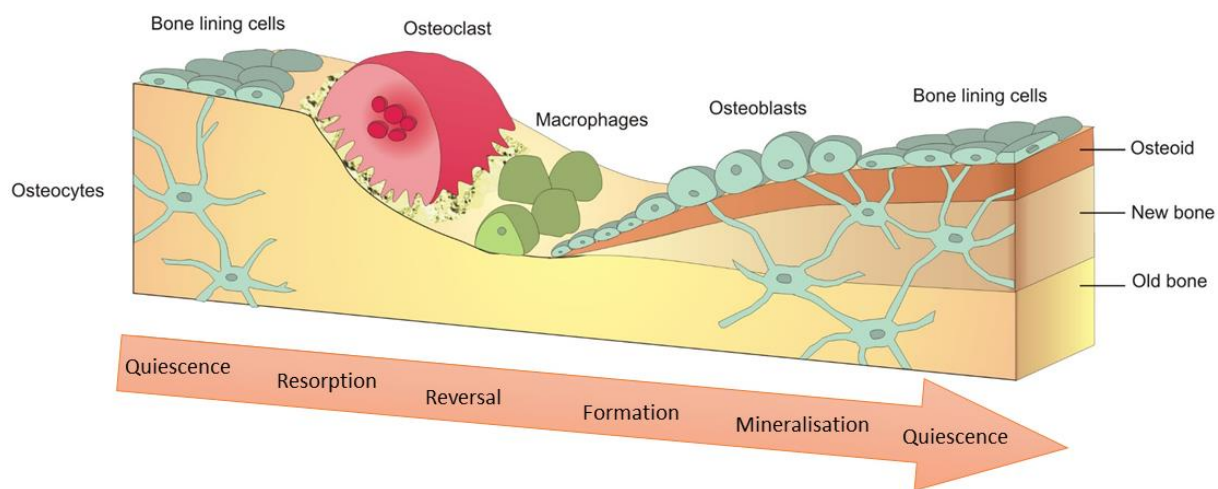
Figure 2   Bone remodelling

Bone is constantly remodelled to maintain tissue integrity. During remodelling osteoclasts resorb old bone, which is replaced with osteoid secreted by osteoblasts. The osteoid mineralises to create new bone matrix. The complete remodelling process is controlled by osteocytes located within the bone matrix. Used with permission of Biomedical Tissue Research, University of York.

Knowledge of the three-dimensional (3D) structure of the ON&LCN would inform conclusions relating to the function and malfunction of osteocytes for different bone states in development, ageing, disease, disuse or exercise. More specifically, enhanced knowledge would improve the predictive power and accuracy of computational models, which attempt to elucidate the mechanisms of mechanotransduction using 3D geometries for the ON&LCN (Cardoso et al., 2013).

Recent finite element (FE) and fluid-structure interaction (FSI) models have used relatively low resolution image data and made *a priori* assumptions about the dimensions of the ON&LCN, such as the pericellular space (PCS) between the ON&LCN (Vaughan et al., 2014, Verbruggen et al., 2012, Verbruggen et al., 2014). One perspective on OP is that it is a failure of bone's adaptation to functional loading, that is, a failure of its mechanotransduction and/or mechanosensation capacity (Ciani et al., 2014, Sharma et al., 2012). Two mechanisms, direct response to matrix deformation and indirect response to fluid flow alteration have been suggested as possible pathways for mechanotransduction. To determine in detail how these mechanisms enable load transfer and signal transmission, detailed 3D mapping of the ON&LCN is needed. The fine structural details of osteocytes and their processes, the PCS and the connections between cells and the surrounding bone matrix need to be resolved and quantified. However, structural data of the ON&LCN at cellular and sub-cellular scales of adequate quality for realistic computational modelling approaches, have not been provided up to now. This is due to the inaccessible location of the osteocytes and to the sub-micrometre dimensions of the processes and canaliculi.

To date, images have been acquired using 2D methods, which have limited observation depths and 3D imaging techniques, which have either limited spatial resolution or field of view. Much data in the field has been obtained using X-ray computed tomography (μCT), which is an excellent method for imaging the bone matrix and LCN however does not image cellular material such as osteocytes. Electron microscopy (EM) can image cells and serial block face SEM (SBF SEM) is an emerging volume EM (vEM) technology which facilitates imaging of cells in high resolution and in 3D (Goggin et al., 2020). A correlative imaging approach using X-ray μCT and SBF SEM combines the benefits of each method to produce quantitative data on the ON&LCN which will go some way towards filling the unmet need described above.

1.2   Project Summary

This project aims to develop a correlative X-ray µCT and SBF SEM (CXEM) imaging framework, appropriate image processing and quantification methods and to apply this to characterisation of the ON&LCN in ageing and diseased bone tissue. A comprehensive review of the state of the art in high resolution bone imaging has been carried out and published (Goggin et al., 2016). SBF SEM, a novel vEM technique, has been optimised and applied to osteocytes in murine and human bone tissue (Goggin et al., 2020). SBF SEM has been combined with µCT in a CXEM workflow to take advantage of the high resolution hard and soft tissue imaging of the former and the large imaging volume of the latter. Relevant quantitative measures have been defined and extracted from the data. The CXEM workflow has been applied to murine tissue from juvenile and adult animals and to human OP and osteoarthritic (OA) tissue.

WORKING HYPOTHESIS

> **The 3D ON&LCN structure controls bone mechanotransduction and this structure is altered in disease.**

RESEARCH GOAL

> **To develop a framework for correlative X-ray and electron microscopy (CXEM) imaging which will characterise quantitatively, 3D osteocyte microarchitecture in normal and diseased human bone (osteoarthritic and osteoporotic) as well as normal murine bone across the life course.**

This thesis consists of 8 chapters.

Following this introduction (Chapter 1), Chapter 2 contains an overview of bone anatomy and physiology at the organ and cell scales, followed by a review of ultrastructural features.

Bone pathology with relation to osteocytes is then reviewed. Imaging methods in use for osteocytes are described and evaluated and contributions to osteocyte imaging to date sunmmarised. Correlative imaging and its application to bone tissue are described. A discussion of 3D quantitative measures is followed by a summary of the importance of high-resolution 3D imaging to computational modelling of osteocyte mechanobiology. Chapter 3 and Chapter 4 outline the methods optimised during the project and applied in later sections. In Chapter 3 the development and optimisation of sample preparation and image acquisition for bone imaging by CXEM is described. The aim is to prepare bone tissue for CXEM imaging fulfilling the requirements of both SBF SEM and μCT. Imaging methods are optimised so that results show the ON&LCN and produce images that can be segmented to produce informative volume renderings and analysed to produce quantitative data.

The objectives of Chapter 3 are:

- Optimisation of the stages of CXEM sample preparation for bone tissue namely, fixation, staining, decalcification and sample mounting by assessment of images.

- Optimisation of μCT and SBF SEM imaging conditions for bone tissue by analysis of signal to noise ratio, contrast to noise ratio and charging artefacts.

Chapter 4 outlines the image processing carried out on the raw CXEM data and the options for segmentation, quantification and 3D reconstruction. The aim is to process, segment and subsequently quantify 3D CXEM images to yield relevant quantitative data on the ON&LCN in murine and human bone tissue. The objectives of Chapter 4 are:

- To develop image processing strategies for CXEM data.

- To develop appropriate segmentation routines for CXEM data.

- To review existing standardised quantitative metrics for the ON&LCN and select measures relevant for studies of ageing and disease.

- To define new measures necessary for description of the ON&LCN at an ultrastructural level.

- To set out workflows for image processing, segmentation and quantification which will be used in CXEM investigations of murine and human tissue.

These workflows along with those for sample preparation and imaging set out in Chapter 3 form the basis of the methods used in Chapter 5 and Chapter 6 to characterise in 3D at high resolution (sufficient to visualise cell processes) and across length scales (from organ through tissue to cell scales) the ON&LCN of murine and human bone.

Chapter 5 describes the application of CXEM to murine tissue from juvenile and adult animals. Quantitative CXEM data on osteocyte measures across length scales are obtained and compared. Volumes containing tens of thousands of osteocytes and their lacunae are analysed using µCT and the cell density and porosity determined. Sub volumes of the tissues are imaged using SBF SEM at high resolution and detail of the cells, pericellular spaces and cell processes are characterised. This study objectives are:

- Produce and compare quantitative data on the 3D structure of the ON&LCN across length scales from juvenile and adult murine tibia. The data will include osteocyte number density, porosity, volume, shape, size, number of processes, process diameter and pericellular space volume.

- Provide quantitative data which will enable improved computational modelling of mechanobiological processes.

- Demonstrate the efficacy and value of CXEM as an imaging method for the ON&LCN across different length scales.

In Chapter 6, CXEM is applied to femoral head tissue from human donors with OP and OA, yielding quantitative hallmark data across length scales. Comparing the ON&LCN in these bone samples will improve understanding of bone disease and the mechanisms of change in the bone tissue and will produce realistic data which can be used to create computational models of mechanosensation and mechanotransduction. This study objectives are to:

- Produce quantitative data on the 3D structure of the ON&LCN in OP and OA bone. The data will include osteocyte number density, porosity, volume, shape, size, lacunar occupancy, number of processes, process diameter and pericellular space volume.

- Identify changes, if any, in the ON&LCN microstructure and ultrastructure in OP and OA human femoral head tissue.

- Provide quantitative data which will enable improved computational modelling of mechanobiological processes in human bone disease.

Chapter 7 discusses the main findings, sets them in context of the state of the art for bone imaging, summarises conclusions and provides an outlook on future work.

Chapter 2   Literature Review

Parts of this chapter have been published as ***High-resolution 3D imaging of osteocytes and computational modelling in mechanobiology: Insights on bone development, ageing, health and disease***. European Cells and Materials, Vol. 31 2016 (pages 264-295). P.M. Goggin, K.C. Zygalakis, R.O.C. Oreffo, P. Schneider.

This chapter contains an overview of bone anatomy and physiology at the organ and cell scales, followed by a review of ultrastructural features. Bone pathology with relation to osteocytes is then reviewed. The chapter describes and evaluates imaging methods in use for osteocytes, their advantages and disadvantages, correlative imaging and its application to bone tissue. A discussion of 3D quantitative measures is followed by a summary of the importance of high-resolution 3D imaging to computational modelling of osteocyte mechanobiology.

2.1   Bone structure

The roles of bone are manifold. The skeleton protects soft internal organs, gives shape to and supports the weight of the body and along with its attached muscles, enables locomotion. Bone tissue is a reservoir for minerals such as calcium and phosphate while the bone marrow stores lipids. The bone marrow is a centre of formation for red and white blood cells and platelets. Bone is capable of these functions because it is light weight, of high stiffness, strong and fracture resistant. At the same time, bone is elastic and flexible, able to absorb energy from deformation and to change shape. The structure and composition of bone are an exquisite design which contribute to its success as perhaps the ultimate biomaterial.

2.1.1   **Bone macrostructure**

The gross anatomy of long bones can be divided into the diaphysis (tubular centre) and epiphyses (proximal and distal ends). The walls of the diaphysis are composed of dense cortical (compact) bone, with a hollow centre which houses bone marrow. The epiphyses are coated with compact bone and are filled with trabecular (spongy or cancellous) bone (Figure 3). Cortical bone has a lamellar structure, perforated by canals carrying blood vessels while trabecular bone is a porous mesh of small beams or rods. The outer surface of compact bone is covered by a cellular/fibrous layer called the periosteum while the similar layer lining the interior and the surfaces of the trabeculae is the endosteum.
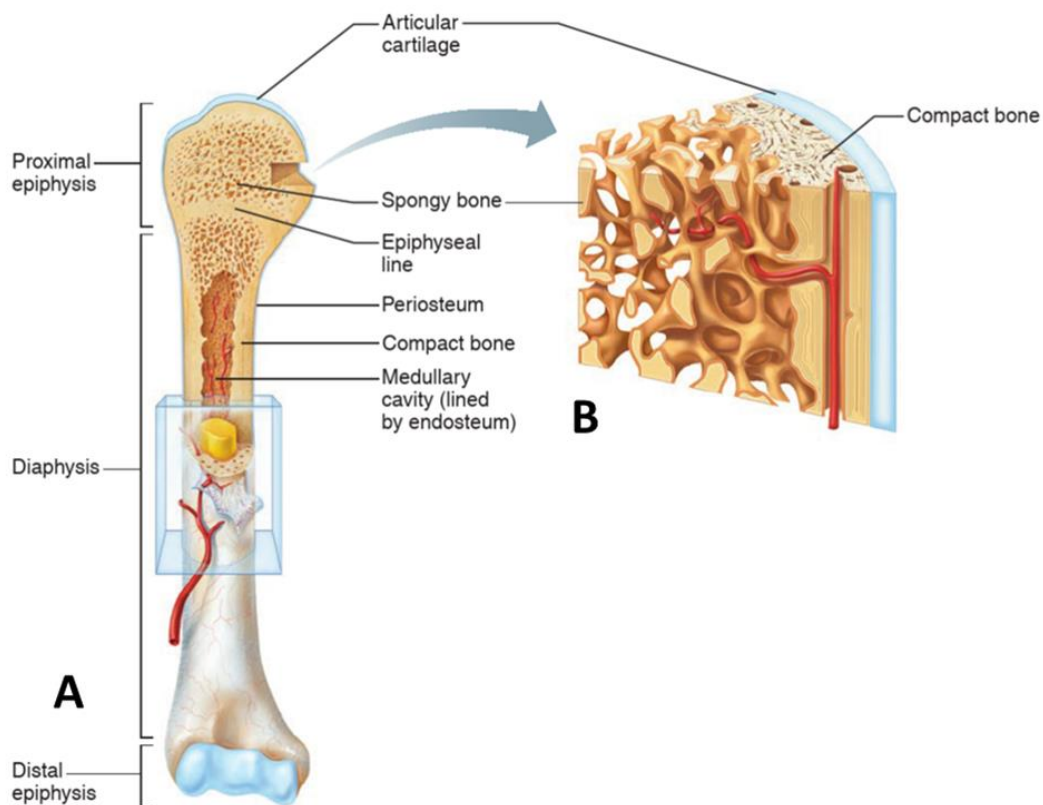
Figure 3   Anatomical structures of a typical long bone (humerus).

A   Anterior view of bone with longitudinal section cut away.

B   Diagram of the epiphysis showing spongy (trabecular) bone, compact (cortical) bone, cartilage (blue) and blood vessels (red). Adapted from (Marieb and Keller, 2017).

In humans, most mammals and some bird, reptile, and amphibian species the microstructural unit of bone is an osteon. Murine cortical bone does not have an osteonal arrangement (Jilka, 2013). Osteons are cylindrical structures 0.25 – 0.35 mm in diameter and from 1—10 mm in length, at the centre of which is a blood vessel surrounded by concentric layers of bone matrix (Figure 4) (Parfitt, 1994a). In the studies presented in this thesis murine tibial bone and human femoral head bone are used.
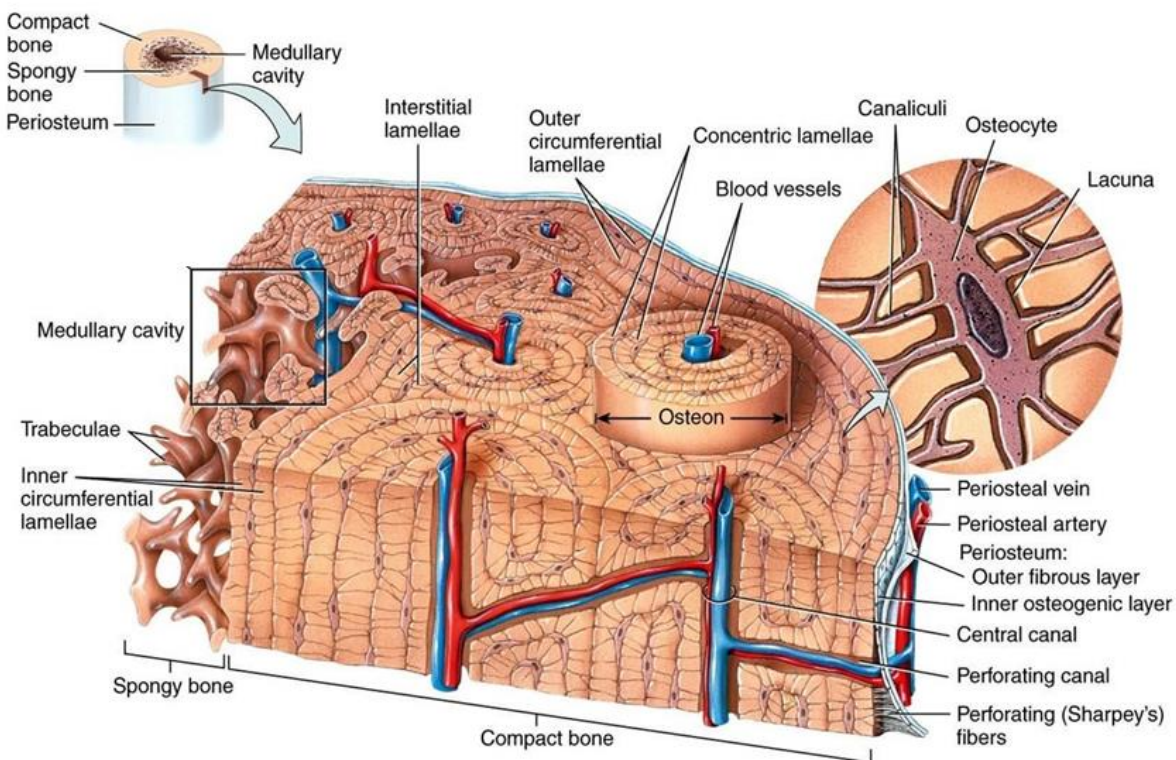
Figure 4   Structure of cortical (compact) bone
Section of the diaphysis of a long bone showing osteons surrounding vasculature (red and blue).
Inset circle shows an osteocyte within a lacuna. (From Tortora, 2012)

2.2   Femoral head anatomy

To set the human CXEM study in context, the anatomy of the human femoral head is briefly reviewed. The femur articulates with the pelvis to form the hip joint. The femoral head is nearly spherical, has a smooth surface covered in articular cartilage and measures 40-54 mm in diameter (Affatato, 2014). Under the cartilage a layer of subchondral bone covers

trabecular bone (Figure 5). Human bone microarchitecture is different from the murine

bone structure investigated using CXEM in Chapter 5 as it has an osteonal structure (Parfitt,

1994a, Jilka, 2013).
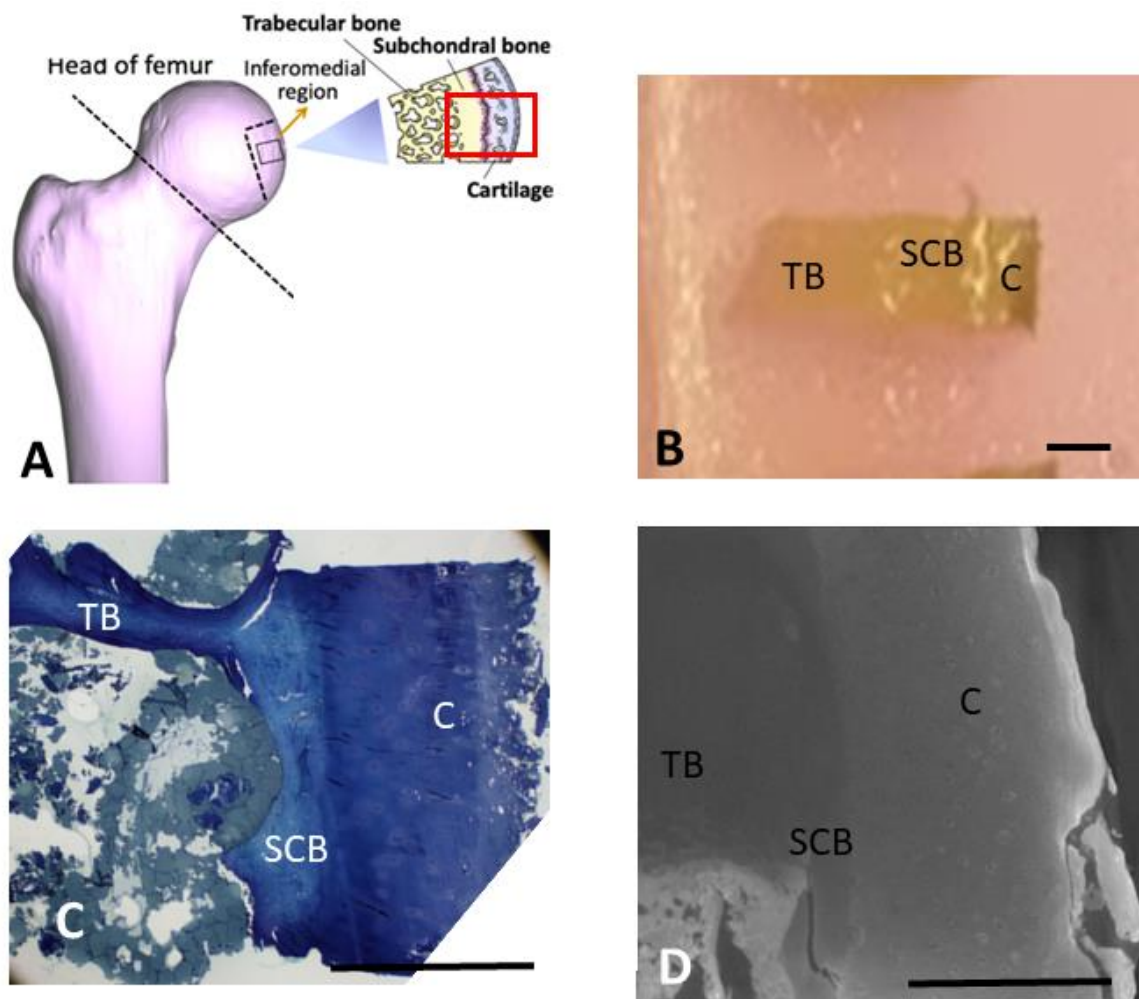
Figure 5   Femoral head anatomy

A   Femoral head and sub volume showing layers of cartilage, subchondral bone and trabecular bone. Adapted from (Cardinali et al., 2019).

B   Fixed human femoral head tissue from the area indicated by red rectangle showing cartilage (C), subchondral bone (SCB) and trabecular bone (TB). Scale bar = 1mm

C   Toluidine blue stained section of human femoral head (area indicated by red rectangle) showing cartilage (C), subchondral bone (SCB) and trabecular bone (TB). Scale bar = 1mm

D   μCT image of human femoral head tissue (area indicated by red rectangle) showing cartilage (C), subchondral bone (SCB) and trabecular bone (TB). Scale bar = 1mm

B-D Tissue prepared and imaged as described in Appendix B

2.2.1 **Bone cells**

Bone modelling, in which bone is resorbed from one surface and deposited on another, takes place during growth (Figure 2). Remodelling, in which bone is resorbed from areas of aged or damaged tissue and replaced by new bone, occurs during adulthood, as a response to injury and exercise. The cellular component of bone, responsible for these processes, is small by volume but crucial for maintaining structural integrity. The 4 main types of bone cell are illustrated in Figure 6 and described below.

2.2.1.1 **Osteoblasts**

Osteoblasts are located in a layer on the surfaces of growing bone and form new bone matrix. Osteoblasts secrete collagen which forms an extracellular matrix known as osteoid. Osteoblasts then produce crystals including hydroxyapatite which are deposited in the osteoid causing it to become mineralised (Capulli et al 2014). Osteoblasts which become entombed in the mineralising matrix become osteocytes.

2.2.1.2 **Osteoclasts**

Osteoclasts are motile, multinucleate cells which are found in areas of old or injured bone and are responsible for bone resorption (Arnett, 2013). Osteoclasts release acids and proteolytic enzymes into an extracellular sealed zone. These secretions dissolve hydroxyapatite crystals and degrade collagen fibres respectively, creating characteristic scalloped pits (Arnett and Orriss, 2018).

2.2.1.3 **Bone lining cells**

Osteoblasts which do not differentiate to osteocytes and do not undergo apoptosis become bone lining cells (BLC) which as suggested by their name, line bone surfaces. (Brown et al., 2013). BLC are slender and flat, anchor hematopoietic stem cells, stop osteoclastic bone

resorption occurring until required and play a crucial role in the transitions of bone remodelling (Kollet et al., 2006).

2.2.1.4 Osteogenic cells

Osteogenic (or osteoprogenitor) cells are multifunctional cells located on bone surfaces which originate from sources including mesenchymal stromal cells, pericytes and chondrocytes. Osteogenic cells can make bone, differentiate into osteoblasts, play crucial roles in control of bone remodelling, act on other bone cells and regulate soft tissues (Marie and Cohen-Solal, 2018).

2.2.1.5 Osteocytes

Osteocytes are stellate cells with numerous thin cell processes, housed within a system of lacunae and canaliculi in the hard bone matrix. Osteocytes are arranged as a network, making connections between other osteocytes, bone cells, bone marrow and the vasculature. The space between the osteocyte and the bone matrix is filled with circulating fluid, which carries solutes to and from the osteocyte. Osteocytes sense mechanical loading and produce biochemical signals to coordinate the activity of osteoblasts and osteoclasts (Bonewald, 2021). The ON&LCN will be described in more detail in later sections. Orchestrated by osteocytes, bone cells balance their activity to form bone during osteogenesis in the embryo, grow bone tissue during development, heal injury and fracture and remodel bone during life (Figure 6 and 7).
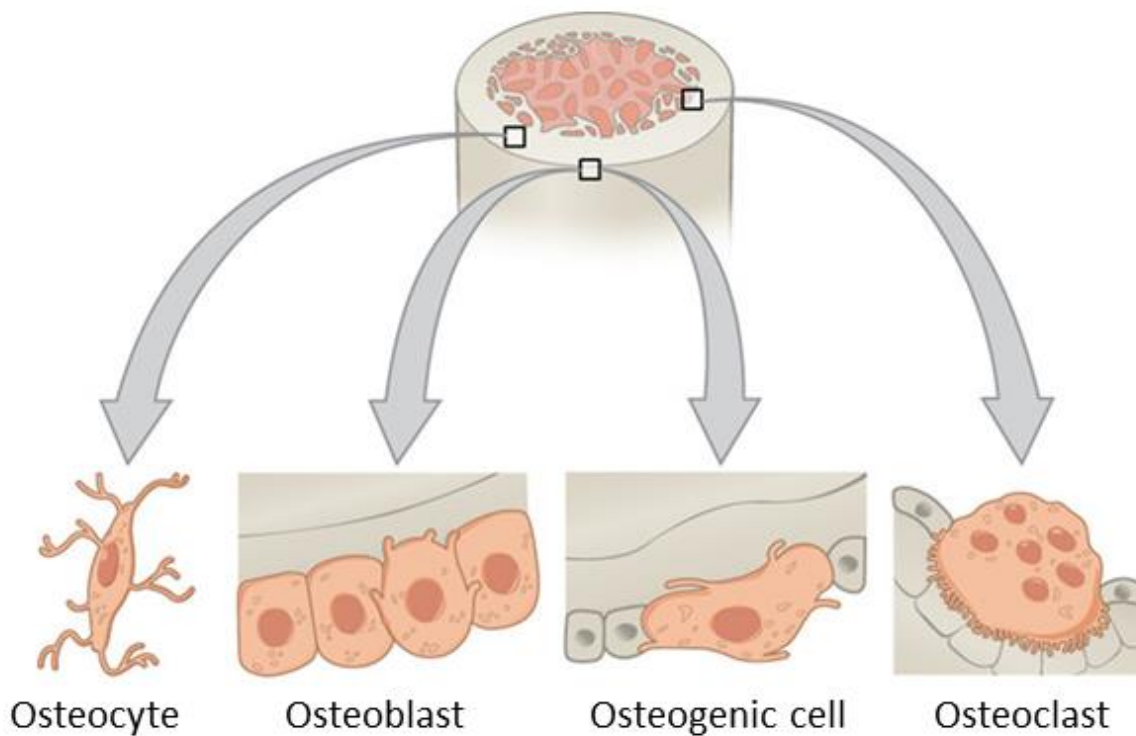
Figure 6   The cell types found within bone tissue

Osteogenic cells in the periosteum develop into osteoblasts which can later become embedded in the calcified matrix, change their structure and function and become stellate osteocytes. Osteoclasts resorb bone material. Adapted from (Betts, 2013) Access for free at https://openstax.org/books/anatomy-and-physiology/pages/1-introduction

2.3   Functions of osteocytes – direct and indirect

Osteocytes were once considered to be 'passive placeholders in bone' however, increasing knowledge has disproven this statement and shown that osteocytes are multi-functional (Robling and Bonewald, 2020). Osteocytes are at once communicators, mechanosensors, orchestrators of bone modelling and remodelling as well as endocrine cells and regulators of mineral homeostasis (Robling and Bonewald, 2020). The following section reviews the known functions of osteocytes, including direct interactions with the local environment and indirect regulation of other bone cells and distant organs (Figure 8).

2.3.1   **Mechanosensation and mechanotransduction**

When loading is applied to bone through exercise and activity, mechanical cues are sensed by osteocytes which secrete signalling molecules to osteoblasts and osteoclasts enabling the adaptation of bone in response. There is speculation around the signal reception mechanism(s) and physical stimulus/i detected during osteocyte mechanosensation. Candidates for signal reception include integrins (Geoghegan et al., 2019), primary cilia (Lee et al., 2015), spectrin, (Wu et al., 2017) calcium channels and gap junctions (Uda et al., 2017), discussed in Section 2.4.3. The stimulus producing a response to loading is also unclear – see Section 2.9.1. Mechanisms of mechanotransduction may include intracellular Ca^{2+} and extracellular adenosine triphosphate (ATP), nitric oxide (NO), prostaglandins (PGE2) and Wnt signalling molecules (Uda et al., 2017).

2.3.2   **Matrix remodelling and calcium homeostasis**

When physiological demand for calcium is increased, osteocytes can remove and replace bone matrix adjacent to the cell body and processes by perilacunar modelling. Enlarged lacunae observed during lactation and hibernation are attributed to this process which releases calcium rapidly and reversibly (Qing et al., 2012, Wysolmerski, 2013) . The removal of perilacunar matrix by osteocytes also occurs during diseases such as OP and rickets (Tsourdi et al., 2018) (Lane et al., 2006).

2.3.3   **Communication**

The arrangement of embedded osteocytes in a network which links to other bone cells, the bone marrow and the vasculature is essential for the functioning of bone as an organ. Interstitial fluid between the cells and bone matrix transports nutrients and biochemical

signals through the bone tissue, facilitating communication and helping to maintain cell

viability (Bonewald, 2007, Knothe Tate et al., 2004, Bonewald, 2006).

2.3.4 Regulation of osteoblasts

Osteocytes can both stimulate and inhibit osteoblasts. Osteoblastogenesis promoting

factors produced by osteocytes include Wnt proteins, nitric oxide (NO) and adenosine

triphosphate (ATP). Osteocytes regulate bone formation by producing sclerostin, which

inhibits formation of bone by osteoblasts (Joeng et al., 2017) (Figure 8).
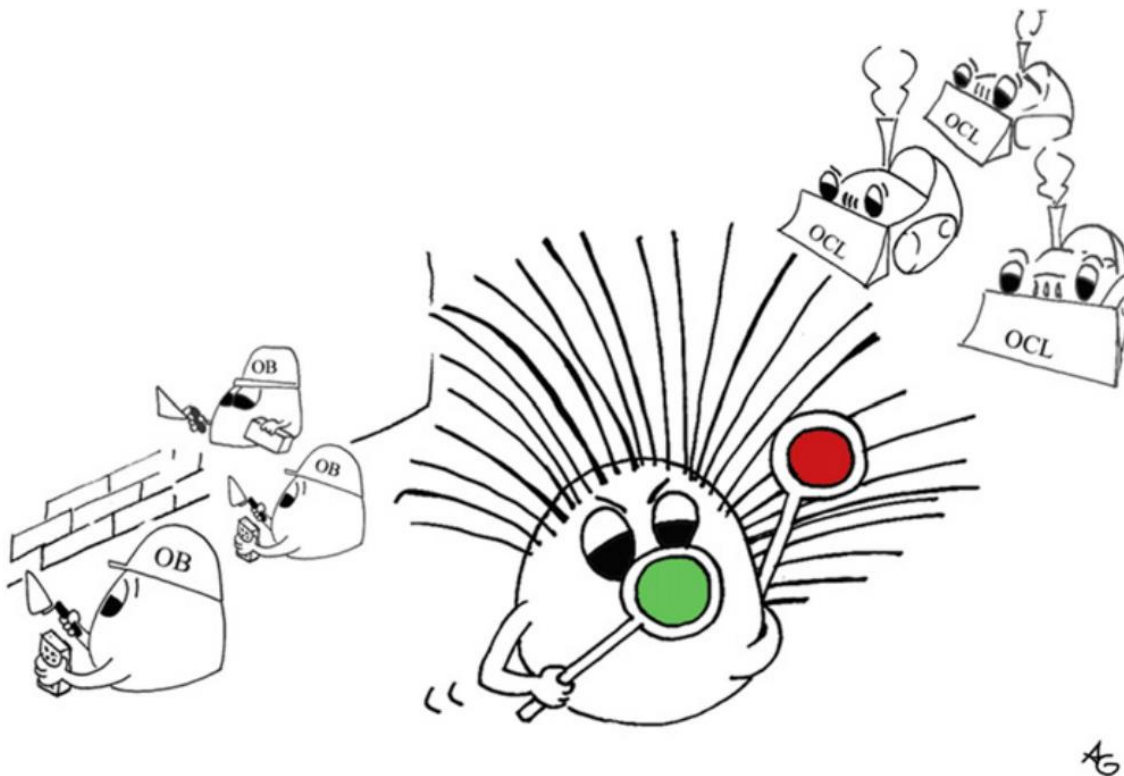
Figure 7   A representation of the central role of osteocytes in bone remodelling

Osteocytes sense mechanical load and produce signalling molecules which regulate the activity of osteoclasts (OCL) and osteoblasts (OB), leading to adequate bone mass and architecture. From (Klein-Nulend et al., 2013).

2.3.5 Regulation of osteoclasts

Osteocytes can influence bone resorption in both positive and negative directions (Figure

8). Production of receptor activator of NF-κB ligand (RANKL) by osteocytes is an activator

of osteoclast formation and function leading to a reduction in bone mass (Nakashima et al., 2011). Osteocytes produce osteoprotogerin (OPG) which inhibits osteoclastogenesis and NO which can supress resorption resulting in an increase in bone mass (Kong et al., 1999). Osteocyte death via apoptosis, in the presence of microdamage or bone fatigue may be a recruiting signal to osteoclasts, increasing resorption and local bone remodelling to repair damage (Verborgt et al., 2000).

2.3.6 Endocrine functions

In addition to affecting cells within bone, osteocyte secreted factors influence distant organs such as kidney showing that the osteocyte acts as an endocrine cell (Figure 8).

2.3.7 Additional functions

In addition to the functions outlined above, osteocytes may control hemopoietic stem cell mobilisation and lymphopoiesis (Divieti Pajevic and Krause, 2019) and have roles in cancer metastasis (Atkinson and Delgado-Calle, 2019) and the immune system (Zhou et al., 2019).

In summary, osteocytes are multi-functional cells, crucial for normal skeletal function, which integrate hormonal and mechanical signals to regulate bone mass. Osteocytes are mechanosensors, have the capacity to remodel their environment, act as endocrine cells, regulators of phosphate, bone resorbtion and bone formation. This is an extraordinary range of functions attributed to a cell type long considered to be inactive.
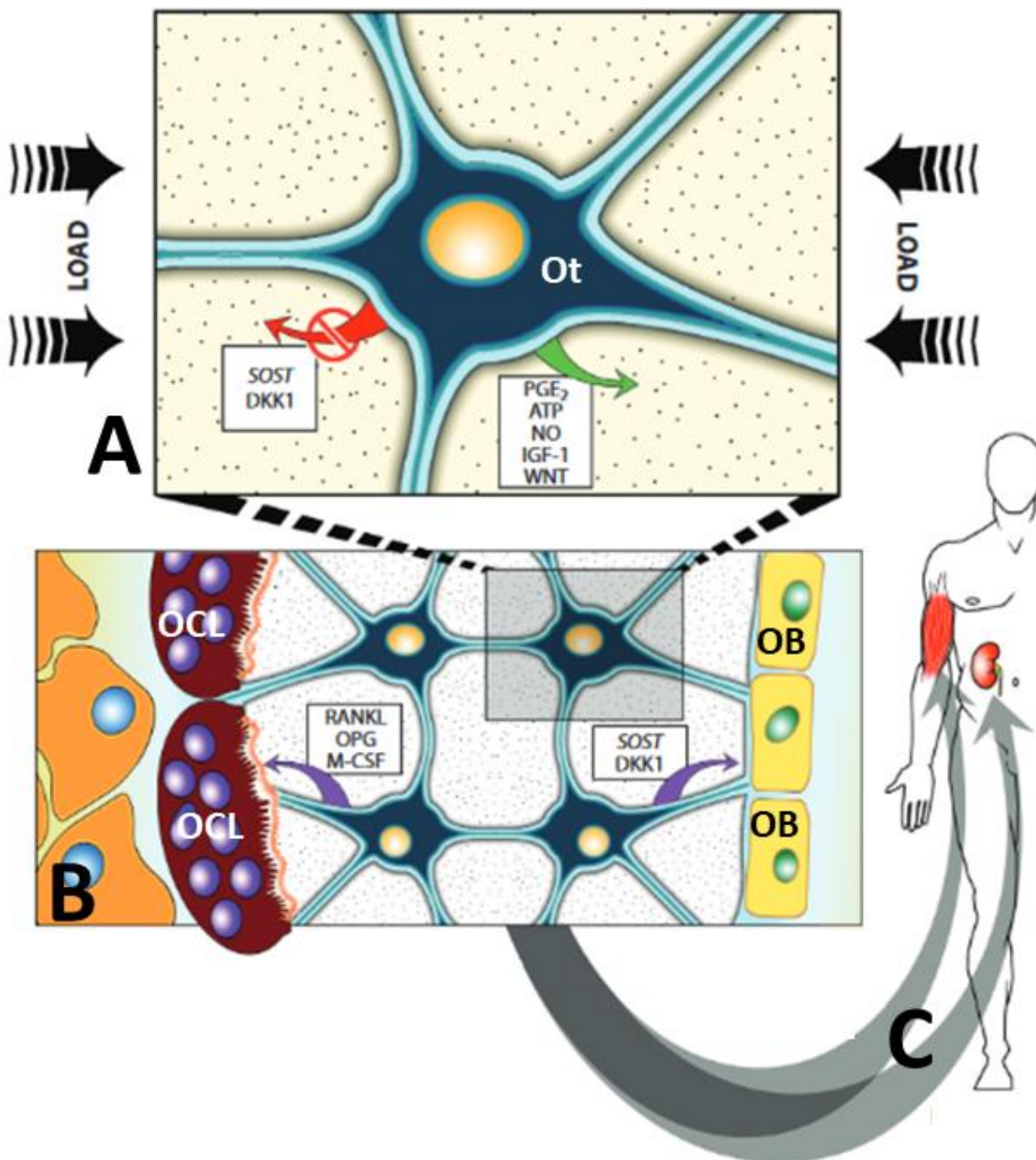
Figure 8   Direct and indirect relationships between osteocytes, bone cells and organs

A   Osteocytes (Ot) sense mechanical loading and either release or inhibit regulatory molecules (SOST - gene coding for the protein sclerostin, DKK1 - Dickkopf gene coding for an inhibitor of Wnt signaling, PGE2 - prostaglandin E2, ATP – adenosine triphosphate, NO – nitric oxide, IGF-1 – insulin-like growth factor 1).

B   Osteoblasts (OB) create and osteoclasts (OCL) resorb bone to maintain bone homeostasis in response to signalling molecules (RANKL, receptor activator of NF-κB ligand, OPG, osteoprotegerin, M-CSF, macrophage colony stimulating factor).

C   Osteocytes act as endocrine cells regulating phosphate in the kidney and maintaining muscle tissue.

From (Robling and Bonewald, 2020).

2.4 Identification of microstructural phenotypes of bone at the cellular and sub-cellular levels

This section reviews microstructural bone phenotypes and specifically, the structures of the ON&LCN (Figure 1) in different bone conditions. The following nomenclature will be adopted to describe different hierarchical levels of bone structure: internal bone structure at cellular level, studied by light microscopy (LM), including osteocyte cell bodies and osteocyte lacunae (in the μm range), internal bone microstructure at a level accessible by methods which overcome the diffraction limit of visible light, including osteocyte processes and canaliculi (μm-nm), and bone ultrastructure, including cell organelles, which can be observed by EM (in the nm range).

2.4.1 Anatomy and physiology of the ON&LCN

The significance of osteocytes was underestimated until it was reported that intermittent loading of tissue produces strain-related effects on the metabolism of both osteocytes and periosteal cells (Skerry et al., 1989). Fundamental questions remain unanswered as to how mechanical loading is sensed by osteocytes, how the signals are conveyed to other cells and how the mechanical signals are translated into biochemical signals (Bonewald, 2021, Klein-Nulend et al., 2013, Hemmatian et al., 2017a). For instance, one hypothesis is that interstitial fluid flow between the ON&LCN, driven by both extravascular pressure and cyclic mechanical loading, is the mechanism by which bone cells are informed of, and activated by internal and external mechanical stimuli (Cowin et al., 1991, Weinbaum et al., 1994a, Fritton and Weinbaum, 2009, Verbruggen et al., 2014, Klein-Nulend et al., 2013, Bonivtch et al., 2007, Gardinier et al., 2018). An alternative hypothesis involves direct matrix-cell mechanotransduction, where mechanical signals are transmitted from the whole-bone to the ON on a cellular and sub-cellular level (Nicolella et al., 2005, Wang et

al., 2015a, Nicolella et al., 2006). These postulated mechanisms are discussed in more detail in the context of computational modelling in Section 2.9.1 .

Variations in structure and connectivity of the ON&LCN have profound effects for both these postulated mechanisms (Jacobs et al., 2010). As the movement of bone fluid over the cell surface is significant, changes to the cell surface area and/or volume and fluid pressure will affect sensation. Changes in volume of lacunae, cells and pericellular spaces (PCS) would influence the magnitude of mechanical signals sensed by the osteocytes. The number of cell processes, the surface area, tortuosity and branching may also be significant in mechanosensation and thus need to be represented accurately in computational models. As strain sensing mechanisms depend on topology and geometry, it is essential to investigate these features (Sharma et al., 2007). The following sections will describe in more detail the microstructure (Section 2.3.2) and ultrastructure (Section 2.3.3) of the ON&LCN, changes in which may have implications for bone mechanobiology in health and disease.

2.4.2 Microstructure of the ON&LCN and bone matrix

Lacunar number density is reported to range from 14,600 (Bach-Gansmo et al., 2016b) to 90,000 (Hannah et al., 2010) per mm^3 in healthy human bone tissue, with most studies reporting values in the range 20,000 to 37,000 per mm^3 (Carter et al., 2013b, Gauthier et al., 2018, Dong et al., 2014b) . Osteocyte number density is between and 40,000 and 60,000 per mm^3 in healthy murine bone tissue (Tiede-Lewis et al., 2017). To the knowledge of the author, no comprehensive 3D studies of osteocyte density in human bone tissue have been reported to date.

Osteocyte number density in remodelling bone is elevated compared with inactive tissue in both healthy controls and in women with hip fracture, indicating that osteocytes may

contribute to bone homeostasis (Power et al., 2002). Mice with targeted deletion of osteocytes are resistant to bone loss induced by unloading (Tatsumi et al., 2007), and load-related morphological and biochemical responses have been observed in osteocytes, supporting the theory that osteocytes act as mechanosensors (Zhang et al., 2006).

Occupancy data, the proportion of osteocyte lacunae occupied by a cell, reflecting the loss of some osteocytes and the survival of others, is an important consideration when using lacunar density data as a representation of osteocyte data. The number of empty lacunae increases with age (Qiu et al., 2002b, Tiede-Lewis et al., 2017, Piemontese et al., 2017). As empty lacunae are the result of osteocyte cell death, changes in lacunar occupancy could be indicative of changes in osteocyte cell death (Milovanovic and Busse, 2020). In a study of female human femoral neck tissue (mean age 81 ± 2.9) the mean percentage lacunar occupancy was 48.2 ± % (Power et al., 2001). With age, lacunar occupancy in the human femoral head is known to decline from 88 ± 7% (10-29 years) to 58 ± 12% (70-89 years) (Dunstan et al., 1990).

Each osteocyte lacuna in human bone tissue has 53-126 canaliculi (Varga et al., 2014). In murine tissue the number of canaliculi per lacuna is 40 – 60 and the number of processes per cell is 20-40 (Tiede-Lewis et al., 2017). Human osteocytes are estimated to have between 18 – 106 processes (Beno et al., 2006). Moreover, the shape and size of the osteocyte and the PCS reflect cell viability (Knothe Tate et al., 2004), while studies of rat bone have found a relationship between age and the number of canaliculi (Okada et al., 2002). At the same time, the number and orientation of osteocyte cell processes are changed over the life course (Holmbeck et al., 2005), with increased numbers of processes extending towards the vascularity than towards the mineralisation front when the cell is fully developed and enclosed in the mineralised matrix (Knothe Tate et al., 2004). Time-

lapse microscopy has shown that cultured osteocytes, observed during the mineralisation process, can expand and contract within lacunae, and extend and retract their processes (Veno P.A., 2007, Dallas and Bonewald, 2010, Dallas and Moore, 2020, Shiflett et al., 2019). Thus, osteocytes could be considered as dynamic structures which may alter in response to external stimuli (Dallas and Bonewald, 2010, Dallas et al., 2009). Finally, changes to the shape, size and organisation of osteocytes have been observed in histological studies of pathological bone conditions (Knothe Tate et al., 2004), which will be discussed in more detail in (Section 2.6.2).

The amplification of strain in osteocyte lacunae is affected by the local bone tissue properties with maximum strain relating inversely to the perilacunar tissue modulus (Nicolella et al., 2006, Bonivtch et al., 2007). Therefore, changes in bone matrix properties will affect osteocyte mechanosensation. Studies have revealed that the mass density of bone matrix varies with distance from the LCN (Hesse et al., 2015, Nango et al., 2016, Stachnik et al., 2020) with the matrix adjacent to the LCN porosity being most dense. This observation supports the hypothesis that mineral exchange occurs at the interface of the LCN in bone mineralisation and mineral homeostasis.

2.4.3 ON&LCN at the ultrastructural level

In addition to typical cell machinery (nucleus, mitochondria, endoplasmic reticulum, Golgi apparatus, etc.) the ON exhibits other ultrastructural features important for mechanobiology, which are discussed in the following and illustrated in Figure 9.

2.4.3.1 Tethering elements

Interstitial fluid flow within the LCN is hypothesised to generate shear stress which may stimulate the osteocyte and its processes (Weinbaum et al., 1994b, Wittkowske et al.,

2016). A transmission electron microscopy (TEM) image-based model of strain amplification (Han et al., 2004) introduced the concept of tethering elements, which are protein links connecting osteocyte processes and the surrounding mineralised canaliculi. The model predicts that fluid flow deforms the tethering elements, creating drag force that imposes a hoop strain on actin bundles within the process. It has later been expanded to include integrin attachments to conical projections on the canalicular wall, which can amplify the mechanical strain (Figure 10) (Wang et al., 2007, Geoghegan et al., 2019).

2.4.3.2   **Glycocalyx**

The strain amplification model described for the tethering elements (Han et al., 2004, Wang et al., 2007) suggests that only the osteocyte processes are sensitive to mechanical load, and that the cell body is insensitive to strain. Although studies using cultured cells suggest that both are mechanosensitive (Burra et al., 2010), the exclusive sensitivity of the processes is supported by further studies (Thi et al., 2013, Adachi et al., 2009, Bonivtch et al., 2007, Han et al., 2004). Furthermore, these studies indicate that the glycocalyx of the osteocyte processes (but not of the cell body) plays an essential role for bone mechanotransduction (Burra et al., 2010). In particular, the glycocalyx of the osteocyte processes was found to be required for the formation of integrin attachments, which may be important mechanotransducers conveying mechanical signals to the osteocyte (Burra et al., 2010, Han et al., 2004). It has also been shown that an intact glycocalyx is necessary for certain biochemical signals to be released in response to fluid flow (Reilly et al., 2003). The ECM projections where integrins are located have been found to have the highest sensitivity and are likely to produce a mechanobiological response *in vitro* (Verbruggen et al., 2014).
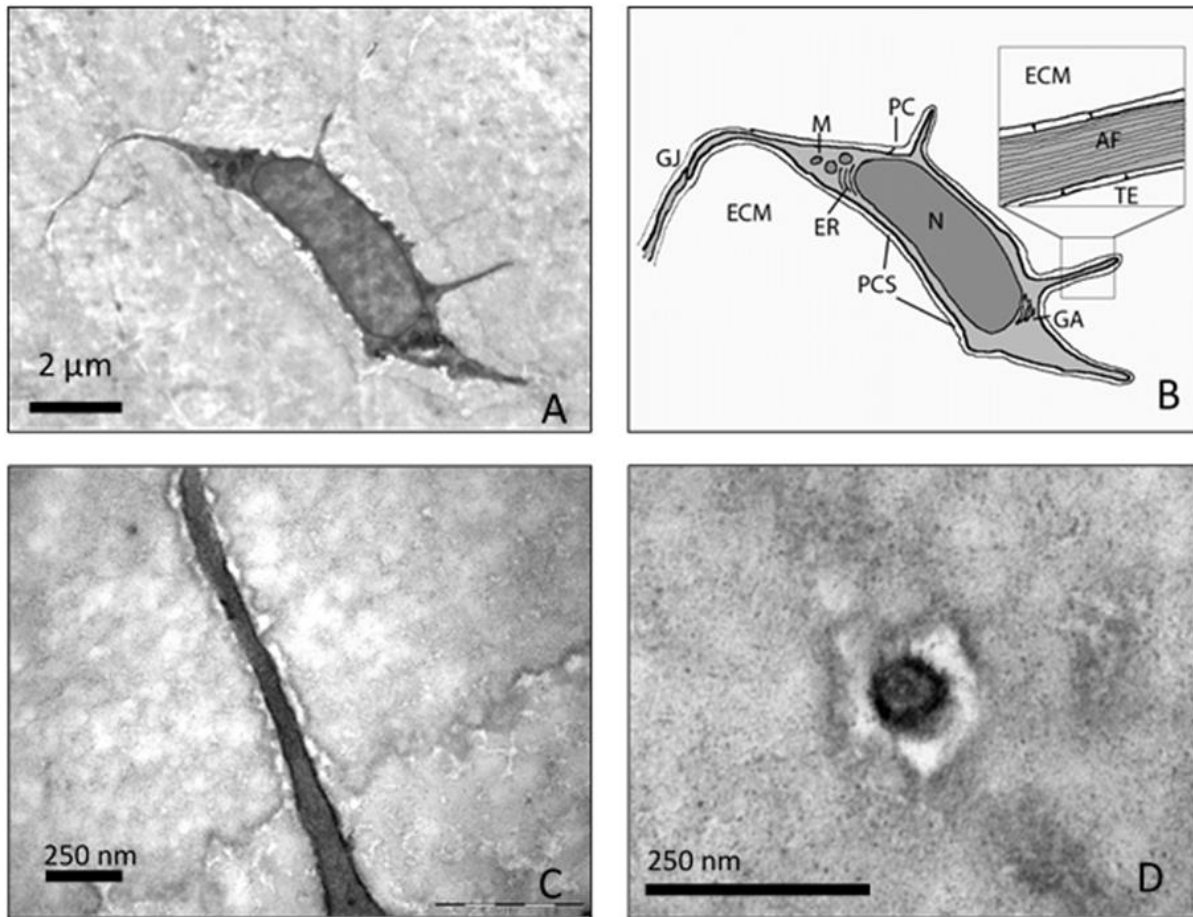
Figure 9   Osteocyte and typical cell machinery

A   TEM image of an osteocyte in murine tibia.

B   Diagram of the osteocyte in A and the typical cell machinery. Abbreviations: actin

             filaments (AF), endoplasmic reticulum (ER), extracellular matrix (ECM), gap junction

             (GJ), Golgi apparatus (GA), mitochondria (M), nucleus (N), primary cilium (PC),

             pericellular space (PCS), tethering elements (TE).

C   Higher magnification of cell process in longitudinal section.

D   Higher magnification of cell process in transverse section. From (Goggin et al., 2016)

2.4.3.3   Cytoskeleton

The cytoskeleton consists of a network of filaments in the cytoplasm which give the cell

shape and stability. Actin filaments are present in the cell body and form the core of

osteocyte processes. The cytoskeleton is crucial for the maintenance of cell shape,

membrane tension and cell-cell connections (Tanaka-Kamioka et al., 1998). Connections

between actin filaments in the cell processes and the PCM may be important in mechanical strain transduction and amplification (You et al., 2001, You et al., 2004, Han et al., 2004).
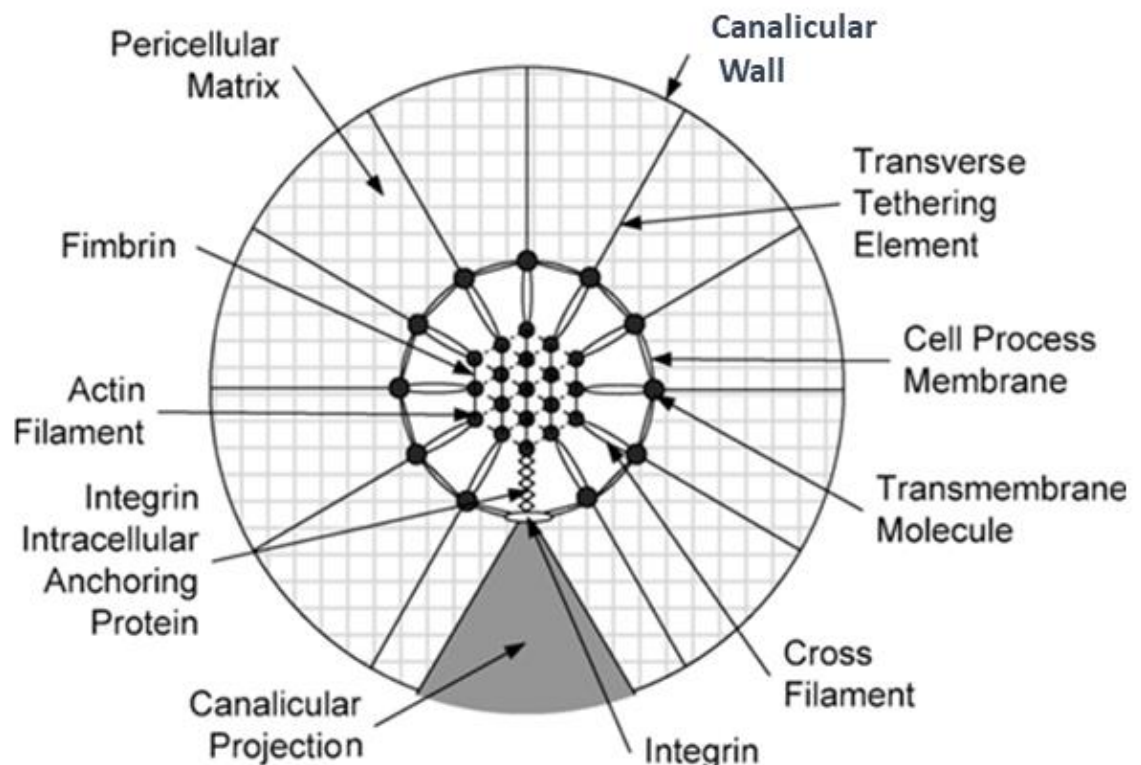
Figure 10   Structural model for an osteocyte cell process within a canaliculus

Transverse cross-section of an idealised structural model for a cell process in a canaliculus attached to a focal attachment complex and tethered by the PCM. The sketch (not to scale) shows the osteocyte process and its attachment to the canalicular wall, including the structure of the central actin filament bundle and the tethering elements. Image from (Wang et al., 2007)

2.4.3.4   Gap junctions

Cells communicate through gap junctions aligned with those on neighbouring cells (Figure 9). Gap junctions are found between osteocytes and between osteocytes and osteoblasts (Doty, 1981, Palumbo et al., 2004), raising the possibility that gap junctions can transmit information from signals, sensed by embedded osteocytes, to cells at the bone surface. Fluid flow has been shown to result in opening of gap junctions in osteocyte-like cells in culture (Cheng et al., 2001).

2.4.3.5   **Primary cilia**

Primary cilia act as flow sensors in the embryo and are linked to mechanotransduction in polycystic kidney disease (Ong and Wheatley, 2003). Accordingly, it has been suggested that osteocyte primary cilia may play a role in bone mechanotransduction and mechanosensation by acting as flow or strain sensors (Whitfield, 2004, Temiyasathit and Jacobs, 2010, Malone et al., 2007). This hypothesis is supported by studies in mice, which show that deletion or disruption of ciliary genes leads to a disruption of skeletal mechanosensing (Xiao et al., 2011) or reduced bone formation (Qiu et al., 2012). However, cilia are only present on a small fraction of osteocytes and it is also suggested that cilia act as chemical or hydrostatic pressure sensors rather than fluid flow sensors (Coughlin et al., 2015, Bell, 2008). These results conflict with studies carried out in rat tibiae, where 94% of osteocytes expressed primary cilia (Uzbekov et al., 2012), leaving the involvement of primary cilia in mechanotransduction open to debate.

2.4.3.6   **Integrins**

Integrins are receptors and transducers that connect the cytoskeleton and the ECM (Figure 10). It has been proposed that integrins play a role in bone mechanotransduction and mechanosensation (Salter et al., 1997, Haugh et al., 2015, Thi et al., 2013). The transfer of force across adherins allows stress applied to the cell membrane to influence organelles including the nucleus and mitochondria (Aarden et al., 1994, Ozcivici et al., 2010, Ross et al., 2013, Geoghegan et al., 2019).

2.5 Identification of microstructural phenotypes of developing bone at the cellular and sub-cellular levels

2.5.1 Changes in bone during development

The involvement of osteocytes in bone development has been little explored to date. During embryonic development, hyaline cartilage, formed by chondroblasts, acts as a matrix template. Osteoblasts start the ossification process by replacing the cartilage with osteoid, a soft collagenous matrix, into which is deposited hard hydroxyapatite-based mineral. This first primary bone has an irregular arrangement of collagen fibres, a relatively low mineral content and is replaced by stronger, more organised, secondary or lamellar bone during foetal development. After ossification, cartilage remains only at the joint surface and the epiphyseal plate. Blood vessels invade the tissue and bones continue to grow in length due to activity at the epiphyseal plate and in diameter through modelling at the periosteum until early adulthood, at a rate controlled by hormones (see Figure 11). During development, bone shape and competence are affected by mechanical load, hormones, growth factors and genetics (Gkiatas et al., 2015).

Rapid growth in young animals, including humans, is characterised by increases in bone size, mineral mass and mechanical properties (Ferguson et al., 2003). Lamellar bone displays increased mechanical resistance and bone quality (characterised by higher bone volume fraction, better microscale organisation and higher bone mineralisation) compared to woven bone (Zimmermann et al., 2019).
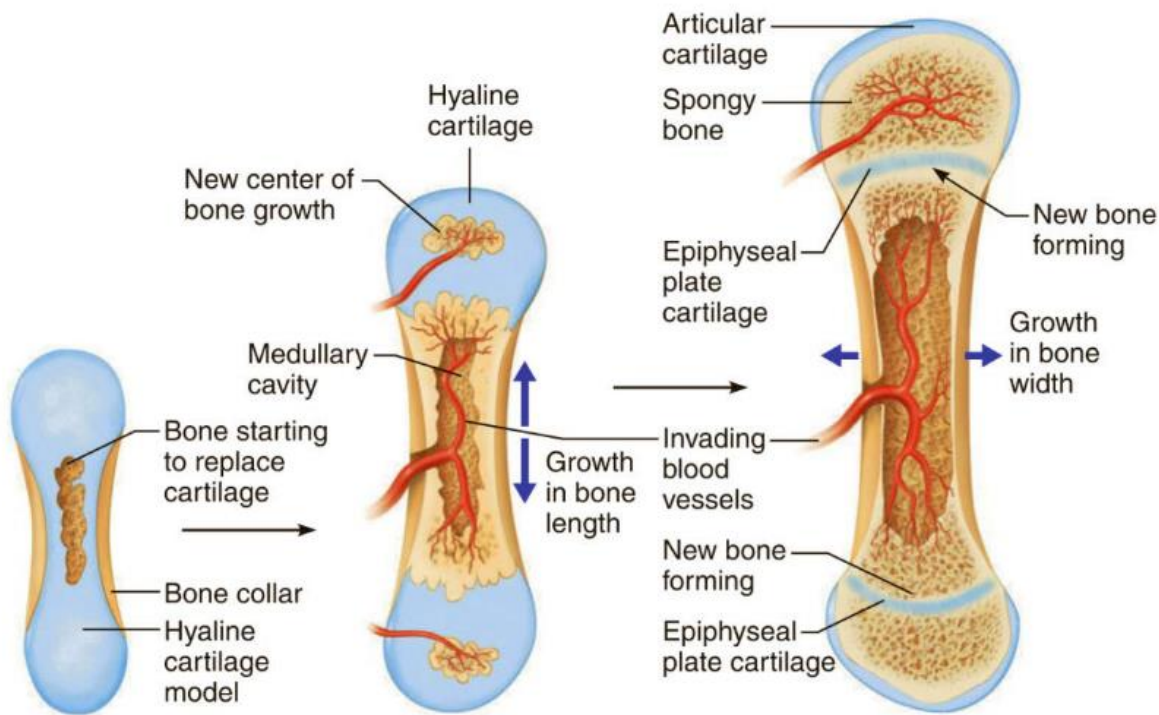
Figure 11   Endochondral ossification across the lifecourse

Stages of long bone formation in an embryo, foetus and child. During development the hyaline cartilage model (blue) is vascularised and replaced by bone (yellow). From (Marieb, 2019).

Previous imaging studies of bone development are outlined in Table 1. Interestingly, the minimum and maximum ages used to represent stages of development vary considerably. Definitions of terms like embryonic, foetal, infantile, young, juvenile, mature and old are open to interpretation. The species under investigation include rat, mouse, chick, rabbit and human. Several studies comparing the ON&LCN in different species found that there were no correlations in osteocyte shape, size, distribution and number density with the species (Ferretti et al., 1999, Remaggi et al., 1998, Palumbo et al., 2004, Sugawara et al., 2011). However, the variation in species, anatomical location and ages chosen to represent stages of development make direct comparisons between results of these studies of bone development difficult to interpret.

Table 1   Studies of developing bone, imaging techniques, species and age ranges

Reference	Species	Bone	Imaging technique	Age minimum	Age maximum
(Okada et al., 2002)	Rat	Mandible	SEM	3 weeks	80 weeks
(Ferguson et al., 2003)	Mouse	Femur	LM	4 weeks	104 weeks
(Zimmermann et al., 2019)	Human	Femur	LM, SR X-ray diffraction	Foetal (22 weeks gestation)	14 years
(Wang et al., 2016)	Chick	Calvaria	LM	19-21-day embryo (young osteocyte)	19-21-day embryo (mature osteocyte)
(Hirose et al., 2007)	Mouse	Femur	LM	3 days	12 weeks
(Sugawara et al., 2013)	Mouse	Femur	CLSM	Embryonic (19 day)	6 weeks
(Holmbeck et al., 2005)	Mouse	Femur, tibia	LM and TEM	20 days	70 days
(Jandl et al., 2020)	Human	Iliac crest	µCT, LM, SEM	Infant (0-6 months)	Young adult (18-25 years)
(Glatt et al., 2007)	Mouse	Femur, tibia, vertebra	µCT, LM	1 month	20 months
(Brodt et al., 1999)	Mouse	Femur, tibia	LM	4 weeks	24 weeks
(Buie et al., 2008)	Mouse	Vertebra, tibia	µCT (in vivo)	6 weeks	48 weeks
(Kamioka et al., 2009)	Chick	Calvaria (parietal and orbital ridge)	UHVTEM	16 day embryo parietal site	16 day embryo orbital ridge site

SEM – scanning electron microscopy, LM – light microscopy, SR – synchrotron radiation, CLSM – confocal laser scanning microscopy, TEM – transmission electron microscopy, µCT – micro computed tomography, UHVTEM – ultra high voltage TEM.

Publications on the involvement of osteocytes in bone development include a study of the development of bone in zebrafish (Jemielita et al., 2013) and a study of the expression of sclerostin in the developing zebrafish (McNulty et al., 2012) both using light microscopy. X-ray micro-computed tomography (µCT) and histology have been used to study skeletal mineralisation in mice (Hafez et al., 2015). A study of rats at different ages, using acid-

etched resin casting and scanning electron microscopy (SEM) to investigate the LCN, showed a developing canalicular system fusing with neighbouring canaliculi and round osteocyte lacunae with short and thick canaliculi (Okada et al., 2002). Investigation and imaging of developing bone phenotypes is an area which requires further exploration in order to clarify the functional role of osteocytes. Chapter 5 of this thesis contains a further discussion of bone development and an investigation of the ON&LCN of juvenile and adult murine bone.

2.5.2 Changes in the ON&LCN during development

Following examination of the changes during bone development, at a macro level, this section will consider the changes in the ON&LCN which occur from foetus through juvenile to adult such that the changes can later be related to changes in quantitative hallmarks derived in the current CXEM study. This section will consider the changes in the ON&LCN which occur from foetus through juvenile to adult such that the changes can later be related to changes in quantitative hallmarks derived in the CXEM study of murine bone in Chapter 5.

Osteocytes develop during embryonic and juvenile bone formation when osteoblasts become embedded within osteoid and differentiate to a stellate shape (Figure 12). This transition is accompanied by a reduction in cell volume and cell organelle content and the formation and elongation of thin cytoplasmic processes extending from the cell body (Knothe Tate et al., 2004, Palumbo et al., 2004, Hirose et al., 2007) firstly towards the mineralised matrix, and later towards the vascular space (Palumbo, 1986, Barragan-Adjemian et al., 2006).

Between 3 and 14 days after birth an increased number of osteocytes is observed in mouse bone, followed by a subsequent decrease (Bortel et al., 2015). In rodent studies, 32-week-

old mice displayed 8.1% lower number density than 15-week-old animals (Lai et al., 2015).

A SR CT study of mouse tibia revealed no significant difference in lacunar number density

between 15-week-old and 10-month-old animals (Núñez et al., 2018).
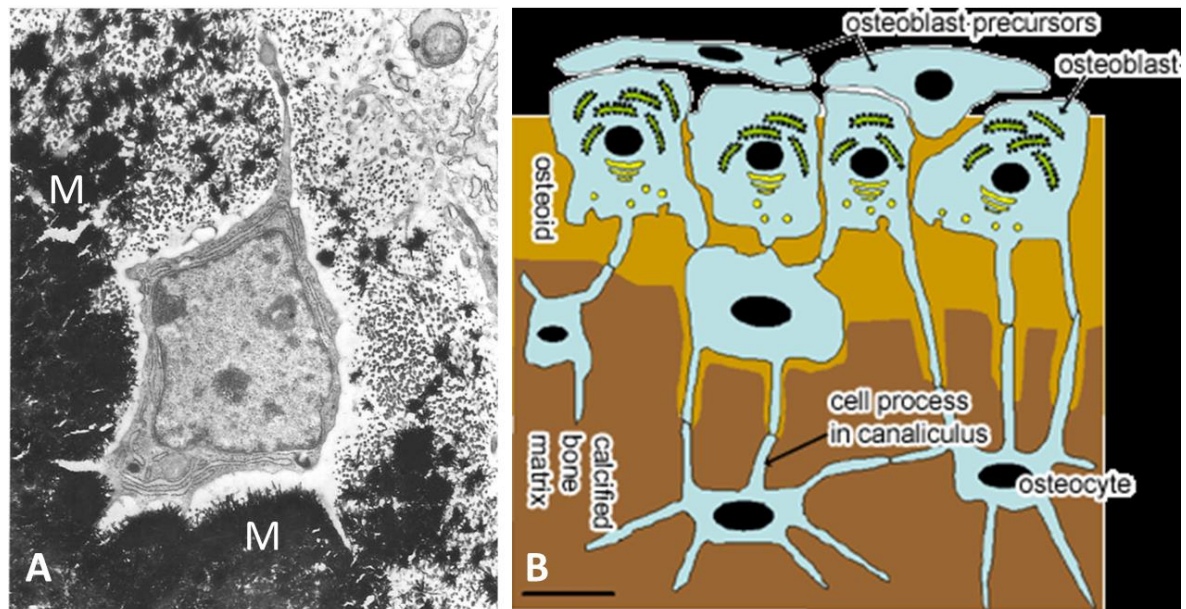
Figure 12   Development of osteocytes

A   TEM image of a pre-osteocyte during the embedding process almost completely
     surrounded by mineral crystals (M). Note the long slender processes extending from the
     cell (Palumbo, 1986). This micrograph was originally published without a scale bar.

B   Diagram showing the stages of osteocyte development from osteoblast precursor cells,
     through osteoblasts to embedded osteocytes. Scale bar = 10 μm. (Peckham, 2003).

Osteocyte lacunar number density based on lacunar area measurements was observed to

be higher in foetal to 1-year-old woven human bone tissue compared with 2 to 14-year-old

lamellar human bone tissue (Zimmermann et al., 2019). Lacunar density is significantly

increased in infants (0-6 months) and children (2-8 years) compared to young adults (8-25

years) based on area measurements (Jandl et al., 2020). Lacunar number density decreases

with age in humans by as much as 39% (30-91 years) (Mullender et al., 1996b).

Osteocyte processes become interconnected as the processes become embedded and develop into a 3D network. Previous studies, conducted using 2D imaging methods, reported that in mice and in humans, the osteocyte network becomes progressively more regular during bone growth (Sugawara et al., 2013, Hirose et al., 2007, Zimmermann et al., 2019, Holmbeck et al., 2005). A study in chick bone found that the length of the processes between osteocytes increased (non-significantly) during development (Wang et al., 2016).

Young osteocytes and lacunae in rat and chick bone are spherical and become ellipsoid during development (Okada et al., 2002, Kamioka et al., 2009, Wang et al., 2016). Osteocyte and lacunar size decrease with growth in humans (Jandl et al., 2020, Zimmermann et al., 2019) and (by 22%) in chick (Wang et al., 2016). Lacunae from adult rat bone have more canaliculi and the canaliculi have more branches than juvenile rat bone (Okada 2002).

In summary, during development, osteocytes and lacunae become more elongated in shape, smaller in volume, have more canaliculi and are arranged more regularly. After an initial increase in density, osteocyte and lacunar number density decrease with age.

2.6 Identification of microstructural phenotypes in ageing, disease and other bone states at the cellular and sub-cellular level

Various studies have compared ON&LCN morphology, behaviour and changes in terms of age (summarised in Table 2). It is notable that the inconsistency in species studied, choice of anatomical area, imaging methods used and the variation in reporting measures can make direct comparisons between studies challenging.

2.6.1 Ageing

With age, bone mineral density and cortical bone thickness decrease and there is an increase in bone porosity (Seeman, 2013). Lacunar number density decreases with age, by

as much as 39% (Mullender et al., 1996b, Qiu et al., 2002a, Busse et al., 2010, Ashique et al., 2017). It has also been observed that there is no significant change in lacunar density with age (Carter et al., 2013a, Hemmatian et al., 2018). The number of empty lacunae increases with age (Qiu et al., 2002b, Tiede-Lewis et al., 2017, Piemontese et al., 2017). A study using human bone tissue provided evidence that the decline in lacunar density is associated with the accumulation of microcracks (Vashishth et al., 2000). In the same study, it was noted that ageing bone tissue is characterised by increased heterogeneity in the spatial organisation of osteocytes. A study of rat bone at different ages using resin casting of the LCN, SEM and CLSM demonstrated that the LCN changes with age. Animals of advanced age had slender, flat lacunae with fewer, smaller canaliculi. (Okada et al., 2002). Smaller, rounder lacunae have been observed in aged humans (Carter et al., 2013a) and in aged mice (Heveran et al., 2018, Hemmatian et al., 2018). A sex difference was observed in one study where all subjects showed a reduction in cell volume with age but only males showed a corresponding reduction in lacunar volume (Tiede-Lewis et al., 2017).

Studies have found a relationship between age and both the number and orientation of osteocyte processes and canaliculi. A roughly 30% reduction in the number of canaliculi has been observed in elderly humans (Milovanovic et al., 2013). A similar result was found in aged mice (Kobayashi et al., 2015). It has been shown that canalicular occupancy by processes also decreases with age (Tiede-Lewis et al., 2017) Conversely, it has been reported that the number density of canaliculi in mouse bone is unaffected by age, but that the dimensions of the PCS (in cortical but not in trabecular bone) increase due to an expansion of the canalicular wall (Lai et al., 2015).

In summary, with increasing age, osteocyte lacunar density (and presumably osteocyte density) decrease, the number of empty lacunae increases, cells become smaller and

rounder, cell connectivity decreases and there is a consequent decrease in osteocyte response to loading (Table 2).

Table 2   Changes in the osteocyte and the lacuno-canalicular networks with age

Measure	Osteocyte /Lacuna	Species/sex	Reference
Number density	=Lacunae	Human F	(Carter et al., 2013a)
	=Lacunae	Mouse F	(Hemmatian et al., 2018)
	↓ Lacunae	Human M+F	(Vashishth et al., 2000)
	↓ Lacunae (-8.1%)	Mouse	(Lai et al., 2015)
	↓ Lacunae	Human M+F	(Busse et al., 2010)
	↓ Lacunae (-21.4%)	Human F	(Ashique et al., 2017)
	↓ Lacunae -24%	Human F	(Qiu et al., 2002a)
	↓ Lacunae -33%	Mouse M	(Heveran et al., 2018)
	↓ Lacunae -39%	Human M+F	(Mullender et al., 1996a)
	↓ Osteocytes	Human M+F	(Qiu et al., 2002a)
Occupancy	↓ Lacunae	Human M+F	(Qiu et al., 2002a)
	↓ Lacunae	Mouse	(Tiede-Lewis et al., 2017)
	↓ Lacunae	Mouse	(Piemontese et al., 2017)
	↓ Canaliculi	Mouse	(Tiede-Lewis et al., 2017)
	↓ Canaliculi 77-97%	Human F	(Qiu et al., 2006)
Volume	↓Osteocyte	Mouse M+F	(McCreadie et al., 2004)
	↓Lacunae	Mouse M	(Tiede-Lewis et al., 2017)
Shape	Slender flat	Human F	(Okada et al., 2002)
	Smaller rounder	Human F	(Carter et al., 2013b)
	Smaller rounder more oblate	Mouse M	(Heveran et al., 2018)
	Smaller rounder more oblate	Mouse M	(Hemmatian et al., 2018)
Processes and canaliculi	↑ Number canaliculi	Rat M	(Okada et al., 2002)
	↑ Branching canaliculi	Rat M	(Okada et al., 2002)
	↓ Number canaliculi -30%	Human	(Milovanovic et al., 2013)
	↓ Organisation canaliculi	Mouse	(Kobayashi et al., 2015)
	↓ Canalicular area	Human F	(Ashique et al., 2017)
	= Number canaliculi	Mouse M	(Lai et al., 2015)
Spatial organisation	↓Spatial organisation	Human M+F	(Vashishth et al., 2000)
	↓Spatial organisation	Mouse M	(Heveran et al., 2018)

Note: species, sex, ages and anatomical areas vary in these studies.

2.6.2   **Pathology**

This section will consider the changes to the ON&LCN observed in bone diseases, starting with osteoporosis (OP) and osteoarthritis (OA), followed by less prevalent pathologies.

2.6.2.1   **Osteoporosis and osteoarthritis**

OP is a widespread systemic skeletal disease characterised by low bone mineral density (BMD), micro-architectural disruption of bone tissue, increased bone fragility and an elevated risk of low-impact fractures, most commonly of the hip, spine or wrist (Figure 13). According to WHO criteria, patients with OP have a BMD or 'T-score' less than 2.5 standard deviations below the mean of the young adult population (Kanis et al., 1994, WHO, 1994).

OP is associated with a decrease in oestrogen levels and mainly occurs 10-15 years after menopause in women and at about 75-80 years old in men (Ji and Yu, 2015). OP is characterised by an imbalance in bone formation and breakdown, both processes coordinated by osteocytes (Ji and Yu, 2015).

OA, by contrast, is characterised by damage to articular cartilage caused by a complex interaction of genetic, metabolic, biochemical, and mechanical factors with secondary components of inflammation (Chen et al., 2017) (Figure 13). OA is known to affect all tissues of a joint, and typically also involves muscle, ligament and synovium. Around a third of the UK population aged 45 years and over, a total of 8.5 million people, have OA (Versus-Arthritis, 2019).

Both OA and OP are associated with altered bone mass and a disordered balance between bone formation and bone resorption. Elucidating the possible changes in ON&LCN structure and function is crucial to the understanding of these pathologies. Analysis of OP

and OA bone tissue, in particular the ON&LCN, using CXEM will produce quantitative data, which can contribute to the understanding of structure and will provide data for computational models to facilitate study of mechanisms of osteocyte mechanosensation and mechanotransduction as discussed in Section 2.9.
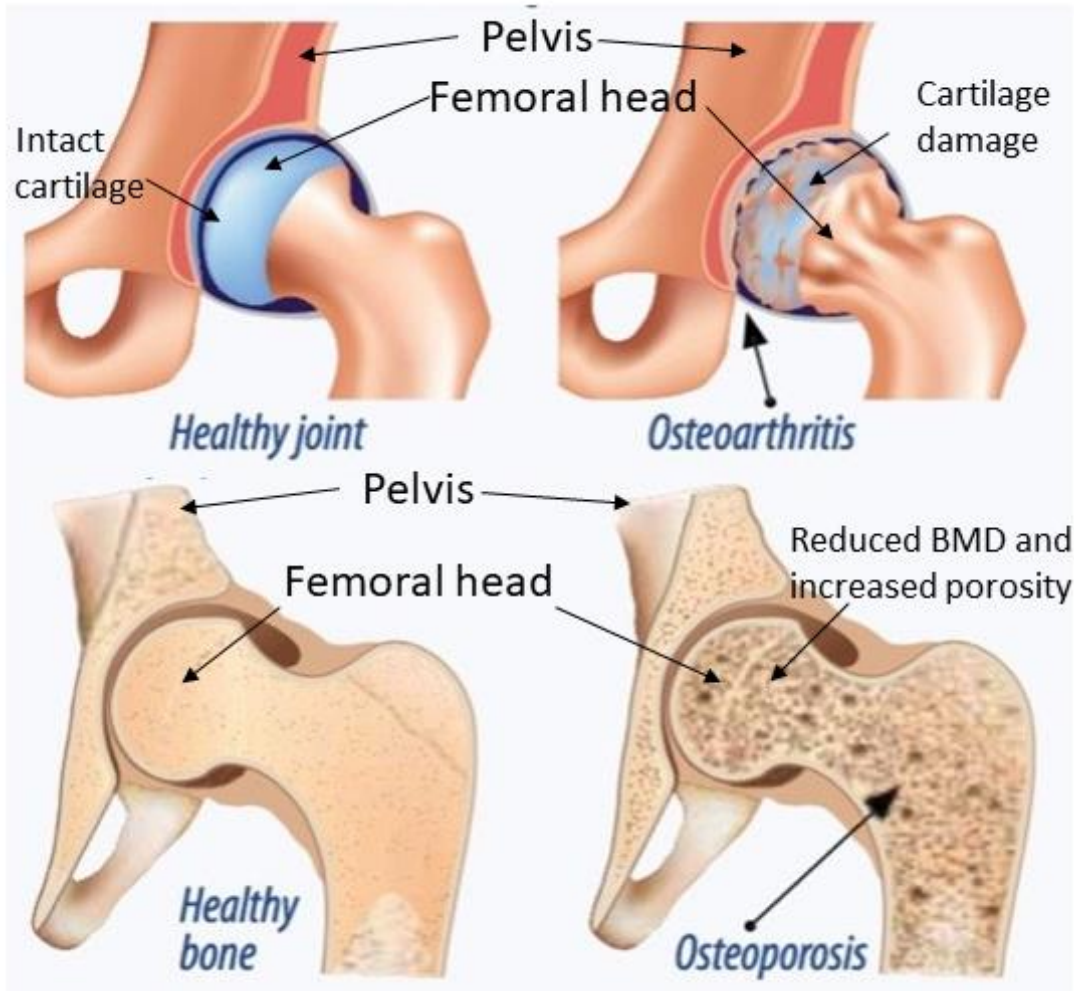
Figure 13   Osteoarthritis v osteoprosis in human femoral head.

Top   Osteoarthritis involves deterioration of cartilage (blue), leading to pain and stiffness in the joint.

Bottom   Osteoporosis is characterised by a reduction in bone density and quality, which may only become evident after a fracture has occurred.
           Images adapted from the Cleveland Clinic Arthritis Advisor website – accessed 01/02/21 (Clinic, 2021)

2.6.2.2 **Oestrogen deficiency and OP**

For a summary of the changes to the ON&LCN found in OP see Table 3.

Oestrogen is essential for maintenance of the skeleton as it suppresses bone turnover and balances the formation and resorption of bone tissue, preventing bone loss (Cummings and Melton, 2002). Ovariectomy increases bone turnover and induces bone loss (Wronski et al., 1985, Frost and Jee, 1992). Therefore, ovariectomised mice act as a model for OP, which mimics the reduction in oestrogen after the menopause, leading to an OP-like bone phenotype and related changes in bone structure and material properties, which are detrimental for bone mechanics (Frost and Jee, 1992). Studies have shown that ovariectomised rats have differences in bone matrix collagen arrangement, possibly changing the permeability of the matrix and affecting interstitial fluid flow (Sharma et al., 2012). Oestrogen deficiency induces apoptosis, which could alter osteocyte communication and interconnectedness (Brennan et al., 2014a, Brennan et al., 2014b, Tomkinson et al., 1997). Any or all of these changes could affect bone mechanics by modifying mechanotransduction pathways and with that, signals perceived by osteocytes from strain or fluid flow, eventually triggering osteocyte biochemical outputs. A study demonstrated higher lacunar and osteocyte number densities in OP individuals and significantly reduced lacunar area in OP individuals (Mullender et al., 1996b). Another study using human biopsies confirmed that osteocyte number density declines with age, where this decline occurs only in older bone and significantly in both pre- and post-menopausal women (Qiu et al., 2002a). Bone cells derived from patients with OP show an impaired osteocyte response to mechanical loading (Sterck et al., 1998). OP patients have 34 % fewer osteocytes than healthy controls (Qiu et al., 2003). Overall, patients whose bone houses fewer osteocytes are more likely to sustain fracture, demonstrating their crucial role in

bone maintenance (Qiu et al., 2003). To date, and to the best knowledge of the authors, it is not known if the lower osteocyte number is a cause or rather a consequence of OP. The proportion of occupied lacunae was found to be the same in healthy and diseased patients, indicating that the change is not the result of premature osteocyte death, but a consequence of reduced osteocyte formation (Qiu et al., 2003). Using a sheep model for OP, reduced osteocyte number density, reduced bone volume, osteoid surface area and bone formation rate were observed, while the number density of empty lacunae increased, when compared to controls (Zarrinkalam et al., 2012). Another study found that osteocyte density was lower in OP females compared to healthy females (Mullender et al., 2005). Almost all studies of the ON&LCN in OP bone to date have been carried out using LM methods. These studies have produced conflicting results on lacunar and osteocyte number densities which are either increased (Jordan et al., 2003, Mullender et al., 1996a), unchanged (Tomkinson et al., 1997) or most often, decreased compared to controls (Qiu et al., 2003, Mullender et al., 2005, Zarrinkalam et al., 2012). Lacunar occupancy is unchanged between controls and OP (Jordan et al., 2003, Qiu et al., 2003, Power et al., 2001). It has been found that lacunar area is decreased (Mullender et al., 1996) or unchanged (Mullender et al., 2005, McCreadie et al., 2004) and that neither lacunar volume nor shape is changed in human OP patients (McCreadie et al., 2004).

A decrease in connectivity between osteocytes is shown in OP bone compared to healthy bone (Knothe Tate et al., 2004). An increase in osteocyte death via apoptosis, is observed after the induction of cell death by oestrogen deficiency in 'osteocyte-like' cells (Brennan et al., 2014b) and in hypo-oestrogenic human bone (Tomkinson et al., 1997). Osteocyte cell death and a reduction in cell process connectivity presumably lead to impaired cell communication. In summary, many of the changes in OP are similar to those observed in

aging, namely a decrease in osteocyte and lacunar number density and a decrease in connectivity.

Table 3   Changes in the ON&LCN with osteoporosis/oestrogen deficiency

Measure	Osteocyte /Lacuna	Species	Reference
Number density	↑ Lacunae 32% mm^2	Human M+F	(Mullender et al., 1996b)
	↑ Lacunae 20% mm^2	Human M+F	(Jordan et al., 2003)
	↑Osteocytes 27% mm^2	Human M+F	(Mullender et al., 1996b)
	=Lacunae	Rat	(Sharma et al., 2012)
	=Lacunae	Sheep iliac crest	(Zarrinkalam et al., 2012)
	=Lacunae	Human F (deficiency)	(Tomkinson et al., 1997)
	↓ Lacunae -35%	Human F	(Qiu et al., 2003)
	↓ Lacunae -21%	Sheep lumbar spine	(Zarrinkalam et al., 2012)
	↓Osteocytes 14%	Sheep iliac crest	(Zarrinkalam et al., 2012)
	↓Osteocytes	Human M+F	(Mullender et al., 2005)
	↓Osteocytes-35%	Human F	(Qiu et al., 2003)
Occupancy	= approx. 50%	Human M+F	(Jordan et al., 2003)
	= 12.4 - 99.2%	Human F	(Power et al., 2001)
	= 90 %	Human F	(Qiu et al., 2003)
Area	= Lacunae	Human	(Mullender et al., 2005)
	= Lacunae	Human F	(McCreadie et al., 2004)
	↓ Lacunae 39.1-44.1 μm^2	Human M+F	(Mullender et al., 1996b)
Volume	=	Human F	(McCreadie et al., 2004)
Shape	=	Human F	(McCreadie et al., 2004)
Number of processes canaliculi	↓ Fewer, more tortuous and slack osteocyte processes	Human	(Knothe Tate et al., 2004)
Orientation	↓Osteocytes less oriented with respect to each other and to the vasculature	Human	(Knothe Tate et al., 2004)
Apoptosis	↑ between 170 % (lumbar spine) and 210 % (iliac crest)	Sheep	(Zarrinkalam et al., 2012)
	↑	Human F	(Tomkinson et al., 1997)

2.6.2.3   Osteoarthritis

For a summary of the changes to the ON&LCN found in OA see Table 4.

As in OP, there are conflicting results from studies of the changes in osteocyte and lacunar number density in human bone during OA. Both increased number density (Rabelo et al., 2020, Jaiprakash et al., 2012) and decreased number density (Knothe Tate et al., 2004, Power et al., 2010, Jordan et al., 2003) have been reported. Lacunar and osteocyte area and volume decrease in OA (van Hove et al., 2009, Mazur et al., 2019). Results based on acid-etched resin casting have shown that osteocyte lacunar morphology is rougher and rounder in OA compared to control samples, (Jaiprakash et al., 2012). Osteocytes in OA human bone are elongated compared with those from osteopenic and osteopetrotic bone (van Hove et al., 2009). A histological investigation showed an increase in osteocyte death in OA patients compared to controls (Wong et al., 1987). OA bone exhibited a decrease in connectivity of the ON&LCN compared to healthy bone, while the orientation of osteocyte processes to each other and to the blood supply was preserved (Knothe Tate et al., 2002). Perilacunar and canalicular remodelling are suppressed and the canalicular network is diminished in OA. A study has demonstrated that various functional and morphological properties of osteocytes appear to be hampered in patients with OA, indicating that these cells could play an important pathological role in subchondral bone sclerosis (Prasadam et al., 2013) and it is suggested that there is an increase in microdamage in tissue from OA patients (Fazzalari et al., 1998).

Table 4   Changes in the ON&LCN with osteoarthritis

Measure	Osteocyte /Lacuna	Species	Reference
Number density	↑Osteocytes	Human osteophytes	(Rabelo et al., 2020)
	↑Lacunae	Human	(Jaiprakash et al., 2012)
	↓Osteocytes	Human	(Knothe Tate et al., 2004)
	↓Osteocytes 18%	Human	(Power et al., 2010)
	↓Lacunae 24% mm^2	Human	(Jordan et al., 2003)
Occupancy			No studies
Area	↓Surface area	Human	(van Hove et al., 2009)
	↓Total OLNC 38-46%	Human	(Mazur et al., 2019)
Volume	↓Lacunae	Human	(van Hove et al., 2009)
Shape	Elongated	Human	(van Hove et al., 2009)
	Rounder	Human	(Jaiprakash et al., 2012)
Number of processes canaliculi	↓Osteocyte processes	Human	(Knothe Tate et al., 2004)
	↓ Osteocyte processes	Human	(Jaiprakash et al., 2012)
	↓Fewer and shorter 51-54%	Human	(Mazur et al., 2019)
Orientation	= No change	Human	(Knothe Tate et al., 2004)
	More oriented to the loading direction than osteopetrotic	Human	(van Hove et al., 2009)
Apoptosis	↑Increased	Human	(Wong et al., 1987)
Microcracks	↑ More microdamage	Human	(Fazzalari et al., 1998)

2.6.2.4   **Lacunar occupancy in age, OA and OP**

As discussed in Section 2.3.2, consideration of lacunar occupancy, osteocyte viability and

cell death are important for understanding the function and dysfunction of the ON&LCN.

As osteocytes are agents of mechanotransduction, osteocyte number density is more

biologically significant than lacunar number density and thus lacunar occupancy is a critical

measure, the quantification of which will help to understand changes in the ON&LCN

during OA and OP. This section will review changes in lacunar occupancy observed in age,

OA and OP.

In a study of female human femoral neck tissue (mean age 81 ± 2.9) the mean percentage lacunar occupancy was 48.2% (Power et al., 2001). Many other studies of human bone tissue report a decrease in occupancy with age (Wong et al., 1987, Wong et al., 1985, Frost, 1960, Rolvien et al., 2018, Zhang et al., 2019, Dunstan et al., 1990) although no change has also been reported (Mullender et al., 1996a).

Investigations of lacunar occupancy in subjects with fractured bone (Power et al., 2001), and OP (Mullender et al., 1996a, Qiu et al., 2003) found no significant differences to control tissue. Lacunar occupancy has been shown to be significantly lower in glucocorticoid induced rodent OP bone compared to control tissue (Ciani et al., 2018, Achiou et al., 2015) and in a study of sheep OP (Zarrinkalam et al., 2012). A complete absence of osteocytes was noted in samples of human OP tissue using TEM (Shen et al., 2009). In summary, lacunar occupancy decreases with age in human bone tissue, is found to decrease or remain unchanged in OP and has not been investigated in human OA tissue.

2.6.2.5   Sclerostin-related bone diseases

Sclerostin is produced by osteocytes, encoded by the SOST gene. Studies of sclerosteosis and van Buchem disease, both rare high-bone mass diseases, have led to the identification of sclerostin as a key negative regulator of bone mass (Balemans et al., 2001; Staehling-Hampton et al., 2002). Sclerostin binds to LRP5/6 co-receptors and inhibits the intracellular Wnt signalling pathway, leading to decreased bone formation by osteoblasts, reviewed in (Bonewald and Johnson, 2008; Klein-Nulend et al., 2013). It is suggested that sclerostin plays a role in the regulation of perilacunar mineralisation by osteocytes, enabling extraction of calcium from the perilacunar area when needed, followed by mineral restoration when the demand has been met (Atkins and Findlay, 2012; Kogawa et al., 2013). Studies in rats found that treatment of OP animals with sclerostin antibody produced

marked increases in bone formation, reversing the changes induced by ovariectomy (Li et al., 2009, Ominsky et al., 2014). In contrast to most other therapeutic treatments, which involve anti-resorptive agents to prevent or decelerate further bone loss, sclerostin has the potential to restore lost bone mass and strength. Phase III studies have shown the efficacy of romosozumab, an anti-sclerostin antibody in fracture prevention in postmenopausal women (Padhi et al., 2011, Fabre et al., 2020).

2.6.3 Changes to the ON&LCN with sex, site and loading

2.6.3.1 Sex

Several studies suggest that there are no differences of the ON&LCN related to sex in the non-OP population (Vashishth et al., 2000; Qiu et al., 2002; Jordan et al., 2003; Miszkiewicz, 2016). However, it has also been reported that osteocyte number density is 15 % higher in healthy females compared to healthy males (Mullender et al., 2005). A sex difference was also observed a CLSM study where all subjects showed a reduction in cell volume but only males showed a corresponding reduction in lacunar volume with age (Tiede-Lewis et al., 2017).

2.6.3.2 Site and loading

Variations in the ON between bones from different sites are assumed to be due to the influence of loading direction and intensity and they are discussed here together. Increased loading triggers the addition of new bone while unloading or disuse results in bone resorption. Various biochemical responses including sclerostin have been shown to be affected by loading of different frequency, timing and intensity, reviewed in (Bonewald, 2013). Osteocyte populations are 4–8 times higher in faster growing woven bone than more organised and slowly formed lamellar bone (Parfitt, 1983), supporting the theory that osteocyte density is linked to bone formation (Bromage et al., 2009).

Fibular osteocytes are elongated and aligned with each other, parallel to the loading direction. On the other hand, calvarial osteocytes are more spherical and not aligned in any particular direction, with the more loaded fibular osteocyte lacunae being larger (Vatsa et al., 2008). Prolonged unloading in rats reduces lacunar density and lacunar volume (Britz et al., 2012a). A study of women aged from 20-86 years, where a reduction in loading with increasing age has been assumed, found that lacunae became smaller and more spherical (Carter et al., 2013a). In a synchrotron radiation-based CT (SR CT) study, lacunar number density of healthy human femora varied significantly within individuals, with the anterior region having a lower density than both medial and posterior regions (Carter et al., 2014). These variations are postulated to be related to loading and bending of the femoral shaft, but the reasons are unclear (Carter et al., 2014).

2.6.4   **Summary**

Studies to date suggest that lacunar number density decreases and lacunar area increases with age, but conflicting evidence exists regarding change in the numbers of canaliculi. Loaded bone has more and larger osteocyte lacunae than unloaded bone. With age, cell shape changes from round to slender, the size of the PCS increases and the level of osteocyte organisation decreases. Studies on the influence of sex provide contradictory results, where most studies did not identify significant differences between males and females. Finally, osteocytes have been reported to align in the direction of loading and they are smaller when loading is reduced.

Many of these findings are drawn from data from 2D imaging techniques, and most measure only the LCN, not the ON residing within. High resolution 3D imaging of both the ON and the surrounding LCN would improve the knowledge of cell and lacunar morphology and the overall connectivity.

2.7 Imaging of the ON&LCN

This section will firstly consider the 'ideal imaging method' and how it might be achieved considering real world limitations, then review imaging methods used to investigate the ON&LCN before discussing correlative imaging, quantitative 3D morphology and computational models.

2.7.1 The ideal imaging method

2D images provide only a small part of the complete context of any cell. Accurate morphology including cell shape, size or location cannot be derived reliably from 2D images. Furthermore, the relationship between structures – both within and without a cell – are often invisible in 2D. Viewing and analysing structures in a 3D context avoids misinterpretation. It is however a challenge to obtain 3D data, especially at high spatial resolutions. Novel (high-resolution) 3D imaging techniques are currently being developed as discussed in Section 0 and at the end of this chapter in the section on the future role of high-resolution 3D imaging in osteocyte anatomy and pathology.

In addition to providing 3D data, the ideal technique for imaging bone cells and their ECM at cellular and sub-cellular scales would be a high-resolution, non-destructive method, capable of imaging large volumes *in situ* and *in vivo* and offering concurrent hard and soft tissue image contrast. Furthermore, the imaging modality would be widely available at a reasonable cost and produce quantitative hallmarks of healthy and diseased tissue, which are easy to interpret and analyse.

To meet all of these criteria compromises have to be made in practice. The ON&LCN extend throughout the bone matrix. To reveal the true degree of connectedness between contiguous osteocytes the ideal imaging method should be able to visualise a volume

containing many cells. However, in the real world, imaging techniques depend on various sample preparation protocols and there exists a broad range of experimental limitations during imaging. Most imaging techniques require tissue to be excised from the body, many require mechanical sectioning to some degree, and some of the techniques need harsh chemical treatment to render tissue suitable for imaging, which can change the state of the native biological sample and thus, complicate interpretation of the gathered image data (Weston et al., 2010).

Many imaging modalities have been used in high-resolution studies of the ON&LCN, each presenting advantages and disadvantages. For comprehensive comparisons of these techniques see Table 5 and Table 6, (Goggin et al., 2016, Schneider et al., 2011) and the following sections. In brief, LM, including CLSM, allows functional imaging of cells but is limited in spatial resolution by the diffraction limit of visible light (~ 200 nm). EM provides high-resolution images of cell ultrastructure, including the organelles, cytoskeletal components and membranes, but requires complex sample preparation. In addition, standard EM is an inherently two-dimensional (2D) technique. In contrast, X-ray CT has enabled timely imaging of large volumes of bone tissue in 3D without the need for complex sample preparation. Standard X-ray imaging techniques however lack sufficient resolution for substantial sub-micrometre imaging and do not provide enough imaging contrast for weakly X-ray absorbing soft tissues such as the ON. This limitation for soft tissues means that using standard (i.e., absorption- based) X-ray imaging, only the hard mineralised bone matrix – the negative imprint of the ON – can be assessed at sufficiently high contrast levels, but not the weakly X-ray absorbing soft cells within the LCN. This weak vision for soft tissues reduces the informative value of such results when used for instance in computational modelling studies aimed at understanding mechanotransduction processes using cell geometries based on experimental data. It is often assumed that every lacuna imaged

contains an osteocyte, without considering osteocyte loss through cell death. Cell density is arguably more significant than lacunar density since cells are the active mechonsensors. Lacunar density is thus not a reliable indicator of osteocyte density (Iwamoto et al., 2010, Britz et al., 2012a).

Table 5   Light and electron microscopy based techniques used in ON&LCN studies

A summary of light and electron based imaging modalities which have been used in studies of the ON&LCN, their advantages, disadvantages and relevant references. Adapted from (Goggin et al., 2016)

Technique	2D/3D	Max resolution	Advantages	Disadvantages	Reference
LIGHT MICROSCOPY					
Light microscopy	2D	300 nm	• Functional imaging through fluorescent labelling. • Soft tissue contrast.	• Inherently 2D • Low resolution	(Marotti et al., 1995)
High-resolution episcopic microscopy	3D	1 µm	• Large FOV	• Low resolution • Destructive	(Mohun and Weninger, 2012)
Light sheet microscopy	3D	10 µm	• Large FOV (1 cm³) • Live cell imaging	• Low resolution • Requires optical clearing	(Weber et al., 2014)
Confocal laser scanning microscopy (CLSM)	3D	300 nm	• Functional imaging through fluorescent labelling • Soft tissue contrast	• Limited range of depth (~100-150 µm) • Low resolution (> 100 nm)	(Kamioka et al., 2001)
ELECTRON MICROSCOPY					
Scanning electron microscopy (SEM)	2D	< 2 nm	• High resolution	• Inherently 2D	(Okada et al., 2002)
Serial section SEM (ATUM SEM)	3D	2 nm (*x/y*) and 60-90 nm (*z*)	• Large volumes (2.5 x 6 mm² sections) • Re-examination possible	• Complex sample preparation	(Tapia et al., 2012)
Transmission electron microscopy (TEM)	2D	< 1 nm	• High resolution	• Limited FOV • Inherently 2D	(You et al., 2004)
TEM tomography	3D	2 nm	• High resolution	• Limited VOI (depth 3-5 µm) • Long acquisition times • Missing wedge problem	(Kamioka et al., 2009)
Serial section TEM	3D	< 1 nm (*x/y*) and 60 nm (*z*)	• High resolution	• Technically difficult • Time-consuming	(Palumbo et al, 1990)
GridTape TEM	3D	4 nm (x/y) and 40 nm z	• High resolution • Relatively large volume (64 million µm³)	• Not commercially available • Complex sample prep	(Graham et al., 2019)
Serial focused ion beam SEM	3D	< 10 nm	• High resolution (20 nm in z)	• Destructive (not completely) • Slow • Small FOV (as small as 20 µm²)	(Schneider et al., 2011, Hasegawa et al., 2018)
Serial block face SEM (SBF SEM)	3D	< 10 nm	• High resolution (x/y)	• Destructive • Extensive sample preparation • Non-isotropic data	(Peddie and Collinson, 2014, Smith and Starborg, 2019)

Abbreviations: Field of view (FOV), volume of interest (VOI)

Table 6   X-ray and scanning probe imaging techniques used in ON&LCN studies

A summary of X-ray based and scanning probe imaging modalities used in studies of the ON&LCN, their advantages, disadvantages and relevant references. Adapted from (Goggin et al., 2016)

Technique	2D/3D	Max resolution	Advantages	Disadvantages	Reference
X-RAY TECHNIQUES					
X-ray absorption CT (desktop µCT and SR CT)	3D	< 1 µm	• Non-destructive • Simple sample preparation • Relative sub-µm mineral density quantification	• Limited VOI • Low resolution • High radiation dose	(Schneider et al., 2007)
Ptychographic CT	3D	< 100 nm	• Non-destructive • High resolution • Absolute sub-µm mineral density quantification	• Limited VOI • High radiation dose	(Dierolf et al., 2010)
Transmission X-ray microscopy CT	3D	< 50 nm	• Non-destructive • High resolution • Relative sub-µm mineral density quantification	• Limited VOI • High radiation dose	(Andrews et al., 2010)
X-ray phase tomography (holotomography)/X-ray phase nanotomography	3D	120-150 nm	• Non-destructive • Simple sample preparation	• Requires access to synchrotron radiation facility	(Langer et al., 2012)
SCANNING PROBE MICROSCOPY					
Atomic force microscopy (AFM)	2D	20-50 nm	• Can image in aqueous medium • High resolution • Information on mechanical properties	• Small FOV (150x150 µm²)	(Reilly et al., 2001)

Abbreviations: Field of view (FOV), synchrotron radiation-based computed tomography (SR CT), volume of interest (VOI)

Factors to consider when choosing an imaging method include:

- Sample preparation to reflect the native state

- Adequate spatial resolution of microstructural and ultrastructural detail

- Adequate volume to visualise cell networks and tissue matrix

- 3D visualisation

2.7.1.1   Sample preparation and method validation

Imaging tissue in its native state is an often elusive ideal. Chemical interventions to preserve tissue and/or enhance image quality, such as heavy metal staining or decalcification, can have unwanted effects such as tissue shrinkage (Buytaert et al., 2014).

Where artefacts are introduced the microscopist must be aware of their impact and be able to compensate for them experimentally or post hoc during data processing. Nanophosphor particles delivered by bioballistic particle delivery systems can be used to monitor morphological changes in tissue during processing (Bushong et al., 2015). As bone is a composite material made up of a hard mineralised and a soft collagenous phase, the task of measuring artefactual change and of identifying and applying validating techniques, in order to ensure that the native tissue state is preserved and assessed, is more challenging than in homogenous tissues. Novel fixation techniques have been applied to osteocytes to optimise preservation. Acrolein, a small molecule which penetrates the tissue rapidly, has been used as fixative to improve the cell membrane preservation and reduce shrinkage (McNamara et al., 2009). Ruthenium based fixatives and stains enhance the preservation of cell and matrix proteoglycans (You et al., 2004; Shah et al., 2015b). Validation of sample preparation and imaging techniques, to ensure that results accurately reflect the tissues and cells being examined, is important. Using more than one technique on the same sample and comparing the results can increase confidence in a novel method (Smith et al., 2006). Comparisons between the same tissues prepared for 'standard' EM and using cryo methods provide insight into changes which occur during sample preparation. Statistical methods have been used to overcome limitations of some EM data (Russo and Passmore, 2014). Beyond that, the issue of validating new 3D EM techniques has been reviewed by a task force set up to provide recommendations in 2012 (Henderson et al., 2012). It resulted in the creation of a unified data resource called EMDataBank (http://www.emdatabank.org), with the aim to develop validation reports and establish validation standards for 3D EM.

2.7.1.2   Adequate spatial resolution of microstructural and ultrastructural detail

Imaging techniques are needed that can resolve the detail of the cell processes (diameters in the order of ~ 100 nm) and ultrastructural cell details described above which may be relevant for mechanobiology (You et al., 2004).

2.7.1.3   Adequate volume to visualise cell networks and tissue matrix

For most imaging techniques there exists an inverse relationship between spatial resolution and maximum possible sample volume to be assessed, due to experimental limitations. These limitations can be found on the side of image acquisition, such as the dimension of the detector or the time available to record images at a sufficient signal-to-noise ratio. Consequently, sampling smaller volumes allows working at higher spatial resolutions, while mitigating to some extent the problem of the limited penetration depth of the light and electrons used for imaging. However, small volume analysis introduces sampling errors and reduces the validity of results as the smaller number of cells examined cannot be considered to be representative (anymore) of the tissue. Due to the high tissue penetration depth of hard X-rays (energies typically > 10 KeV), X-ray CT offers the largest volumes of interest of all the imaging techniques under consideration here, with whole-bone scanning being common. The volume of tissue which may be analysed using other techniques can also be limited by physical conditions such as the technical challenges of producing serial TEM sections, the restriction of the field of view in serial FIB SEM to sometimes less than 100 μm^2 (Knott and Genoud, 2013; Peddie and Collinson, 2014) and the loss of the 'missing wedge' in electron tomography (Ercius et al., 2015).

2.7.1.4   3D visualisation

Elucidation of the mechanisms of mechanotransduction will require images and quantitative measures of the ON&LCN in 3D at different levels (cellular, sub-cellular,

ultrastructural). LM and CT techniques produce 3D data at low (~ 300 nm) and high (< 100 nm) spatial resolutions. While traditional EM techniques are 2D, the relatively new techniques of serial FIB SEM and serial block-face SEM (SBF SEM), produce 3D data sets by repeatedly imaging a resin block-face, as ultra-thin tissue sections are removed from the surface, either by an ion beam (serial FIB SEM) or by a remotely controlled ultramicrotome inside an SEM (SBF SEM) (Peddie and Collinson, 2014).

2.7.2   Imaging techniques used for ON&LCN investigations

For a more complete review of imaging techniques applied to bone tissue see (Goggin et al, 2016).

2.7.2.1   Light Microscopy

Since Hooke first observed and coined the term 'cell' in 1665, light microscopy (LM) has elucidated details of the structure of bone tissue. Much work has been carried out using LM on stained histological bone sections, fundamentally a 2D observation method (Gaytan et al., 2020, Hirose et al., 2007, Ferretti et al., 1999, Remaggi et al., 1998, Marotti et al., 1995) (Figure 14). Improved optics and the advent of digital imaging have enhanced the capabilities of LM, but as with all light-based microscopy methods, the spatial resolution of most LM methods is restricted by the diffraction limit of visible light to around 200 nm.

In confocal laser scanning microscopy (CLSM) a point source laser excites tissue which is either auto fluorescent or has been stained with fluorescent dyes specific for cell components (Kamel-ElSayed et al., 2015). Tissue is imaged at sequential focal planes using a pinhole detector to exclude light outside of the focal plane. A stack of 2D optical sections is acquired, which enables production of 3D representations of bone microstructure (Figure 14). CLSM images have a spatial resolution of at best 200 nm in-plane and slightly worse

(up to 450 nm) out-of-plane, dependent on the objective lens. Limitations of CLSM, when imaging in dense mineralised tissue, include the limited working distance (90-300 µm) of high-quality, high-numerical aperture objectives and the decrease in signal with depth. The practically achievable penetration depth of CLSM in mineralised tissue is 100-150 µm (Jones et al., 2005). CLSM has been successfully used to characterise the spatial organisation, orientation and morphology of the ON&LCN (Kamioka et al., 2001; Vatsa et al., 2008; Sugawara et al., 2011; Cardoso et al., 2013; KamelElSayed et al., 2015). It is notable that some CLSM studies which measure osteocytes also stain the PCS and thus overestimate cell size measures (Verbruggen et al., 2012, Verbruggen et al., 2014).

Time-lapse LM is used to observe and capture cellular dynamics by imaging live cells at predetermined time intervals. Live cell imaging has shown that the osteocyte embedding process in living bone tissue is highly dynamic and that the cells can extend and retract their processes (Dallas et al., 2009; Dallas and Bonewald, 2010). Tracer injections have been used to demonstrate the connection between the blood and canalicular fluid (Wang et al., 2004).

In light sheet microscopy (LSM) a sheet of laser light is used in place of the point source to illuminate and image tissue in slices (Weber et al., 2014). LSM provides images of intermediate spatial resolution (~ 10 µm) from samples up to 1 cm^3 in size. LSM has so far not been used extensively for bone imaging. Studies to date include the development of bone in zebrafish embryos (Jemielita et al., 2013) and simultaneous imaging of the soft and hard tissue of mouse cochlea (Buytaert et al., 2013). The reduced amount of photodamage and the ability to image larger volumes than for CLSM are advantages of LSM, which could lead to wider use in future osteocyte studies.
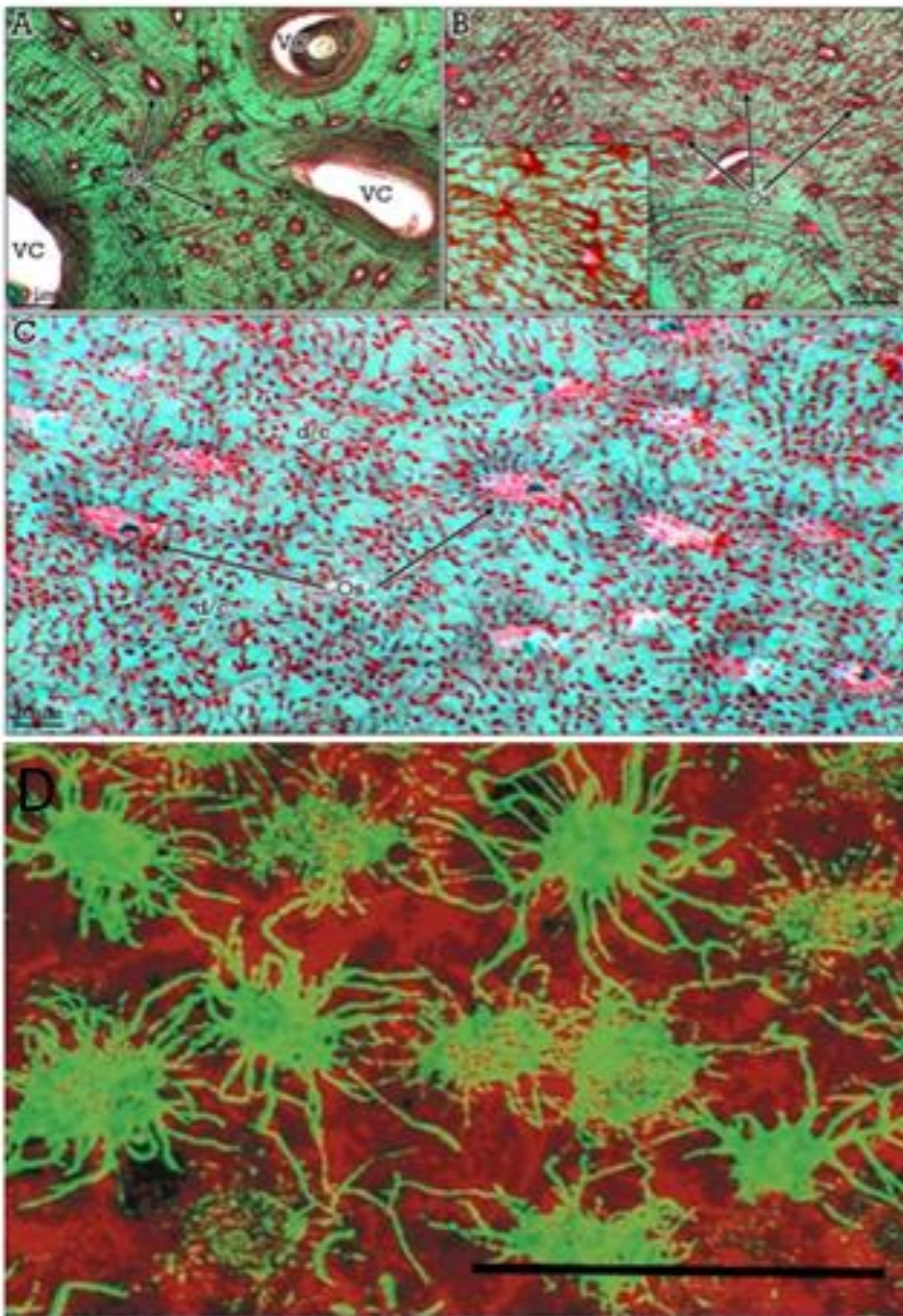
Figure 14   Light microscopy (LM) and confocal laser scanning microscopy (CLSM)

A-C   Trichrome staining of compact bone. Osteocytes (Os) are arranged concentrically (A,B) around vascular channels (VC), showing abundant processes/canaliculi. In (C), the dense process/canalicular system (d/c) can be appreciated at higher magnification. Scale bars = 30 µm and 10 µm. From (Gaytan et al., 2020)

D   A fluorescence image of a chick calvarial fragment reconstructed from 40 CLSM images. Cells labelled in green are osteocytes, and cells in red are osteoblasts on the surface of the bone. The staining clearly delineates the osteocyte processes. Scale bar = 20 µm. Adapted from Kamioka et al., 2001

In recent years LM has moved beyond the aforementioned diffraction limit of light by the development of 'super resolution' microscopy techniques. Structured illumination super resolution microscopy (SIM) and stochastic optical resonance microscopy (STORM) (Cabahug-Zuckerman et al., 2018) have been used to investigate integrin sites at near EM resolution. In time, these approaches may provide valuable insights to osteocyte structure and mechanobiology either alone or in a correlative framework.

2.7.2.2 Electron Microscopy

EM takes advantage of the shorter wavelength of electrons compared to visible light to extend resolving power. EM uses a beam of accelerated electrons to improve the theoretical spatial resolution to the atomic range with aberration corrected instruments (Pennycook et al., 2015). In practice, the best spatial resolution with a lab-based TEM system for biological tissue is approximately 2 nm.

2.7.2.2.1 Transmission electron microscopy (TEM)

In TEM a beam of electrons is transmitted through an ultrathin (≤ 100 nm) section of fixed, stained, dehydrated and resin-embedded tissue. Some electrons pass through the tissue and others are scattered to form an image (Figure 9). This has been the favoured technique for high-resolution imaging of cell ultrastructure since its development in the 1930s. Preparation of ultrathin sections capable of withstanding high vacuum and bombardment by high energy electrons requires complex sample processing that can introduce artefacts such as shrinkage. Bone presents the further challenge of a hard, mineralised matrix requiring an additional step of decalcification to facilitate sectioning (An and Martin, 2003). Cryofixation preserves tissue in a more life-like state but has the disadvantage that only small (~ 200 μm deep) volumes of tissue can be preserved.

The first published record of TEM bone studies dates back to 1950 (Barbour, 1950). More recently it has been used to investigate tethering fibres between osteocytes and the PCM (You et al., 2004; McNamara et al., 2009) and the changes in osteocytes and surrounding collagen fibres during osteocytic osteolysis (Hongo et al., 2020). The 2D nature of TEM imaging has been somewhat overcome by serial section TEM, TEM tomography, automated grid tape TEM and ultra-high voltage EM (UHVEM). Serial section TEM is technically difficult and time-consuming but provides high-resolution results (White et al., 1986; Harris et al., 2006) such as those used to elucidate the 3D shape of osteocytes (Palumbo et al., 1990). Grid tape TEM is a novel technique combining automated serial sectioning and automated high throughput TEM imaging (Graham et al., 2019). TEM tomography involves imaging a section repeatedly while it is incrementally tilted around its axis producing a series of projections from which a 3D image is reconstructed (Bonetta, 2005; McIntosh et al., 2005). UHVEM is not widely available but studies have produced 3D images of osteocytes from 3 μm sections at 16 nm per pixel resolution (Kamioka et al., 2009), discussed further in Section 2.8.

2.7.2.2.2   Scanning electron microscopy

Scanning electron microscopy (SEM) employs a beam of electrons raster-scanned over a sample, usually fixed, dehydrated, dried and made conductive with a metal coating. The beam interacts with the sample producing secondary electrons, backscattered electrons and X-rays that are collected to form images. SEM resolution depends on the accelerating voltage, spot size, scan speed and vacuum level. SEM has been used to evaluate the number density of canaliculi in human bone (Marotti et al., 1995). Resin-casted and acid-etched samples have been examined using SEM, showing the distribution, size and surface details of osteocyte lacunae and the vasculature (Figure 15) (Feng et al., 2006; Kawakami et al.,

2009; Kubek et al., 2010). Although SEM images have a characteristic depth of field and convey a 3D impression, the technique is essentially 2D.
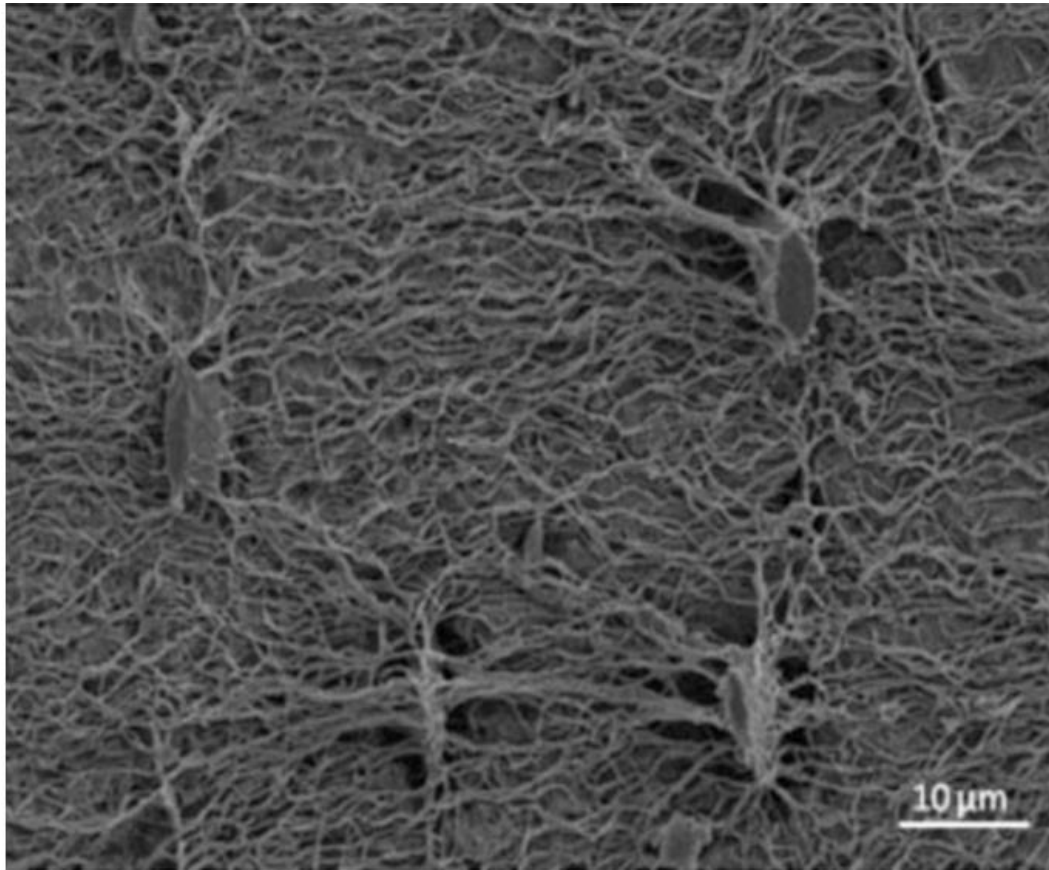
Figure 15   Scanning electron microscopy (SEM)
SEM image of an acid etched plastic embedded section of mouse femur showing osteocyte lacunae and canalicular processes. From Kubek et al., 2010

2.7.2.2.3   Volume EM (vEM)

The vEM techniques considered here are array tomography (AT), serial focussed ion beam SEM (FIB SEM) and serial block face SEM (SBF SEM). In AT multiple ribbons of serial tissue sections are collected on a conductive substrate and subsequently viewed by SEM (Wacker and Schroeder, 2013). AT is suitable for examining large volumes at high x-y-resolution (z-resolution is limited by the section thickness). The sections can be re-examined many times (Tapia et al., 2012).

Both serial FIB SEM and SBF SEM produce high-resolution 3D data using automated sectioning techniques. The x/y-resolution is comparable to TEM (< 5 nm), whereas the z-resolution is limited by the sectioning technique, typically 10 nm for serial FIB SEM and 30-100 nm for SBF SEM.

 In serial FIB SEM a focused ion source mills the surface of the resin-embedded tissue. The block-face is imaged using SEM and the process repeated until the volume of interest has (partly) been milled away. A proof-of-concept study for serial FIB SEM on bone tissue successfully imaged parts of two adjacent osteocyte lacunae (Figure 16) (Schneider et al., 2011) and a later study imaged osteoblasts and osteocytes from a 20 x 20 x 25 µm volume (Hasegawa et al., 2018).

In SBF SEM, a remotely controlled ultramicrotome within an SEM removes ultrathin layers from the tissue block, which is consecutively assessed by a back-scattered electron detector to extract morphologies from 3D stacks with spatial resolutions comparable to TEM. SBF SEM can cover large volumes of interest (up to 0.5 x 0.5 x 1 mm) and provides simultaneous imaging contrast for soft and hard tissues such as the ON&LCN respectively. During this project sample preparation protocols for SBF SEM of bone tissue have been developed (Chapter 3) and first results reported (Figure 17) (Goggin et al., 2020, Goggin et al., 2016). These methods will be applied to murine and animal tissue in later chapters of this thesis.
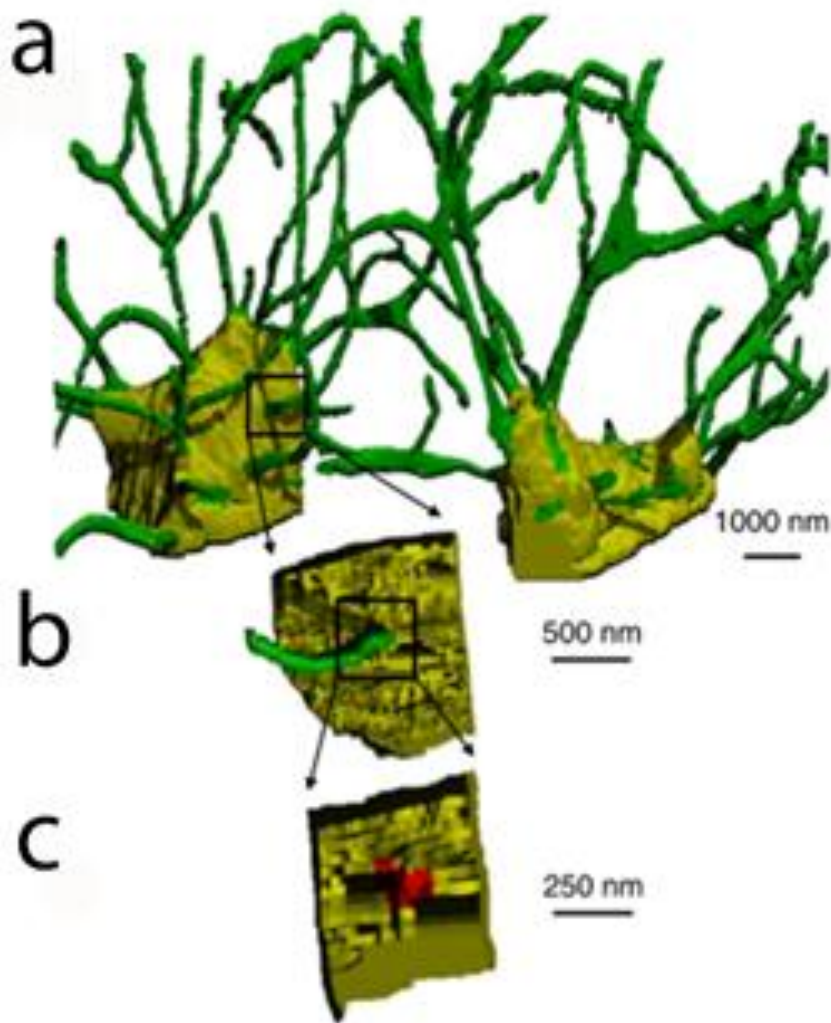
Figure 16   Serial focused ion beam scanning electron microscopy (FIB SEM).

A   3D representation of the LCN from a murine femur produced by serial FIB SEM showing osteocyte lacunae (yellow) and canaliculi (green).

B,C   The junction of an osteocyte lacuna and a canaliculus. The interface between lacuna and canaliculus is shown in red. From (Schneider et al., 2011)
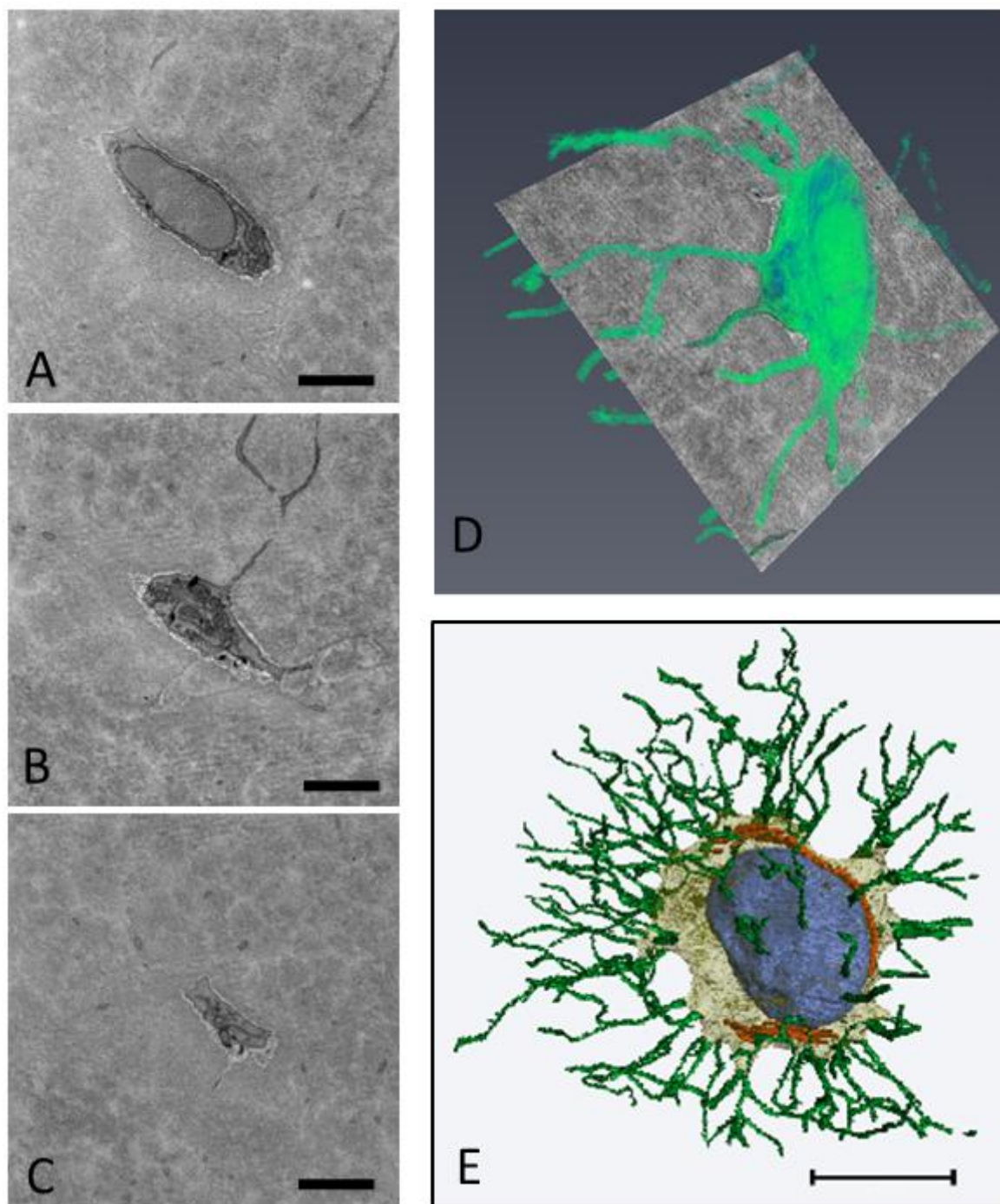
Figure 17   Osteocytes from mouse tibia imaged by SBF SEM

A-C   Individual images of section numbers 0, 40 and 80 from an SBF SEM stack.

D   3D volume reconstruction of 150 SEM sections of an osteocyte from mouse bone

E   Osteocyte ultrastructure reconstructed from SBF SEM data. The cell body is shown in pale yellow, processes in green, the nucleus in blue and mitochondria in orange. Scale bars A-D = 2 μm, E = 5 μm. From (Goggin et al., 2016 and Goggin et al, 2020)

2.7.2.3 **X-ray imaging**

2.7.2.3.1 Conventional X-ray computed tomography (CT)

Unlike light, X-rays penetrate bone easily. Attenuation of X-rays by bone tissue provides image contrast for (2D) X-ray projections at different angular positions, which are used to reconstruct the 3D map of the specimen. Sample preparation requirements are minimal, the technique is non-destructive and once set up, operator involvement is low. Bone can be imaged and analysed at different levels (organ, tissue, cellular) using micro-computed tomography (µCT) at isotropic resolutions < 1 µm (Müller, 2009). It is notable that CT studies do not generally provide soft tissue contrast; reconstructions depict the LCN only, which is the negative imprint of the mineralised bone tissue surrounding the ON.

Lab-based X-ray µCT systems are commonly used to investigate bone microstructure (Müller, 2009; Draenert et al., 2012; Peyrin et al., 2014). A range of spatial resolutions from about 100 µm to below 1 µm can be reached, comparable to the resolution obtained using LM, but not reaching the resolution of EM. Thus, µCT allows visualisation of lacunae, but not the fine detail of canaliculi. Commercially available µCT systems with improved spatial resolution are available, some of which claim voxel sizes in the order of 100 nm at volumes of 1 mm^3. Studies using this equipment have investigated differences in morphology of lacunae from different sites in the mouse (Vatsa et al., 2008) and compared morphology of lacunae in humans with different bone diseases (Vatsa et al., 2008; van Hove et al., 2009). A disadvantage of µCT at voxel sizes below the micrometre range is the long acquisition time of many hours that are required for a signal-to-noise ratio sufficient to resolve individual osteocyte lacunae.
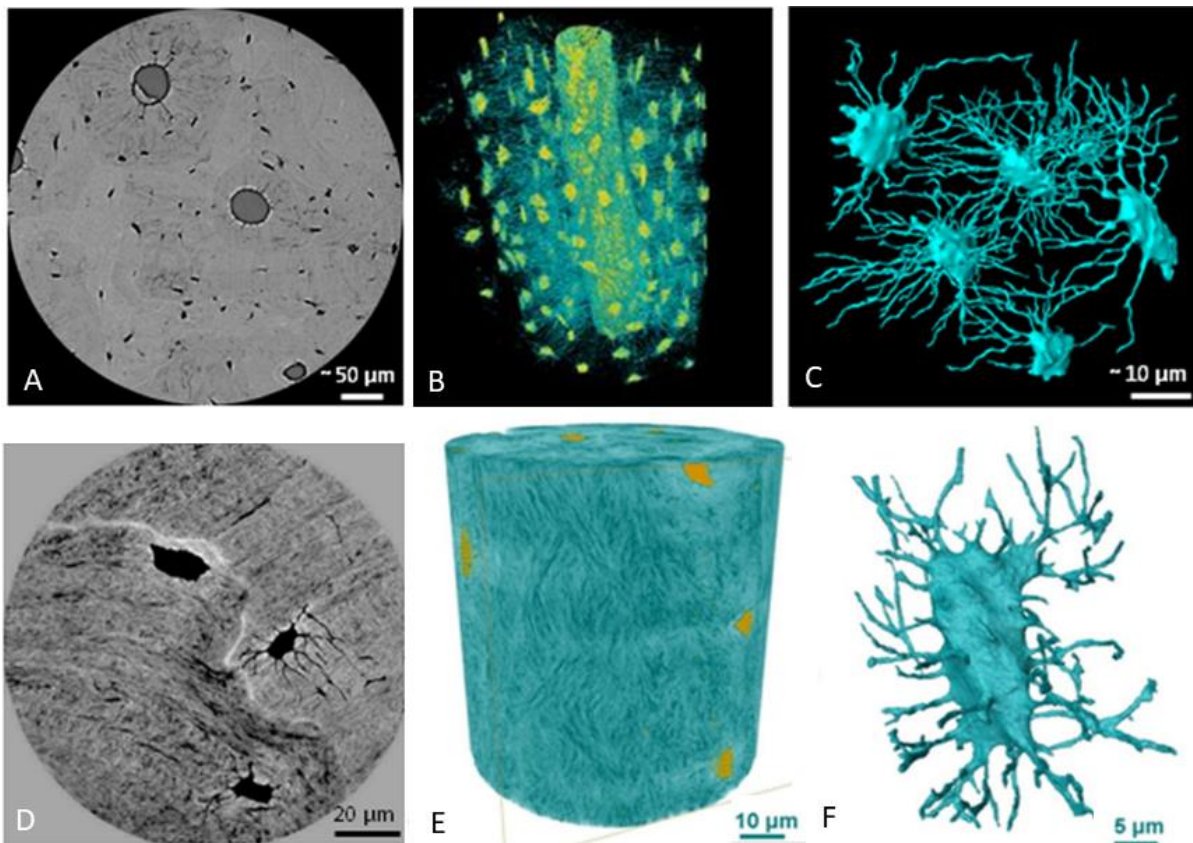
Figure 18   Synchrotron radiation computed tomography images of human femur.

A   CT slice showing osteons, osteocyte lacunae and canaliculi. Voxel size = 300 nm

B   3D rendering of the LCN from the top osteon in A (lacunae = yellow, canaliculi = blue)

C   A segmented 3D data set of five lacunae and their canaliculi. Voxel size = 300 nm

D   High-resolution phase nano-CT slice with lacunae and canaliculi in black. (Voxel size = 60 nm)

E   3D rendering of the apparent texture of the collagen fibres from D.

F   Detailed rendering of one lacuna and its canaliculi from D.

Adapted from (Peyrin et al., 2014)

Synchrotron sources, operated as large-scale electron accelerators at a small number of sites worldwide (http://www.lightsources.org/regions), offer quasi-monochromatic X-rays and much higher photon fluxes with small X-ray source spot sizes, thereby providing spatial resolutions sufficient to resolve trabecular and internal bone microstructures on a sub-μm scale (Salome et al., 1999). SR CT has been used to investigate trabecular architecture and osteocyte lacunae (Figure 18) (Peyrin et al., 1998; Schneider et al., 2007). In addition to X-ray absorption based CT, coherent synchrotron light also provides phase contrast imaging

capability, where the induced phase shift by the sample is exploited in comparison to the use of X-ray absorption only, generally involving a phase retrieval step before actual CT reconstruction. Phase contrast-based CT imaging yields images with improved contrast, particularly useful for weakly X-ray absorbing portions of the sample such as collagen. Experimental SR-based imaging techniques include transmission X-ray microscopy (TXM) (Andrews et al., 2010), ptychographic X-ray CT (Dierolf et al., 2010) and X-ray phase tomography (holotomography)/X-ray phase nanotomography (Langer et al., 2012). For a more complete review see (Goggin et al., 2016).

In summary, SR CT has been used to image and quantify the LCN, including image-based modelling approaches of bone mechanotransduction on sub-micrometre scales. Nonetheless, these newer X-ray CT imaging methods all operate for the moment at resolutions close to the dimensions of the relevant internal bone microstructures (e.g. osteocyte cell processes and canaliculi), and thus, care must be taken when interpreting X-ray CT image data with respect to bone mechanobiology.

2.7.2.4 **Scanning probe microscopy**

Atomic force microscopy (AFM) is a high-resolution scanning probe technique, which generates images of surface topography and information on mechanical properties (hardness, roughness) of tissues and materials. The ability to image in aqueous media is an important advantage of AFM, enabling closer to native-state imaging than other techniques. Compared to SEM, AFM offers a small field of view (in the order of 100 μm^2) and the scan times are longer. AFM studies have imaged the LCN and the collagen structure of the matrix (Figure 19) (Reilly et al., 2001; Lin and Xu, 2011; Katsamenis et al., 2013). In a study on rat femora AFM has been used to analyse the mineral phase of rat bone over the lifecourse for comparison with SEM, μCT and chemical analysis (Zhang et al., 2015). In

addition, AFM has been used to investigate the crystal structure of the bone matrix (Tong

et al., 2003; Kwon et al., 2009).
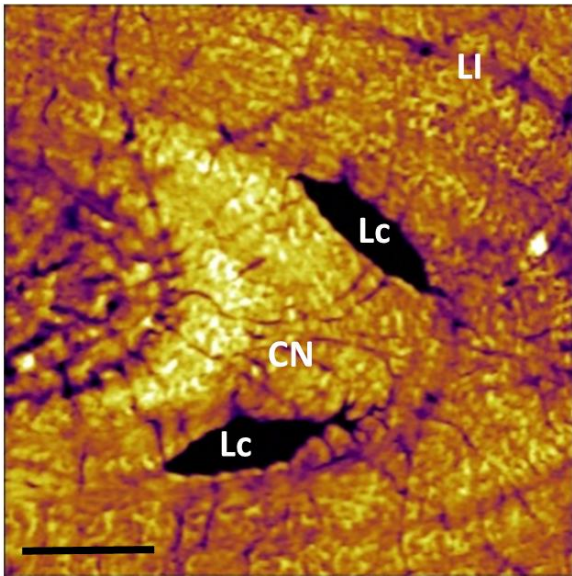
Figure 19   Atomic force microscopy (AFM).

An AFM image of demineralised osteon in bovine femur revealing microstructural and
ultrastructural features such as osteocyte lacunae (Lc), the canalicular network (CN) and lamellar
interfaces (LI). Scale bar 10 µm. Adapted from (Katsamenis et al., 2013)

2.7.2.5   Novel imaging methods

Dual-purpose fluorescent and electron-dense labels for EM (SOG, miniSOG, APEX2) are

genetically encoded tags for correlative light and electron microscopy (Shu et al., 2011; Lam

et al., 2015), which could be applied to the ON&LCN. Through-focus scanning optical

microscopy (Attota et al., 2013), confocal soft X-ray scanning transmission microscopy

(Spath et al., 2015) and intravital microscopy (subcellular imaging in living animals)

(Masedunskas et al., 2012; Alexander et al., 2013) are techniques which may add to the

repertoire for osteocyte investigation.

In this project SBF SEM has been adopted to retrieve 3D data from the ON and the LCN

simultaneously. SBF SEM facilitates the collection of quantitative 3D information by

visualising the cell morphology and internal ultrastructure, the association with the PCM and ECM and in CXEM, the distribution of osteocytes within the bone matrix.

2.7.3 Correlative imaging

2.7.3.1 Correlative imaging approaches in biology

Correlative imaging merges complementary microscopy methods used on the same sample to overcome the limitations of individual techniques by producing composite images and enhancing the quality and quantity of information produced by either technique used alone (Muller-Reichert, 2012, Braet and Geerts, 2009, Caplan et al., 2011). The advantages of correlative microscopy have been neatly expressed as '1+1 = 3' (Verkade, 2013). The most widely used correlative technique is correlative light and electron microscopy (CLEM), which uses fluorescent LM imaging to capture structural or dynamic information, followed by fixation, processing, TEM imaging and subsequent overlay of the images (Peddie et al., 2014). 3D CLEM studies using vEM include (Markert et al., 2017, Collman et al., 2015), using AT, (Lucas et al., 2014, Lucas et al., 2017, Armer et al., 2009, Schieber et al., 2017, Bushby et al., 2012) using FIB SEM and (Russell et al., 2016, Lees et al., 2017) using SBF SEM.

Correlative studies using fluorescence LM and soft x-ray tomography have been carried out using synchrotron radiation (Carzaniga et al., 2014, Duke et al., 2014, Kapishnikov et al., 2017). Correlative micro-computed tomography and fluorescence LM are being used in studies of fixed human lung tissue (Scott et al., 2015, Jones et al., 2016). The development of super resolution LM has paved the way for super-resolution CLEM, which provides more accurate correlation of proteins to cellular structures (Peddie et al., 2017).

X-ray μCT imaging, LM and TEM have been combined in studies of adipose tissue in mouse limbs (Sengle et al., 2013), a molluscan excretory system (Handschuh et al., 2013) and cultured cells (Keene et al., 2014).

X-ray μCT has been used to pre-screen both resin embedded blocks of tissue infected with parasites and rare events in neuronal tissue (Starborg, 2017) (Karreman et al., 2017). Here, X-ray μCT is used to produce reference images as a guide for trimming, then the SBF SEM block-face image is compared to the μCT data to confirm the location.

The switch from photons to electrons as an imaging source can require complex manipulation of the sample. However, it is imperative that consecutive steps of sample processing preserve chemical and physical properties of structures to fit the requirements of the each imaging modality. Transfer and processing of samples between microscopy modalities require additional care to retain regions of interest, preserve ultrastructure and prevent artefacts and contaminants. Recent developments include correlative Raman and FIB SEM imaging (Timmermans et al., 2016), correlative LM and AFM (CLAFEM) (Janel et al., 2017) and correlative super-resolution LM and AFM (Fantner and Lafont, 2019).

2.7.3.2   Correlative studies of bone tissue

Much correlative work to date has been carried out on cell cultures, often using cryo methods such as high-pressure freezing. Challenges arise in the application to bulk tissue samples, including bone, which are not well suited to such preservation methods. In 1979 SEM and TEM were used correlatively to investigate bone healing (Sela and Bab, 1979). Methods for correlative LM and backscattered SEM of bone have been described (Goldman et al., 2000, Goldman et al., 1999). Bone sections examined by LM can be subsequently processed for SEM and TEM to evaluate bone morphology at a bone/implant interface (Figure 20) (Trirè et al., 2010). CLSM images of the LCN and bone mineral data quantified

using synchrotron small-angle X-ray scattering are correlated in a study of ovine bone (Kerschnitzki et al., 2013). A correlative approach to image cellular dynamics and surface modifications of osteoclasts used LM, SEM and AFM (Shemesh et al., 2016). Correlative examinations of bone can also involve merging results of imaging and mechanical measurements such as mechanical strain mapping (Jang et al., 2016) and dual energy X-ray absorptiometry (Guenoun et al., 2017). Correlative microscopy techniques have much to offer the bone biology and imaging community. Using CLEM techniques may allow molecular events to be observed and investigated while the combination of SEM with analytical methods such as failure testing and energy dispersive X-ray microanalysis has potential to reveal details of bone microstructure and behaviour (Shah et al., 2019).
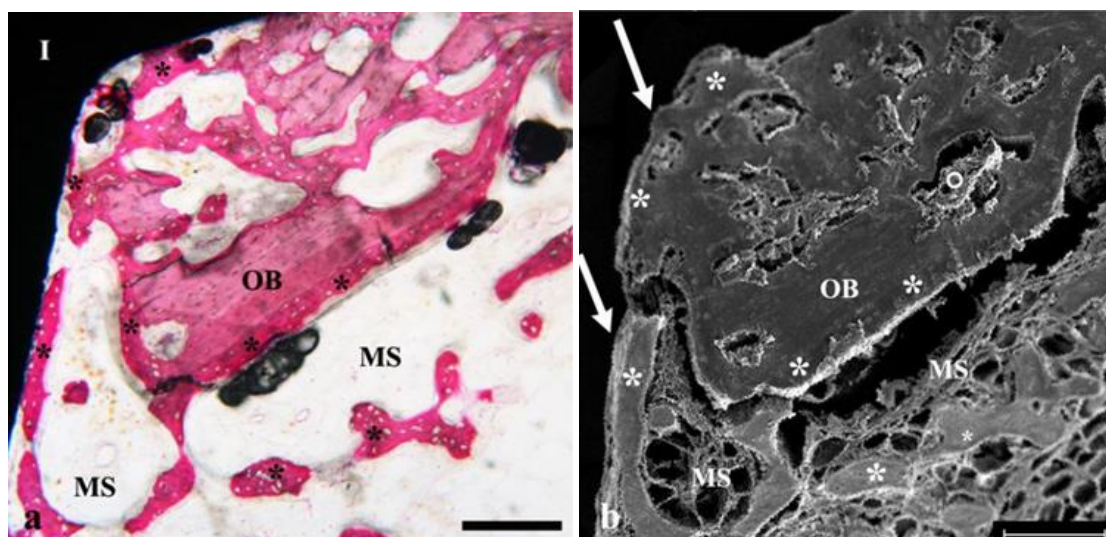
Figure 20   Correlative LM-SEM imaging of sheep tibia implanted with a titanium screw.

A   LM image of bone section and implant (I) showing medullary spaces (MS), newly formed bone (*) and old bone (OB).

B   The same section after removal of embedding medium and SEM processing. Osteocytes (o) are visible within lacunae and vascular tissue within the medullary spaces. The implant (I) has been removed to reveal the bone implant surface (arrows). Scale bar = 200 μm From (Trirè et al., 2010)

2.7.3.3 **CXEM**

Given that mechanotransduction mechanisms act across length scales, from the whole bone to the cell ultrastructure, bone tissue must be assessed at different hierarchical levels (Lucas et al., 2012). No imaging technique exists that can cover so many different scales at the same time, due to physical limitations. Even to image the different features of the ON&LCN in a restricted field of view, several length scales must be covered, from the osteocytes and the lacunae (~ 10 µm) down to the canaliculi (< 1 µm) and the cell processes and PCS (< 100 nm). As discussed, an ideal imaging method is one which can achieve this range of resolutions in *vivo*, in 3D, and over large volumes. In the absence of this 'holy grail' correlative microscopy offers an incremental improvement in imaging.

The correlative imaging approach developed in this project combines X-ray and electron microscopy modalities (CXEM) and will bridge some gaps between the individual methods (Table 7). Relatively large volumes will be analysed to quantify measures of many thousands of cells (X-ray µCT) and high-resolution quantitative information (SBF SEM) will be obtained concurrently from both the cellular and matrix components across tens of cells from within the original image volume.

This section has reviewed the history and the state of the art in techniques and tools applied to describe and quantify the microstructure and ultrastructure of the ON&LCN. Much has been learnt about the morphology of cells and processes, lacunae and canaliculi, the organisation of the networks and the changes which occur in aging and disease. However, there is a lack of information on the details of the relationships between the cells and the matrix as often they are imaged separately and the context is lost. 3D high resolution imaging of whole cells in relation to each other and to the matrix is also desirable. As geometry of the ON&LCN can impact strain sensation, those mechanisms

have been and are investigated by simulation to determine local matrix strains around cells (Wang et al., 2018) and to study wall shear stresses at the cell fluid interface (Anderson et al., 2005). However, it has been shown that idealised geometries are not appropriate to calculate local strain and cause underestimation of forces felt by cells (Anderson and Knothe Tate, 2008). So, more refined models are required based on 3D data (number of processes, process diameter, tortuosity) to enable more realistic *in silico* simulations. Our data will provide 3D measures of cell, lacunar and PCS volumes along with process and canalicular measures and variations in those measures across many cells.

Table 7　　　Quantitative measures produced by CXEM.
Quantitative data obtainable using µCT and quantitative data obtainable with SBF SEM are shown. Using CXEM expands the range of measures.

Measure	µCT	SBF SEM	CXEM
Osteocyte/Lacunar number and volume densities			
Osteocyte/Lacunar distribution			
Lacunar occupancy (%)			
Osteocyte/Lacunar volume			
Mean osteocyte/lacunar volume			
Osteocyte/Lacunar dimensions			
Osteocyte/Lacunar anisotropy			
Osteocyte/Lacunar orientation			
Pericellular space volume and dimensions			
Number of processes/canaliculi			
Orientation of processes/canaliculi			
Process/canaliculi dimensions			
Process/canaliculi tortuosity			
Ultrastructural details (e.g. nuclear contents, cell health)			

Section 2.8 of this chapter will discuss in greater detail the development of computational models for ON&LCN mechanobiology.

2.8   3D quantitative morphometry

In this section, the importance of standardised quantitative measures of the ON&LCN, the historical perspective on standardisation, and the identification of further measures required across length scales are reviewed and discussed. As outlined in the previous sections, gaining an understanding of the role of osteocytes in mechanobiology is important to bone health. As osteocyte function can be affected by cell and network morphology and the surrounding matrix environment, the spatial relationships between the ON and LCN are crucial to measure and later to model.

Reliable quantitative characterisation of both the ON and the LCN based on advanced 3D imaging across different length scales will inform computational models of bone mechanotransduction and will allow realistic predictions of ON&LCN activity during health and disease (Buenzli and Sims, 2015). As highlighted in previous sections, many imaging techniques have been used and in these studies many reporting methods have been used. This, in combination with the use of different species and anatomical areas can make comparisons between studies extremely difficult. Standardisation of measures can go some way towards making results more comparable.

Standardised quantitative morphometry of ON&LCN structures demands a consistent and well-defined set of descriptive quantitative 3D measures, independent of imaging technique and experimental conditions. Quantification of the ON&LCN structures should ideally be user-independent and automated to ensure consistency and efficiency.

This section will outline how standardised terminology for ON&LCN morphology was first introduced and how it has evolved with the introduction of new imaging methods.

In 1987 a report by the American Society for Bone and Mineral Research histomorphometry nomenclature committee was published (Parfitt et al., 1987). It aimed to create a unified system of standardised terminology by merging existing systems of nomenclature (when up to nine different terms were in use for a single measure) into a single system. These guidelines were adopted and subsequently reviewed and updated (Dempster et al., 2013). The guidelines include standardised nomenclature, symbols and units for reporting bone histomorphometry. 3D measurements are limited to surface, volume and thickness and all 3D measures are derived from 2D data. The guidelines are based on data from LM methods and thus while they do include sub-cellular measures including nuclear volume and cytoplasmic volume they do not extend to microstructural detail such as osteocyte processes or canaliculi.

With the advent and more widespread use of imaging techniques with improved resolution including µCT, the need for clearly defined and robust 3D measures was again highlighted. Measures of vascular canal connectivity were introduced (Cooper et al., 2003) and a committee was set up to address the need for consistent reporting of both image acquisition parameters and microstructural measures of bone tissue (Bouxsein et al., 2010). The guidelines produced define and describe 3D measures for trabecular and cortical bone morphology. As these standards are aimed at researchers producing data using lab based and SR µCT they do not extend to ultrastructural details of bone tissue and do not include measures for osteocytes.

A study using SR µCT and nano-CT introduced tissue level vascular canal indices and cellular level lacunar indices including number of lacunae (N.Lc), lacuna number density

(N.Lc/Ct.TV), lacuna volume (Lc.V) and lacuna volume density (Lc.V/Ct.TV) (Schneider et al., 2007). Canalicular indices for bone were introduced in a FIB SEM study of the LCN (Schneider et al., 2011). Measures defined include canalicular volume (Cn.V), canalicular volume density (Cn.V/Ct.TV) and canalicular thickness (Cn.Th).

It should be noted that the standard definition allocated to the abbreviation Ca is canal(icula)(r) (Dempster et al., 2013). As this does not distinguish between vascular canals and lacunar canaliculi, researchers have used Ca for both vascular canals (Schneider et al., 2013) and canaliculi (Buenzli and Sims, 2015). The abbreviation Cn is allocated to the term cancellous in (Dempster et al., 2013). Thus, care is needed in interpretation and comparison of quantitative measures.

Other studies carried out on the ON&LCN which have produced descriptive measures of shape, orientation, number densities, and occupancy ratios include (Britz et al., 2012b, Carter et al., 2013b, Schneider et al., 2007, Sugawara et al., 2005, van Hove et al., 2009, Ascenzi et al., 2008, Kerschnitzki et al., 2011, Schneider et al., 2011). A further framework was proposed for the 3D quantitative characterisation of osteocyte lacunae and their 3D spatial relationships across length scales from global to cellular levels (Mader et al., 2013). This framework includes shape, orientation, number density, spatial distribution and alignment and has been used to quantify lacunar properties in bone (Bach-Gansmo et al., 2015, Mader et al., 2015, Heveran et al., 2018, Wittig et al., 2016). In a study of the ON, measures related to connectivity and spatial distribution including canalicular connectivity between nodes, links and cells were compared (Kerschnitzki et al., 2013).

Dong and colleagues used automated quantification to extract 3D shape descriptors from SR CT data including number of lacunae (N.Lc), lacunar number density (N.Lc/BV), number of canaliculi (N.Cn) and canalicular branches (Dong et al., 2014b). The lacunar shape

descriptors degree of equancy (Lc.Eq), degree of elongation (Lc.El) and degree of flatness (Lc.Fl) have been introduced (Carter et al., 2013a). The total number of osteocytes, osteocyte connections and the size of the LCN in the human skeleton have been derived from quantitative data from 3D images of the LCN (Table 8)(Buenzli and Sims, 2015).

Table 8   Osteocyte network quantities for the human skeleton

ON measures used in calculations in (Buenzli and Sims, 2015). (Human unless stated otherwise).

Description (abbreviation)	Formula	Value
Osteocyte density (N.Ot/BV)	(N. Ot/N. Lc) × (N. Lc/BV)	19,000–28,500 mm^{-3}
Total number of osteocytes (Tt.N.Ot)	(N. Ot/BV) × BV	41.6 × 10^9 (~42 billion)
Total number of lacunae (Tt.N.Lc)	(N. Lc/BV) × BV	43.8 × 10^9 (~44 billion)
Total number of osteocyte dendritic processes (Tt.N.DP)	Tt. N. Ot × (N. DP/Ot)	3.7 × 10^{12} (3.7 trillion)
Total number of osteocyte connections (Tt.N.Ot.Cx)	(N. Cx/DP) × (N. DP/Ot) × Tt. N. Ot/2	23.4 × 10^{12} (~23 trillion)
Number of terminal connections per osteocyte (N.Cx/Ot)	(N. Cx/DP) × (N. DP/Ot)	1128
Number of terminal connections per dendritic process (N.Cx/DP)	$\frac{1}{\langle k \rangle} + \left(1 - \frac{1}{\langle k \rangle}\right) \frac{(\text{Tt.DP.L/DP})}{\langle l \rangle}$	12.7
Total cumulated length of osteocyte dendritic processes (Tt.DP.L)	(Tt. DP. L/BV) × BV	175,000 km
Cumulated length of osteocyte processes per osteocyte (Tt.DP.L/Ot)	$\frac{(\text{Tt.DP.L/BV})}{(\text{N.Ot/BV})}$	4.2 mm
Cumulated length of a single osteocyte process (Tt.DP.L/DP)	$\frac{(\text{Tt.DP.L/BV})}{(\text{N.Ot/BV}) \times (\text{N.DP/Ot})}$	47 μm
Total lacuno-canalicular system surface area (Tt.LCN.S)	Lc. S × Tt. N. Lc + 2π × Ca. Rd × Tt. DP. L	215 m^2
Total lacuno-canalicular volume (Tt.LCN.V)	Lc. V × Tt. N. Lc + π × Ca. Rd^2 × Tt. DP. L	35.8 cm^3
Lacuno-canalicular porosity	$\frac{\text{Tt.LCN.V}}{\text{BV}}$	2.05%
Total extracellular lacuno-canalicular volume (Tt.EC.LCN.V)	Lc. S × g × Tt. N. Lc + π(Ca. Rd^2 − DP. Rd^2) × Tt. DP. L	24.2 cm^3
Number of osteocytes replaced per unit time	Rem. R × (N. Lc/BV)	3.33 × 10^9 cells/year 9.1 × 10^6 cells/day

A study of human bone tissue using CLSM described quantitatively the canalicular density (Ca.Dn) and its variation within osteons (Repp et al., 2017). Canalicular network metrics using topological descriptors derived from complex network theory have also been developed (Kollmannsberger et al., 2017).

Bone J (Doube et al., 2010) is an ImageJ (Schindelin et al., 2012) plug-in designed specifically to provide standard measures for bone image analysis in an easily accessible and open-source approach. BoneJ has provided a significant contribution to the field. It allows calculation of several whole-bone, trabecular, and osteocyte lacunar measures including surface area, volume, and orientation but lacks the flexibility to perform a number of different analyses, necessary for large-scale studies and detailed analysis of distribution, alignment, and other osteocyte lacunar measures. BoneJ requires that data be isotropic for many functions and as the SBF SEM data produced here is anisotropic and re-sampling to

produce isotropy would remove much of the x-y detail which is crucial to this project the application of BoneJ was limited in this project.

Combining the measures in the existing guidelines while adding measures for osteocytes and ultrastructural detail would lead to a more comprehensive standard data set. In summary, a quantitative framework should include, although not be limited to, detail such as; osteocyte number density, spatial distribution and alignment, microstructural information including cell, pericellular space and lacunar shape and volume as well as ultrastructural detail such as process and canaliculus dimensions and tortuosity.

Here the historic and current situations have been reviewed and it is concluded that systematic quantitative characterisation of the ON&LCN based on 3D imaging across length scales is required. The contribution of quantitative measures to the field is illustrated by the use of anatomical data of osteocyte processes from TEM images which allowed the fluid flow strain amplification model to be tested and refined (You et al., 2001, You et al., 2004). TEM provided high-resolution measures of process diameter, PCS and canalicular structure as well as evidence for the presence of and spacing between the tethering elements which form a crucial part of the model. The model did not explain the molecular mechanism of sensation so has been further expanded to include integrins, identified using LM and immunohistochemical staining (Wang et al., 2007, McNamara, 2006, McNamara, 2009). As continually improving imaging data has provided critical input for theoretical models, allowing and improving realistic quantitative predictions, so it is hoped that CXEM imaging of bone will also provide data for future models and valuable insights into how structural changes affect mechanobiology. For example, data on canalicular occupancy and the number of cells which make connections with vascular and other structures, would improve accuracy when calculating the number of connections between osteocytes and

related cell networks. Modelling different cellular connectivity states may help to show how communication and mechanobiology are affected at different length scales.

As quantitative data is obtained in 3D over larger volumes and in greater detail the existence and use of a standard framework becomes more important, as does the automation of data acquisition and subsequent data handling. A standard set of measures for 3D quantitative characterisation of the ON&LCN has been created but is as yet incomplete, when high resolution and direct osteocyte imaging are considered. Further measures defined for inclusion are outlined in Chapter 4.

2.9 Computational models

Strains applied to whole bone are much lower than strain levels required to cause intracellular signalling, so must be amplified to elicit a biochemical response (You et al., 2000). To investigate and explain this phenomenon, pathways in bone mechanobiology must be understood. As direct experimental measurement in bone is challenging, *in silico* models have been widely used. In this section, proposed mechanisms for strain amplification and mechanotransduction and the importance of high-resolution 3D imaging to this computational modelling are reviewed.

2.9.1 Proposed mechanisms for strain amplification

Candidates for the mechanosensory system in bone were initially reviewed in the early 1990s, and included changes in whole tissue strain, hydrostatic pressure and streaming potentials generated by fluid flow through pores in a charged matrix (Cowin et al., 1991). More recently, theoretical and experimental studies have provided evidence in favour of interstitial fluid flow, driven by extravascular pressure and loading and also of direct matrix strain, where mechanical signals are transmitted from the whole bone to the ON. A further

possibility is the sensation of microdamage which stimulates removal and/or repair of damaged bone.

2.9.1.1 **Interstitial fluid flow**

Mechanical loading-induced fluid flow facilitates cell nutrition and waste removal (Piekarski and Munro, 1977). Early mathematical models of LCN fluid flow assumed simple cells without processes (Kufahl and Saha, 1990). More refined models, which took into account both the PCM and the osteocyte processes showed that fluid flow is driven to the centre of osteons and that a molecular sieve is present in the PCS (Zeng et al., 1994), later confirmed when tracer studies delineated the interstitial fluid space (Wang et al., 2004). In the mid-1990s attention was focused on interstitial fluid flow as the key mechanism for bone mechanotransduction (Weinbaum et al., 1994b, Cowin et al., 1995, Klein-Nulend et al., 1995). A model for strain amplification by fluid flow and mechanical stimulation of osteocyte processes was developed (Cowin and Weinbaum, 1998, You et al., 2001). It was hypothesised that the cell process was attached to the bone matrix by tethering fibres and that during loading the fluid passing through the PCS creates a drag on the bone matrix, which in turn creates tension on the tethering fibres and leads to strain experienced by the osteocyte process membrane. This model predicted strain amplifications from tenfold to hundredfold and confirmed earlier predictions (Weinbaum et al., 1994b) with the difference that the activating signal was the fluid flow-induced drag on the tethering fibres, and not the fluid shear stress. TEM subsequently revealed organised actin filament bundles within processes, less organised actin within the cell body, tethering elements and matrix material within the PCS (Tanaka-Kamioka et al., 1998, You et al., 2004) leading to a more refined model (Han et al., 2004). This model demonstrated that mechanical strains applied to the whole bone can be amplified enough to elicit cell signalling (You et al., 2004).

Immunohistochemical analysis revealed αVβ3 integrins on conical structures protruding from the ECM, connected to the membrane of the osteocyte process and tethering fibres (Wang et al., 2007, McNamara et al., 2009). A model introducing the concept of integrin-based initiation of intracellular signalling was developed (Wang et al., 2007) (Figure 10). This model exhibits rigid integrin attachments at the tip of the conical structures, tethering complexes at the osteocyte process membrane linked to the central actin bundle, and actin filaments that slide relative to each other. This model leads to greatly amplified axial strains in the membrane near the integrin attachments, which are sufficient to initiate electrical signalling. The role of αVβ3 integrin attachments has been further investigated using cultured cells showing that blocking integrin function changes osteocyte morphology and disrupts the release of biochemical responses to shear stress (Haugh et al., 2015). Analytical models indicate that the viscosity of the interstitial fluid and the permeability of the PCM significantly affect flow in the LCN (Sansalone et al., 2013). Models based on UHVEM predict that the geometry of the PCS affects the velocity of fluid flow (Kamioka et al., 2012). Fluid structure interaction (FSI) studies take into account the elasticity and potential deformation of the cell membrane in response to fluid flow. CLSM data has been used with FSI modelling to predict the mechanical environment of osteocytes during loading and showed that stimulation is greater in the cell processes than the cell body (Verbruggen et al., 2014).

2.9.1.2   Direct matrix-cell deformation

An alternative mechanism to interstitial fluid flow is direct matrix-cell deformation (Nicolella et al., 2005) the effects of which have been studied by *in vivo* strain measurements during physical activity, (Hoshaw et al., 1997, Milgrom et al., 2004). These studies do not account for microstructural inhomogeneity and variations in local tissue/cell

strains (Nicolella et al., 2006), therefore, FE models have been used to quantify local tissue deformation and response to changes in the local environment (Bonivtch et al., 2007, Deligianni and Apostolopoulos, 2008). It has been proposed that the osteocyte lacuna acts as a strain amplifier and that the amplification factor is related to the properties of the surrounding bone matrix (Nicolella et al., 2006, Bonivtch et al., 2007). FE modelling found that changes in the material properties of the surrounding bone matrix had significant effects on strain levels with maximum strains resulting from decreased tissue modulus (Bonivtch et al., 2007). A simplified 3D FE model of the ON&LCN has been used to explore the relationship between strain amplification and loading (Wang et al., 2015b). This study suggests that the strain amplification factor increases with loading frequency and increased strain. A multilevel FE approach, using idealised LCN geometry, related loads applied to whole bone with strains at a single lacuna and canaliculi (Deligianni and Apostolopoulos, 2008). This study revealed that osteocytes may experience much larger strains than those measured *in vivo*, which may be sufficient to elicit cell responses, suggesting that loads directly mediated through the mineralised bone matrix may produce a reaction similar to fluid flow.

2.9.1.3   **Microcrack theory**

Disruption or deformation of osteocytes by microcracks in the bone matrix caused by loading and fatigue has been shown to trigger firstly localised apoptosis and subsequently, targeted bone remodelling (Martin, 2000, Martin, 2002, Noble et al., 2003, Heino et al., 2009, Cardoso et al., 2009). Microcracks are also likely to affect the fluid flow within bone and consequently, bone mechanobiology. In a study measuring microstructural strain in cortical bone, it was found that the presence of a microcrack caused increased strain amplification (Nicolella et al., 2005). In an FE modelling study for a simplified Haversian

system, where strain-induced interstitial fluid velocities in osteons were evaluated, it was shown that the presence of a microcrack reduced fluid velocity, modifying the cellular environment and thus mechanobiological mechanisms (Nguyen et al., 2011). It is also suggested that microcracks do not cause a reduction in local signal sensation but a reduction in transduction (Ridha et al., 2015). A computational study incorporating both mechanical strain and microdamage suggested that there is a damage threshold below which osteocyte processes can sense changes in strain and fluid flow and above which osteocyte signalling is disrupted and apoptosis occurs (McNamara and Prendergast, 2007). In line with that, an FE model based on ruptured osteocyte connections suggests that microcracks inhibit transmission of signals through the osteocyte network (Ridha et al., 2015).

2.9.1.4   **Proposed mechanotransduction mechanisms**

Mechanotransduction is the conversion of a mechanical signal into a biochemical response, transmitted to an effector cell, resulting in a coordinated response causing appropriate architectural changes. Osteocytes detect load via a mechanical signal, likely perceived by one or more of the mechanisms discussed above. Osteocytes respond by releasing a range of biomolecules such as intracellular calcium, NO, prostaglandins, Wnt proteins, bone morphogenetic proteins and sclerostin (Figure 8) (reviewed in (Klein-Nulend et al., 2013). These signalling molecules modulate the recruitment and activity of osteoblasts and osteoclasts. This process is suspected to depend largely on the network topology, architecture and connectivity of the ON&LCN. The following section will discuss the contribution that improved high resolution 3D imaging can make to the success of future computational models.
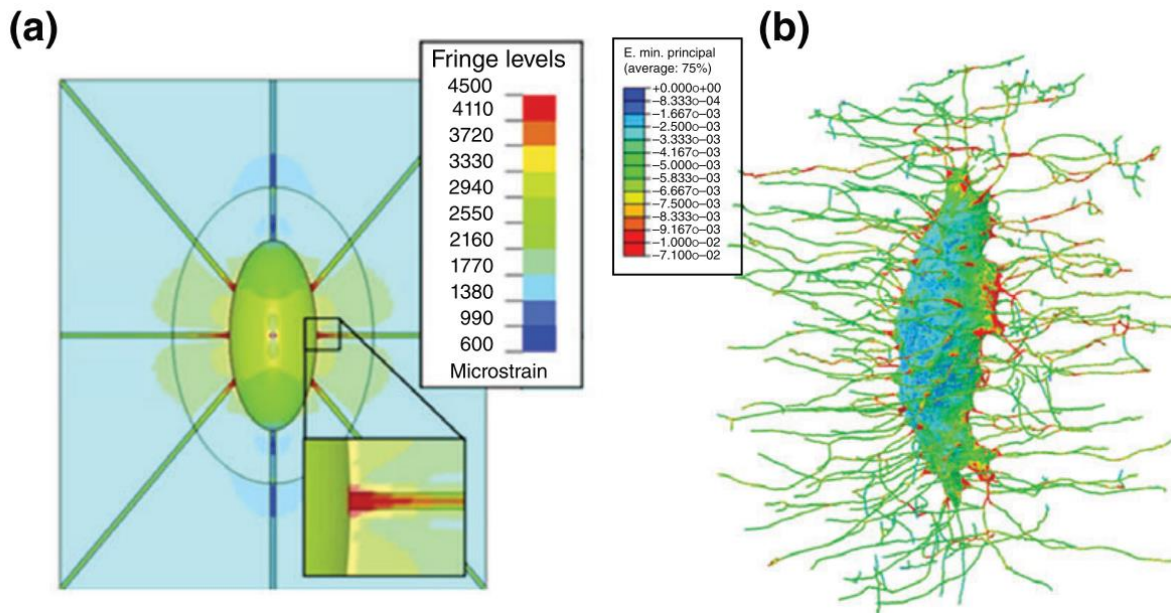
Figure 21   An illustration of the evolution of finite element models of bone cells

A   An FE model based on an idealized lacuna (Bonivtch et al., 2007)

B   An FE model based on realistic cell geometry from X-ray nano-tomography .

Adapted from (Giorgi et al., 2016)

2.9.2   **The importance of high-resolution 3D imaging to computational modelling in bone mechanobiology**

Computational modelling studies on bone mechanotransduction can be limited by the use of idealised ON&LCN geometries, which have been shown to be inappropriate when investigating local mechanical strains (e.g. simplifying the lacuna as an ellipsoid) (Figure 21) (McCreadie et al., 2004). Comparing the use of actual and idealised pericellular and canalicular geometries in computational fluid dynamics shows the influence of physiological geometry on force magnitudes imparted to cells through load-induced fluid flow. Idealisation resulted in underestimation of flow and shear stresses imparted by fluid drag on osteocytes (Anderson and Knothe Tate, 2008). A numerical study of murine osteocytes highlighted large differences between the results derived from idealised and from more realistic models for the ON&LCN, the PCM and ECM (Verbruggen et al., 2012). However, LCN geometry in this study was approximated based on CLSM images, which does

not offer spatial resolution sufficient to capture the fine details of the canaliculi. In an FSI study CLSM was used on rat bone sections to create a realistic ON&LCN model, which was further informed by earlier TEM data in terms of the conical ECM projections (Verbruggen et al., 2014). This study predicted that the cell process is the most mechanically active and mechanosensitive region of the osteocyte, confirming the results from an earlier study using an idealised model (Anderson et al., 2005). Some limitations of this study are the spatial resolution (~ 100 nm) not being adequate to detect the narrower processes, and the use of 2D TEM data to create a 3D model. Furthermore, assumptions were made about material properties of the cell and the bone matrix, the PCM was excluded and the anisotropy of the cell and the influence of the actin cytoskeleton were not reflected in the model. This does not undermine the value of this study, but rather underlines the complexity of modelling mechanotransduction processes at cellular and sub-cellular scales. As the reliability of FE analyses is largely determined by the accuracy of the input, accurate spatial description and quantification of the ON&LCN geometry is an essential prerequisite for more realistic models. In line with this, FE modelling of the LCN using high-resolution imaging techniques (ptychographic X-ray CT) data of mouse bone has been carried out (Dierolf et al., 2010, Schneider et al., 2012b) and provided evidence that high strain magnifications are limited to pericanicular regions and that FE modelling based on experimentally derived images of the LCN leads to higher strain magnification in comparison with idealised models.

A fluid dynamics modelling approach employed ultra-high voltage EM tomography to reconstruct a small section of a canaliculus in 3D (ignoring tethering elements and proteoglycans in the PCM) (Kamioka et al., 2012). Contrary to previous work (Wang et al., 2007, McNamara et al., 2009) no conical projections from the matrix wall were found (based on a single sample). In addition, the study showed that variations in the roughness

of the canalicular wall influenced the loading-induced flow of the interstitial fluid. One conclusion of this study was that fluid flow simulations based on 2D data may lead to inaccurate findings about mechanotransduction mechanisms.

In an FE study, human bone was imaged using synchrotron X-ray phase nanotomography at a voxel size of 50 nm (Varga et al., 2014). The LCN morphology was quantified and the osteocyte and processes artificially reconstructed using *a priori* assumptions from TEM and CLSM studies to approximate cell shape, canalicular occupancy and PCM and osteocyte process dimensions. FE models were generated and subjected to uniaxial compression confirming the existence of strain magnification through direct matrix-cell mechanotransduction. Furthermore, it was reported in the same study that cell deformations were localised at the cell-process junctions. These results confirm findings of previous investigations (Bonivtch et al., 2007, Deligianni and Apostolopoulos, 2008). A limitation of this study was the lack of original imaging data describing the cell shape.

In summary, the contribution of *in silico* models to the understanding of bone mechanobiology is undeniable. Recent improvements in computing power have allowed modelling to become a more important tool to test theories and develop new hypotheses. Modelling cell mechanobiology is challenging because of the small scales involved and the limitations of imaging to date. The discipline has progressed from 2D models to more complex 3D models, incorporating increasing levels of micro-architectural and physiological detail, which include actin fibres, focal attachments and more realistic geometries.

As the central question of bone mechanobiology asks how loading is transferred from the macroscopic organ level to the microscopic cellular level, computational approaches should integrate models across organ, tissue and cell scales, to allow realistic predictions

(Webster and Muller, 2011, Giorgi et al., 2016). Multiphysics modelling methods which combine the effects of several physical phenomena reflecting more realistically the *in vivo* environment should also be adopted (Giorgi et al., 2016). Further improvements in computational power and techniques along with reliable quantitative characterisation of both the ON&LCN based on advanced 3D imaging across different length scales will enhance both the predictive and descriptive ability of computational models and consequently enable the development of novel hypotheses and experimental studies (Buenzli and Sims, 2015). For example, data on canalicular occupancy and connectivity between cells and vasculature, would improve accuracy when calculating the number of connections between osteocytes and related cell networks.

In general, many computational models take a reductive approach, using simplified structures, such as models of individual cells used to represent a complex system. In future, expanded, more holistic, multiscale, multiphysics methods will be within reach and data from CXEM studies may contribute to this.

2.10   Conclusion

The ON&LCN are crucial for normal physiological functions of bone and other tissues, including homeostasis, repair and endocrine functions. The structure of the ON&LCN are changed across scales from the organ level – (distribution and density) to the cell level (number of processes, cell death) in development, ageing, oestrogen loss and diseases including OP. As changes in the structure of the ON&LCN affect mechanobiology, understanding these changes and their causes may help to clarify the pathophysiology of bone and eventually help identify therapeutic or preventative targets for diseases including OP.

In order to achieve this imaging is required. Ideally that imaging would be *in vivo*, large volume, high resolution and functional. However that possibility does not exist today and as a compromise a method for high resolution 3D imaging across length scales achieved using correlative µCT and EM (CXEM) is proposed.

In this spirit of furthering understanding of ON&LCN characteristics and the effects of both on mechanobiology, this project aims **t**o develop a framework for CXEM imaging to characterise quantitatively, across length scales, 3D osteocyte and lacunar microarchitecture in diseased human bone as well as of bone tissue across the animal life course.

The review process in this chapter has highlighted particular measures which are not systematically characterised to date. Data produced using CXEM will quantify both the ON and LCN and provide 3D measures of PCS, lacunar occupancy, cell process and canalicular dimensions, all lacking as described above.

Computational models have developed, improved and produced useful and relevant results as computing power has increased and as experimental data to 'feed' the models has improved. CXEM data can contribute to this continuing improvement.

In this chapter, the hierarchical structure of bone and the ON&LCN were described from the organ, through microstructural and ultrastructural scales. Bone cells were described, functions of osteocytes outlined and the changes observed to date in ON&LCN structure during ageing and pathology outlined. The properties of the ideal imaging method, imaging methods in use for ON&LCN imaging today and the advantages of correlative imaging have been discussed. Finally, a review of existing 3D quantitative morphometry used for characterisation, and identification of new measures required was followed by a discussion

of the progress of computational modelling in mechanobiology and the relevance of high resolution, 3D imaging to computational modelling.

In the following chapters, the development of methods for CXEM are outlined, followed by the application of these techniques to human and animal bone in health and disease.

Chapter 3   Development of correlative µCT and SBF SEM sample preparation and imaging protocols

Parts of the work presented in this chapter are also contained in the paper ***Development of protocols for the first serial block-face scanning electron microscopy (SBF SEM) studies of bone tissue***. Bone 2020 Feb;131:115107

Patricia Goggin, Elaine M.L. Ho, Helmut Gnaegi, Stuart Searle, Richard O.C. Oreffo, Philipp Schneider

3.1   Introduction

As established in Chapter 2, there is a need for a high-resolution 3D imaging technique that can simultaneously image the soft and hard tissue components of bone over a volume containing a substantial network of cells. Correlative X-ray and electron microscopy (CXEM), designed to meet this need, combines SBF SEM and tomography µCT in a correlative technique. CXEM will allow imaging and analysis of quantitative hallmarks of bone structure in 3D, at high resolution and across length scales. In order to apply CXEM to bone tissue, optimisation of the sample preparation and subsequent image processing and analysis protocols is essential.

The aim of the optimisation process described in this chapter is to prepare bone tissue for CXEM imaging and to refine the imaging processes. This necessitates fulfilment of the requirements of both SBF SEM and µCT, which will be discussed below. Imaging methods are optimised so that results show the ON&LCN and produce images that can be subsequently segmented to produce quantitative data and informative volume renderings.

SBF SEM can visualise both osteocyte ultrastructure and the surrounding bone matrix in 3D and segmented images provide a source of quantitative information. Bone tissue decalcified and prepared for SBF SEM will also be imaged using µCT, allowing imaging of osteocytes and vascular tissue..

The objectives of this chapter are:

- Optimisation of the stages of CXEM sample preparation for bone tissue namely, fixation, staining, decalcification and sample mounting.

- Optimisation of CXEM imaging conditions for bone tissue by analysis of signal to noise ratio, contrast to noise ratio and charging artefacts.

In this chapter, SBF SEM and µCT are introduced and the development of protocols for bone tissue preparation outlined. Complete protocols are set out in Appendix A. Image processing and analysis methods for the data are set out in Chapter 4 and Appendix B. The application of CXEM to bone tissue will facilitate qualitative and quantitative 3D studies of tissue microstructure and ultrastructure in bone development, ageing and pathologies such as OP and OA, to be described in Chapters 5 and 6.

3.1.1 Introduction to SBF SEM

3.1.1.1 Historical perspective on SBF SEM

Leighton and Kuzirian developed a promising technique for 3D imaging in the 1980's known as serial block-face imaging (SBFI) (Leighton, 1981, Leighton and Kuzirian, 1987) (Figure 22). In an SEM chamber, sections were cut from a resin block using a tungsten-coated glass knife, then the block-face was etched with oxygen plasma, which etches away resin faster than tissue, thus providing relief on the block-face and improving visualisation of tissue and

cellular components. The block-face was sputter-coated with gold to render it conductive and allow imaging free of charging artefacts, before a secondary electron image was recorded and the cycle repeated. The quickest cycle time for sectioning, etching, coating and imaging was 10 minutes.
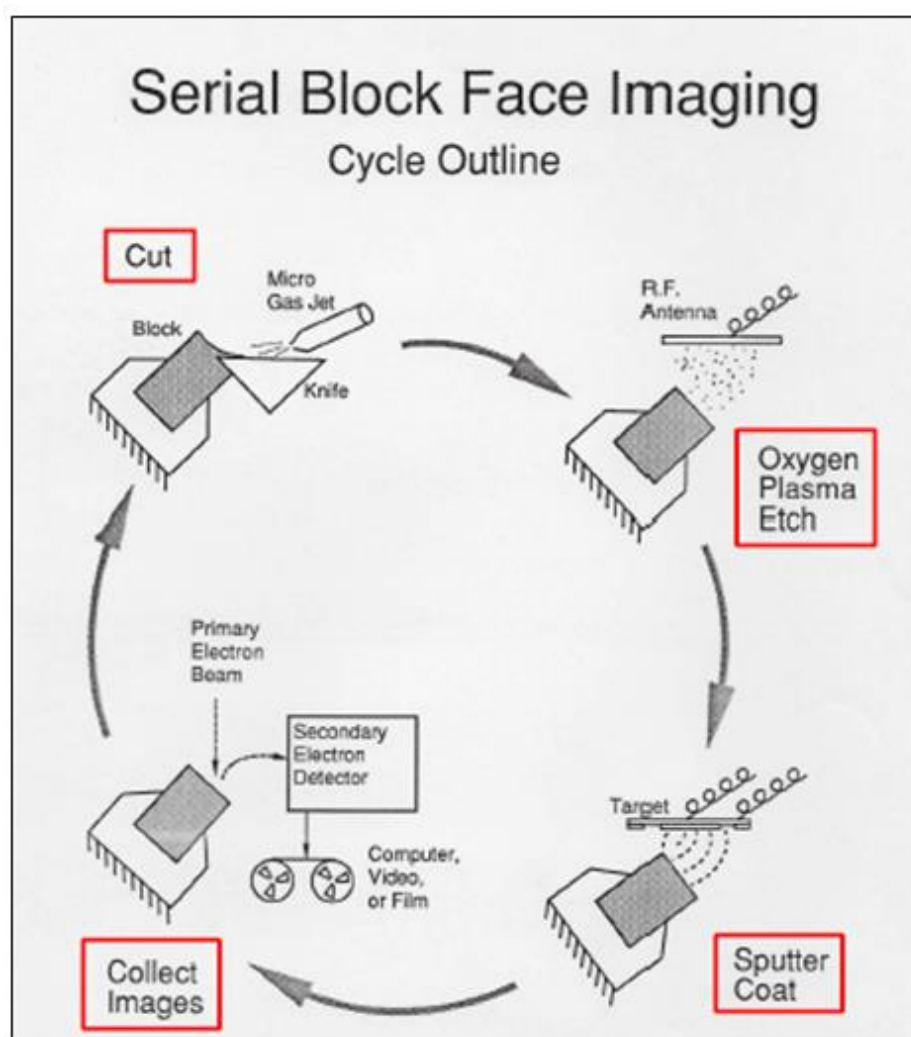
Figure 22   Cycle of SBF SEM imaging in the prototype apparatus.

In a high-vacuum SEM chamber sections were cut from a resin block using a tungsten-coated glass knife, then the block-face was etched with oxygen plasma improving visualisation of tissue and cellular components. The block-face was sputter-coated with gold to render it conductive and allow charge-free imaging before a secondary electron image was recorded and the cycle begun again. The best cycle time for sectioning, etching, coating and imaging was 10 minutes. Reproduced with the permission of Alan Kuzirian.

Due to limited funding, the contemporaneous development of confocal microscopy, subsequently adopted by many researchers, and due to the limitations of the existing vacuum and imaging technology, such as the restriction to high-vacuum imaging and the collection of data on film or video, SBFI was neglected for a certain time (personal communication, Alan Kuzirian). A meeting between Leighton, Kuzirian and the German physicist Winfried Denk led to further research and development in the early 2000's (Denk and Horstmann, 2004) and the launch of a commercial SBF SEM system through Gatan, Inc. (Abingdon, UK), known as the 3View® system. Alternative platforms such as the Teneo VolumeScope™ SEM (Thermo Fisher Scientific) (Korkmaz, 2016), and the Katana Microtome (ConnectomX, Oxford, UK) have also been launched.

3.1.1.2   Modern SBF SEM

Modern SBF SEM produces high-resolution 3D data using automated sectioning techniques. Lateral (x-y) resolution is comparable to TEM (< 5 nm), whereas the z-resolution is limited by section thickness (typically 30-70 nm). Using a remotely controlled ultramicrotome within an SEM, nanoscopic layers are removed from the tissue block, which is consecutively assessed by a back-scattered electron (BSE) detector to extract morphologies from 3D datasets with spatial resolutions comparable to TEM (Figure 23 and Figure 24). SBF SEM can cover large volumes of interest (~ 0.5 mm^3) and in principle, provides imaging contrast for soft and hard tissues at the same time, such as the ON&LCN, respectively.
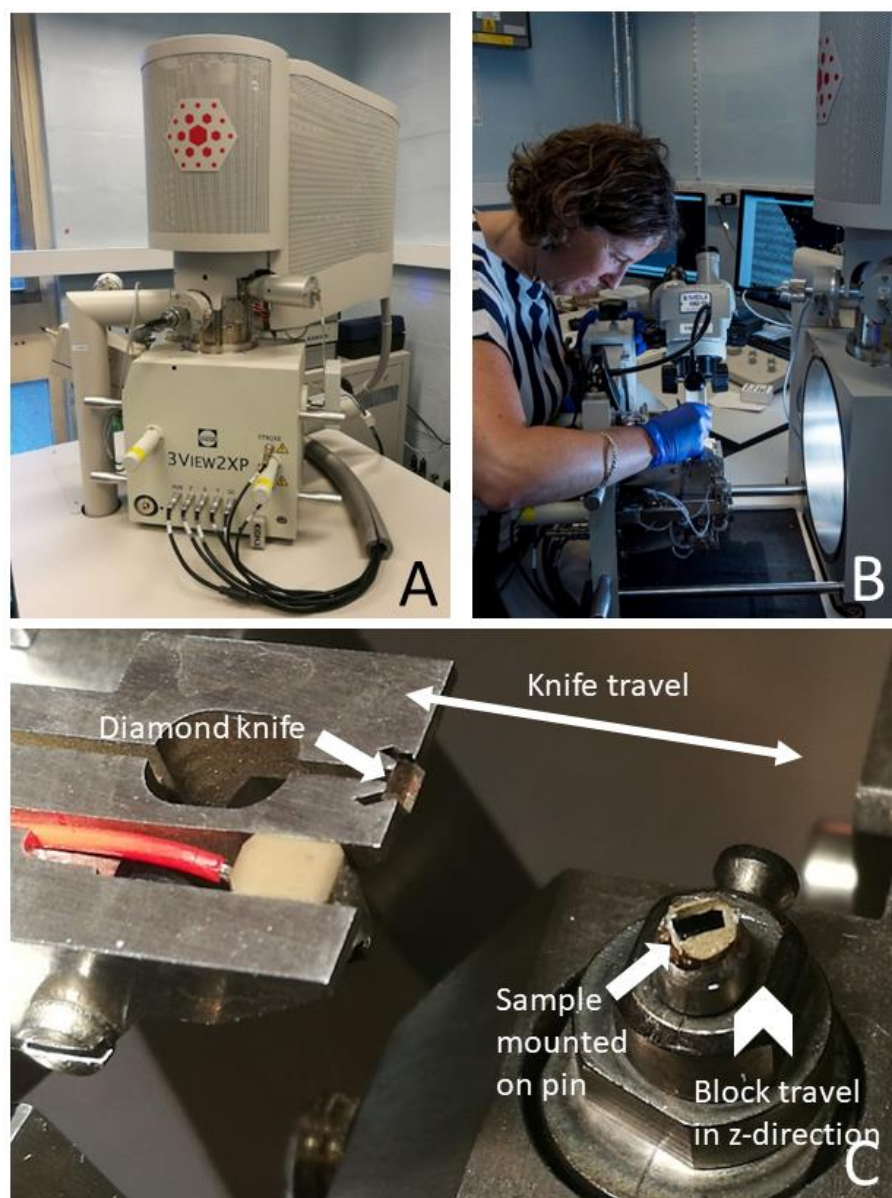
Figure 23   The SBFSEM system used in this project.

A   Gatan 3View®2XP system fitted in an FEI Quanta 250 field emission gun SEM. The original door supplied with the microscope is replaced by the 3View® system.

B   User mounting block into the 3View® system fitted to the SEM chamber door.

C   Detail of sample block mounted on a pin (arrow) and diamond knife in situ. The double-headed white arrow shows the travel of the knife and the arrowhead the movement of the block. During operation the knife moves over the specimen which stays fixed in place in the x-y plane but moves upwards a pre-determined increment in the z-plane (arrowhead), allowing the removal of a section when the knife returns to its original position. The block-face is imaged while the knife is retracted as above. From (Goggin et al., 2020)
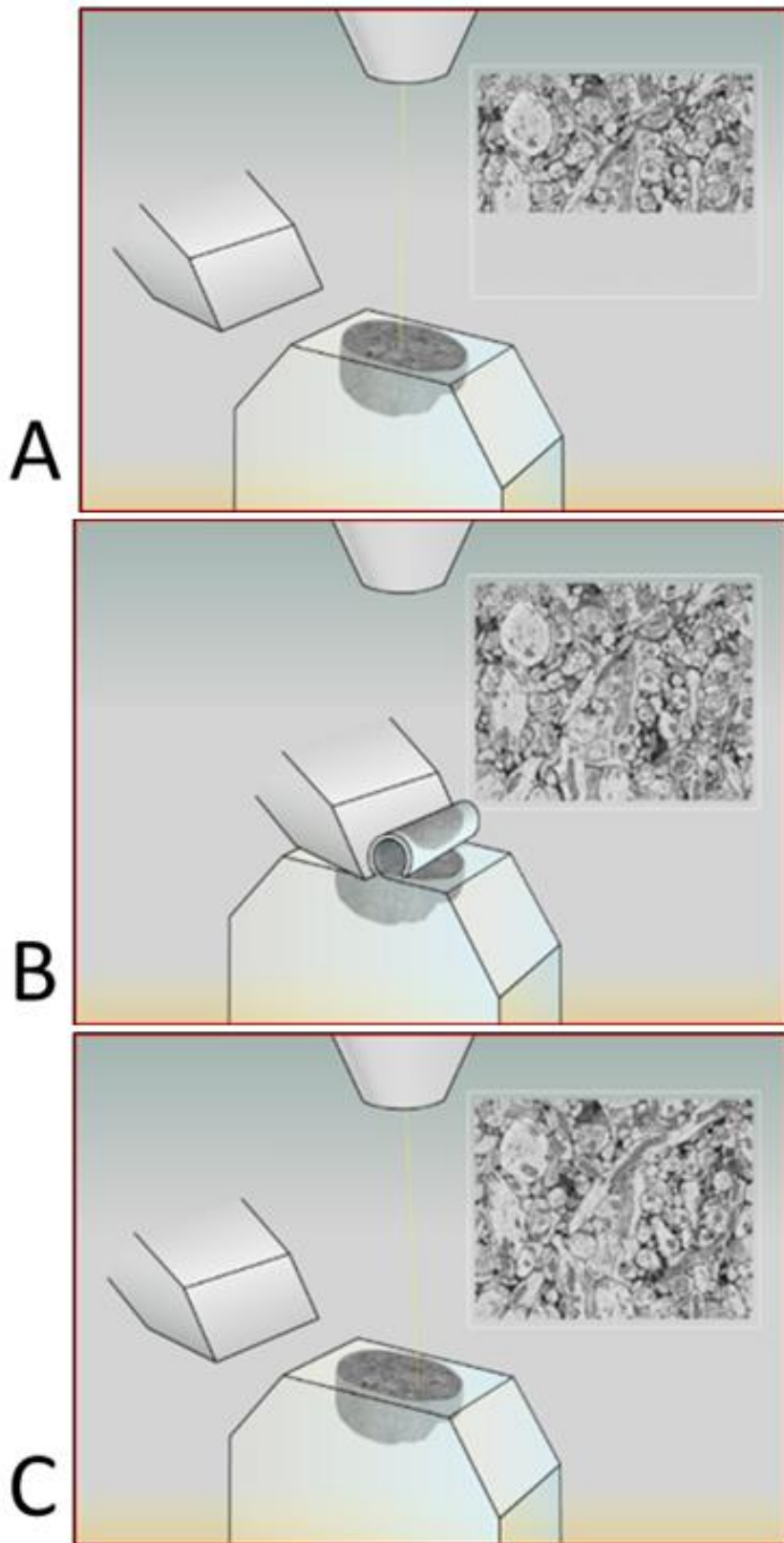
Figure 24   The principle of SBF SEM

A   The block face is scanned

B   A 50 nm slice is taken using a diamond knife

C   The freshly exposed block-face is scanned again (Images adapted from www.gatan.com)

3.1.1.3 **Application of SBF SEM to hard tissues**

CLSM, µCT and EM have made significant contributions to the understanding of bone and osteocyte structure and mechanobiology as outlined in Chapter 2. Serial FIB SEM has been used (Schneider et al., 2011, Tanoue et al., 2018) to image the ON&LCN covering 2-5 osteocyte lacunae at high spatial resolution. SBF SEM, which can image simultaneously the soft and hard tissue components of bone over a volume containing a network of up to 100 cells or more has received scant attention to date in the analysis of mineralised tissues. This is partly due to the availability of the technique. There are hundreds of µCT systems in the UK compared to < 15 SBF SEM systems (personal communication, Paul Spellward, Gatan UK). The lack of uptake to date is also due to the perceived difficulty of ultramicrotomy of harder materials including the risks of section, block and knife damage, and so the prevalent research focus on the mineralised hard bone matrix using X-ray based methods.

3.1.2 **Introduction to µCT**

3.1.2.1 **Historical perspective**

X-rays were discovered by Röntgen in 1895 and were used for imaging both in 2D and 3D. The mathematical basis for CT image reconstruction was set out some time before the first system was developed, reviewed in (Landis and Keane, 2010). The technique was in use as a clinical tool before the first X-ray µCT system, incorporating a revolving stage and with pixel size about 50 µm, was designed and built in the early 1980s (Elliott and Dover, 1982). Later, the first µCT scanner to evaluate the 3D micro-structure of trabecular bone was built (Feldkamp et al., 1989). In the 1990s, with the launch of commercial bone µCT scanners (Rüegsegger et al., 1996) this technique started to become a standard method in bone research.

3.1.2.2   **Modern μCT**

In modern μCT, the specimen is placed in the path of an X-ray beam so that a projection image is formed on a scintillator or other X-ray-sensitive detector array. The specimen is rotated and repeatedly imaged at different angles and the series of images is "back-projected" to reconstruct the x-ray absorption at each point within the specimen (Figure 25). As discussed in Chapter 2, lab-based X-ray μCT systems are widely available and commonly used to investigate bone microstructure (Muller, 2009, Draenert et al., 2012, Peyrin et al., 2014), while less widely available SR facilities provide higher resolution capabilities (Obata et al., 2020).

3.1.2.3   **Application of μCT to hard tissues**

Attenuation of X-rays by bone tissue provides image contrast for (2D) μCT. The technique is non-destructive and allows imaging of bone at isotropic resolutions ranging from about 100 μm to below 1 μm thus providing imaging at organ, tissue and cellular levels (Müller, 2009). μCT reaches similar resolution to LM, but does not achieve the resolution of EM. Thus, μCT of mineralised bone allows visualisation of lacunae, but not the fine detail of canaliculi.

3.1.3   **Correlative X-ray and Electron Microscopy**

As outlined in Section 2.7.3, combining μCT and SBF SEM in CXEM (Table 9) allows information to be obtained from an increased volume over SBF SEM alone and gives the ability to choose regions of interest for SBF SEM. SBF SEM provides high-resolution data from the cells and surrounding matrix. This is advantageous because as discussed in Chapter 2 understanding ON&LCN structure across scales and at high resolution is required to investigate mechanobiology of normal and pathological conditions in bone.
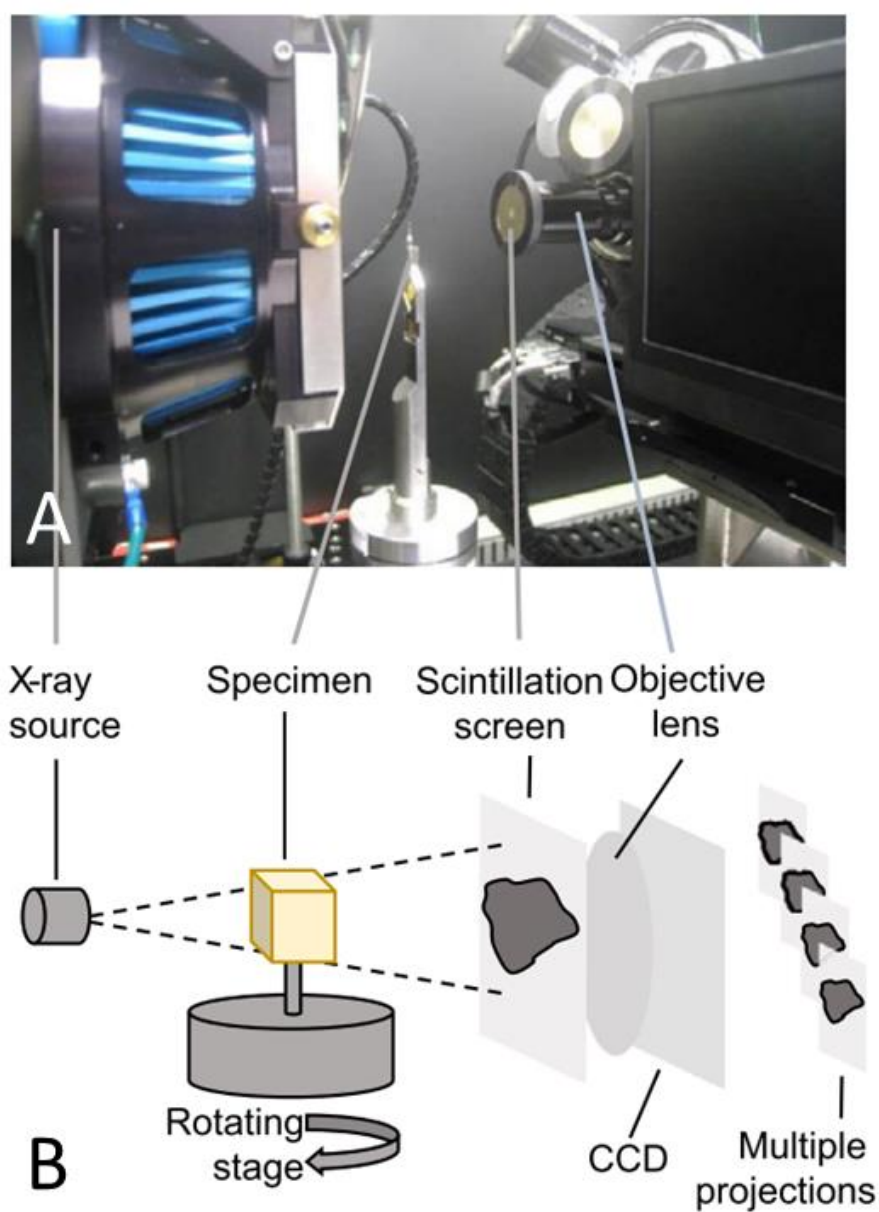
Figure 25   Principle of µCT

A   Interior of an Xradia Versa 510 µCT system

B   Schematic illustration of A showing the main components: X-ray source, revolving sample
           stage, objective lenses and scintillation screens which together form the detector and
           charge coupled device (CCD) for image capture.
           Adapted from (Shearer et al., 2016)

Table 9   Imaging capabilities of µCT and SBF SEM

	µCT	SBFSEM
Typical volume	$>10^9$ µm^3	10^5 µm^3
3D	Yes	Yes
Destructive	No	Yes
Resolution	< 1 µm	< 10 nm (x/y)
Cell and matrix imaging	No	Yes

The following details the optimisation of sample preparation, followed by the image collection settings. Chapter 4 will outline the image processing and analysis steps, which have been developed to extract the aforementioned quantitative data.

3.2   Optimisation of sample preparation

The aphorism 'Rubbish in, Rubbish out' is as relevant to microscopy as any other field (Peddie, 2019). How the samples are treated prior to imaging has a huge effect on the final results and can lead to the production of misleading data if not carefully considered and controlled. [1]

It is imperative that sample processing for correlative imaging preserves structural integrity and fits the requirements of the each modality used, although not always simultaneously. In addition to the demands of each imaging technique, the transfer of samples and processing steps required between microscopy modalities must be carried out with care to

---

[1] On two occasions I have been asked, "Pray, Mr. Babbage, if you put into the machine wrong figures, will the right answers come out?"... I am not able rightly to apprehend the kind of confusion of ideas that could provoke such a question.

— *Charles Babbage, Passages from the Life of a Philosopher*[1]

retain orientation and regions of interest and to prevent the introduction of artefacts and contaminants.

Sample preparation required for µCT imaging of mineralised tissue is minimal, while imaging of non-mineralised tissues requires the addition of contrast agents such as iodine, osmium, silver or phosphotungstic acid (Metscher, 2009). During decalcification, which can improve sectioning in SBF SEM, the contrast provided by minerals is removed, however when heavy metals stains are introduced, contrast (now negative) is restored.

In order to produce good quality SBF SEM images, tissue to be examined must be rendered electron dense to produce contrast in the images and made conductive to prevent charging artefacts that distort the images. The stages of processing are similar to those used in preparation for TEM imaging (Figure 26). In this section, the optimisation of each processing stage will be considered in turn and in the following section the µCT and SBF SEM imaging conditions.

3.2.1 Optimisation of sample preparation for SBF SEM

TEM processing involves fixation to preserve the size and structure of the cell components, staining with heavy metals to introduce electron density, dehydration and infiltration with resin followed by embedding and polymerisation to create a block of uniform hardness. Subsequent on-section staining with more heavy metal further enhances contrast. As bone tissue is mineralised, a decalcification step may be included to render the tissue more suitable for microtomy (Figure 26). These steps preserve the native shape and organisation of the cells, render the tissue able to withstand the electron beam and the vacuum environment without shrinking or tearing, produce contrast between the tissue structures and make the block of sufficient and uniform hardness to be sectioned easily (Hayat, 1989).

It is important to recognise however that each of these processes takes the tissue away from its hydrated *in vivo* condition and that this must be must considered when interpreting results. The principles of TEM specimen preparation apply equally to SBF SEM with the added demands that the tissue should be as conductive as possible in order to allow scanning of the block-face without charging and should have enhanced electron density to allow a high-contrast BSE signal to be produced. Staining and imaging facilitate segmentation of 2D images, 3D volume rendering and quantitative analysis. Sample preparation steps were optimised using murine and in human tissue and determined approaches optimised for imaging of the ON&LCN.
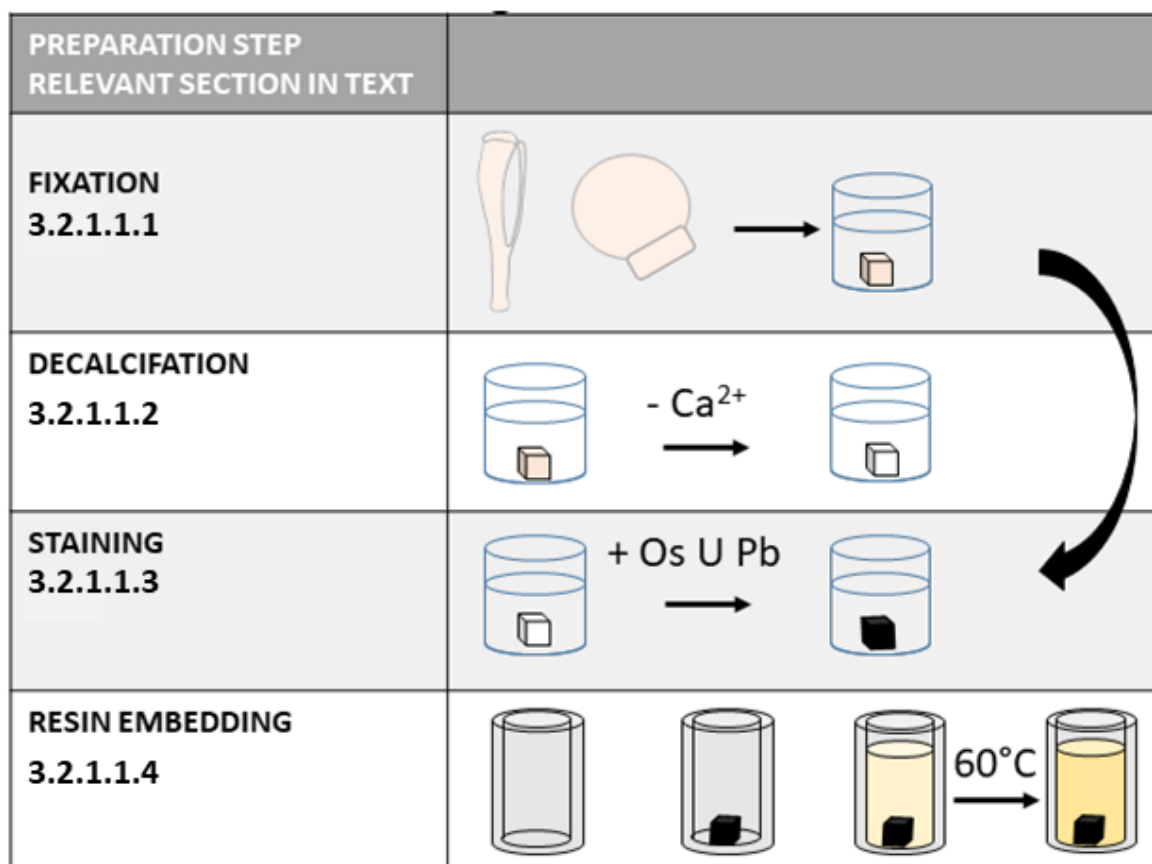
Figure 26   Workflow for SBF SEM sample preparation

Workflow diagram showing the sequence of processing stages in SBF SEM and CXEM preparation. The curved arrow shows where decalcification may be omitted. The relevant sections in the text that cover these individual steps are indicated. Adapted from (Goggin et al., 2020).

This section will describe the stages of sample preparation (fixation, decalcification, staining and resin embedding) and the optimisation work carried out. The recommended sample preparation protocol for CXEM imaging of bone tissue is set out in Appendix A.

3.2.1.1 Introduction to sample preparation steps

3.2.1.1.1 Fixation

Observation of bone structures at a cellular level and in a close-to-native state is challenging since most imaging techniques require tissue processing and/or sectioning, which entail a plethora of chemical and physical changes (Hayat, 1989, Mollenhauer, 1993). The criteria for 'good' preservation were summarised by Dr Audrey Glauert as:

'Obvious structural damage should be absent, membranes should be continuous; the perinuclear space should not be swollen and empty; there should be no empty spaces in the ground substance or within organelles. Loss of material and dimensional changes should be kept to a minimum.' (Glauert, 1975).

Fixation should result in images that reflect the native state of live cells, without artefacts such as shrinkage, which can lead to misinterpretation. Chemical fixation for EM most often uses aldehydes, which form crosslinks (covalent bonds) between tissue proteins, arresting the movement of proteins and adding rigidity to the tissue. Perfusion of chemical fixatives is ideal because the cells are fixed immediately at the moment of death. However, for ethical and practical reasons, as the entire organism must be sacrificed and large volumes of fixative are required, for example when samples of mammalian origin are used, immersion fixation is preferred. Tissue should be fixed immediately after excision, not allowed to dry out, thus avoiding artefacts of cell collapse, and dissected into blocks < 2 mm^3 (to ensure complete penetration of all processing solutions) while submerged in

fixative solution. Mineralised tissue is a challenging material for precise and immediate dissection into such small blocks due to the hardness of the tissue. Diamond saws, sharp single-edged razor blades and bone trephines may be used to facilitate production of suitably sized tissue blocks.

The most commonly used EM fixatives are 1-4% glutaraldehyde (GA) ($C_5H_8O_2$) and 2-4 % formaldehyde (FA) (CH_2O). FA penetrates tissue quickly and although the rate of diffusion of GA is slower it forms stronger links within tissue (Hayat, 1989). Additions to aldehyde fixatives can improve aspects of bone cell preservation. Acrolein is a small molecule which has been used for its rapid penetration qualities (McNamara et al., 2009) and Ruthenium III hexamine trichloride (RHT) improves fixation of proteoglycans (You et al., 2004).

3.2.1.1.2   Decalcification

Undecalcified bone tissue can be sawn into wafers, then treated with abrasive to form 'ground' sections (~ 10 μm), with or without resin embedding (An and Martin, 2003). FIB milling (Bakhsh, 2016, Bakhsh et al., 2015), cryo FIB milling (Bakhsh et al., 2015) and argon ion beam thinning (Palamara et al., 1981) can be used to produce thin sections of mineralised bone for TEM by using a focussed ion beam to erode the specimen to a thin layer. Sections can also be produced using a heavy duty microtome with a tungsten carbide blade or a diamond knife although this can cause artefacts such as scratching, section splitting or loss of sample by pulling the mineralised material across the surface of the block. Knife damage is also a possibility. As ion beam milling is a specialised technique and it is difficult to produce non-damaged sections of even thickness by microtomy of mineralised tissue, in most cases the bone tissue is decalcified (inorganic salts extracted) before processing for EM. Optimal decalcification of bone for SBF SEM should result in

images which show no signs of scoring, tearing or sample loss and should remove minerals from tissue without changing the cell structure, introducing artefacts affecting staining.

Tissue should be fixed before decalcification begins, although combined fixative and decalcifying solutions are commercially available (An and Martin, 2003). During decalcification strong mineral acids (nitric, hydrochloric), weak organic acids (formic, picric) or chelating agents (EDTA) remove Ca^+ ions (An and Martin, 2003). Strong acids decalcify rapidly but can affect the stainability of tissue (Callis and Sterchi, 1998, Sangeetha et al., 2013, Sanjai et al., 2012). EDTA affects only the bone mineral thus has less potential to cause cellular damage but it decalcifies more slowly than acids. A study using bone decalcified by both EDTA and hydrochloric acid found that the lacuno-canalicular network was preserved after demineralisation (Lin and Xu, 2011). The decalcification process can take days or weeks depending on the block size, concentration of decalcifying agent, agitation and temperature. Microwaves can be used to accelerate the decalcification process in bone and teeth and it is also suggested that a more even staining results (Sangeetha et al., 2013, Pitol et al., 2007) although this process is not widely used in routine bone microscopy. Post embedding block decalcification is possible but would not be suitable for use with SBF SEM (Shah et al., 2015). SBF SEM imaging of mineralised and decalcified bone tissue were compared.

3.2.1.1.3   Staining

Contrast in EM depends on the interaction of the electron beam with structures of differing electron density. Soft tissue structures do not have inherent electron density so stains must be attached to the organic molecules. The effectiveness of a stain is related to atomic weight so the most widely used are heavy metals. Staining for TEM can be carried out *en*

bloc during sample preparation and/or on grid-mounted sections before imaging. However, for SBF SEM all stains must be in the block before imaging. In addition to enhancing contrast, heavy metals make tissue more conductive, reduce charging and thus improve sectioning and imaging quality.

Osmium has long been used as a TEM fixative and stain (Palade, 1952). While sufficient to provide contrast in TEM, tissue stained with osmium alone does not have enough contrast for SBF SEM where low (2-5 kV) accelerating voltages and a BSE detector are used. Thus, protocols have been developed to increase the impregnation of heavy metals including the osmium-thiocarbohydrazide-osmium (OTO) method where thiocarbohydrazide acts as a bridging reagent allowing more osmium to bind to tissue (Seligman et al., 1966, Malick and Wilson, 1975) and the ferrocyanide-reduced osmium tetroxide methods (R-OTO) (Willingham and Rutherford, 1984, Karnovsky, 1971). More recent protocols combine these methods with prolonged uranyl acetate and *en bloc* lead aspartate staining (Deerinck, 2010), tannic acid treatment (Starborg et al., 2013) and uranyl acetate, lead aspartate, copper sulphate and lead citrate (Tapia et al., 2012) to increase the yield of BSE. Large volume staining for whole mouse brains is also possible (Mikula and Denk, 2015, Hua et al., 2015). 'Tried and tested' stains originally developed for TEM imaging, for example zinc iodide, are being trialled and found effective as SBF SEM stains potentially allowing imaging of precious and unique archive material prepared using these stains many years in the past (Kittelmann et al., 2016, Boulogne et al., 2020).

3.2.1.1.4 Resin embedding

Biological samples for SBF SEM need to be embedded in resin, which supports the tissue, creates block of uniform hardness and allows the block to remain stable, resist shrinkage

and maintain integrity in the electron beam. Assessment of radiation damage with TEM and AFM topographical analysis have shown that HardPlus and a Durcupan/Epon mixture are suitable resins for FIB SEM, maintaining stability and dimensional integrity during imaging and processing (Kizilyaprak et al., 2015). To date no comprehensive comparison of resins for SBF SEM has been carried out. One group comparing CY212, TAAB LV and Agar100 Hard resins favoured Agar100 Hard (Starborg et al., 2013). Resins used in SBF SEM studies have included Spurr resin (Kremer et al., 2015, Hondow et al., 2016), Epon (Kremer et al., 2015), Agar 100 (Hughes et al., 2013), Araldite (Arkill et al., 2014) and Durcupan (Armer et al., 2009, Russell et al., 2016, Deerinck et al., 2010). All commercially available resins are non-conductive. However, recent developments have suggested that the addition of carbon-based material such as carbon nanotubes or Ketjen black can produce a conductive resin which reduces charging artefacts and improves resolution (Nguyen et al., 2016, Ellisman, 2015). SBF SEM data produced from bone tissue embedded in three resins were compared to determine the most suitable.

3.2.1.2   Optimisation of sample preparation steps

3.2.1.2.1   Comparison of fixatives for SBF SEM of bone tissue

The effects of fixatives on human osteocytes were examined, using measurement of cell process shrinkage and a novel scoring system to evaluate the results in TEM images. Assignment of scores to aspects of EM images is an established quantitative technique (Baandrup et al., 1981, Grab et al., 1993, van den Bergh Weerman MA, 2008, Kuhn et al., 1975, Shami et al., 2014).

The four fixatives used were:

A: 1.5% GA, 1.5% FA, 1.5% acrolein in 0.1M piperazine-N,N'-bis(2-ethanesulfonic acid) (PIPES) buffer

B: 3% GA, 4% FA in 0.1M PIPES buffer

C: 3% GA, 4% FA, 0.7% RHT in 0.1M PIPES buffer

D: 3% GA in 0.1M sodium cacodylate buffer

Five human femoral heads (male 63 y/o, 72 y/o, 50 y/o and female 61 y/o, 50 y/o) were obtained from patients undergoing hip replacement surgery, with approval from the Southampton Hospital Ethics Committee (LREC 194/99) and appropriate patient consent. The femoral heads were immersed in fixative B within 2-20 min of excision. B is the most acceptable fixative to use in the clinic setting as the contents, while harmful are non-toxic. Blocks (< 2 mm^3) from the femoral head (FH) were cut using a fine toothed saw with hardened double blades, set at 2 mm distance (JLC, Czech Rep). Blocks were immersed in fixatives A-D for 6 h, rinsed in the appropriate buffer and placed in 2% aqueous osmium tetroxide (TAAB, Aldermaston, UK) for 1 h, all at room temperature on a rotator. Samples were decalcified and processed for TEM according to the protocol in Appendix A.

Table 10   Scoring scheme used to evaluate fixation quality

SCORE	2	1	0
Cell membrane	Regular, continuous, intact and clearly distinct.	Changes to regularity, less well defined, membrane protrusions.	Disrupted, broken, discontinuous, irregular, indistinct, blebbing.
Lamina Limitans	Well-defined, continuous, electron dense.	Discontinuous, not well defined.	Not visible, indistinct.
Cytoplasm	Fine granular homogenous appearance, no gaps/extraction, even staining.	Condensation of cytoplasmic material.	Spaces/gaps/vacuolation, irregular staining.
Nuclear membrane	Double membrane intact and regular.	Separation of membranes, widened perinuclear cisternae.	Disrupted, irregular
Nucleus	Regular shape, euchromatin and heterochromatin homogenous and distinguishable with chromatin masses adjacent to membrane, no chromatin aggregates.	Condensation of nuclear material, spaces in nucleus. Change in nuclear:cytoplasmic ratio.	Signs of apoptosis, membrane disruption.
Mitochondria	No swelling or shrinkage, no dilation of intracristal space, no distortion in morphology membranes outer double membrane and cristae intact, dense matrix.	Some swelling or shrinkage, distortion of cristae.	Swelling, shrinkage, 'blown', distended or peripherally located cristae, spaces.
Separation artefact	None	Small (< 250 nm)	Large (>250 nm)

The scoring system evaluates the morphology of the cell membrane, lamina limitans, cytoplasm, nucleus, nuclear membrane and mitochondria (Table 10 and Figure 27). The appearance of these features was assessed in each cell observed with perfect preservation scoring 2, compromised preservation 1, and very poor preservation 0, giving a maximum quality score of 14. Percentage shrinkage of cell processes was calculated using the methods set out in (Shah et al., 2015). Briefly, the diameter of the process in relation to the canalicular width was measured and the percentage area calculated.
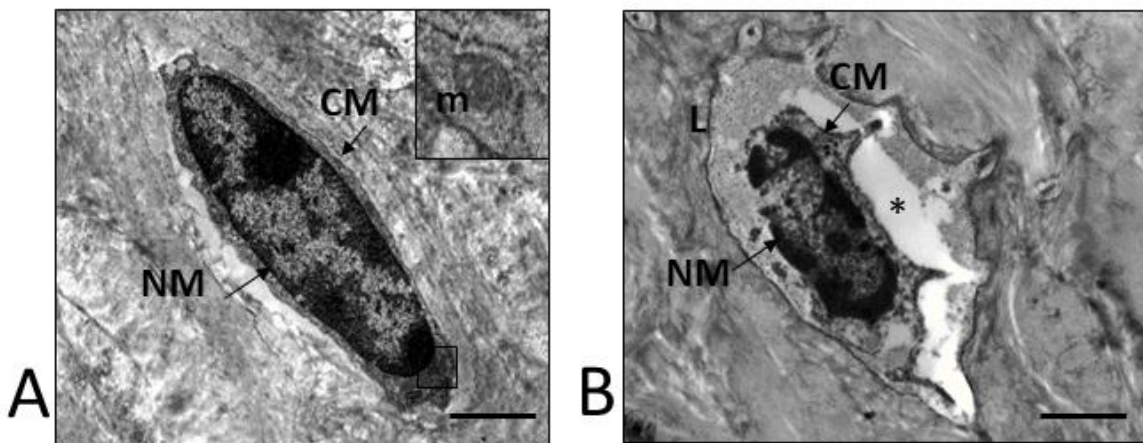
Figure 27   Preservation of cell ultrastructure

A   A TEM image of an osteocyte showing good preservation, cell (CM) and nuclear membranes (NM) are intact, the separation artefact is small*, mitochondria (m) (inset) have intact cristae and no swelling is observed.

B   A TEM image of an osteocyte showing poor preservation, cell (CM) and nuclear membranes (NM) are broken, nuclear material is clumped, there are spaces in the cytoplasm, a large separation artefact is present *, however the lamina limitans (L) is well defined.

        Scale bars = 2 µm

In order to determine which fixative, if any, produces the highest fixation quality scores, the inter-patient variation and any sex differences, quality scores for fixatives and patients and were compared to determine the effect on the quality and thus suitability for future work. Percentage process shrinkage was similarly compared. Results were plotted and analysed using one-way ANOVA tests in GraphPad Prism.

3.2.1.2.2   Comparing mineralised and decalcified bone tissue for SBF SEM

A 10-week-old C57BL/6 mouse (Home Office Project Licence Number 30/3095) was perfused with 4% FA, 3% GA, in 0.1M PIPES buffer, pH7.2, the tibiae removed and blocks approximately 2mm^3 cut with a single edged razor blade from the mid-tibial shaft without allowing the tissue to dry out.   4 blocks were decalcified using a 7% EDTA solution with continuous rotation for one week while the remaining blocks were stored in buffer. The EDTA was changed daily. Blocks were processed for SBF SEM as described in Appendix A and imaged using the 3View® XP2 (Gatan, Abingdon, UK) in a Quanta 250 FEG SEM (FEI, Eindhoven, Netherlands) at 3.5 kV, spot 3.5, 40 Pa, 8192 x 8192 pixels at 6.5 nm pixel size.

3.2.1.2.3   Staining for SBF SEM imaging

A slightly adapted version of the 'Ellisman' protocol (Deerinck, 2010) has been used on murine and human tissue and is included in the sample preparation protocol (A.4).

3.2.1.2.4   Comparing resins for SBF SEM imaging

Murine tissue blocks prepared for SBF SEM as described 3.2.1.2.2 above were embedded in Agar low viscosity (ALV) (Agar Scientific, Stanstead, UK) (a Spurr resin replacement), Durcupan (TAAB, Aldermaston, UK) and TAAB (TAAB, Aldermaston, UK) resins, imaged in the SBF SEM and the resulting image stacks compared by eye.

3.2.1.3 **Results of sample preparation optimisation**

3.2.1.3.1 **Comparison of fixatives for SBF SEM of human bone tissue**

Comparing male and female patients, no significant difference in either preservation quality or shrinkage was observed. Comparing patients, a significant difference (p=0.0436) was seen in the quality scores. No significant difference inter-individual difference was observed in shrinkage. There was no significant difference in either quality or shrinkage with the various fixatives (Figure 28).

3.2.1.3.2 **Comparing mineralised and decalcified bone tissue for SBF SEM**

The SBF SEM data from mineralised tissue can be produced in a shorter time and have more widespread electron density as the calcified matrix produces a high BSE signal. No block-face damage from cutting was seen on either dataset – discussed later in section 3.2.2.1. The images of decalcified bone show much greater detail within the osteocytes (Figure 29).
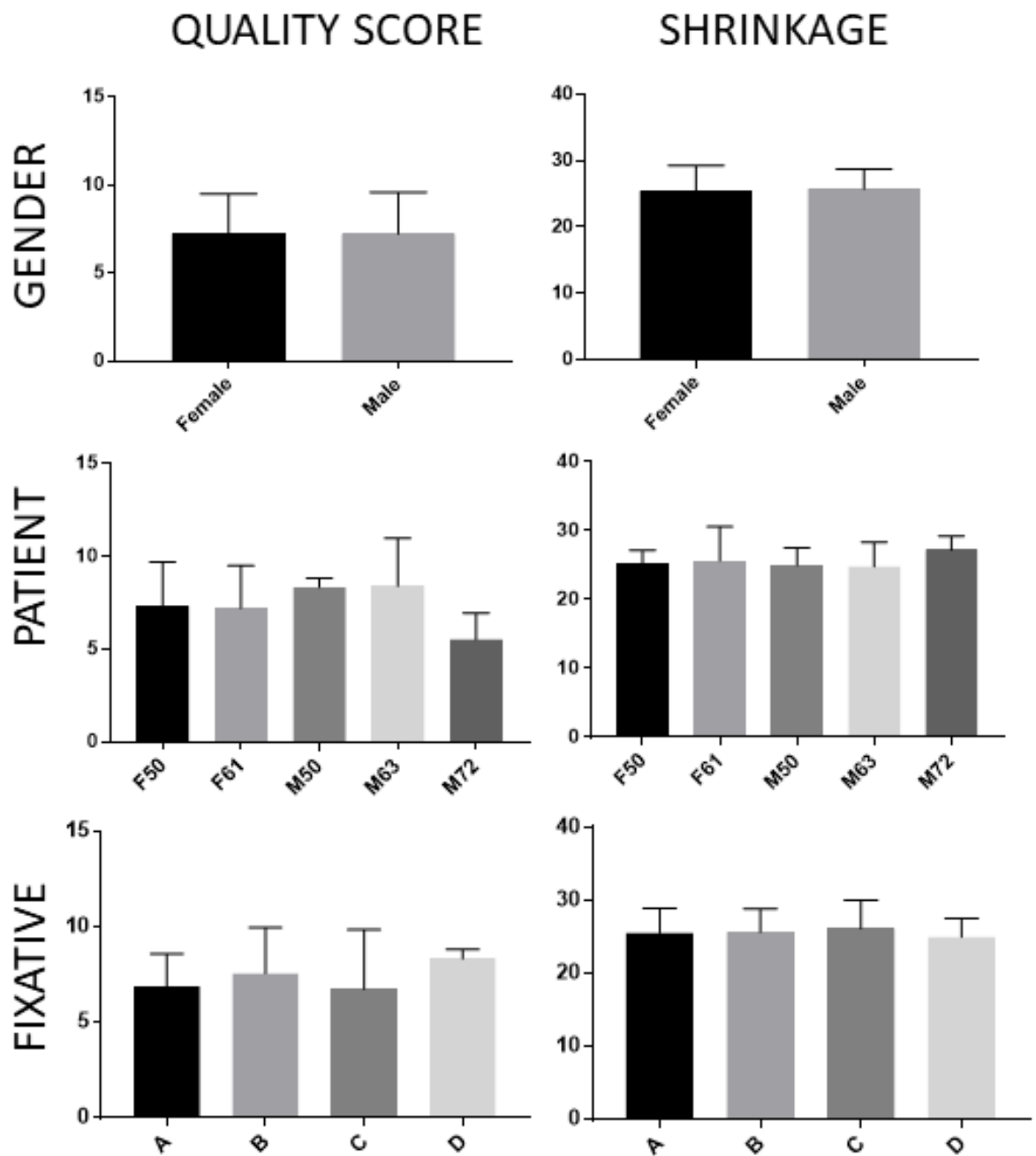
Figure 28   Analysis of quality scores and percentage shrinkage data.

Quality scores and shrinkage data compared for sex, patients and fixatives. There were no significant differences in scores between males and females. There was a significant inter-individual difference ($p < 0.05$) in quality scores but not in percentage shrinkage. There was no significant difference in scores for different fixatives. n = 3 males, n = 2 females.

3.2.1.3.3 Comparing resins for SBF SEM imaging

TAAB resin shows surface damage at a lower electron dose than either Durcupan or ALV

(Figure 30).
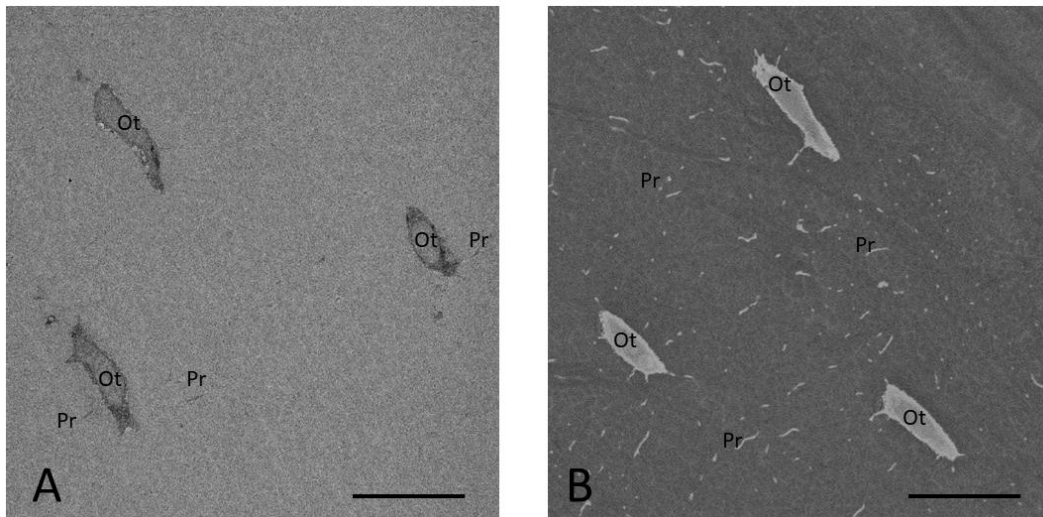
Figure 29 SBF SEM images of decalcified and mineralised murine bone tissue

A   Mouse bone decalcified using 7% EDTA for 1 week, changing solution every day.

B   Undecalcified tissue imaged with SBF SEM. Scale bars = 10 μm
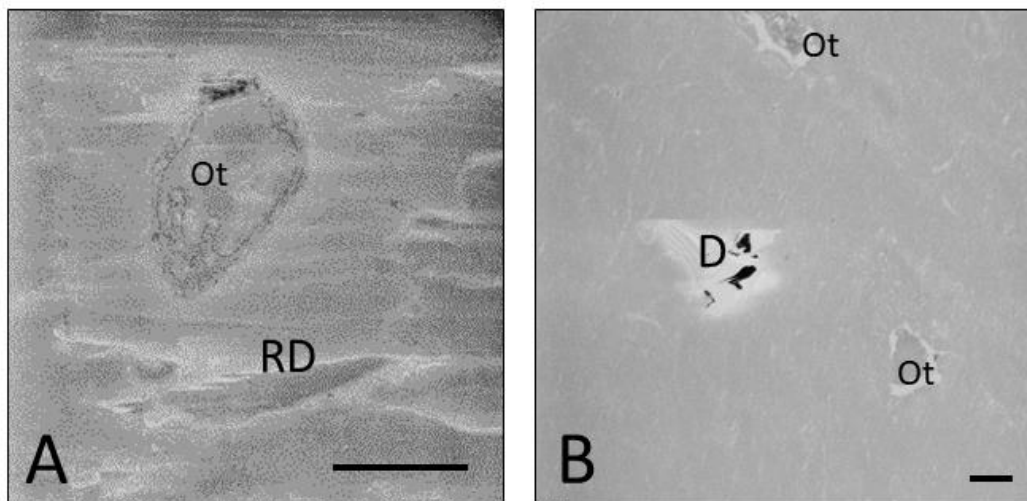
Figure 30 Resin comparisons

A   TAAB resin-embedded murine bone tissue showing an osteocyte (Ot) and surface
         resin damage (RD)

B   ALV resin-embedded murine bone tissue showing an osteocyte (O) and debris (D) on
         the surface. Scale bars = 5 μm

3.2.1.4   Discussion of sample preparation for SBF SEM

All four fixatives appear to produce similar quality scores; there is no significant difference between the sexes. There is a significant difference observed in the patient v quality score. It must be noted that all patients have some disease and the ideal would be to compare healthy controls to these samples. The ethics in place for sample collection do not provide us with clinical information to allow severity of disease to be taken into account. Considering that results of fixation are equal, hazards associated with fixatives are taken into consideration. Acrolein is volatile, flammable, corrosive, a danger to the environment and toxic, sodium cacodylate buffer contains arsenic and is toxic and RHT is corrosive. In order to reduce exposure to hazards during the project Fixative B is judged a suitable choice for the sample preparation protocol (A.4).

The SBF SEM data from mineralised tissue is closer to the native state than the decalcified tissue. The datasets can also be produced in a shorter time. No block-face damage from cutting was seen on either dataset – discussed later in section 3.2.2.1. The images of decalcified tissue have less contrast between the cell and matrix but show much greater detail within the osteocytes allowing the ultrastructure to be segmented and thus quantified more easily (Figure 29). SBF SEM of undecalcified tissue, while not directly applicable to this project has been applied in other fields such as dentine tubule imaging (Mahmoodi et al., 2020).

Variations of the so-called 'Ellisman' protocol (Deerinck, 2010) have gained wide acceptance among the SBF SEM community as reliable staining protocols resulting in maximum contrast and conductivity and minimising charging artefacts (Kremer et al., 2015,

Peddie and Collinson, 2014). In Section 3.2.2 staining methods developed for SBF SEM are compared to determine their effect on μCT imaging.

Durcupan is a viscous resin, which can be difficult to use. Spurr resin has been used previously for the preparation of mineralised bone for light microscopy (Xipell and Gladwin, 1972) and it is found that ALV resin, which now replaces Spurr for safety reasons, is a suitable choice for this project. Its hardness allows a higher electron dose to be used before cutting artefacts start to appear (Starborg et al., 2013), its low viscosity makes it easy to use and it provides rapid and excellent infiltration, however the hardness can cause the sections removed to shatter. The addition of a small amount of contact adhesive (Pattex Kontaktleim, Henkel AG &Co., Germany) to one edge of the block adheres the slices of tissue to the knife edge and reduces the risk of problems caused by 'free floating' resin sections which might include masking detail on the block, obscuring apertures or contaminating the detector.

Traditionally tissue blocks for electron microscopy are cut into thin sections for later observation in TEM. To enable this, tissue blocks are usually embedded in plastic capsules, surrounding the block with resin. The minimal resin embedding method originally introduced for targeted FIB-SEM milling (Schieber et al., 2017) to reduce the amount of surrounding resin and thus the volume of the block is adopted in this project. After μCT scanning, the minimally embedded blocks can be re-embedded in capsules with surrounding resin for the trimming step of SBF SEM, which follows.

3.2.1.5 **Comparison of TEM and SBF SEM images**

Finally, to determine whether SBF SEM provides images of sufficient resolution to visualise cell ultrastructure, TEM and SBF SEM imaging of osteocytes are compared. Murine and human bone tissue blocks were processed and imaged for TEM and SBF SEM using the methods in Appendix A.

Figure 31 shows SBF SEM and TEM images of murine and human osteocytes in decalcified tissue. The images exhibit sufficient spatial resolution and image contrast for visualisation of cell ultrastructure and, critically, illustrate the features of cells that have been well fixed. The cell membrane and nuclear membrane remain intact and regular, the mitochondria show neither swelling nor shrinkage and there is no cell shrinkage evident. Using SBF SEM images it is also possible to determine whether lacunae are occupied by an osteocyte and similarly, whether canaliculi house a cell process or not.

TEM

SBF SEM

MURINE

HUMAN
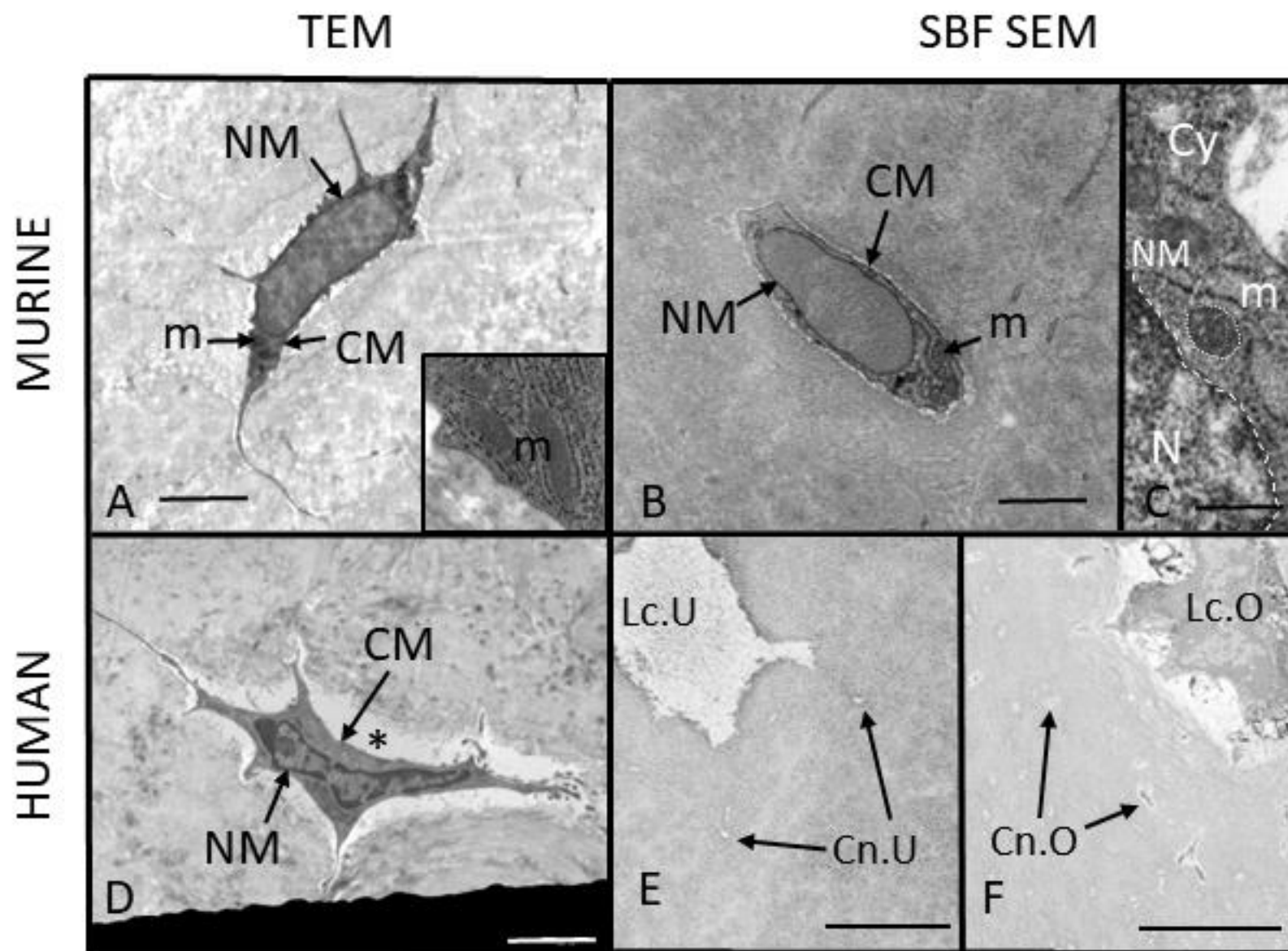
Figure 31   Assessment of EM sample preparation quality and lacunar occupancy.

A   TEM image of a murine osteocyte in perfusion-fixed, decalcified bone showing sufficient spatial resolution and image contrast for visualisation of cell ultrastructure. The cell membrane (CM) and nuclear membrane (NM) are intact and regular, the mitochondria (m) show neither swelling nor shrinkage and there is no cell shrinkage evident. Inset shows mitochondria (m) and rough endoplasmic reticulum from a different osteocyte.

B   SBF SEM image of a murine osteocyte in perfusion-fixed, decalcified bone showing sufficient spatial resolution and image contrast for visualisation of cell ultrastructure. The cell membrane (CM) and nuclear membrane (NM) are intact and regular, the mitochondria (m) show neither swelling nor shrinkage and there is no cell shrinkage evident.

C   Detail of nucleus (N), nuclear membrane (NM, dashed line), cytoplasm (Cy) and mitochondrion (m, dotted line) from an SBF SEM image of a murine osteocyte.

D   TEM image of a human osteocyte in immersion-fixed, decalcified tissue showing intact cell membrane (CM) and nuclear membrane (NM). The pericellular space (*) is enlarged, probably due to cell shrinkage.

E, F SBF SEM image of immersion-fixed, decalcified human bone tissue showing occupied (Lc.O) and unoccupied (Lc.U) osteocyte lacunae and occupied (Ca.O) and unoccupied (Ca.U) osteocyte canaliculi.

Scale bars A, B and D = 2 µm, C = 200 nm, E and F = 5µm From (Goggin et al., 2020)

3.2.2   **Optimisation of sample preparation for µCT**

Correlative imaging must accommodate the requirements of different techniques by specific sample preparation while achieving well-fixed and stained tissue. As µCT is already an established technique, fewer optimisation steps are required. µCT is usually applied to mineralised bone. Studies have been carried out on stained non-mineralised tissues (Metscher, 2009), however the approach of scanning decalcified and stained bone tissue is novel. Correlative approaches can involve additional sample preparation steps between modalities but as preparation for SBF SEM, especially fixation, is crucial and must be carried out immediately the tissue is excised it was considered best to prioritise the demands of SBF SEM.

3.2.2.1   **Introduction to μCT sample preparation steps**

3.2.2.1.1   Fixation

As SBF SEM fixation was considered the priority in this work and the spatial resolution of μCT does not allow visualisation of cellular ultrastructure, no fixation comparisons were carried out specifically for μCT.

3.2.2.1.2   Decalcification

To determine how the presence of mineral in bone affects the results of μCT scanning resin embedded bone samples with and without decalcification were imaged.

3.2.2.1.3   Staining

To determine how staining affects the results of X-ray μCT scanning resin embedded bone samples with and without heavy metal staining were imaged. To further optimise image quality, the images resulting from SBF SEM staining methods were compared. Several staining methods have been developed for SBF SEM and some are particularly designed for large tissue samples (Section 3.2.2.2.2). To identify whether one of these will provide even staining with sufficient contrast for μCT imaging of osteocytes in bone tissue bone tissue blocks were stained and scanned using these protocols. The brain-wide reduced-osmium staining with pyrogallol-mediated amplification (BROPA) technique was not included as the protocol duration of 2-3 months was thought impractical (Mikula and Denk, 2015). The aim is to produce evenly stained blocks, which allow the cellular components of the bone tissue to be visualised and segmented for quantification.

3.2.2.1.4   Resin

As cutting for SBF SEM was considered the priority in this work and the type of resin was considered unlikely to affect µCT imaging results, no resin comparison steps were carried out specifically for µCT imaging.

3.2.2.2   **Materials and Methods**

3.2.2.2.1   Decalcification

Tissue from human femoral head was prepared as described in Appendix A. The decalcification step was omitted on some blocks. Samples were scanned using the set-up shown in Figure 32 and settings in Table 11. The blocks were imaged using an Xradia Versa 510 (Zeiss X-ray Microscopy Inc., Pleasanton, California, USA) scanner. Following acquisition, the data were reconstructed using commercial reconstruction software (XMreconstructor, Zeiss X-ray Microscopy Inc, Pleasanton, California), which uses a filtered back-projection algorithm and reconstructed slices were exported as 16-bit tiff files. These settings were chosen based on the previous experience of the operator.

Table 11   Scan settings for bone tissue blocks

Preparation	Voxel size (µm)	Binning	Voltage/ Power	Number of projections	Filter	Objective lens	Exposure (s)	Scan time (h)
Stained Mineralised	1.5	1	80/7	2001	LE1	x 4	7	6
Stained Decalcified	1.5	1	80/7	2001	LE1	x 4	7	6
Unstained Decalcified	1.5	1	80/7	2001	LE1	x 4	7	6
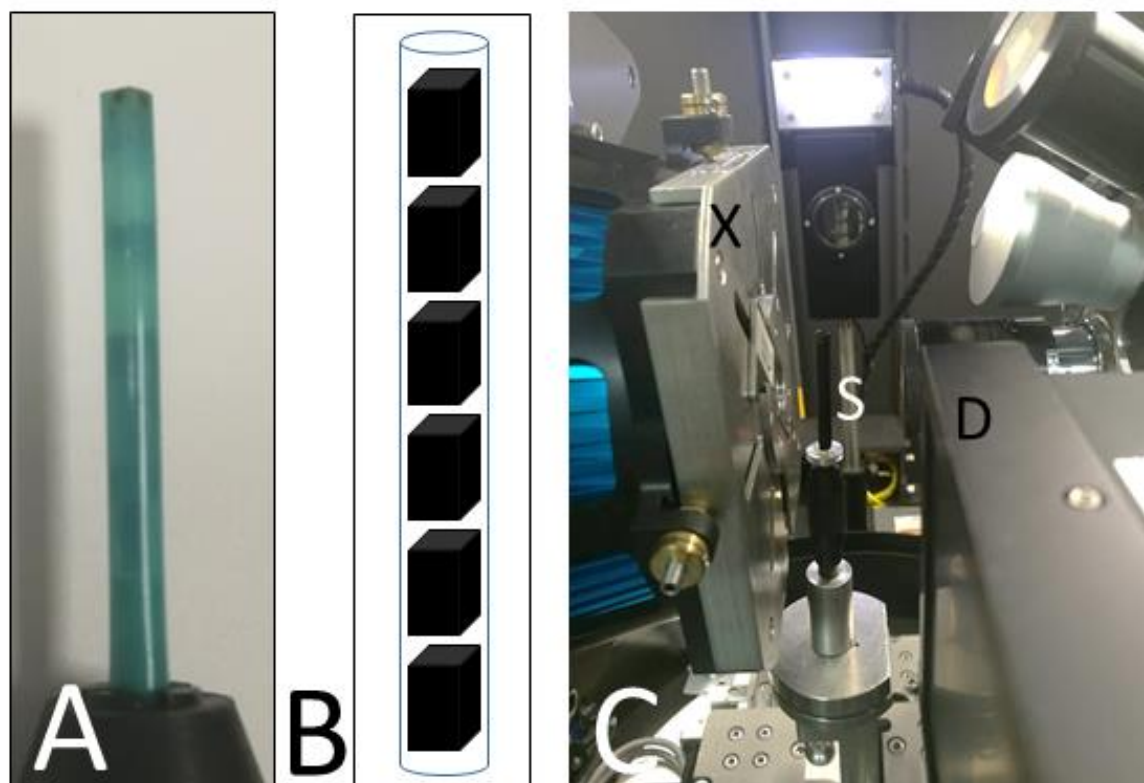
Figure 32   Set up for CT scanning.

A   Stained bone samples mounted within a plastic straw for scanning.

B   Schematic representation of A.

C   Image taken inside the Xradia Versa 510 µCT scanner showing the straw containing samples (S), X-ray source (X) and detector (D).

3.2.2.2.2   Optimisation of staining for µCT imaging

Tissue from human femoral head was prepared as described in Appendix A, omitting the staining steps on some blocks and scanned as described above. Tissue blocks were also stained as set out in Table 12 to compare results of staining protocols. Staining followed the 'Ellisman' protocol, the same protocol with decalcification carried out afterwards (Deerinck, 2010), the Hua protocol (Hua et al., 2015), the fast BROPA protocol (Genoud et al., 2018) (based on (Mikula and Denk, 2015)) carried out with and without lead aspartate and a high osmium inclusion protocol (Knott and Genoud – personal communication, EMBL workshop, 2018). Scanning was carried out at the settings in Table 11.

Table 12   Table of preparation steps.

The table shows the staining protocols tested and the steps in each. BROPA - brain-wide reduced-osmium staining with pyrogallol-mediated amplification, fBROPA – fast brain-wide reduced-osmium staining with pyrogallol-mediated amplification, fBROPA – fast brain-wide reduced-osmium staining with pyrogallol-mediated amplification. LA = lead aspartate, TCH = thiocarbohydrazide, UA = uranyl acetate, DEHY = dehydrate

PROTOCOL																				
Ellisman pre-decal	FIX	Wash	OsO_4		$OsO_4+KFeCN$		Wash			TCH	Wash	OsO_4	Wash	UA	Wash	LA	Wash	decal	DEHY	RESIN
Ellisman	FIX	Wash		decal	$OsO_4+KFeCN$		Wash			TCH	Wash	OsO_4	Wash	UA	Wash	LA	Wash		DEHY	RESIN
Hua	FIX	Wash	OsO_4	decal	OsO_4	KFeCN	Wash			TCH	Wash	OsO_4	Wash	UA	Wash	LA	Wash		DEHY	RESIN
fBROPA	FIX	Wash	OsO_4	decal	$OsO_4+KFeCN+$ formamide			OsO_4	Wash	Pyrogallol	Wash	OsO_4	Wash						DEHY	RESIN
fBROPA +LA	FIX	Wash	OsO_4	decal	$OsO_4+KFeCN+$ formamide			OsO_4	Wash	Pyrogallol	Wash	OsO_4	Wash			LA	Wash		DEHY	RESIN
High Os inclusion	FIX	Wash	OsO_4	decal	$OsO_4+KFeCN$			OsO_4	Wash					UA					DEHY	RESIN

References: Ellisman - (Deerinck, 2010), fBROPA -   (Genoud et al., 2018), High Osmium inclusion - (Knott and Genoud – personal communication, EMBL workshop, 2018), Hua - (Hua et al., 2015)

3.2.2.3   **Results**

3.2.2.4   **Decalcification**

µCT images of mineralised human femoral head tissue stained using heavy metals have sufficient contrast to show the cartilage and bone layers (Figure 33 A and D). Chondrocytes within the cartilage, osteocyte lacunae in the bone and vasculature are visible. Decalcified and stained tissue also has sufficient contrast to distinguish cartilage and bone, chondrocytes, osteocytes and vasculature (Figure 33 B and E). Tissue which was decalcified and unstained showed little contrast and no microstructural detail (Figure 33 C and F).

3.2.2.5   **Optimisation of staining for CT imaging**

µCT images of mineralised and decalcified human femoral head tissue which has been stained using heavy metals has sufficient contrast to show the cartilage and bone layers (Figure 33 A and D, B and E). Chondrocytes within the cartilage, osteocyte lacunae in the bone and vasculature are visible. Tissue which was decalcified and unstained showed little contrast and no microstructural detail (Figure 33 C and F). Stained tissue blocks displayed a notable bright layer at the edge of the block (Figure 35 D and E). The blocks with notable brightness around the edge (Figure 34 B) would be difficult to segment automatically. The smallest staining gradient was found to be from the 'Ellisman' protocol without a pre-Os step (Figure 34 A). Tissue stained with this method had visible soft tissue components (osteocytes and blood vessels) and could be segmented using methods to be outlined in Chapter 4 and Appendix B (Figure 35).
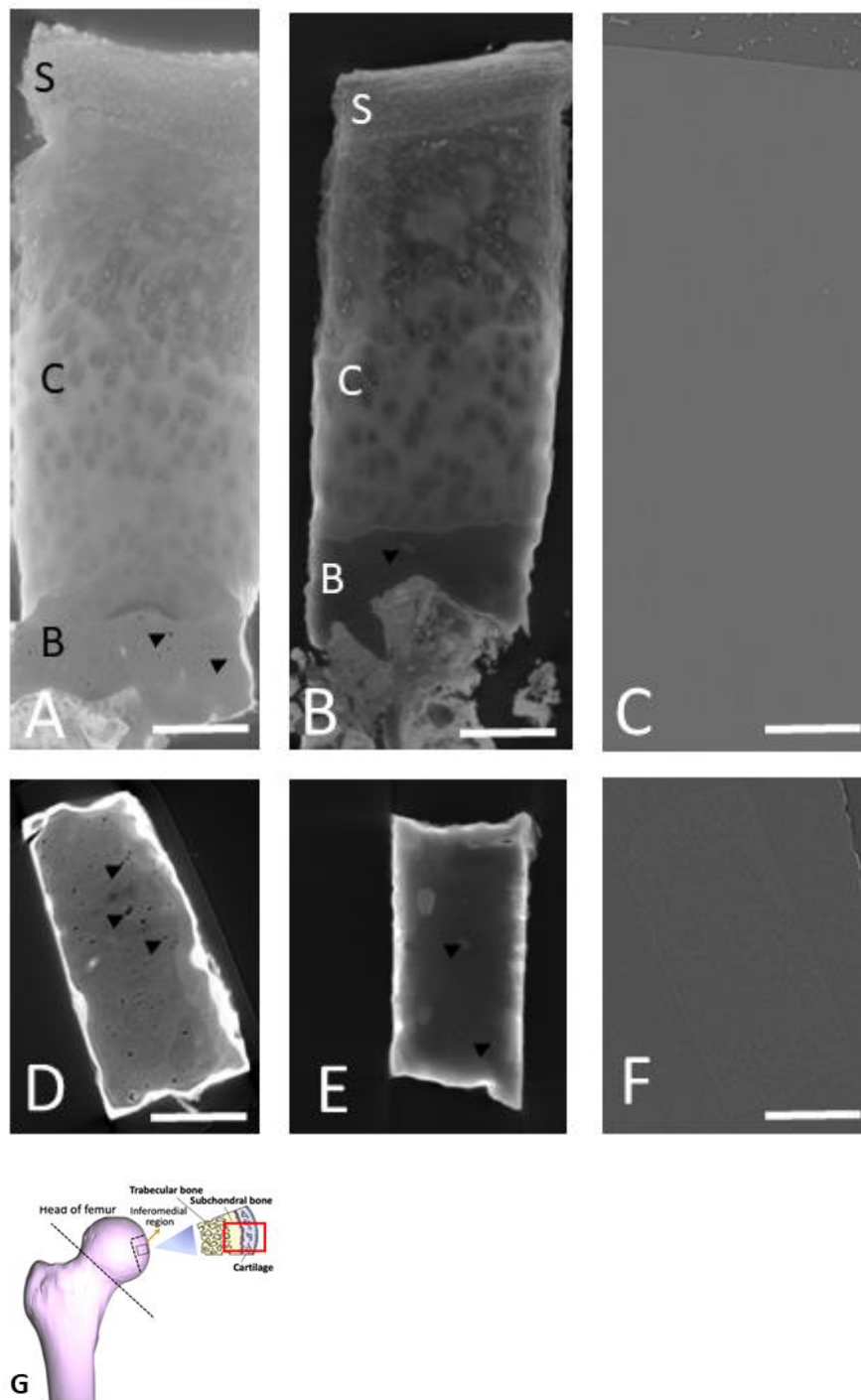
Figure 33   Reconstructed µCT data of human femoral head.

Longitudinal slices through cartilage and bone tissue (top) and transverse slices through bone tissue (bottom) showing bone surface (S), cartilage (C) and bone (B) layers. Scale bars = 400 µm

A, D   Mineralised tissue, heavy metal stained

B, E   Decalcified tissue, heavy metal stained

C, F   Decalcified tissue, no stain

G   Diagram showing sampling location. Adapted from (Cardinali et al., 2019)
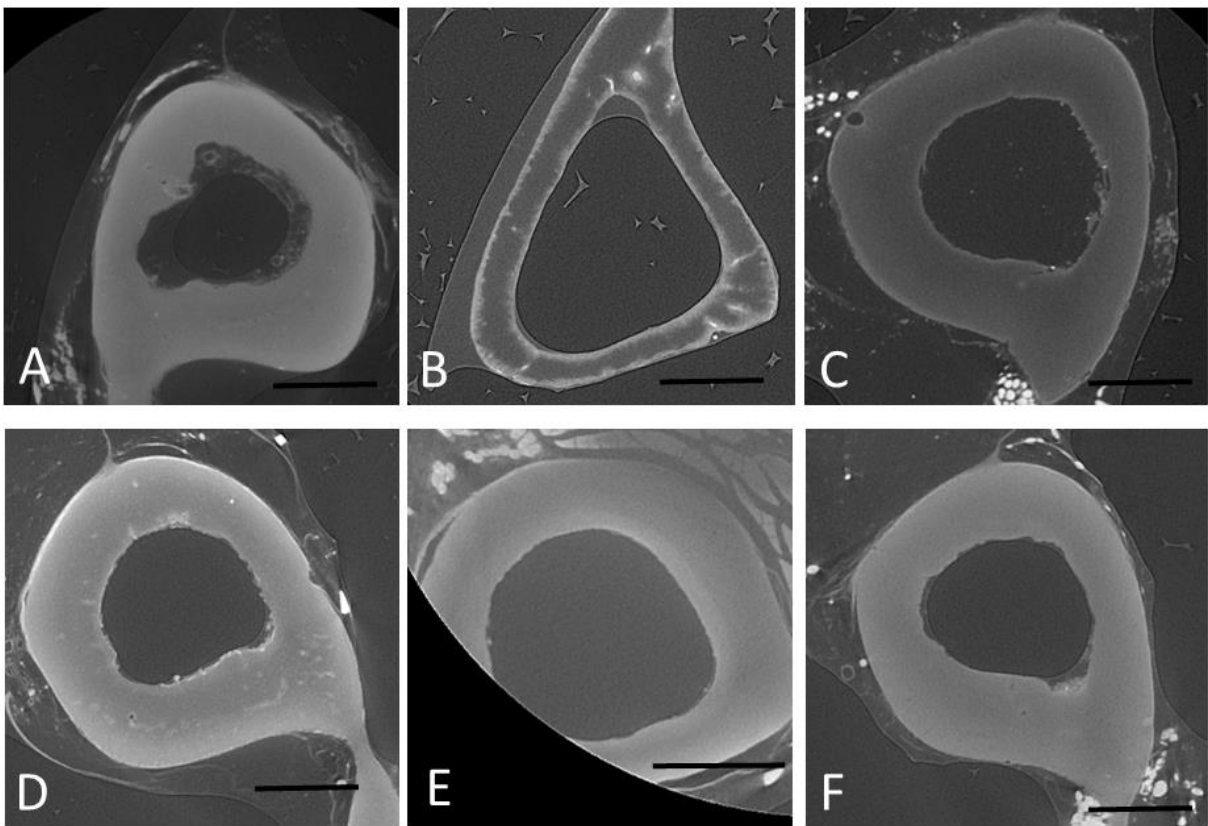
Figure 34   Results from µCT imaging of staining protocol comparisons.

Scale bars = 200 µm

A	'Ellisman' without first osmium	D	'Ellisman'
B	'Ellisman' pre-decalcification	E	fBROPA with lead aspartate
C	fBROPA without lead aspartate	F	High osmium inclusion

3.2.2.6   Discussion of sample preparation for CXEM

Each aspect of CXEM sample preparation has been examined and options explored. It has been found that the fixative chosen does not significantly affect the preservation of osteocyte ultrastructure, that there are no marked differences in preservation quality between the sexes. A significant inter-individual variation was observed. Full clinical history of these patients is not available so it is difficult to interpret this finding. For human femoral head and murine tibia bone tissue it is preferable to use decalcification, a modified 'Ellisman' staining protocol (Deerinck, 2010) and ALV resin to produce consistent SBF SEM results (Goggin et al., 2020). The same sample preparation protocol produces X-ray µCT

images from which osteocyte cell bodies and vascular tissue can be segmented. These images will allow reconstruction of the ON&LCN and quantification of hallmark properties thereof during growth and in disease, which will be detailed in Chapters 5 and 6.

The effect of time to fixation on preservation quality has not been investigated. Studying this would give us an indication of the minimum possible time allowable between excision and fixation of human tissue before cell changes occur. At present, that time is kept to a minimum while observing ethical and practical guidelines imposed by theatre staff. The options of cryofixation and preparation (Mahamid et al., 2011) have not been trialled as the resources required (high pressure freezing, cryosubstitution, cryo-ultramicrotomy) are not available within the scope of this project.

A complete investigation of all possible options for staining and embedding, including the use of microwaves or resin additives to improve conductivity and image quality has not been carried out here (Nguyen et al., 2016). A comprehensive study of all possibilities is beyond the scope of this project. The chosen methods provide images of sufficient quality for segmentation, qualitative and quantitative analysis and those quantitative results reflect well those obtained by other imaging methods. Again, it is important to state that each step in this process takes the tissue away from its native hydrated state and thus interpretation must consider this.

All human tissue used in these studies is from patients undergoing hip replacement surgery and results may reflect pathology present in the tissue, which can resemble fixation artefacts. Checking light microscopy sections can identify areas of obvious pathology and these can be excluded. Chapter 6 will review the comorbidity of bone diseases.
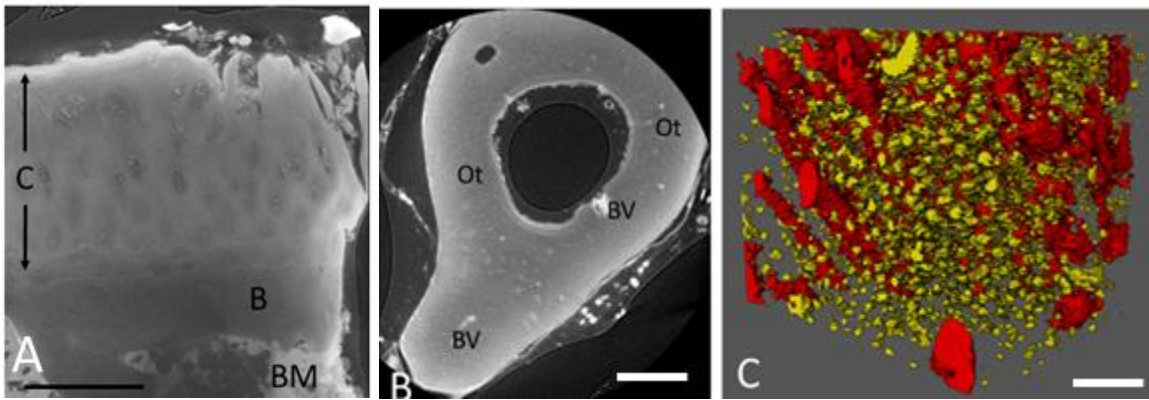
Figure 35   µCT data – identification of microstructure and segmentation

A   CT image of decalcified and heavy metal stained human bone tissue showing cartilage layer (C), underlying bone (B) and bone marrow (BM). Scale bar = 500 µm

B   Slice from reconstructed µCT stack of murine bone tissue stained with the 'Ellisman' protocol. Scale bar = 200 µm

C   Volume rendering of a segmented sub volume of scanned bone tissue showing osteocytes (yellow) and blood vessels (red). Scale bar = 50 µm

3.3   Optimisation of imaging

3.3.1   Optimisation of µCT imaging of decalcified, heavy metal stained bone tissue

3.3.1.1   Introduction

In this section, the optimisation of X-ray µCT scanning of fixed, decalcified and heavy metal stained bone tissue, which is in a state suitable for subsequent SBF SEM imaging is described. µCT imaging should yield images suitable for segmentation in a timely, non-destructive manner to produce quantitative data on the distribution and size of osteocyte cell bodies. Additionally it should allow selection of volumes of interest for high-resolution imaging using SBF SEM. As discussed, µCT is a much used technique in the field of bone imaging – although the CXEM approach is different, established settings for biological samples are known and adopted here. Little optimisation work was required.

Bone tissue, stained with heavy metals, whether decalcified or mineralised, has image contrast in images produced by µCT. Decalcified and unstained tissue has no image contrast

(Figure 33). It is possible to distinguish areas of bone and cartilage in μCT images of decalcified and heavy metal stained bone tissue, thus allowing targeted trimming for SBF SEM. X-ray μCT imaging of heavy metal stained blocks shows an uneven intensity in some blocks which may be caused by stain build up at the block surface. Line intensity profiles of the evenly stained blocks show no gradient through the centre of the block, suggesting even stain diffusion. Cellular components of bone tissue, vasculature and osteocytes, are distinguishable within the matrix and can be segmented for later quantification (Figure 35).

3.3.2 Optimisation of SBF SEM imaging

As SBF SEM had not been applied to bone tissue previously more optimisation was required.

3.3.2.1 Selection of area of interest, trimming and mounting

Semithin (0.5-1 μm) and/or ultrathin (~90 nm) sections may be taken from resin embedded blocks and examined by LM and/or TEM before proceeding to SBF SEM to confirm orientation, allow selection of the area of interest and confirm fixation, tissue quality and orientation (Figure 36).

The block-face is trimmed with a single edged razor blade or glass knife to a surface area < 500 μm^2 with the region of interest near the centre and removed from the resin block using a sharp single edged razor blade (Figure 38). A piece of laboratory film placed over the surface during removal protects against loss of the region of interest. Conductive glue (CW2400, Chemtronix, Kennesaw, GA, USA) which is used to attach the block to an aluminium pin enhances conductivity and thus reduces the build-up of negative surface charge and its adverse effects such as blurring and deformation of the image (Figure 37 and

Figure 37). Mounted samples can be sputter-coated with a layer of metal (Au, Pt or Pd) to further increase conductivity and reduce charging.
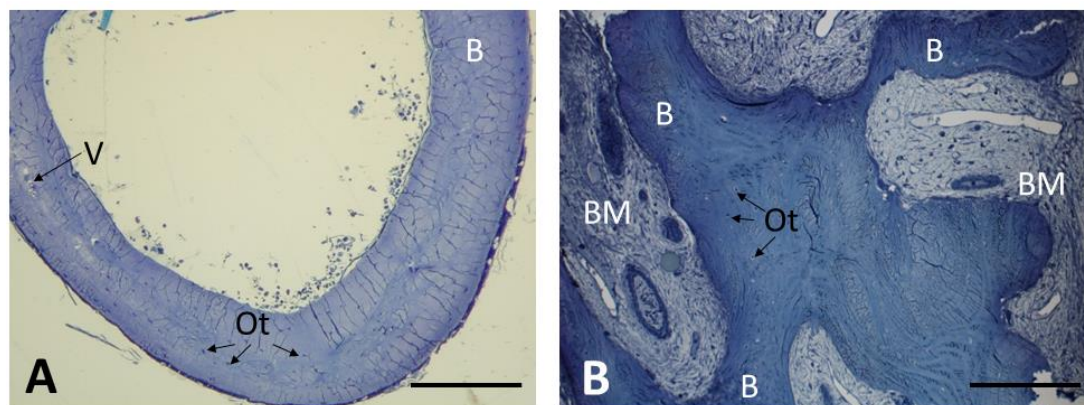
Figure 36   LM images of decalcified and heavy metal stained bone tissue.

A   Semi-thin section of murine tibia stained with toluidine blue showing osteocytes (Ot) and vasculature (V).

B   Semi-thin section of human femoral head stained with toluidine blue showing trabecular bone (B), bone marrow (BM) and osteocytes (Ot).
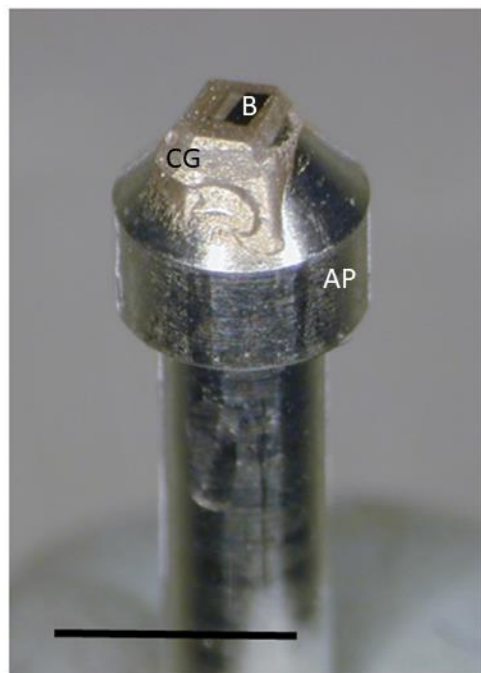
Figure 37   Mounting pin

Resin embedded bone tissue sample (B) mounted on aluminium pin (AP) surrounded by conductive glue (CG). Scale bar = 3 mm
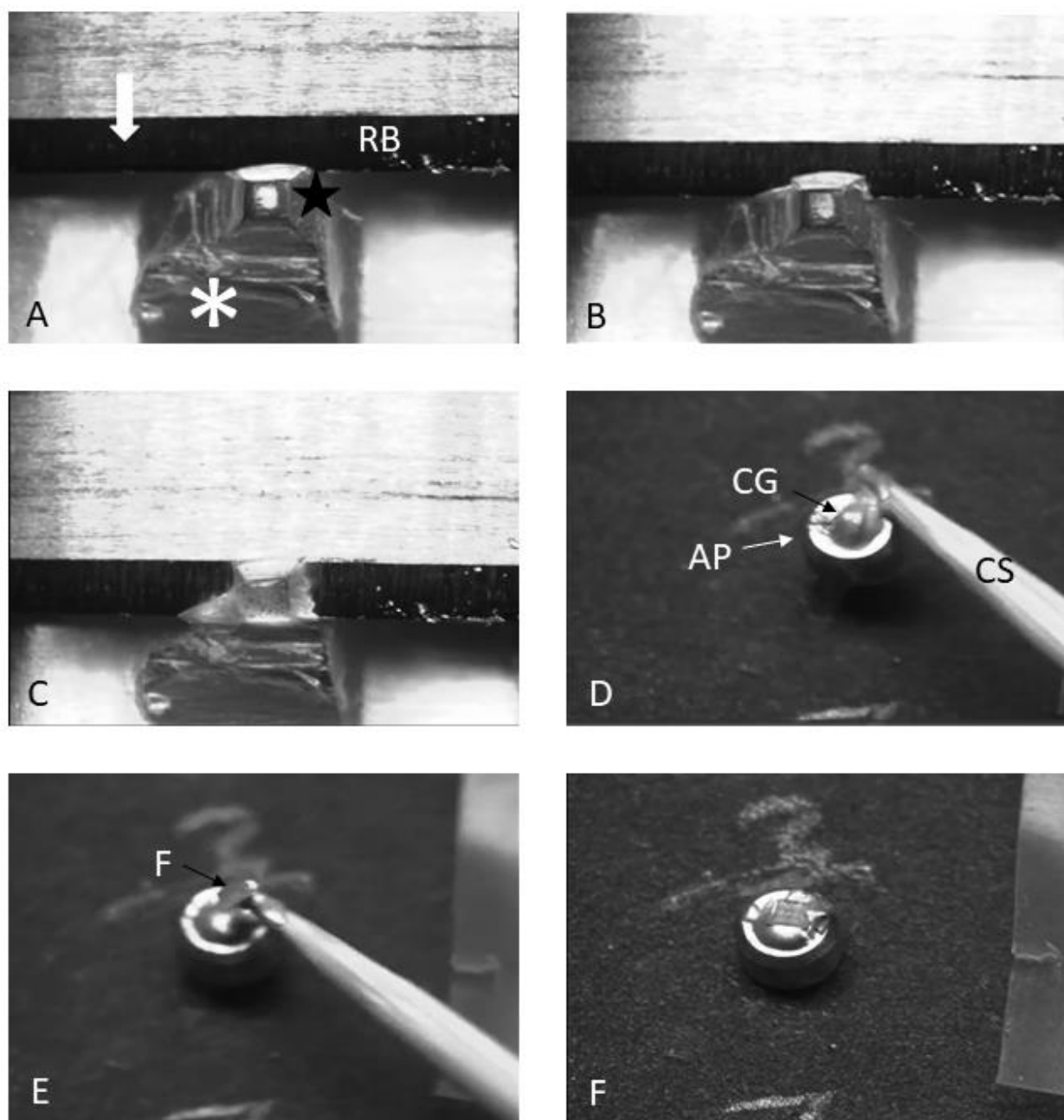
Figure 38   Removal of frustum from resin block and mounting on pin for SBF SEM.

A-C   The volume of interest (star) is trimmed proud of the main resin block (*) and is cut using a single edged razor blade (RB) in the direction shown by the arrow.

D   Conductive glue (CG) (CW2400, Chemtronix, Kennesaw, GA, USA) is placed on an aluminium pin (AP) using a domestic cocktail stick (CS).

E   The frustum (F) is placed on the conductive glue.

F   After hardening of the glue the pin is ready for SBF SEM. Adapted from (Russell et al., 2016)

3.3.2.2 **Microtomy**

The diamond knife, invented in 1955 (Patent No. US3190047A) (Fernandez-Moran, 1965), was made of the hardest known material at the time of development and is commonly used to produce ultrathin tissue sections (~100 nm) of tissue for examination by TEM. Diamond knives are sharp and long-lasting, but also delicate, expensive and costly to re-sharpen. The optimum combination of knife angle, sharpness, oscillation and cutting speed is essential for minimising damage to the block-face and consequently avoiding artefacts in the images (Hashimoto et al., 2016). The knife can introduce artefacts to both the section removed from the block and to the block-face, including but not limited to chatter (an artefact of vibration evidenced by regular stripes perpendicular to the direction of cutting), tissue compression/shearing, knife marks on the block-face and the removal of hard particles embedded in the tissue. Damage caused by sectioning may not always be visible as SBF SEM images the block-face rather than the removed sections, and because it uses BSE, which originate from a deeper interaction volume and are less affected by surface topography Figure 39).

A 3View® knife (Diatome Ltd, Nidau, Switzerland) was tested on mineralised bone tissue prepared as described in Appendix A. After cutting 4,000 sections, no evidence of damage was visible on the block-face nor the knife-edge. The knife-edge was subsequently assessed by sectioning a blank epoxy resin block and examining the block-face using incident light by a Nomarski DIC microscope. This technique shows up even the smallest imperfections in the block-face as 'tramlines'. Areas of the knife showed more wear after use on mineralised bone than on decalcified bone, but still enabled good quality cutting and imaging.

3.3.2.3   **Image Acquisition**

During SBF SEM imaging, the operator must find a balance between image quality, data volume, acquisition speed and sample damage (Table 13 and Table 14). The BSE detector images the block-face controlled by specialised custom software with minimal user interaction. Automatic focus and stigmator checks are used to maintain image quality on long runs (up to 4 weeks - personal communications Dr T. Starborg, University of Manchester, and Dr L. Collinson, Francis Crick Institute, London). Imaging quality has a large impact on the results and the ease of subsequent segmentation, so must be carefully optimised for each sample type, magnification setting and desired resolution. Working distance is usually a consideration in SEM imaging but in the 3View® system, it is not in the power of the operator to vary this. To optimise imaging and to avoid tissue damage it is essential to limit the electron dose, as above a certain dose, resin embedded samples break down, become damaged and image quality is compromised.

Dose, the number of incident beam electrons hitting the surface per unit area, can be calculated using the following equation:

$$\text{Electron dose } (e^-/nm^2) = \text{beam current (amperes) x } (6{:}24151\text{x}10^{-18} \text{ (coulombs/electron))} \times \text{pixel dwell time (s)/pixel size}^2 \text{ (nm)}$$

Increased electron dose results in better image quality (higher signal-to-noise ratio (SNR)) but above a certain threshold can cause breakdown of the resin and charging leading to image distortion and non-uniform cutting thickness. Ideally, the slice thickness should measure less than the depth of beam electron penetration and interaction. This ensures that the newly exposed block-face is undamaged and when scanned will produce an artefact free image. A dose calculator has been created (by Stuart Searle, Gatan) to predict best settings and assess the effects of changing settings (Goggin et al., 2020) (Figure 40). The maximum dose varies with tissue type, sample preparation, slice thickness and

instrumentation. It has been suggested that a maximum of 20 electrons/nm^2 is the limit for

successful SBF SEM imaging of brain tissue embedded in Durcupan resin (Kubota, 2015). It

is a useful exercise to establish the maximum dose for samples prepared by a particular

protocol to guide image optimisation. The maximum dose can be established by setting up

at recommended 'starting points' (for the FEI Quanta 250: 2kV, spot size 3, 1k x 1k image

size, dwell time 4 μm and slice thickness 50 nm) and visually assessing damage using both

SE and BSE. If damage is seen, the dwell time should be reduced and imaging re-started

until no damage is seen. Calculations indicate that the maximum dose for decalcified heavy

metal stained bone tissue samples and the imaging setup used in this project is 15.6 e$^-$/nm^2

at 50 nm thickness.
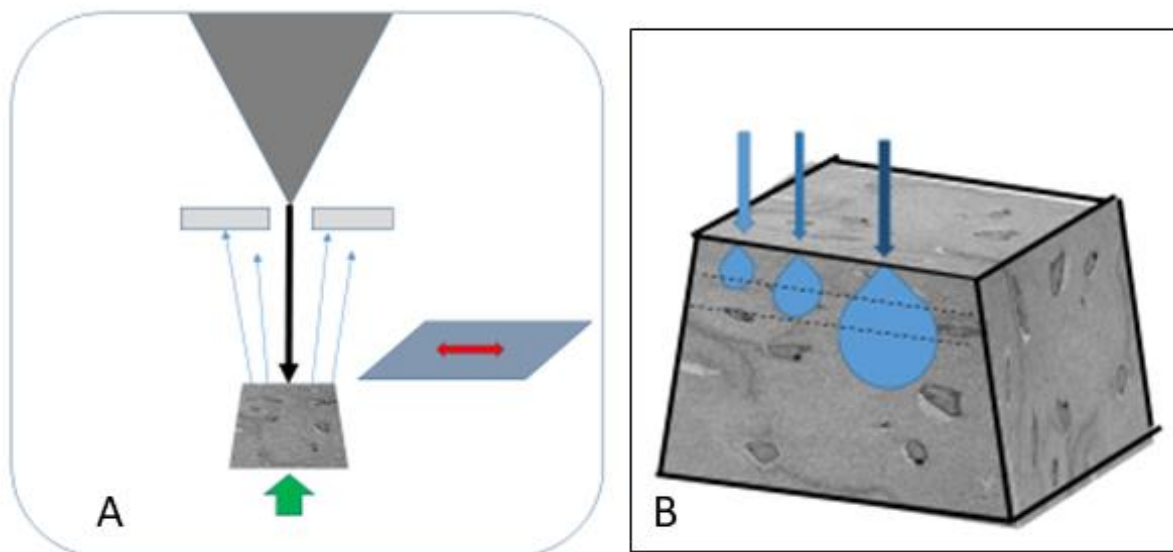
Figure 39   Beam-sample interactions during SBF SEM

A   The incident electron beam (black arrow) scans the block-face and BSE (blue arrows) are
         produced and detected. The diamond knife (red arrow) cuts a thin section after which
         the block is moved upwards (green arrow) and the process re-starts.

B   Increasing the accelerating voltage of the beam leads to deeper penetration of incident
         electrons. If electrons penetrate deeper than the slice depth, surface damage is likely to
         be observed. (Goggin et al., 2020)

		Value	
		Green = editable cells	
		Yellow = Key figures	
		Common units	Value expressed in SI units
User adjustable parameters	Dwell time (µs)	20	0.00002
	FOV (µm)	12	0.000012
	HT (kV)	3	3000
	Probe current (nA)	907	0.000000907
	frame width (pixels)	2048	2048
	Cut thickness	100	0.0000001
Calculated parameters	frame time	83.88608	5.859375
	pixel size	5.85938E-09	
	electrons per second in probe	5660587000	
	electrons per pixel	113211.74	
	pixel area (nm^2)	34.33227539	3.43323E-17
	electrons per nm^2 (DOSE)	3297.53	3.29753E-06
	Fraction of electrons exceeding cut thickness	2.7673E-08	
	Fraction of electrons stopping per nm (in Z direction depth) at cut thickness	7.56985E-09	
	electrons per nm^3 at cut thickness	2.49618E-05	2.49618E+22
	electrons per nm^3 below cut thickness	3.635645908	3.63565E+27
	energy density entering surface (kJ/m^2)	1582.814846	1.582814846
	energy density deposited directly at cut depth (kJ/m^3)	1.19817E-05	1.19817E-08
	power density (kW/m^2)	18.86862333	0.018868623

Figure 40   Dose calculator

The dose calculator shows the impact on final electron dose of changing imaging and microscope parameters. Green cells can be edited to input imaging and microscope settings. The output values in yellow fields are the key figures which should be considered when deciding on optimum imaging conditions. From (Goggin et al., 2020).

Table 13   A summary of SBF SEM imaging conditions and their effects on output.

Green cells indicate desirable outcomes. From (Goggin et al., 2020)

Parameter	Action	Charging	Contrast	Resolution	SNR	Damage
Accelerating voltage	↑	+	+	+	+	+
	↓	-	-	-	-	-
Chamber pressure	↑	+	-	-	-	N/A
	↓	-	+	+	+	N/A
Magnification	↑	+	N/A	N/A	N/A	+
	↓	-	N/A	N/A	N/A	-
Spot Size	↑	+	+	-	+	-
	↓	-	-	+	-	-
Dwell time	↑	+	N/A	+	+	+
	↓	-	N/A	Possible decrease	-	-
Number of pixels	↑	+	N/A	+	+	+
	↓	-	N/A	Possible decrease	-	-
Slice thickness	↑	-	N/A	z -	N/A	-
	↓	Possible increase	N/A	z +	N/A	Possible increase

SNR = signal-to-noise ratio

Table 14   The effects of changes on file size, acquisition time and field of view.
From (Goggin et al., 2020)

Action	File size	Time	Field of View
Magnification	N/A	N/A	Decrease
	N/A	N/A	Increase
Increase dwell time	N/A	Increased	N/A
Increase frame size/pixel no	Increased file size	Increased	N/A
Increase slice thickness	Decreased file size (because fewer slices/volume)	Decreased (because fewer slices)	N/A
Number of slices	Increased	Increased	N/A

3.3.2.4   **Validation of imaging conditions**

This validation work was carried out with the collaboration of Elaine Ho and formed part of her final year Independent Project.

A series of image analysis experiments was carried out to objectively validate the choice of SBF SEM settings. Ideally, SBF SEM would produce high resolution, noise-free images where significant features are (ideally automatically) segmentable. Noise is unavoidable but is minimised by careful setting of conditions (Table 11). Across a range of accelerating voltages, spot sizes, vacuum levels and slice thicknesses using both decalcified and mineralised tissue SNR, contrast to noise ratio (CNR) and sharpness were compared. SNR and CNR are non-dimensional measures which are used to quantify image quality while sharpness is related to the edge definition of an object.

3.3.2.4.1   **Materials and Methods**

A block of decalcified murine bone tissue obtained and prepared for SBF SEM as described in Appendix A.4 was imaged at spot size 3, vacuum 60 Pa, 4096 x 4096 pixels at 4 nm at a

dwell time of 4 μs. An area of interest containing one osteocyte cell body and surrounding extracellular matrix (Figure 41) was imaged while increasing the accelerating voltage in 0.5 kV increments from 2.0 - 5.5 kV and keeping other conditions constant. Imaging was repeated on freshly exposed block-faces while varying beam current (spot size 2.5 - 4.0 at 0.5 intervals), chamber pressure (30 - 90 Pa at 10 Pa intervals) and slice thickness (100 - 20 nm at 10 nm intervals). These ranges encompass the extremes of feasible imaging conditions. To facilitate SNR and CNR calculations, images of blank resin were taken at the same settings. SNR and CNR were calculated for the region of interest at each setting using Matlab (Mathworks, 2016). To measure sharpness an ROI was defined at a transition between cell and matrix. The edge response assessed in the direction perpendicular to the transition was taken as a measure of sharpness.

3.3.2.4.2   Results

Optimum SNR was observed at an accelerating voltage of 3.5 kV and spot size 2.5-3, while vacuum pressure had no significant effect on SNR. Optimum CNR was observed at an accelerating voltage of 4 kV and spot size 3.5, while vacuum pressure had no significant effect. Sharpness was highest at an accelerating voltage range from 3-5.5 kV, spot size 3, while lower vacuum pressure yielded sharper images.

3.3.2.4.3   Discussion

Blocks prepared for CXEM by decalcification and heavy metal staining have been imaged using X-ray μCT and subsequently a sub-volume of the same tissue block imaged using SBF SEM. No differences in cutting properties were observed between resin blocks which had been scanned and those which had not. The resulting data spans length scales of bone structure. CXEM as a correlative technique can provide a larger volume of interest (here approx. 3 mm^3) than it is possible to image using SBF SEM alone, and high
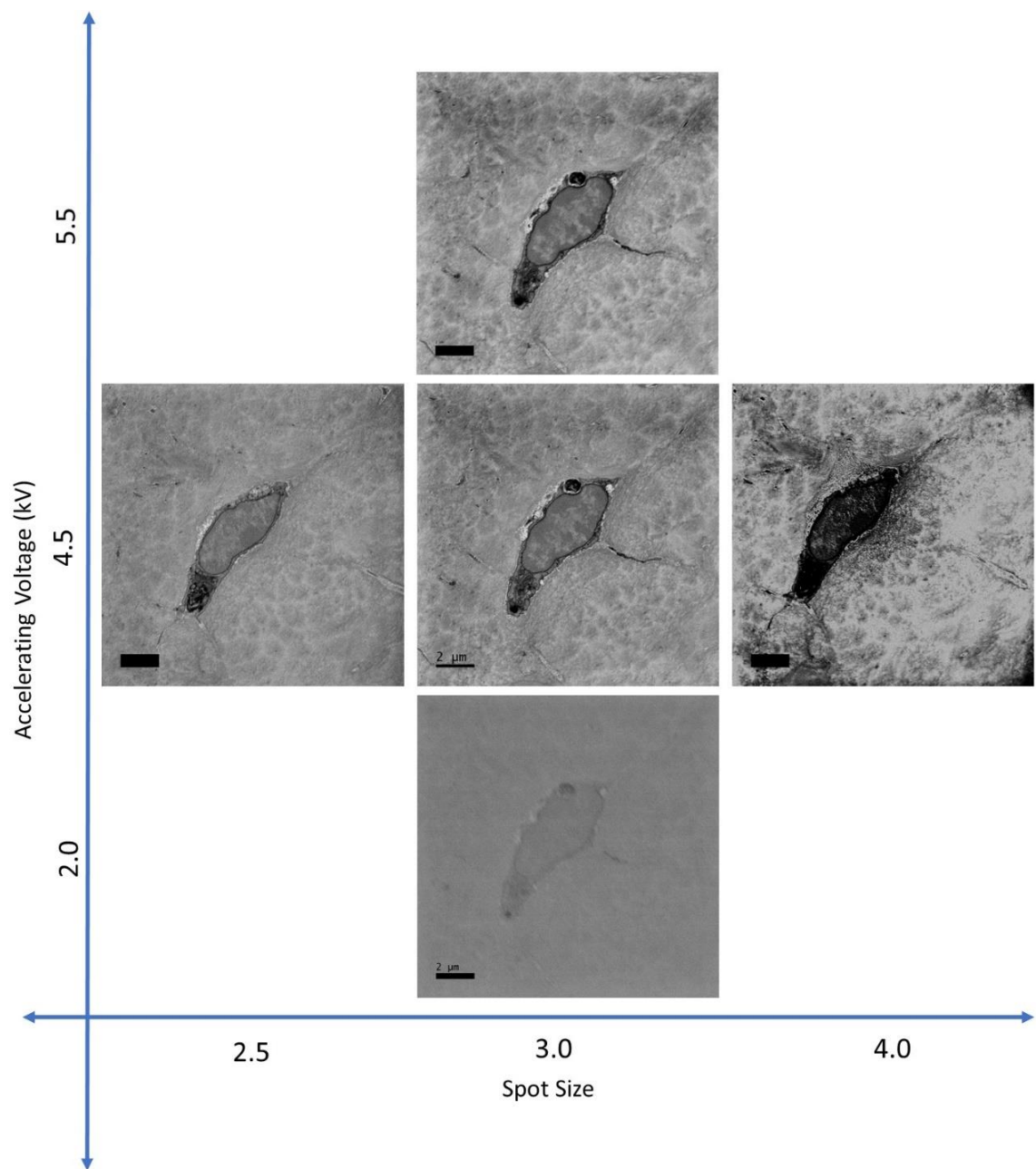
Figure 41   Effects of varying spot size and accelerating voltage on SBF SEM imaging

Images of an osteocyte taken using SBF SEM at pixel size 3.8 nm, 4096 x 4096 pixels, dwell time 4 µs, chamber pressure 60 Pa. Low accelerating voltage and small spot size reduce image contrast, increasing spot size leads to block-face damage. From (Goggin et al., 2020)

spatial resolution in the sub volume scanned with SBF SEM. Uniquely, SBF SEM facilitates concurrent high-resolution 3D imaging of bone matrix and of osteocytes embedded within, including the cell and cell process ultrastructure over a volume including many tens of cells. Tissue changes induced by sample preparation, including shrinkage, must be considered during interpretation of the resulting images. While µCT imaging produces isotropic data, SBF SEM produces typically non-isotropic datasets (different nominal in-plane and out-of-plane resolution), and is inherently destructive to the tissue block.

Sample preparation for CXEM, as with all imaging techniques is extremely important (Peddie, 2019). Immediate tissue fixation is crucial, stopping metabolism and autolytic changes and fixing molecules in their locations. CXEM datasets can be investigated qualitatively by visualisation and quantitatively through retrieving morphometric measures, which will be discussed further in Chapter 4.

The optimised bone tissue preparation and imaging protocols presented in Appendix A will be applied to address relevant questions in bone research. Methods for deriving quantitative 3D ultrastructural data from CXEM imaging of the ON&LCN, including but not limited to the association with the pericellular space and the extracellular matrix, and the distribution of osteocytes within the bone matrix will be outlined in Chapter 4. These data will add to the understanding of bone mechanobiology and changes in the ON&LCN during growth, ageing and pathology. As discussed in Chapter 2, CXEM imaging of the ON&LCN microstructure and ultrastructure will also contribute to efforts in computational modelling of bone mechanosensation and mechanotransduction.

Chapter 4   Processing, segmentation and quantification of CXEM images

4.1   Introduction

In Chapter 3 the development of sample preparation and image acquisition methods for imaging of bone using CXEM were described. The methods in this chapter enable production of standardised measures relevant for bone health from 3D CXEM datasets. The next steps in the process are image processing and segmentation. Segmentation defines the boundaries of an object in order to divide images into regions containing voxels with the same characteristics relating to structures of interest (Tsai et al., 2014). Segmentation is followed by the extraction of quantitative data. Specifically, this chapter first outlines the image processing carried out on the raw µCT and SBF SEM data, the options for segmentation and the rationale for the choices made. A review of existing quantitative measures for bone microstructure, their definition and derivation is included and new measures, necessary for description of ON&LCN ultrastructure are defined. Finally, workflows for obtaining quantitative data from segmentation results are included. These workflows along with those for sample preparation and imaging set out in Chapter 3 form the basis of the methods used in Chapters 5 and 6 to investigate the ON&LCN of healthy murine and pathological human bone tissue.

4.1.1   Aim

The aim of this work is to process, segment and subsequently quantify images produced by 3D CXEM to yield relevant quantitative data on the ON&LCN in murine and human bone tissue.

4.1.2 **Objectives**

- To develop image processing strategies for CXEM data.

- To develop appropriate segmentation routines for CXEM data.

- To review existing quantitative metrics for the ON&LCN and select measures relevant for studies of ageing and disease.

- To define new metrics for description of the ON&LCN at an ultrastructural level.

- To set out workflows for image processing, segmentation and quantification which will be used in CXEM investigations of murine and human tissue, described in Chapters 5 and 6.

4.2 Image processing

4.2.1 **Introduction to image processing**

One important advantage of both X-ray μCT and SBF SEM is the automated nature of data collection. The time taken for data collection is short compared to the total time required to prepare, collect and analyse information. The conversion of raw data to useful information however, is a considerable challenge as while valuable insights can be gleaned from scrolling through the images and examining 3D reconstructions, meaningful quantitative data can only be obtained by segmentation (Tsai et al., 2014).

Raw CXEM data must always be collected with a specific research question in mind in order to ensure resolution and volume are adequate and that relevant structures have sufficient contrast. Appropriate and effective sample preparation, staining, data collection and pre-processing are crucial for efficient segmentation and accurate quantification. The recommendations in Chapter 3 and (Goggin et al., 2020) should be followed during sample

preparation and image acquisition to produce results suitable for quantification. Artefact free, high SNR and CNR raw data is the ideal but most data will need some processing before segmentation to optimise. Figure 42 shows an image processing workflow describing the processes which transform raw data to qualitative and quantitative outputs.
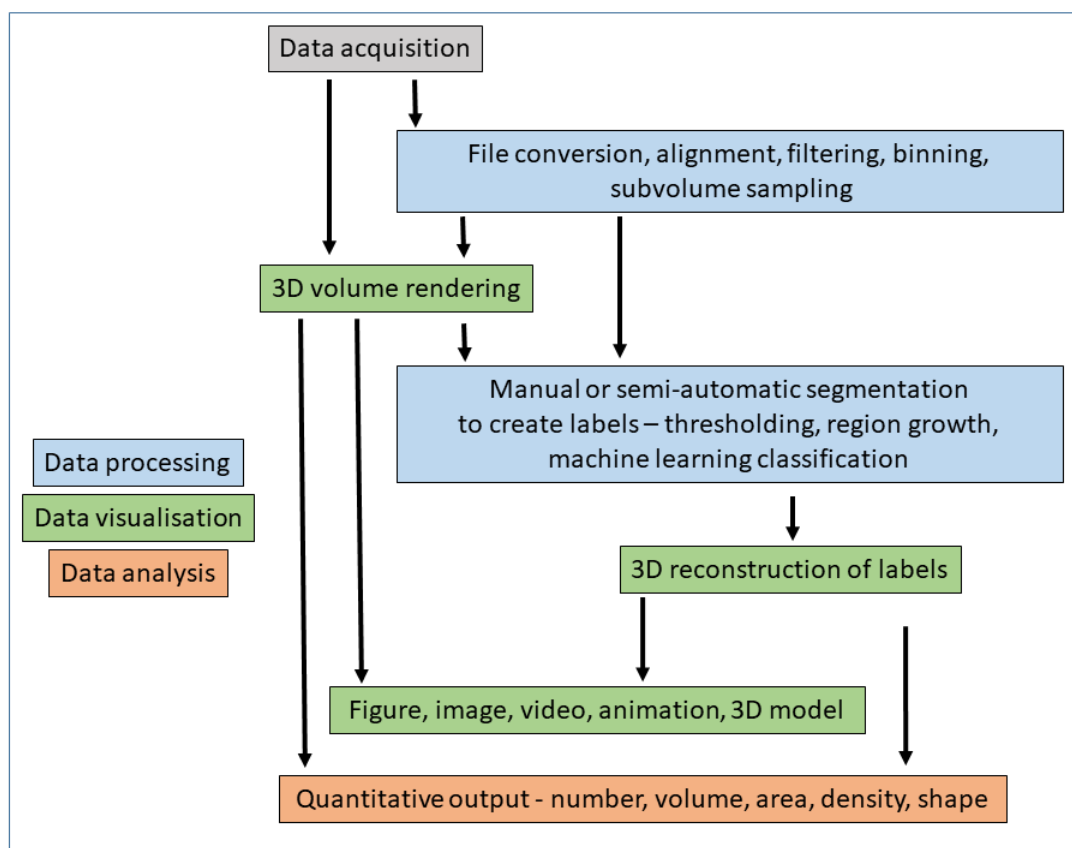
Figure 42   Image acquisition to outputs workflow.

Flowchart showing the main steps applied to CXEM data from image acquisition through processing and segmentation to quantitative and qualitative outputs.

4.2.2   **Choice of software - general**

Important considerations in the design of image processing strategies are the software packages, data processing and storage capabilities and human hours available. Commercial software packages used for image processing, visualisation and analysis include Matlab (Mathworks,Cambridge, UK), Digital Micrograph (Gatan, UK), Avizo/Amira (ThermoFisher Scientific, Cambridge, UK), Volocity (Quorum Technologies, Ontario, Canada) and Imaris

(Oxford Instruments, Oxford, UK). Many of these commercially available packages are easy to use and provide excellent 3D visualisation facilities. Some, however, require considerable financial outlay.

Open access software packages for image processing, visualisation and analysis include FIJI (Schindelin et al., 2012), the associated plugins TrakEM2 (Cardona et al., 2012) and BoneJ (Doube et al., 2010), ITK-SNAP (Yushkevich et al., 2006), IMOD (Kremer et al., 1996), ilastik (Kreshuk et al., 2011), Microscopy Image Browser (Belevich et al., 2016), Reconstruct (Fiala, 2005), Knossos (Helmstaedter et al., 2011), eC-CLEM (Heiligenstein et al., 2017, Paul-Gilloteaux et al., 2017), EM3D (Ress et al., 2004), Blender (Blender Institute, Amsterdam) and Dragonfly (Object Research Systems, Quebec, Canada (not open source, but free for non-commercial research use)). For reviews see (Borrett and Hughes, 2016, Cocks et al., 2018). These open-source packages have transparent algorithm details, support in the form of forums and no ongoing cost implications.

Manual segmentation involves tracing contours directly onto images and is costly in terms of human hours. More desirable is to automate or semi-automate the segmentation process, as this is more objective, faster, cheaper and repeatable. Image processing of large stacks is computationally demanding and simple operations are often beyond the capability of desktop computers. For this reason, the data visualisation service of the Iridis Compute Cluster, the University of Southampton's high performance computing cluster has been used for much of the image processing and segmentation in this project.

4.2.3 Choice of software for CXEM of bone tissue

The software packages used in this project for image processing are the commercial softwares Digital Micrograph (Gatan, UK) and Avizo (ThermoFisher Scientific, Cambridge, UK) and the freeware Fiji (Schindelin et al., 2012).

Digital Micrograph is the software used by 3View® to control the hardware and collect image data. It also offers limited image processing features. Fiji is an open source distribution of ImageJ (Schneider et al., 2012a) which includes a range of organised libraries, plugins, scripting languages, tutorials and documentation to facilitate image analysis. Segmentation plugins such as TrakEM2 and the Trainable Weka Segmentation provide solutions for management, registration, segmentation and annotation of large image data sets. Fiji is easy to install and update and as it is widely used, an active and supportive community of users exists. Avizo is a powerful platform for visualisation and manipulation of data from several imaging modalities. Its ability to handle and segment both EM and μCT data and its interactive visualisation tools are very advantageous.

4.3 Image segmentation

4.3.1 Preparation for segmentation

Reconstructed X-ray μCT data (from the Xradia Versa 510) are exported as 16-bit tiff stacks for visualisation and analysis. To facilitate segmentation, images may be modified by removing noise, smoothing, sharpening, enhancing edges, trying to emphasise features of interest or remove non-relevant ones.

SBF SEM images are collected using Digital Micrograph (Gatan, Abingdon, UK) software as a series of .dm3 files, the proprietary image format used by Gatan. As .dm3 files cannot be opened by many image analysis programmes, the images are converted to .tiff format before processing further.

While SBF SEM produces well aligned data, some post imaging re-alignment may be required. This involves the cross correlation of slices in XY to compensate for drift during acquisition. Pieces of debris and charging may result in occasional slices of different (usually

lower) contrast. Normalisation can be applied to change the range of pixel intensity values to match a slice of 'good' contrast, increasing the dynamic range to achieve consistency in a dataset. Down-sampling reduces file size for ease of handling, storage and computation. Image quality is reduced with down-sampling unless the data has been over-sampled compared to the resolution.

Reslicing of data stacks from µCT and SBF SEM in ortho planes allows viewing and tracking of structures within the volume. Contrast and brightness adjustment enhances the appearance of features of interest. EM images are degraded by noise and blur due to electromagnetic interference and lens systems (Roels, 2018). Image processing tools restore image quality and facilitate segmentation. Filters modify or enhance images by noise removal, smoothing, sharpening, edge enhancement, emphasis or removal of particular features. See detailed descriptions in Appendix B.

4.3.2   Segmentation

Segmentation can be manual, semi-automatic or fully automatic. The disadvantages of manual segmentation are the financial and time costs of human labour and the possibility for variation of interpretation. Some research groups using SBF SEM find volunteers via the Zooniverse, a platform which hosts projects and recruits 'citizen scientists' (Trouille et al., 2019, Spiers et al., 2020). Quanti.us is a platform which employs a crowdsourced workforce to manually annotate images (Jones and Spiers, 2018) and Eyewire is a 'game to map the brain' which combines the manual segmentation efforts of 250,000 participants with artificial intelligence to reconstruct complete retinal neurons (Bae et al., 2018). A number of programmes and algorithms are in development for automatic segmentation of SBF SEM data (Liu et al., 2020, Žerovnik Mekuč et al., 2020), however none is in wide use at present. Challenges in the development of automated segmentation for EM images are the small

size of objects (eg. osteocyte processes) and the low signal-to-noise ratio in SBF SEM images (Jurrus et al., 2009). To date, segmentation algorithms have not been accurate enough nor have they provided a black-box software solution. Many advances have been specific to particular segmentation problems and have not been successfully applied to other tissue types (Guay et al., 2018). Fully automatic segmentation, when developed, will be reproducible, objective, allow analysis of large datasets, be faster and more cost efficient.

While fully automatic segmentation is awaited, semi-automatic methods where user input is combined with computer predictions to classify voxels are the preferred choice. Such tools include interpolation (using segmented data from separated slices to calculate the 'missing data'), intensity threshold filtering (selecting pixels/voxels of defined values and allocating them to materials), region growing (expanding a seed to similar adjacent voxels until an edge is reached), watershed (considering image as a topological landscape which is 'flooded' to separate hills and valleys) or machine learning.

The Trainable Weka Segmentation (Arganda-Carreras et al., 2017), a machine learning tool distributed as part of Fiji (Schindelin et al., 2012) , can be trained to identify segmentation classes from user input to produce a classifier which is then applied to perform the same task on unseen data. It uses a collection of machine learning algorithms and a set of selected image features to allocate pixel based segmentations to pre-defined classes (Figure 43). Detailed workflows for image processing, segmentation and quantitative analysis of CXEM data are included in Appendix B.
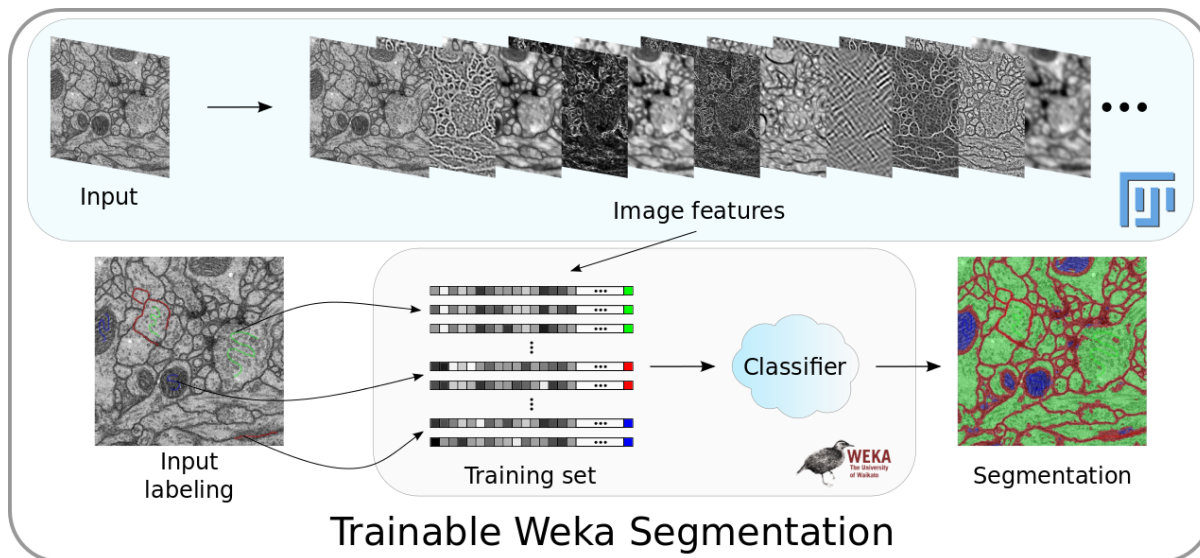
Figure 43   Trainable Weka segmentation for pixel classification.

TOP   Image features are extracted from an input image. A set of pixel samples is defined.
            The Weka is trained on these samples and applied to the remaining image data.

BOTTOM   Interactive user feedback improves results by correcting annotation or adding labels.

From (Arganda-Carreras et al., 2017).

4.3.3   Reconstruction

3D volume reconstruction can be carried out before or after segmentation and allows

observation from different orientations. Resliced, cropped and clipped volumes can help

to illustrate aspects of the structure under investigation. Quantitative outputs such as 3D

prints and videos can be produced from reconstructions (Figure 44). Additionally,

augmented and virtual reality content can be generated and usefully employed in public

engagement activities (Figure 44 D).
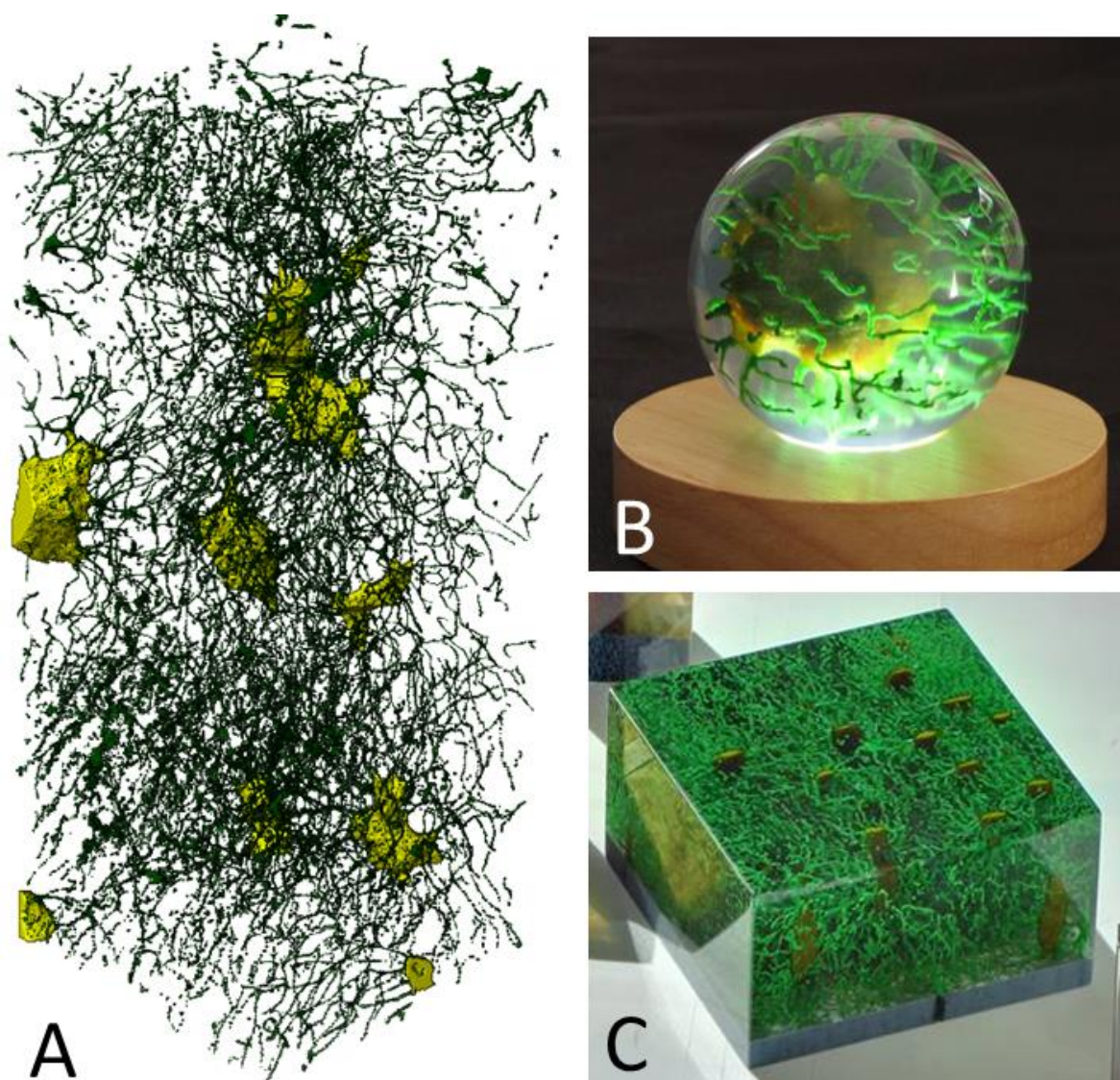
Figure 44   Outputs from CXEM.

A   Video of the reconstructed ON&LCN of mouse tibia with cells in yellow and

             connecting processes in green. View on the BIU YouTube channel

             https://www.youtube.com/channel/UCTERYdnSV_bTQqbHt0Z61ZQ

B, C   3D prints of osteocytes and processes.

D   Poster with augmented reality features and instructions to activate.

Bone
DECONSTRUCTED

This poster has augmented reality features. To activate them:
1. Scan the QR code to download the app (or search for Zappar).
2. Scan the lightning logo with the app.
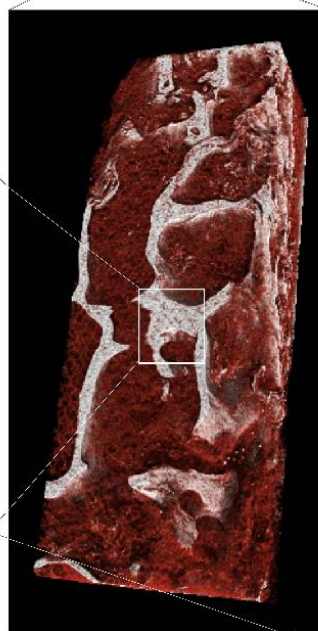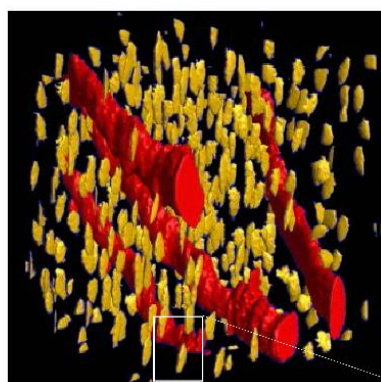
UNIVERSITY OF
Southampton

For more information:
p.goggin@soton.ac.uk

D
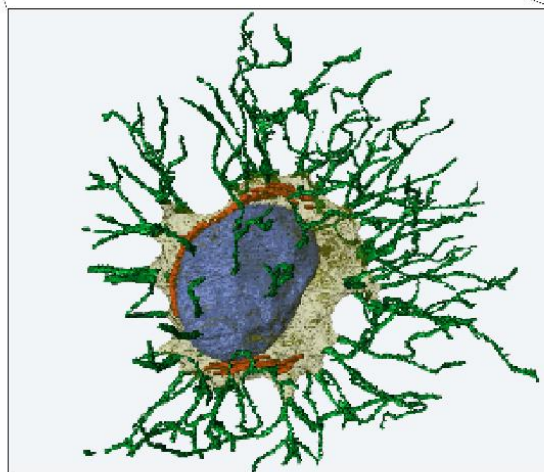
4.4 Quantification of CXEM image data

In this section, the importance of standardised quantitative measures of the ON&LCN is discussed, the historical perspective of standardisation is reviewed, the measures to be used in the CXEM studies in later chapters outlined and the derivation of new measures described.

4.4.1 Existing quantitative measures for the ON&LCN

Studies of network characteristics in the brain have related modifications in organisation to Alzheimer's disease and schizophrenia (Bullmore and Sporns, 2009). A similar view of the osteocyte 'connectome' may provide a useful model to better understand bone anatomy, physiology and pathology (Weinkamer et al., 2019). As discussed in Chapter 2 structural changes in the ON&LCN can affect mechanobiology of bone and overall bone health. As in principle, it may be possible to relate changes in the properties of the ON&LCN to bone pathology, it is crucial how 3D spatial characteristics are quantified. Reliable quantitative characterisation of both the ON and the LCN based on advanced 3D imaging across different length scales will inform computational models of bone mechanotransduction, replacing assumptions, and will allow realistic predictions of the function of this system (Buenzli and Sims, 2015). For example, data on canalicular occupancy and the number of cells which make connections with vascular and other structures, will improve accuracy when calculating the number of connections between osteocytes and related cell networks (Weinkamer et al., 2019).

To describe ON&LCN structure, a consistent and well-defined set of quantitative 3D measures is needed, which should be independent of imaging methods and experimental conditions. Additionally, quantification should be user-independent and automated to

ensure consistency and efficiency, although some human interpretation and intervention will presumably remain necessary.

Combining measures in the existing guidelines with ultrastructural details would lead to a more comprehensive standard data set. In summary, a quantitative framework should include, although not be limited to, detail such as: osteocyte number density, spatial distribution and alignment, microstructural information including cell, pericellular space and lacunar shape and volume as well as ultrastructural detail such as process and canaliculus dimensions and tortuosity.

4.4.2   Derivation and introduction of additional quantitative measures for the ON&LCN

It is necessary and important to define osteocyte measures since most measurements to date have been on the LCN. Previous frameworks, while comprehensive with respect to the LCN, have not considered the ON sepatarely (Mader et al., 2013). Lacunar indices have been introduced analogous to standard morphometry, including number of lacunae (N.Lc), lacuna number density (N.Lc/Ct.TV), lacunar volume (Lc.V), and lacunar volume density (Lc.V/Ct.TV) (Schneider et al., 2007). In this project the corresponding osteocyte measures are adopted: number of osteocytes (N.Ot), osteocyte number density (N.Ot/BV), osteocyte volume (Ot.V) and osteocyte porosity (volume density) (Ot.V/BV). Similarly, measures derived for canaliculi require a corresponding 'process' equivalent. Process diameter (Pr.Dm) and number of processes (N.Pr) are adopted.

Osteocyte surface area (Ot.A), length (Ot.Le), width (Ot.Wi) and breadth (Ot.B) are directly measured while osteocyte anisotropy (Ot.An), flatness (Ot.Fl) and sphericity (Ot.Sph) are calculated (detailed equations in Table 25Table 25, Appendix B.3.2).

The volume of the PCS around the osteocyte is denoted by PCS.V, the thickness of the PCS around the osteocyte by PCS.Th and the maximum width of the PCS around the osteocyte by PCS.Wi. The measures and abbreviations used in this project are listed in Table 15

Table 15   Examples of quantitative measures obtainable from CXEM images listed on a decreasing scale.

Category	Measures and abbreviations	
Organ	• Total tissue volume (TV) • Bone Volume (BV)	
Tissue - ON	• Number of osteocytes (N.Ot) • Osteocyte number density (N.Ot/BV) • Osteocyte volume (Ot.V) • Osteocyte porosity (T.Ot.V/BV) • Mean osteocyte volume (<Ot.V> = T.Ot.V/N.Ot) • Osteocyte surface area (Ot.A)	
Tissue - LCN	• Number of lacunae (N.Lc) • Lacuna number density (N.Lc/BV) • Lacuna volume (Lc.V) • Lacuna porosity (T.Lc.V/BV) • Mean lacuna volume (<Lc.V> = T.Lc.V/N.Lc) • Lacuna surface area (Lc.A)	
Lacunar occupancy	• N.Ot/N.Lc *100	
Cell - Osteocytes	• Osteocyte length (Ot.Le) • Osteocyte width (Ot.Wi) • Osteocyte breadth (Ot.B)	• Osteocyte anisotropy (Ot.An) • Osteocyte flatness (Ot.Fl)
Cell - Lacunae	• Lacunar length (Lc.Le) • Lacunar width (Lc.Wi) • Lacunar breadth (Lc.B)	• Lacunar anisotropy (Lc.An) • Lacunar flatness (Lc.Fl)
Pericellular space	• PCS volume around osteocyte (PCS.V) • PCS porosity ((T.PCS.Ot.V + T.PCS.Pr.V)/BV) • PCS thickness (PCS.Th) – (averaged around cell body) • PCS width (PCS.Wi$_{max}$)	
Processes and canaliculi	• Number of processes per cell (N.Pr) • Process diameter (Pr.Dm) • Process thickness (Pr.Th) – (averaged over length) • Process tortuosity (Pr.To)	

4.5 Conclusion

In this chapter image processing, segmentation and quantification of images of the ON&LCN produced by CXEM are discussed. It is possible to extract quantitative measures relevant for bone health and disease from decalcified heavy metal stained bone tissue imaged by CXEM. Both the ON and the surrounding LCN are imaged simultaneously, meeting a need previously expressed by the research community (Buenzli and Sims, 2015).

Automated image segmentation of CXEM images is not possible at the present time, so methods using semi-automated machine learning are employed. Protocols which will be used in subsequent investigations are established and detailed in Appendix B.2.2.

As CXEM produces images and data on the ON as well as the LCN, new quantitative measures have been introduced. Chapters 5 and 6 will detail how the image processing and analysis protocols, along with the sample preparation and imaging methods in Chapter 3 have been applied to murine tissue to investigate changes with age (Chapter 5), and to human tissue to investigate changes in OP and OA (Chapter 6).

Image data produced by CXEM imaging can be processed, segmented and subsequently quantified to yield relevant quantitative data on the ON&LCN in murine and human bone tissue.

Chapter 5 3D imaging and quantitative analysis of osteocyte and lacuno-canalicular networks across length scales in juvenile and adult mice using CXEM

5.1 Introduction

In this chapter the CXEM methods described in Chapters 3 and 4 are applied to juvenile (4-week-old) and adult (38-week-old) murine tibia to obtain quantitative data on the ON&LCN across different length scales. Osteocyte density and porosity are determined from μCT images of murine tibia containing tens of thousands of osteocytes. The tibia is subdivided into posterior, anterior, medial and lateral quadrants to compare osteocyte number density, osteocyte porosity and cell measures. Sub-volumes of the same tissues are imaged using correlative SBF SEM. The SBF SEM results for osteocyte number density, porosity, cell volume and dimensions, PCS volume and dimensions, number of cell processes per cell and diameter of cell processes are compared. The work showed that CXEM produces unique quantitative data, that there are no significant differences between the ON&LCN in juvenile and adult animals and that using some of the novel findings changes results obtained in previous work on quantifying the human skeleton.

The aim of the work described in this chapter is to use the CXEM workflow illustrated in Figure 45 to demonstrate that relevant data on the ON&LCN across length scales can be produced from decalcified heavy metal stained bone tissue. Secondly, the work aims to determine whether there are significant differences in ON&LCN microstructure and ultrastructure between the tibiae of juvenile and adult mice which may shed light on changes occurring in the ON&LCN during bone development. As discussed in Chapter 2,

suggested means of strain sensation include direct and indirect mechanisms (Han et al., 2004, Vatsa et al., 2008, Fritton and Weinbaum, 2009) which will both be affected by changes in ON&LCN geometry (Uda et al., 2017). Importantly, CXEM allows this geometry to be investigated in 3D, at high resolution and over a larger volume than many other methods such as ET, FIB SEM or SBF SEM alone.

HYPOTHESES

- ON&LCN microstructure and ultrastructure are unchanged across the life course in murine tibia.

- ON&LCN microstructure is unchanged with anatomical area in murine tibia.

This study will:

- Produce and compare quantitative data on the 3D structure of the ON&LCN across length scales from juvenile and adult murine tibia. Data will include osteocyte number density, porosity, volume, shape, size, number of processes, process diameter and pericellular space volume.

- Provide quantitative data which will enable improved computational modelling of osteocyte mechanobiological processes.

- Demonstrate the efficacy and value of CXEM as an imaging method for the ON&LCN across length scales.

The structure and function of bone as an organ and the structure and function of the ON&LCN, described in Sections 2.1 and 2.4 are briefly re-capped and the use of a mouse model is discussed.
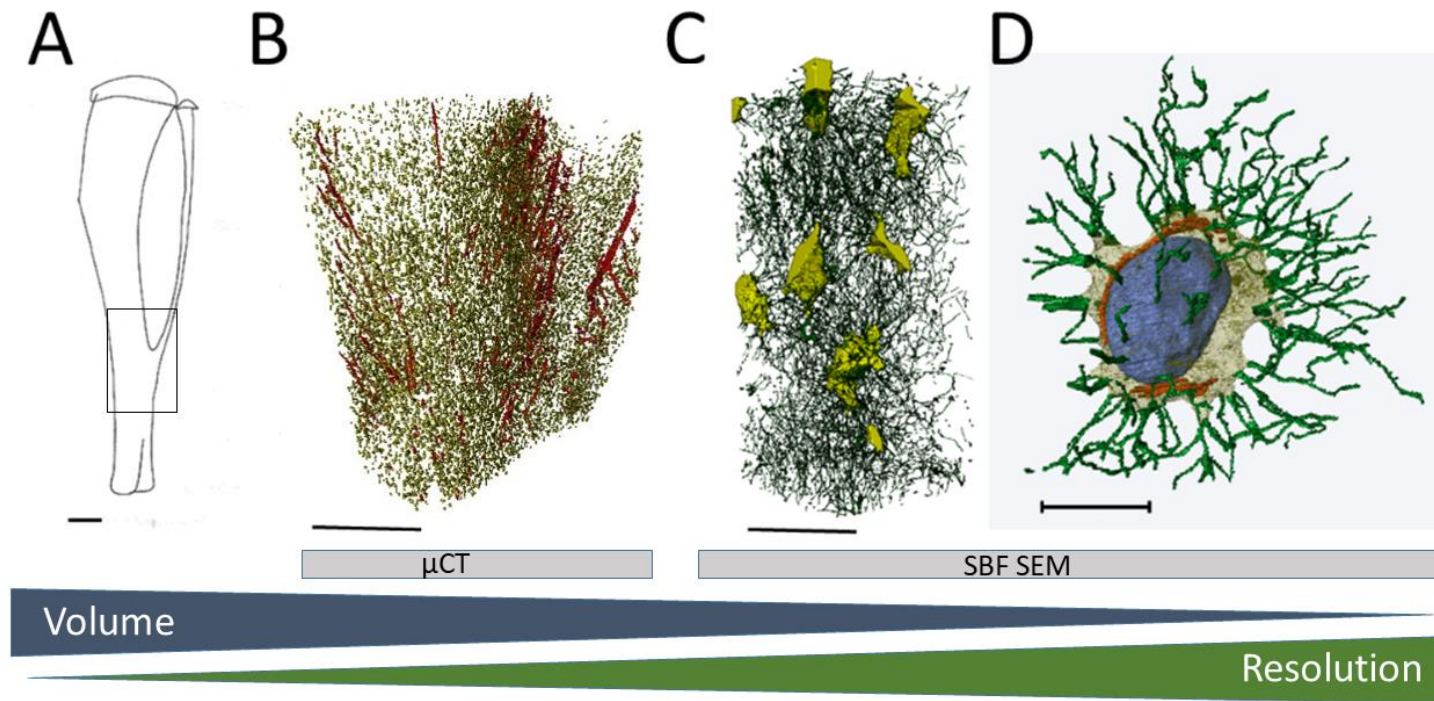
Figure 45   CXEM workflow applied to murine bone tissue.

Examples of 3D images obtained using μCT and SBF SEM, illustrating the range of volume and spatial resolution.

A – Murine tibia showing tibiofibular junction, which is the volume of interest used in this study (rectangle). Scale bar = 1 mm

B – Results from μCT scanning of tibia. Osteocytes are shown in yellow and vasculature in red. *Scale* bar = 0.5 mm

C – SBF SEM output from a sub-volume of B. Osteocytes are shown in yellow and the cell processes in green. Scale bar = 20 μm

D – Image reconstructed from SBF SEM data of a single osteocyte. The cell body is shown in yellow, cell processes in green,

nucleus in blue and mitochondria in red. Scale bar = 10 μm

5.1.1 **Bone structure and function**

As discussed in Chapter 2, bone has a multitude of mechanical, homeostatic, locomotor and protective roles (Robling and Bonewald, 2020). Osteoblasts and osteoclasts coordinated by osteocytes respond to mechanical signals caused by loading re-model the mineralised matrix controlling the mechanical and architectural properties of bone (Schaffler et al., 2014). Osteocytes, the most abundant cells in bone play crucial roles in the many functions of bone. Osteocytes comprise an elongated cell body (10-25 μm), with numerous processes extending from the cell body that connect to osteoblasts, osteoclasts, other osteocytes, bone marrow and the vasculature. The extensive ON is located within a network of voids and channels in the calcified matrix known as the LCN (Figure 46).

5.1.2 **Changes in bone and the ON&LCN during development**

This chapter of the thesis describes a CXEM study which compares the 3D structure of the ON&LCN in adult and juvenile mouse tibia across different length scales. Results and insights into changes of ON&LCN during development determined using light, X-ray and electron imaging techniques described in Section 2.5.22.5.2, will be compared to the results from the current CXEM study. Development from the embryo through the juvenile stage to adulthood, before changes related to ageing take place is considered here. This stage in human is equivalent to the embryo to adulthood (> 10 weeks) in mice (Figure 47) (Dutta and Sengupta, 2016).
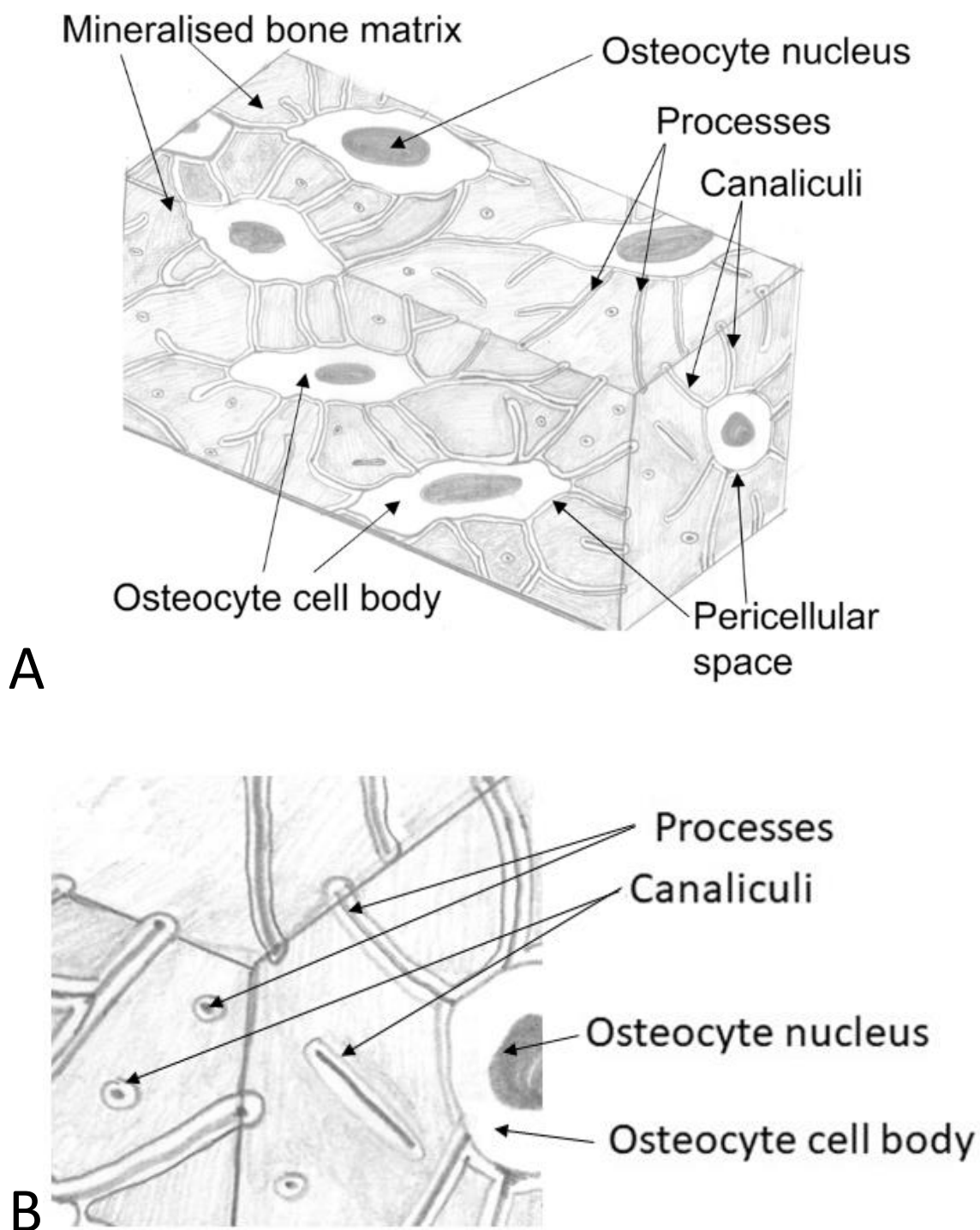
Figure 46   Schematic views of the ON&LCN

A and B The osteocytes and their processes are housed within the mineralised bone matrix in a
void system formed of (osteocyte) lacunae and interconnecting canaliculi. Adapted from
(Goggin et al., 2020).
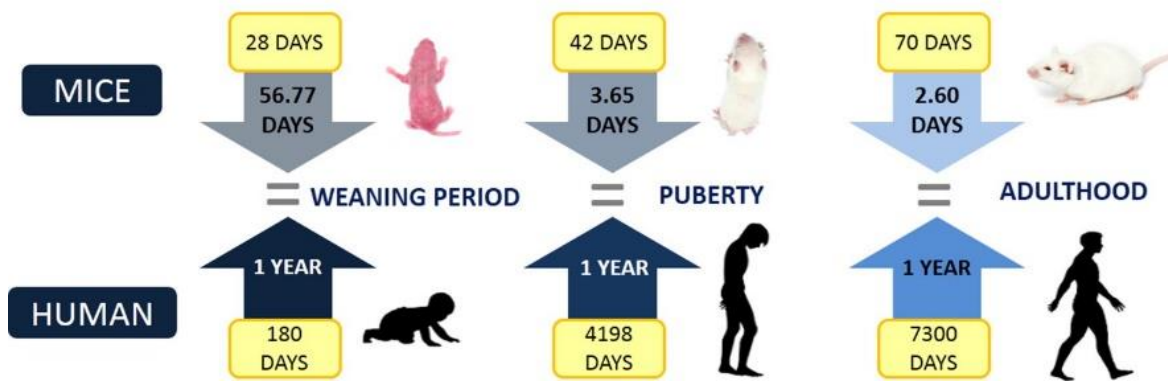
Figure 47   Comparing the ages and developmental stages of life in mice and humans.

From (Dutta and Sengupta, 2016).

5.1.3   Use of a mouse model

Animal models provide more uniform experimental material than humans (Turner, 2001).

The mouse (*Mus musculus*) is widely used for studies of human physiology and pathology

as it has similarities to the human, a short gestation period and a high reproductive capacity

(Jilka, 2013). Similarities to the human include the conservation of 99% of genes, similar

patterns of pathogenesis and physiology (Demetrius, 2006). Comparisons between mouse

and human skeletal physiology conclude that studies of bone in mice should be applicable

to humans when inherent limitations are recognised (Almeida and O'Brien, 2013, Jilka,

2013). The most obvious structural difference between the human and murine skeleton is

that human bone has an osteonal structure where osteocytes are arranged in concentric

rings round a blood vessel (Parfitt 1994). Thus, in humans, but not mice, cortical bone

remodelling by osteoclasts and osteoblasts occurs around a blood vessel (Figure 48).
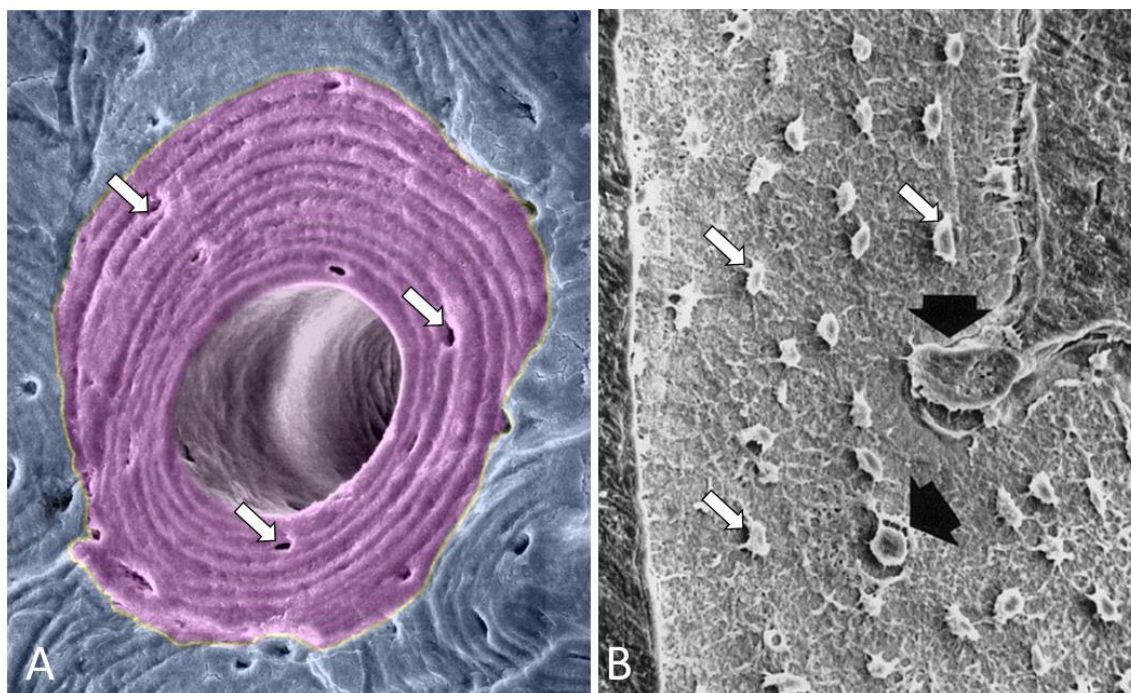
Figure 48   Human and mouse bone structure

A   SEM image of an osteon in human bone showing an osteon (purple), and osteocyte lacunae (white arrows) Adapted from (Brelje, 2019)

B   SEM image bone showing methacrylate casts of osteocyte lacunae (white arrows) and vascular canals (black arrows). Adapted from (Rubinacci et al., 2002)

Skeletal maturity is reached at around 4 months with peak bone mass achieved at 4-6 months in mice. The animals used in the CXEM study described in this chapter are chosen to represent juvenile (4 weeks) and early adult (38 weeks) stages of development. Figure 47 illustrates the relationship between human and mouse developmental stages (Dutta and Sengupta, 2016).

5.1.3.1   CXEM study of changes in bone during development

Reliable quantitative characterisation of both the ON and the LCN in juvenile and adult animals, based on advanced 3D imaging, can be related to the changes described section 2.5.2. Additionally, these data will inform computational models of bone mechanotransduction and will allow more realistic predictions of the complex and dynamic

processes involved in the mechanobiology of the ON&LCN (Buenzli and Sims, 2015, Anderson and Knothe Tate, 2008, Verbruggen et al., 2012).

CXEM extends the range of quantitative measures which can be obtained from each bone sample beyond the range of single techniques used in isolation (Table 9). CXEM provides data from a larger volume than SBF SEM alone and higher resolution data than μCT alone.

The study described in this chapter compares the ON&LCN in juvenile and adult animals. As discussed in Section 2.6 there is an unmet need for 3D high-resolution imaging and analysis of bone tissue during development across different length scales. It is proposed that the present CXEM study comparing juvenile and adult bone can contribute quantitative results on accepted hallmarks of bone structure (Table 15), insights to changes in bone structure during development and data which will contribute to improvements and refinements of computational models of bone mechanobiology.

5.2   Materials and Methods

This section outlines the sample preparation, image acquisition, image processing and image analysis steps for CXEM. For a more detailed description see Chapter 3, Chapter 4, Appendix A and Appendix B.

5.2.1   Sample preparation

Animals were handled according to the guidelines of the Animals (Scientific Procedures) Act, 1986. Murine bones were obtained in compliance with the EU Directive 2010/63/EU and the approval of the Animal Welfare and Ethical Review Board of the University of Southampton under Home Office licence P12102B2A. 4-week-old (n=3) and 38-week-old (n=3) C57BL/6 male mice were transcardially perfused with 3% glutaraldehyde, 4% formaldehyde in 0.1M piperazine-N,N'-bis(2-ethanesulfonic acid) (PIPES) buffer. The right

tibiae were harvested, cleaned of soft tissue and fixed in 3% glutaraldehyde, 4% formaldehyde in 0.1M PIPES buffer overnight. Bones were decalcified for 5 days in 7% EDTA, which was changed daily and constantly rotated. Blocks of tissue 2-5 mm long were cut from the tibiofibular junction (TFJ) (Figure 49). The TFJ was selected as the region of interest as it contains only cortical bone, provides a clear landmark allowing for consistent and reproducible imaging, and has been previously well characterised (Section 5.4.3).

Fixed and decalcified tissue blocks were stained as outlined in Appendix A and (Goggin et al., 2020). A minimal resin embedding technique (Schieber et al., 2017) was employed. Briefly, after resin infiltration the bone samples were placed on absorbent paper and gently moved around until excess resin had been absorbed. Resin in the medullary cavity was removed with a small piece of twisted tissue paper before polymerisation.
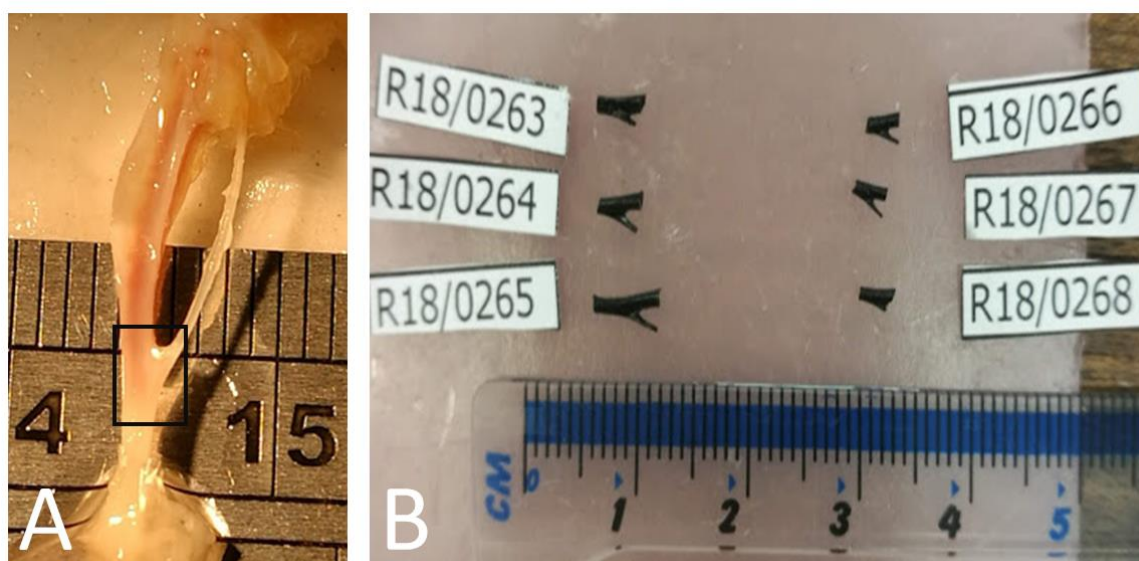
Figure 49   Sample preparation of mouse tibia for CXEM.

A   Mouse tibia after fixation and dissection, rectangle shows volume including tibiofibular junction selected for processing.

B   Adult (left) and juvenile (right) mouse tibiae after decalcification, staining and minimal resin-embedding.

5.2.2   µCT imaging

µCT imaging of the whole sample produces images of a large volume of interest compared to SBF SEM imaging and quantitative data on the distribution, size and shape of osteocytes. µCT imaging also facilitates choice of a sub-volume for subsequent SBF SEM imaging. µCT image acquisition, image processing and image analysis are described in this section.

5.2.2.1   Image acquisition

Bone samples were mounted in a plastic straw and imaged by µCT using a Zeiss/Xradia Versa 510 scanner (Figure 50), which uses an 160 kVp source and a 2048 x 2048 pixel flat panel detector. Imaging settings were as follows: peak voltage 110 kVp, power 9.5 W, binning x 2 leading to a virtual 1024 x 1024 pixel detector, x 4 objective lens, filter 0.34 mm of SiO_2, exposure time 5 s and sampling 2401 projections. Source-to-detector and source-to-object distances were set to 83.56 mm and 18.65 mm, respectively, which along with the selected 4x objective resulted into a radiograph pixel size of 1.5 μm^2 and a field of view of 1.5 mm^2. Following image acquisition, the raw data (X-ray projections) were reconstructed using a standard filtered back-projection (Zeiss reconstruction software), and an isotropic voxel size of 1.5 µm. The reconstructed data were exported as 16-bit tiff stacks for visualisation and analysis. Data is available from DOI: 10.5258/SOTON/D2118
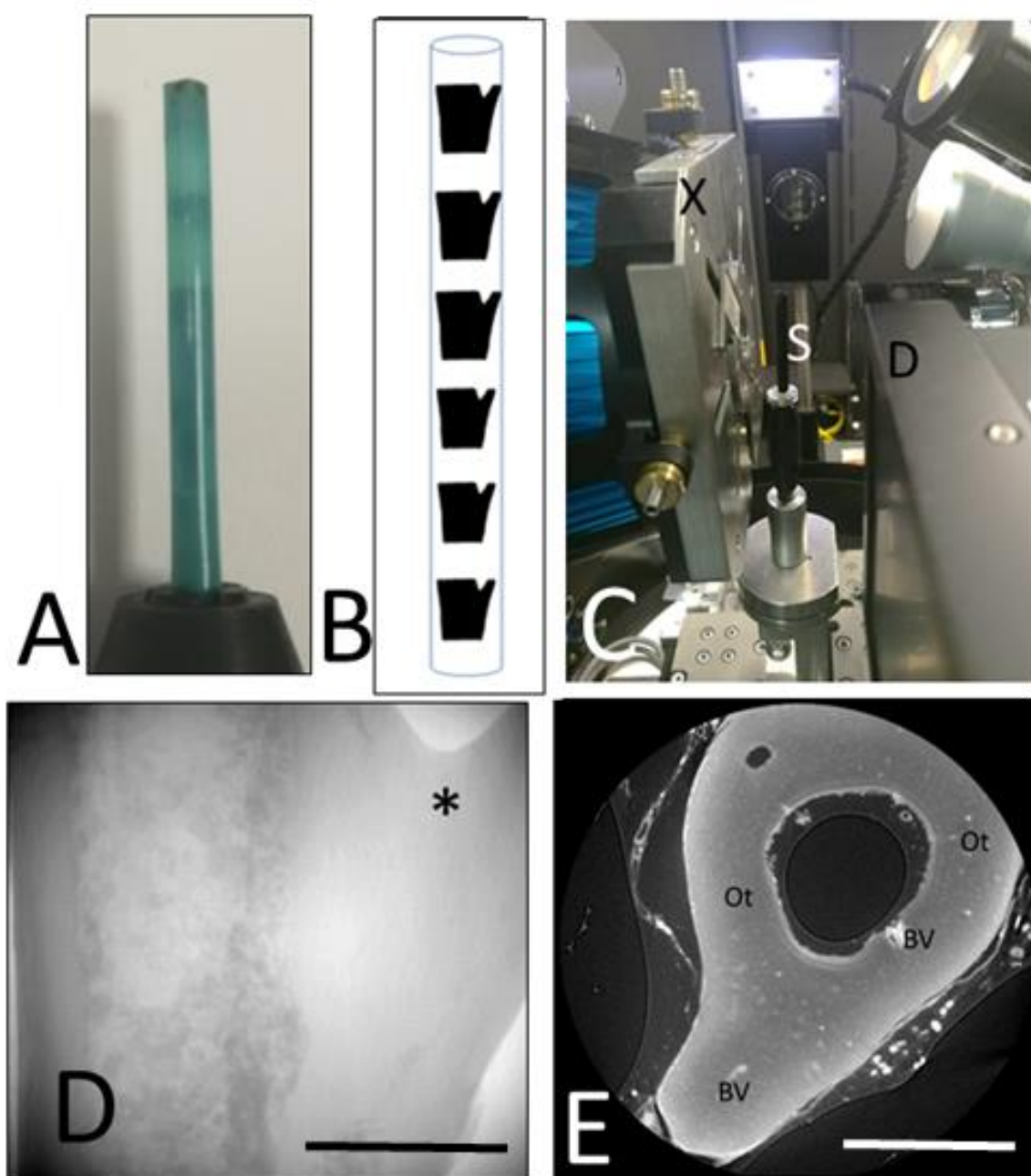
Figure 50   X-ray µCT imaging.

A – Plastic tube containing samples for imaging.

B – Diagram showing sample arrangement inside tube.

C – Tube mounted in Versa scanner X – X-ray source, S = samples, D = detector.

D – Radiography image from Versa showing bone sample in tube and tibiofibular junction (*).

E – Reconstructed CT slice of stained bone tissue showing blood vessels (BV) and osteocytes (Ot).

   Scale bars = 500 µm

5.2.2.2   **Image processing**

Image processing of the μCT data was carried out using Fiji (Schindelin et al., 2012) and Avizo (version 2019.4) (ThermoFisher Scientific), as outlined in Appendix 269B.1. Briefly, bone tissue was separated from the background and bone marrow, the heavy metal stained elements comprising the osteocytes and the vascular tissue were extracted, separated from each other using a volume filter and the osteocytes quantified.

The μCT image data stack was aligned and separated into anatomical quadrants (anterior, posterior, medial and lateral) (detailed method in B.1.1). The data was filtered to enhance edges, reduce gradients and variations in intensity normalised. Cortical bone tissue was segmented semi-automatically from the background and the bone marrow to produce a binary label. This label was separated into posterior, anterior, medial and lateral quadrants for subsequent image segmentation. Segmentation was carried out. Briefly, the heavy metal stained tissue was selected by thresholding, converted to a binary label and the osteocytes and vasculature separated by volume. The quadrant labels were used as masks to select the osteocytes in each quadrant from the complete osteocyte binary label.

5.2.2.3   **Quantification**

The measures listed in Table 16 were retrieved from the whole bone and from each quadrant using the Avizo label analysis function and calculations outlined in Table 25. The measures listed are standard measures defined by (Bouxsein et al., 2010, Dempster et al., 2013, Parfitt et al., 1987) and newly introduced measures outlined in Section 4.4.2.

Table 16   Quantitative measures obtained from µCT data.

Category	Measure and abbreviation
Organ	• Bone Volume (BV)
Tissue - ON	• Number of osteocytes (N.Ot) • Osteocyte number density (N.Ot/BV) • Osteocyte volume (Ot.V) • Osteocyte porosity (T.Ot.V/BV) • Mean osteocyte volume (<Ot.V> = T.Ot.V/N.Ot) • Osteocyte surface area (Ot.A) • Osteocyte sphericity (Ot.Sph)
Cell - Osteocytes	• Osteocyte length (Ot.Le) • Osteocyte width (Ot.Wi) • Osteocyte breadth (Ot.B) • Osteocyte anisotropy (Ot.An) • Osteocyte flatness (Ot.Fl)

5.2.3   SBF SEM

The anterior quadrant was chosen as the volume of interest for SBF SEM imaging. The sub-sample was prepared, imaged and analysed as described here.

5.2.3.1   SBF SEM imaging

For each bone sample a frustum with face approximately 500 µm^2 was trimmed from the anterior section of the tibia. This sub-volume of interest was removed from the resin block and mounted on an aluminium pin using conductive glue (Figure 38). 2 data sets were collected using a 3ViewXP2® system (Gatan Inc., Abingdon, UK) in a Quanta 250 FEGSEM (ThermoFisher, Netherlands) as described in A.4.6 and in (Goggin et al., 2020). Two SBF SEM datasets were collected for each juvenile and adult murine tibia sample, A_1, encompassing the width of the bone from endosteum to periosteum and A_2, a dataset with smaller pixel size including 20-30 cells and their processes (Table 17 and Figure 51). Data is available from DOI: 10.5258/SOTON/D2118

Table 17   Image acquisition settings for SBF SEM.

Experimental settings	Dataset A_1	Dataset A_2
Accelerating voltage	3 kV	3 kV
Spot size	3	3
Slice thickness	50 nm	50 nm
Dwell time	0.5 µs	2 µs
Vacuum	60 Pa	60 Pa
Number of pixels in x-y plane	8192 – 15000	8182
Pixel size	20 nm	10 nm
Number of slices	900-1660	877-1467

5.2.3.2   **Image processing**

The osteocyte cell bodies, processes and the PCS space were segmented and visualised as described in Appendix B.2. SBF SEM images were collected using Digital Micrograph (Gatan, Abingdon, UK) as a series of .dm3 files. The images were aligned and normalised using the automated alignment and normalisation features in Digital Micrograph before being converted to 16-bit .tiff files. As described in Appendix B.2.2, the Trainable Weka Segmentation 3D (Arganda-Carreras et al., 2017) plug-in was used to separate the bone matrix, PCS and cellular components of the image stacks into binary labels.

5.2.3.3   **Quantification**

The measures in Table 18 were derived from SBF SEM data using the methods outlined in B.3. and Table 25. The measures are either defined by (Bouxsein et al., 2010, Dempster et al., 2013, Parfitt et al., 1987) or newly introduced and defined in Section 4.4.2.
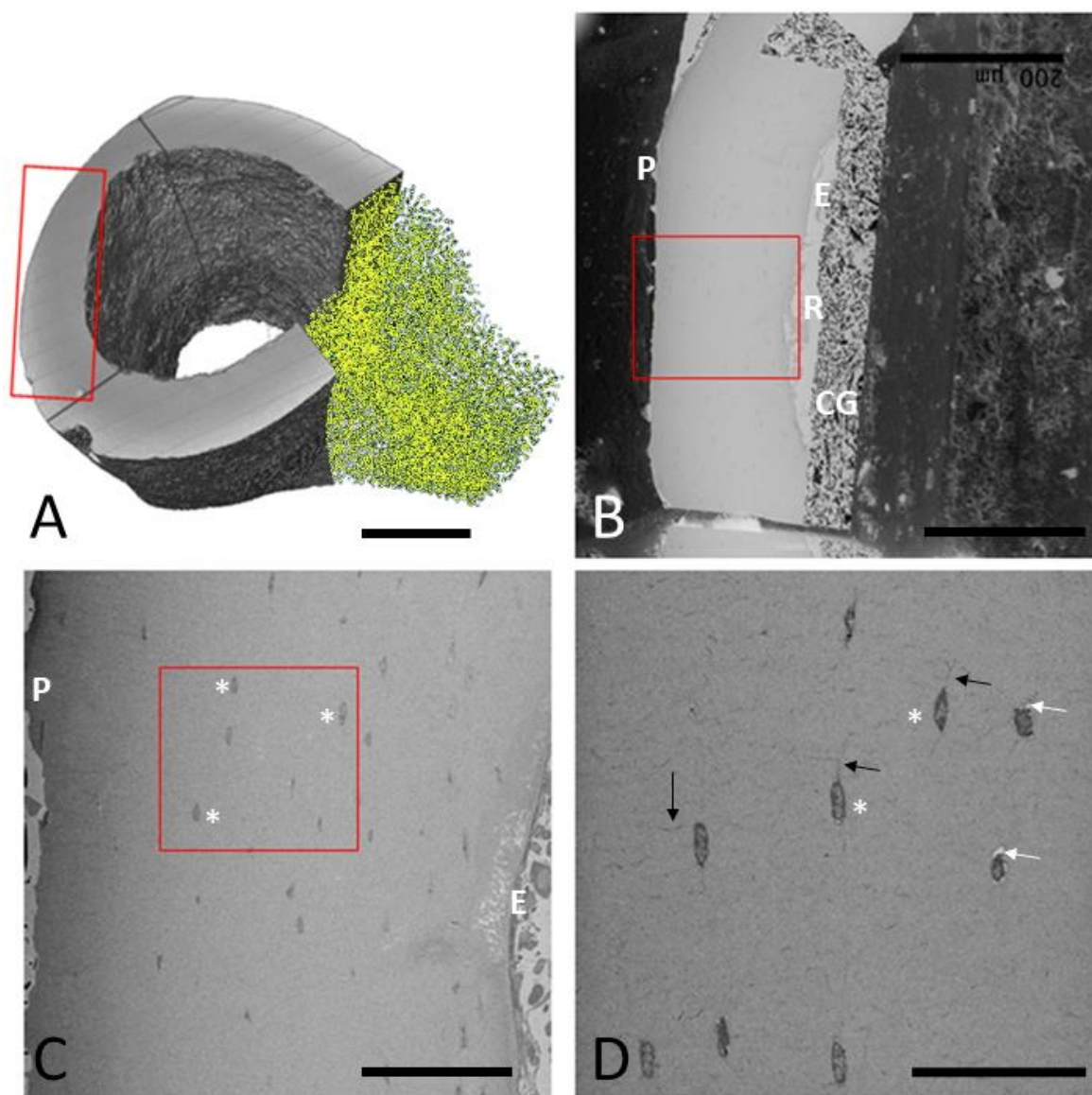
Figure 51   Regions of interest imaged using SBF SEM

A   μCT reconstruction of murine tibia sample showing osteocytes in yellow and the region of interest selected for SBF SEM (rectangle). Scale bar = 200 μm

B   Overview of SBF SEM block showing the region of interest imaged in dataset A_1 (rectangle) conductive glue (CG), resin (R), periosteum (P) and endosteum (E). Scale bar = 200 μm

C   Single image from SBF SEM dataset A_1 showing the region selected for dataset A-2 (square) periosteum (P), endosteum (E) and osteocytes (*). Scale bar = 50 μm

D   Single image from SBF SEM dataset A_2, showing osteocytes (*), osteocyte processes (black arrows) and pericellular spaces (white arrows). Scale bar = 20 μm

Table 18   Quantitative measures derived from SBF SEM data.

Category	Measures and abbreviations
Organ	• Bone Volume (BV)
Tissue - ON	• Number of osteocytes (N.Ot) • Osteocyte number density (N.Ot/BV) • Osteocyte volume (Ot.V) • Osteocyte porosity (T.Ot.V/BV) • Mean osteocyte volume (<Ot.V> = T.Ot.V/N.Ot) • Osteocyte surface area (Ot.A) • Osteocyte sphericity (Ot.Sph)
Cell - Osteocytes	• Osteocyte length (Ot.Le) • Osteocyte width (Ot.Wi) • Osteocyte breadth (Ot.B) • Osteocyte anisotropy (Ot.An) • Osteocyte flatness (Ot.Fl)
Pericellular space	• Pericellular space volume (PCS.V) • Pericellular space porosity ((T.PCS.V)/BV) • Pericellular space thickness (PCS.Th) • Maximum pericellular space width (PCS.Wi)
Processes	• Number of processes per cell (N.Pr) • Process diameter (Pr.Dm) • Process thickness (Pr.Th)

5.2.4   **Statistics**

Statistical analyses were performed using R (version 3.5.1) in R Studio (version 1.1.456) (RStudio Team, 2016). The null hypotheses state that ON&LCN microstructure and ultrastructure are unchanged across the life course and unchanged with anatomical area in murine tibia. ON&LCN measures from the whole bone cross section in adult and juvenile animals were compared to test these hypotheses. The same measures from the posterior, anterior, medical and lateral quadrants were also compared. Data were first tested for normal distribution using a Kolmogorov-Smirnov test or a Shapiro-Wilks test depending on how many data points were present (>35 K-S, <35 S-W). Where data was normally distributed or where data was not normally distributed and more than 30 data points were present an unpaired Student's t-test or one way ANOVA was performed. When data were

not normally distributed or fewer than 30 data points were present a Mann Whitney U test or Kruskal-Wallis teat was used. p-values were considered significant at p ≤ 0.05.

5.3 Results

Using CXEM, the ON&LCN in juvenile and adult murine tibia were visualised and quantified using existing quantitative measures and newly defined measures for processes and the PCS. Using SBF SEM, the ON&LCN were made visible concurrently at high resolution in 3D over a relatively large volume (containing up to 170 osteocytes) for the first time. This section firstly presents the results of the µCT imaging, followed by the SBF SEM imaging and finally compares both sets of results.

5.3.1 µCT

µCT imaging of decalcified, heavy metal stained, resin embedded murine tissue enabled visualisation and quantification of osteocyte cell bodies. It was not possible to image the cell processes as their diameter (~ 100 nm) is beyond the resolution limit of the technique.

5.3.1.1 Total bone volume - osteocyte number density, porosity and cell volume

Mean osteocyte number density (<N.Ot/BV>) is lower in adult animals (57,680 ± 8,874 /mm^3), than in juvenile animals (76,697 ± 10,864 /mm^3), although the difference is non-significant (p = 0.13). Mean osteocyte porosity (<T.Ot.V/BV>) in adult animals (0.98 ± 0.25%) is not significantly different from <T.Ot.V/BV> in juvenile animals (1.19 ± 0.33%) (Figure 52). No significant differences were observed in osteocyte shape and size measures between adult and juvenile animals (Figure 52).

5.3.1.2 **Regional diversity by quadrant**

5.3.1.2.1 **Osteocyte number density, porosity and volume**

The quadrant with highest osteocyte number density (N.Ot/BV) varies. Averaging <N.Ot/BV> over the age groups shows that density is highest in the posterior quadrants of both adult and juvenile groups. Osteocyte porosity is broadly similar across all quadrants in both age groups. <Ot.V> is not significantly different between quadrants (Figure 53) although there is a greater range of Ot.V observed in adult animals. Osteocyte number density values are smaller in separate quadrants than in whole bone because during separation, cells on the dividing lines are split into smaller volumes and removed as noise during image processing.
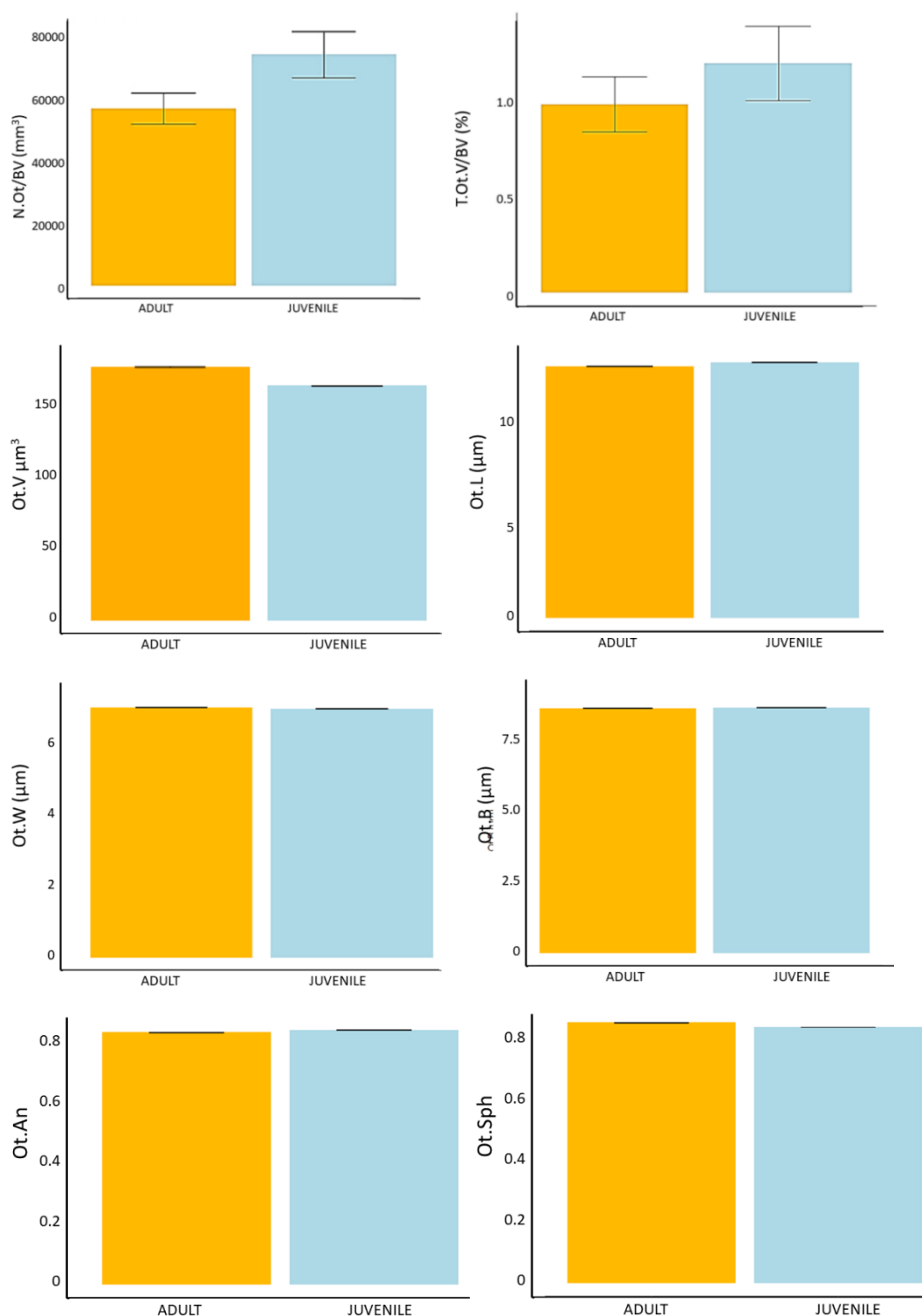
Figure 52   Effect of age on osteocyte network measured using µCT imaging.

Mean osteocyte number density (N.Ot/BV), porosity (T.Ot.V/BV), volume (Ot.V), length (Ot.L), width (Ot.W), breadth (Ot.B), anisotropy† (Ot.An) and sphericity* (Ot.Sph) in adult and juvenile tibia. No significant differences were observed. Values are mean ± SE, n=3 in each group. †deviation of shape from a sphere, sphere An = 0 *how closely shape resembles a sphere, for a perfect sphere Sph = 1.
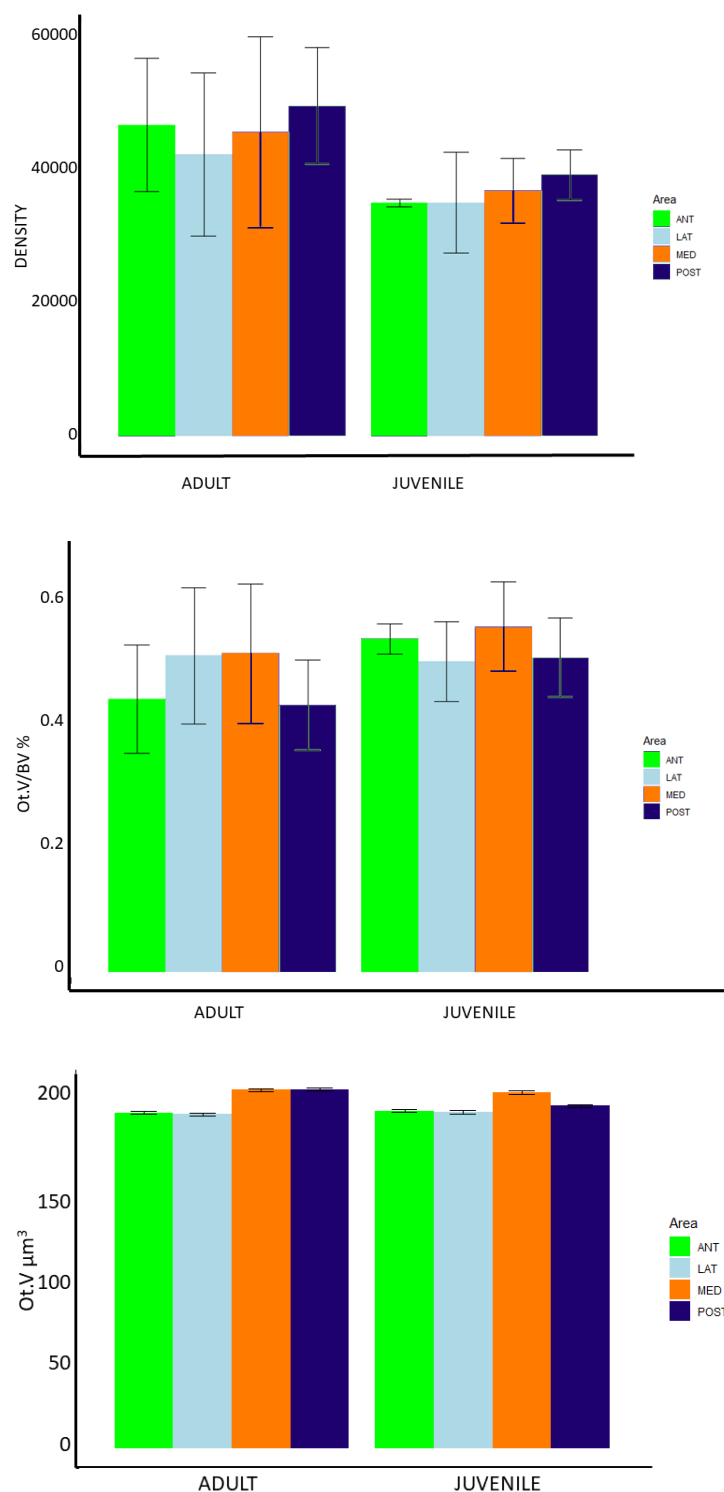
Figure 53   Effect of age on osteocyte network measures in anatomical quadrants

Comparison of osteocyte number density (N.Ot/BV), porosity (T.Ot.V/BV) and osteocyte volume (Ot.V) in anatomical areas and age groups obtained using µCT. No significant differences were found. Values are mean ± SE, n=3 in each group. Ant = anterior, LAT = lateral, MED = medial, POST = posterior

5.3.2 **SBF SEM**

Decalcified, heavy metal stained, resin embedded bone tissue yielded SBF SEM images suitable for segmentation and quantification. SBF SEM images showed well fixed, well contrasted osteocytes within the bone matrix (Figure 54). Fixation quality was judged on the following criteria: the cells have intact cell and nuclear membranes, small separation artefact, mitochondria have intact cristae and no swelling was observed. See section 3.2.1.2.1 for full explanation and scoring system criteria.
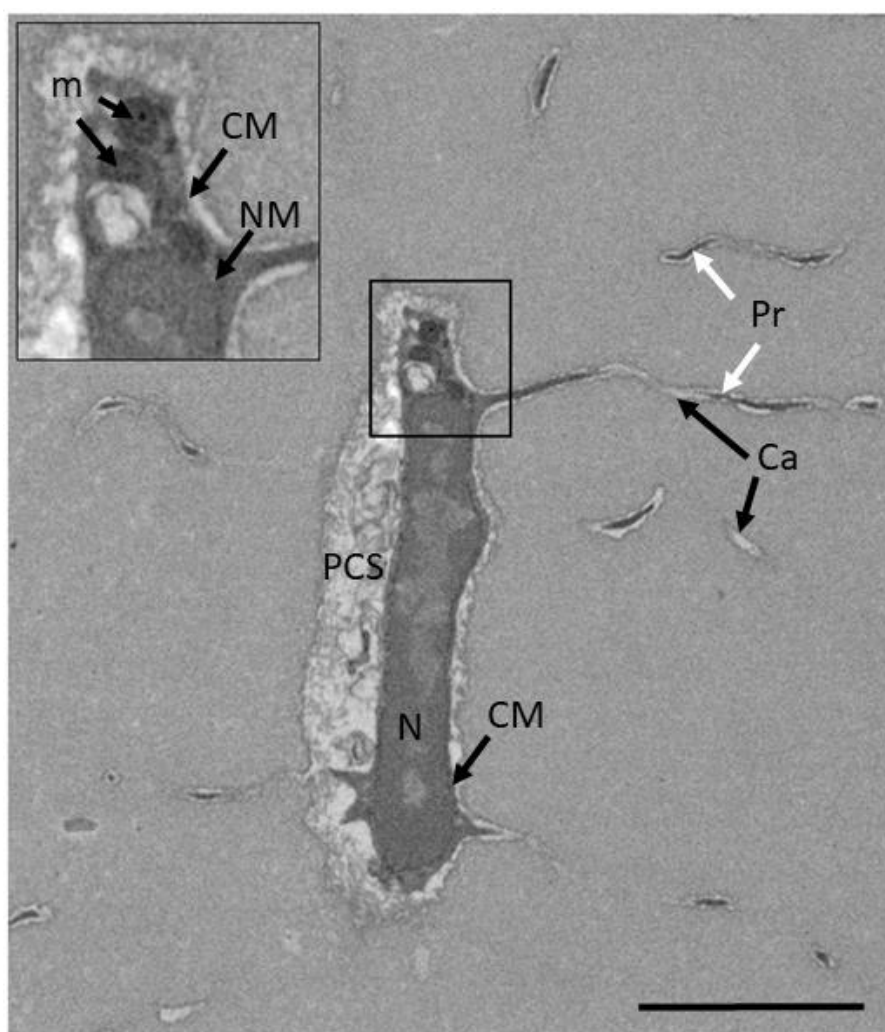
Figure 54   An SBF SEM image showing the features of well-fixed and stained tissue.

An osteocyte embedded in the bone matrix. The image has sufficient resolution and contrast to identify the nucleus (N), nuclear membrane (NM), cell membrane (CM), mitochondria (m), pericellular space (PCS) and cell processes (Pr) within canaliculi (Ca). Scale bar = 2 μm

5.3.2.1 **A_1 dataset**

SBF SEM dataset A_1 contained a field of view from the endosteum to the periosteum and included up to 170 osteocytes or parts thereof per sample and the associated vasculature (Figure 55). <BV> imaged in this dataset is 1.53 x 10^6 μm^3 (Table 19).

Table 19   Dataset A_1 dimensions and volumes

	No. of pixels x	No. of pixels y	Pixel size (nm)	Number of slices z	Slice depth (nm)	Tissue vol (μm^3)	Bone volume (μm^3)
Adult	15000	15000	20	1000	50	1.61E+06	1.52E+06
Adult	10500	12000	20	900	50	2.27E+06	1.94E+06
Adult	10000	12000	20	1660	50	2.24E+06	1.93E+06
Juvenile	10500	10500	20	1000	50	1.56E+06	1.30E+06
Juvenile	13000	15000	20	1089	50	1.38E+06	1.26E+06
Juvenile	8192	8192	20	1130	50	1.52E+06	1.20E+06

5.3.2.1.1 **Osteocyte number density, porosity and volume**

There is no significant difference in osteocyte number density (N.Ot/BV), osteocyte porosity (T.Ot.V/BV) or mean osteocyte volume (<Ot.V>) between adult and juvenile animals (Figure 56). The most frequently occurring value for Ot.V is 160 μm^3 in adult and 110 μm^3 in juvenile animals. <Ot.V> is 140 ± 31 μm^3 in adult animals and 131 ± 39 μm^3 in juvenile animals.

5.3.2.1.2 **Osteocyte measures**

No significant differences were observed in any of Ot.Le, Ot.W, Ot.B, Ot.An, Ot.Fl or Ot.Sph (Figure 57).
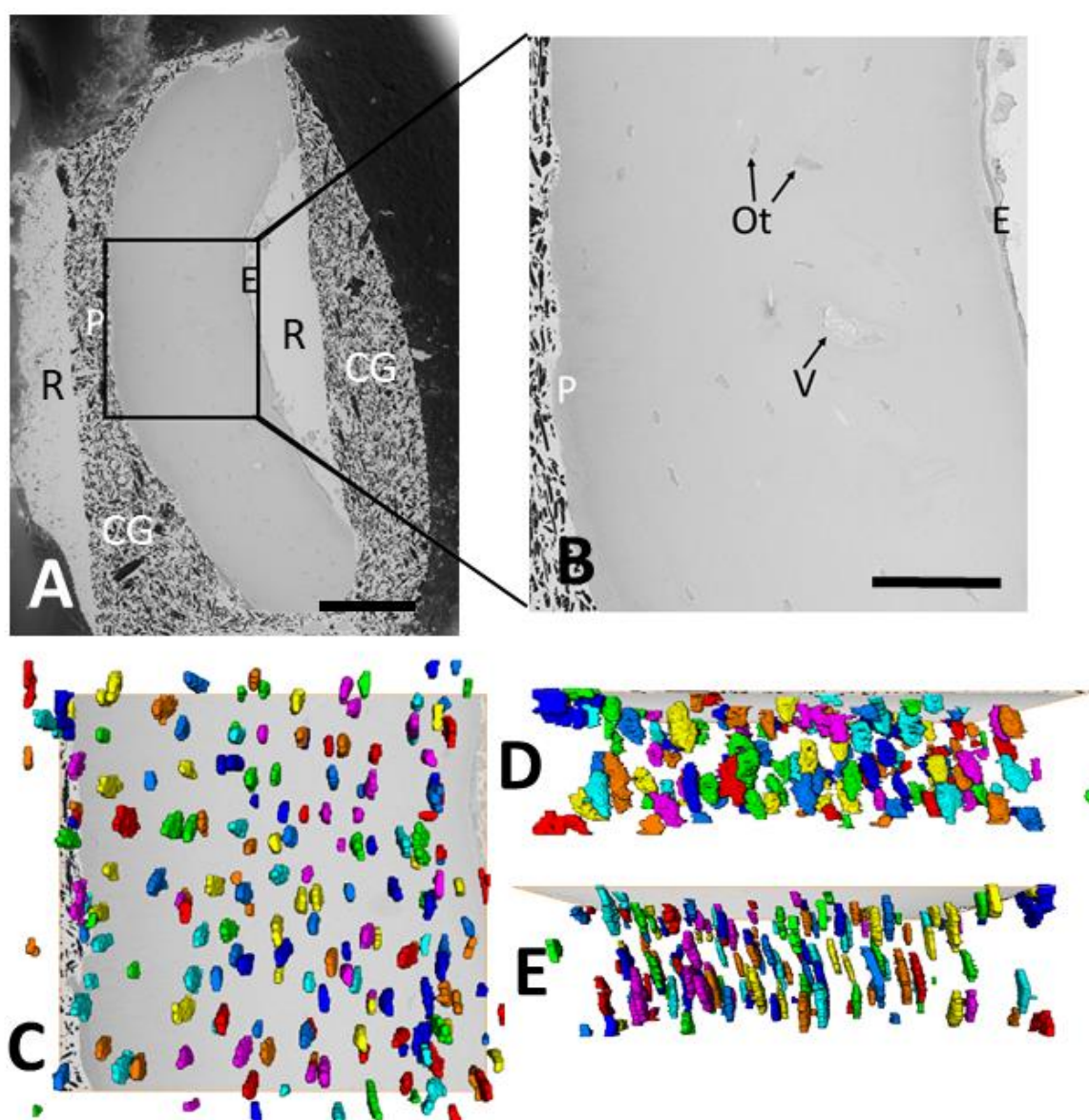
Figure 55   SBF SEM imaging and osteocyte cell bodies segmented from the volume of interest.

A   SBF SEM image of resin block face and region of data collection for dataset A_1 (rectangle) extending from tibial periosteum (P) to endosteum (E). Conductive glue (CG), resin R). Scale bar = 100 µm

B   Region of A_1 dataset including osteocytes (Ot), vasculature (V), conductive glue (CG), resin (R). Scale bar = 50 µm

C   Segmented osteocytes in x-y view.

D   Segmented osteocytes in x-z view.

E   Segmented osteocytes in y-z view.
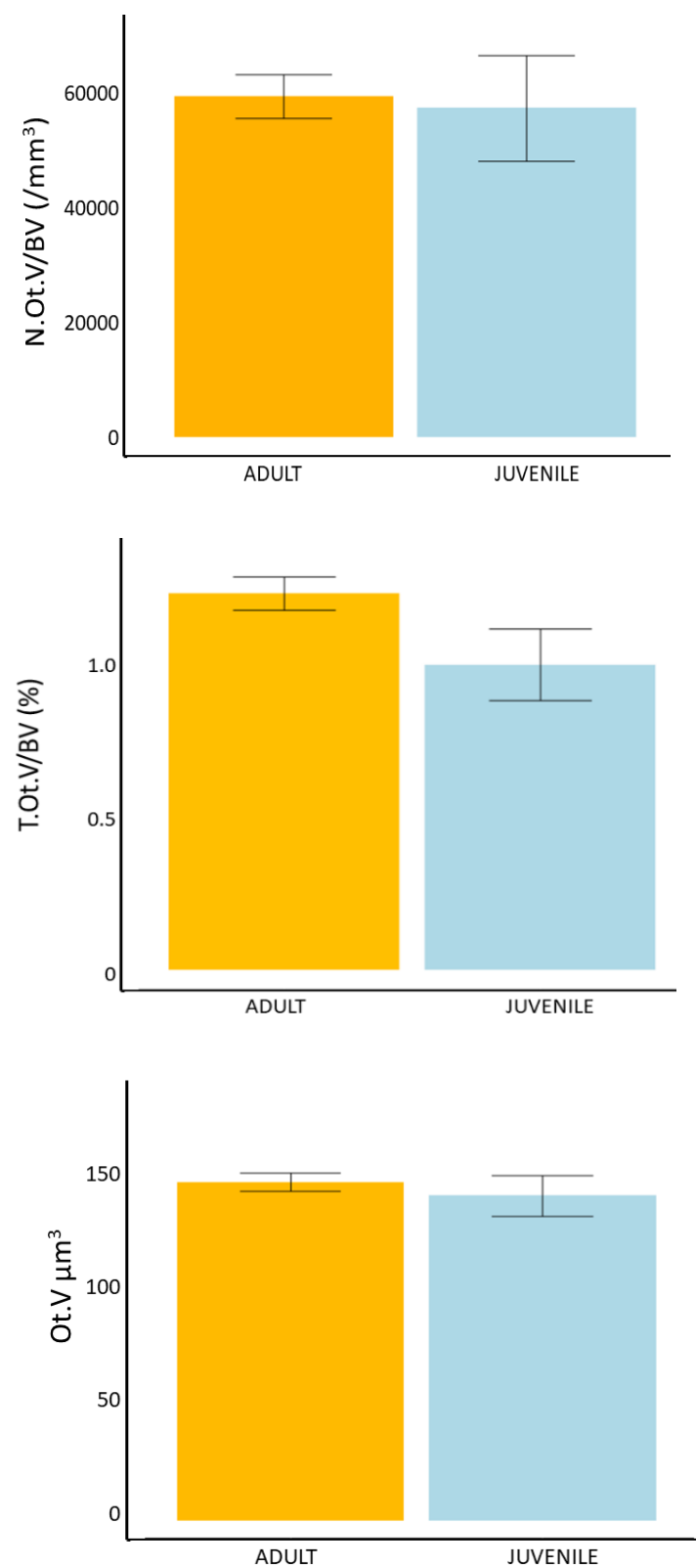
Figure 56   Effect of age on osteocyte network

Mean osteocyte number density, osteocyte porosity and osteocyte volume in adult and juvenile tibia measured using SBF SEM. No significant differences were observed. Values are mean ± SE, n=3 in each group.
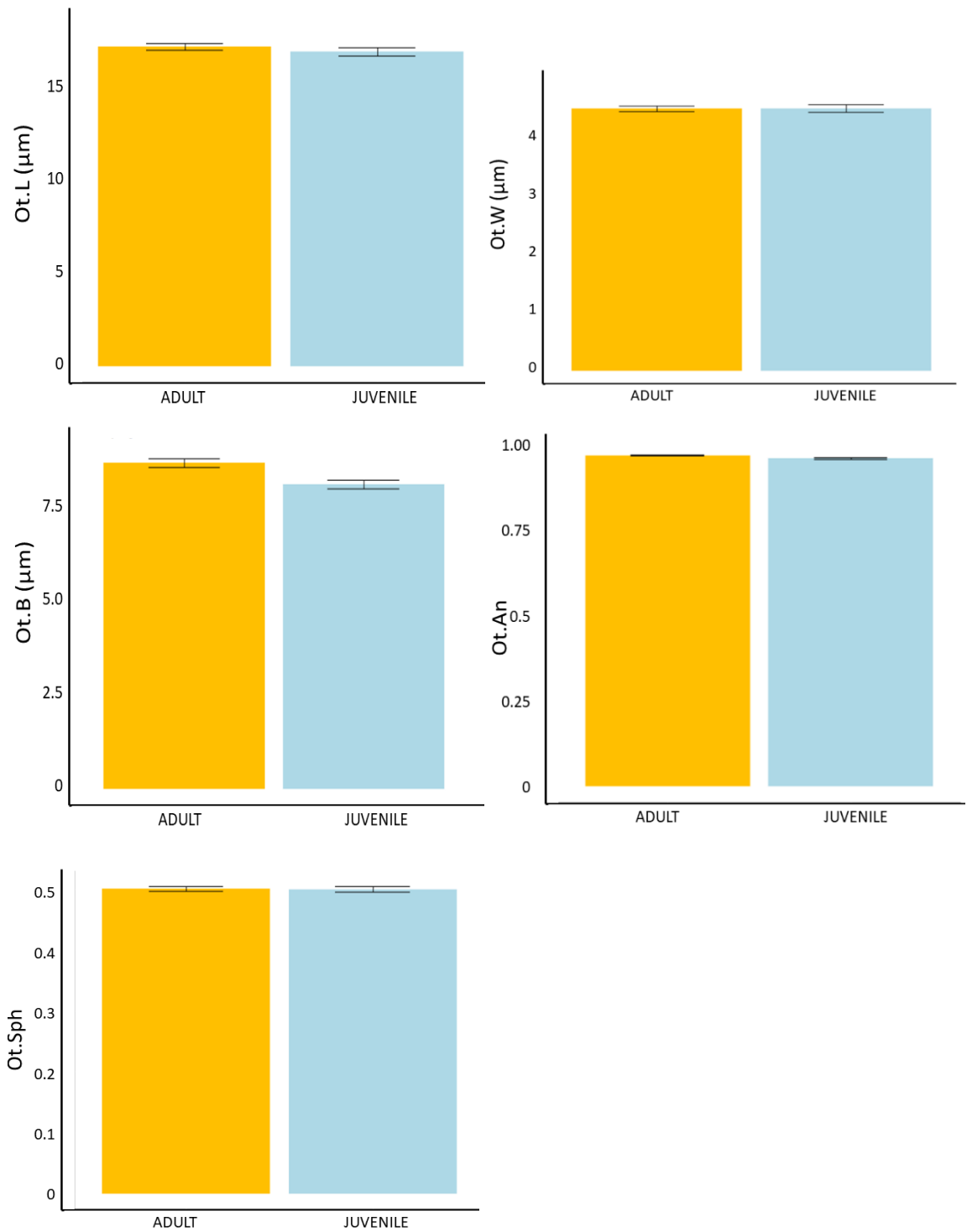
Figure 57   Effect of age on osteocyte cell measures

Mean osteocyte length, width, breadth, anisotropy and sphericity in adult and juvenile tibia measured using SBF SEM. No significant differences were observed. Values are mean ± SE, n=3 in each group.

5.3.2.2   A_2 Dataset A_2

Dataset A_2 uses a smaller pixel size (10 nm) than dataset A_1 to achieve better lateral resolution. The mean bone volume imaged is 3.35 x 10^5 μm^3 (Table 20). This volume enabled imaging of up to 53 cells or parts thereof in each tissue block. Raw data can be viewed at (https://www.youtube.com/channel/UCTERYdnSV_bTQqbHt0Z61ZQ) Osteocyte cell bodies, processes and pericellular spaces were extracted from the data using the methods outlined in Appendix B.2 (Figure 58).

5.3.2.2.1   Osteocyte number density, porosity and volume

Mean osteocyte number density in adult animals was 53,700 ± 16,200 / mm^3 and in juvenile animals was 57,600 ± 14,600 / mm^3. Mean osteocyte porosity in adult animals was 0.64 ± 0.15% and in juvenile animals was 0.65 ± 0.18%. Mean osteocyte volume <Ot.V> in adult animals was 118.97 ± 23.41 μm^3 and in juvenile animals 112.80 ± 19.55 μm^3. The most frequent value for Ot.V was 100 μm^3 in adults and 120 μm^3 in juvenile animals. Osteocyte number density, porosity and <Ot.V> were not significantly different in adult and juvenile animals (Figure 59).

Table 20   Dataset A_2 dimensions and volumes

	No pixels x	No pixels y	Pixel size (nm)	No slices z	Slice thickness (nm)	Bone volume (μm^3)
Adult	8192	8192	10	954	50	3.20E+05
Adult	8192	8192	10	877	50	3.11E+05
Adult	8192	8192	10	878	50	2.93E+05
Juvenile	8192	8192	10	999	50	3.31E+05
Juvenile	8192	8192	10	960	50	3.22E+05
Juvenile	8192	8192	10	1464	50	4.34E+05
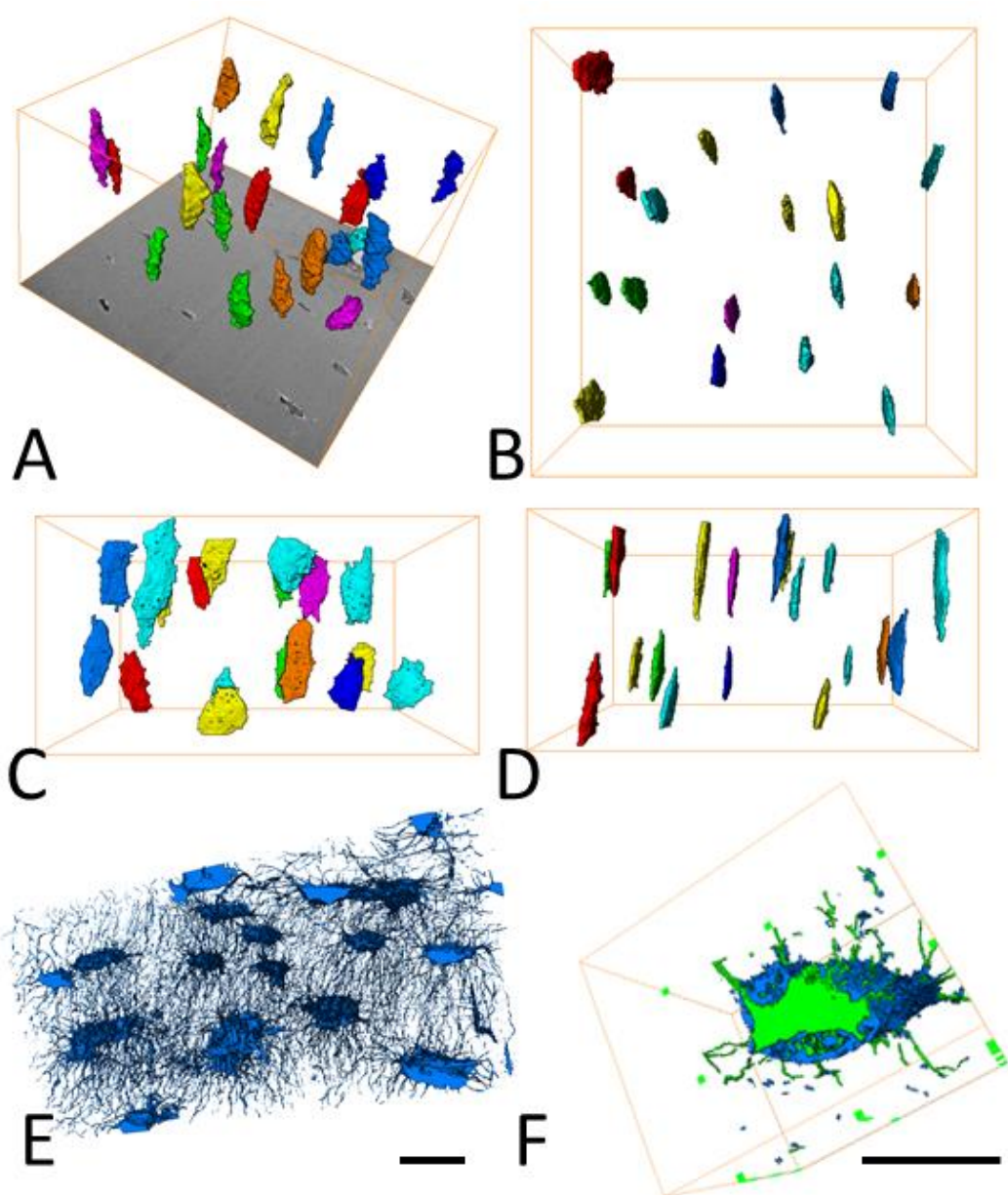
Figure 58   Osteocyte cell bodies, cell processes and pericellular space volumes segmented from murine bone tissue imaged using SBF SEM

A   A slice from SBF SEM with segmented osteocyte cell bodies.

B   Segmented osteocyte cell bodies in x-y view.

C   Segmented osteocyte cell bodies in y-z view.

D   Segmented osteocyte cell bodies in x-z view.

E   Segmented osteocyte cell bodies and connecting cell processes. Scale bar = 5 µm

F   A reconstructed osteocyte and processes (green) surrounded by pericellular space (blue) Scale bar = 5 µm
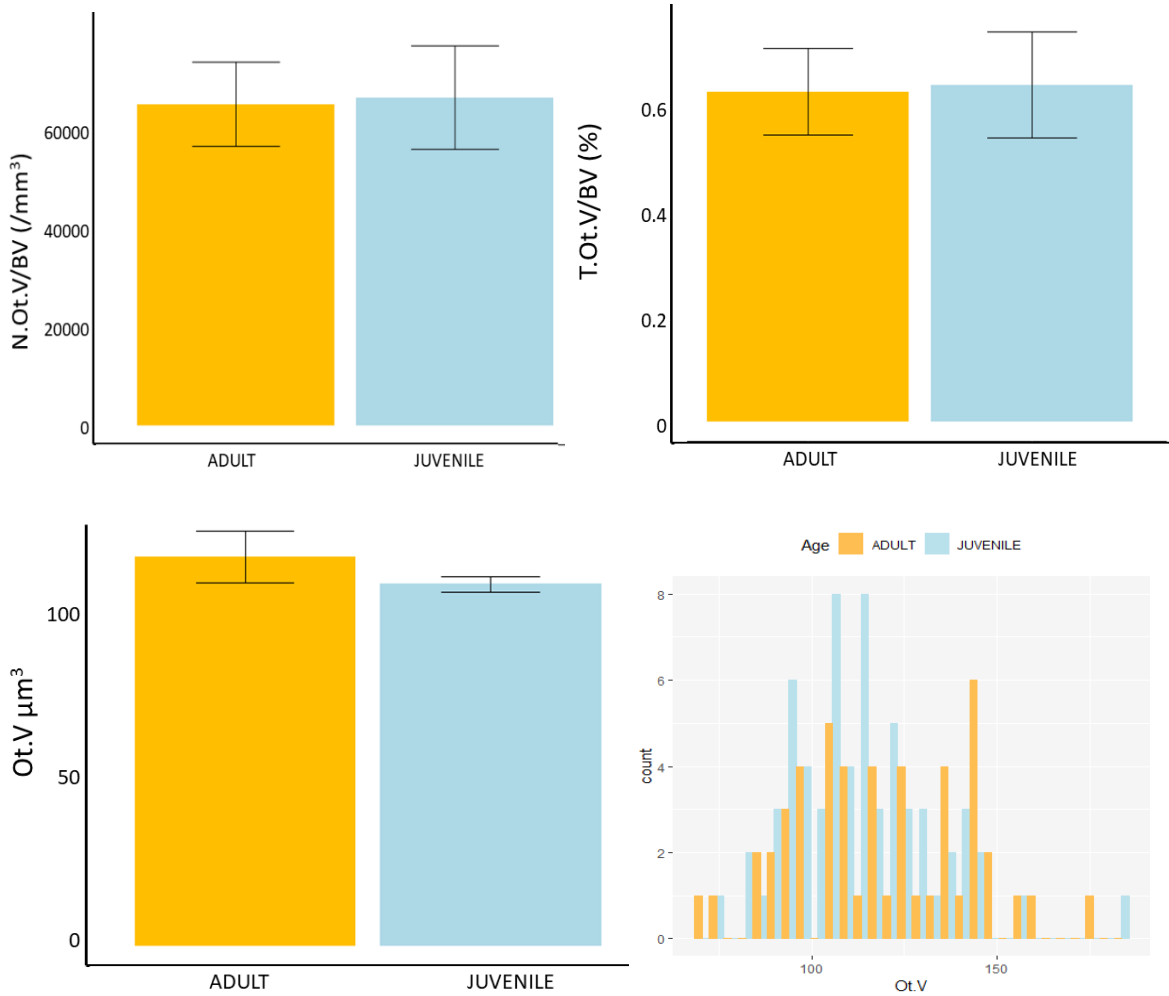
Figure 59   Effect of age on osteocyte measures

Mean osteocyte number density, porosity, osteocyte volume and distribution of osteocyte volumes in adult and juvenile murine tibia measured using SBF SEM imaging. No significant differences were observed. Values are mean ± SE, n=3 in each group.

5.3.2.2.2   Osteocyte measures

There are no significant differences in osteocyte cell measures (Figure 60).
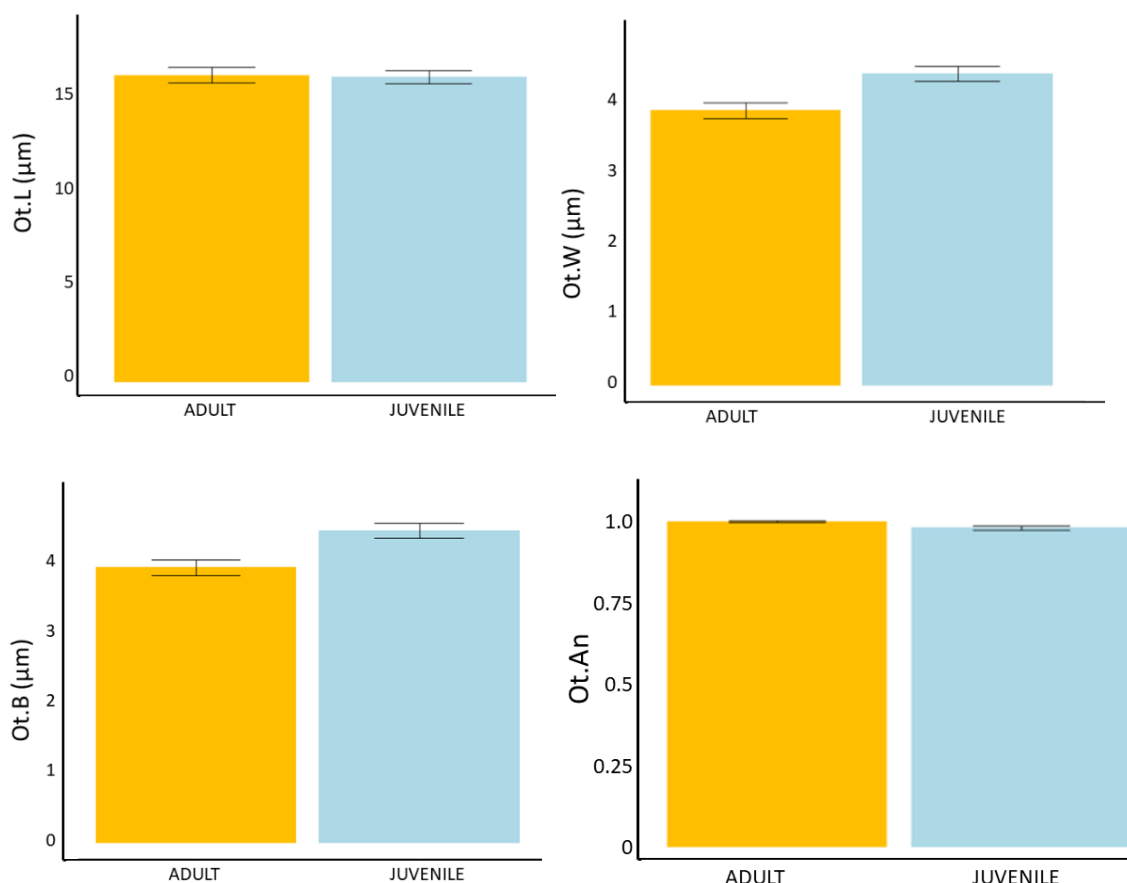
Figure 60   Effect of age on osteocyte measures

Mean osteocyte length, width, breadth and anisotropy in adult and juvenile tibia from murine bone tissue measured using SBF SEM. No significant differences were observed. Values are mean ± SE, n=3 in each group.

5.3.2.2.3   Pericellular space

On visual inspection of the SBFSEM data the pericellular space (PCS) around osteocytes appears larger in juvenile animals (Figure 61). <Lc.V> in adult animals is 131.69 ± 22.61 µm^3 and in juvenile animals is 144.95 ± 39.83 µm^3. Neither Ot.V nor Lc.V were significantly different, however PCS.V, PCS.Th and % Lc.V occupied by an osteocyte were significantly different (p<0.05). Mean PCS thickness (<PCS.Th>) was 0.41 ± 0.36 µm in adult animals and 0.89 ± 0.78 µm in juvenile animals (Figure 62). Mean max PCS.Wi is 1.44 ± 0.66 µm in adult animals and 2.04 ± 0.73 µm in juvenile animals (p = 0.000123).
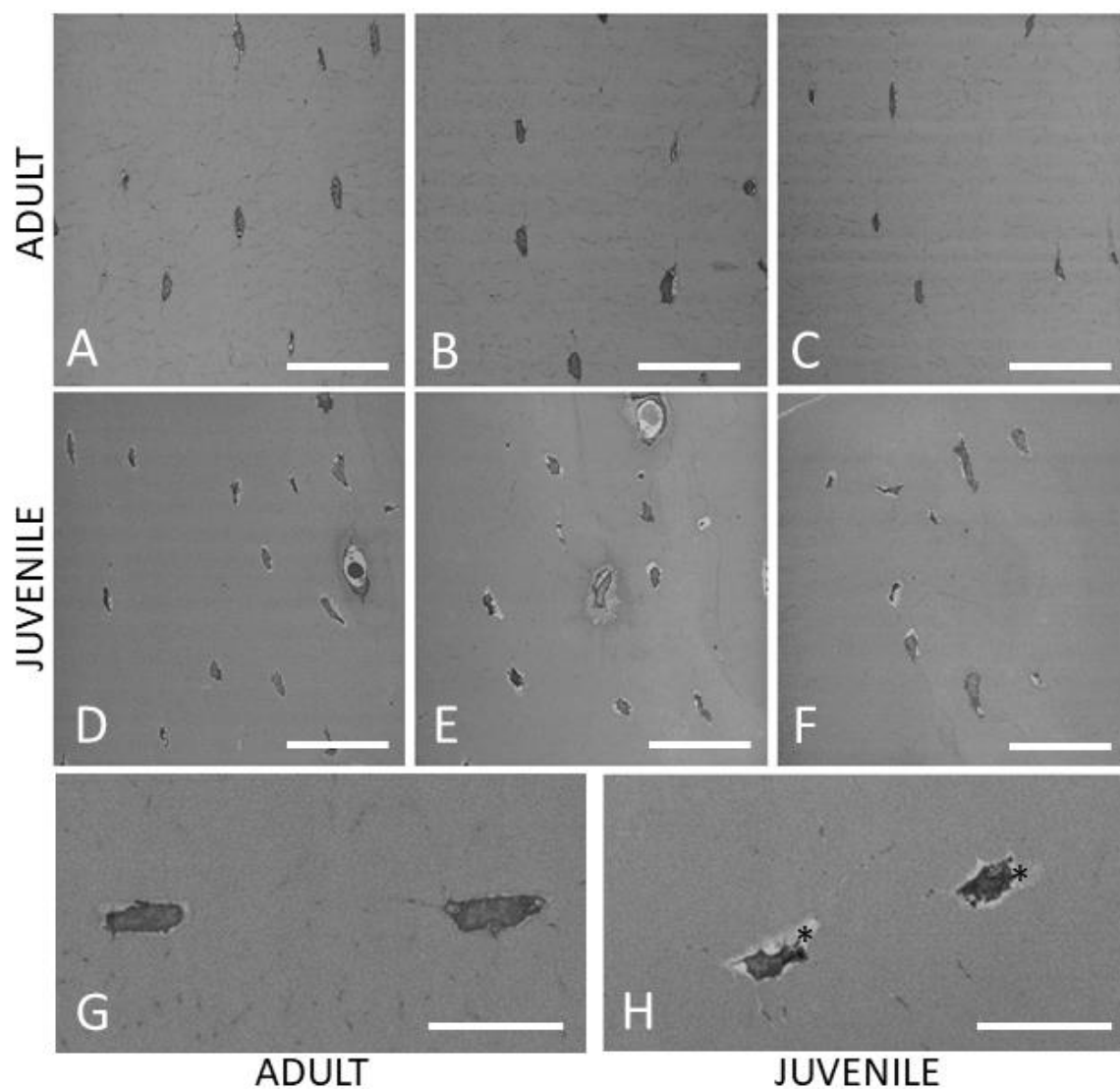
Figure 61   Slices from SBF SEM datasets showing enlarged PCS and occupied lacunae.

A-C   SBF SEM images of adult murine tibia. Scale bars = 20 μm

D-F   SBF SEM images of juvenile murine bone. Scale bars = 20 μm

G   Osteocytes in adult murine tibia. Scale bar = 10 μm

H   Osteocytes in juvenile murine tibia showing the visible pericellular space (*)

             surrounding the osteocytes. Scale bar = 10 μm
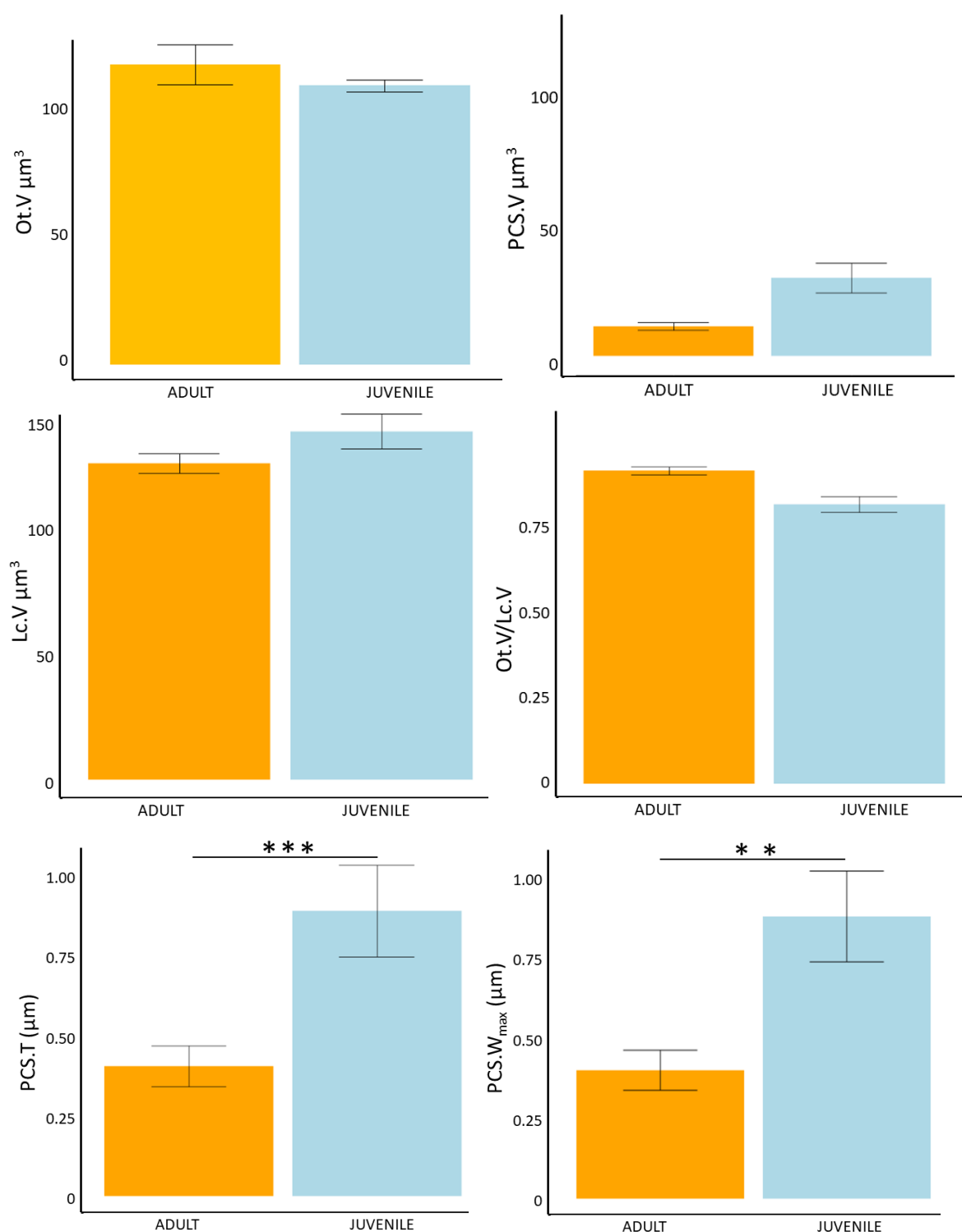
Figure 62   Effect of age on osteocyte, lacunar and pericellular space measures from murine bone tissue measured using SBF SEM.

Mean osteocyte volume, pericellular space volume and lacunar volume in adult and juvenile tibia. Values are mean ± SE, n=3 in each group. Mean proportion of lacuna occupied by osteocyte (Ot.V/Lc.V). Mean PCS.Th and mean maximum PCS.Wi in adult and juvenile animals. ** p<0.01, *** p<0.001

5.3.2.2.4   Osteocyte processes

The mean number of processes (<N.Pr>) per osteocyte in adult animals is 70 ± 22 and in

juvenile animals is 76 ± 17. The mean process diameter in adult osteocyes is 53 ± 28 µm

and in juvenile animals is 46 ± 22 µm (Figure 63).
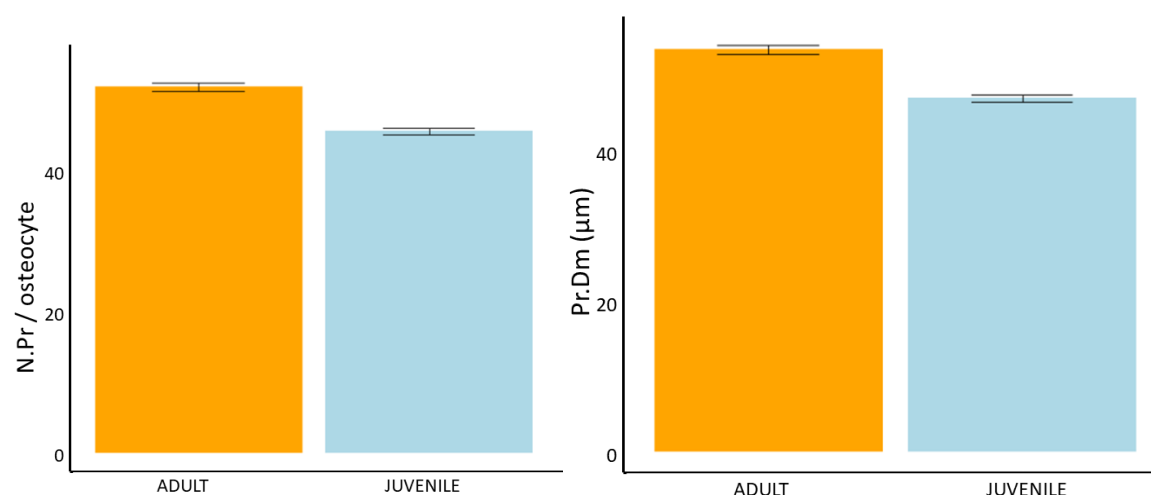
Figure 63   Effect of age on number of processes and process diameter from murine bone
tissue measured using SBF SEM.
Mean number of processes and process diameter per osteocyte in adult and juvenile tibia. Values
are mean ± SE, n=3 in each group.

5.3.3   Occupancy

There were no unoccupied lacunae observed in either adult and juvenile tibia during this

CXEM study (Figure 61).

5.3.4   Comparison of µCT and SBF SEM results

Comparison between µCT and SBF SEM derived distribution, porosity and osteocyte

volume showed good agreement between the two techniques. Osteocyte number density

is 57,700/mm^3 in adult animals and 76,700/mm^3 in juvenile animals using µCT and ranges

from 53,700 to 57,700/mm^3 in adult and 55,700 to 57,500/mm^3 in juvenile animals using

SBF SEM. Average osteocyte porosity measured using µCT is 0.98% in juvenile and 1.19% in

adult animals. Using SBFSEM the mean porosity is 0.64 - 1.2% in adult and 0.71 - 0.98% in juvenile animals. Mean osteocyte volume in adult animals is 168 μm^3 and 153 μm^3 in juvenile animals using μCT and ranged from 121-141 μm^3 in adult and 112-134 μm^3 in juvenile animals using SBF SEM.

5.4   Discussion

One of the objectives of this project was to quantify directly, at high spatial resolutions and in 3D, the detail of the ON in juvenile and adult mouse tibia using the CXEM workflows developed and outlined in Chapters 3 and 4. Bone tissue, which has been decalcified and stained with heavy metals, provides good image contrast for both μCT and SBF SEM. This allows collection of images and quantitative data on the ON, from a volume containing tens of thousands of cells. Subsequently, high-resolution 3D data on both the ON&LCN, from a targeted sub-volume containing a significant number of cells (47 – 119), was obtained. New measures for osteocyte cell processes and the pericellular space have been defined. This section discusses the implications of the tissue used, the CXEM method, the results obtained, the possible effects on future computational models, limitations of the study and finally the opportunities for future work.

5.4.1   Mouse model

As outlined in section 5.1.3, murine bone, unlike that of larger mammals including humans, does not have osteons and does not undergo intracortical remodelling. In the mouse, cortical bone is formed during growth and is subsequently unchanged whereas human bone is extensively remodelled over time (Jilka, 2013, Parfitt, 1994a). Many previous studies of bone have used mouse models and have shown that insight gained into structure can contribute to understanding of biological function and mechanical behaviour (Flurkey,

2007, Jilka, 2013). Mouse models reflect the characteristics and timing of age-related bone loss in humans, including loss of BMD (Almeida et al., 2007, Yuan et al., 2009) and exhibit age-related decrease in cortical thickness and increase in cortical porosity (Ferguson et al., 2003) which may be informative for the situation in aged humans (Jilka, 2013). Healthy murine bone is well characterised and the results from this study are consistent with existing data (see below), confirming that CXEM produces consistent results for osteocyte distribution measures. Adult and juvenile animals were compared and no significant differences in the measures set out in Table 16 and Table 18 were found. As discussed in section 5.2.1 and shown in Table 1, previous studies of bone development use a range of ages, species and anatomical areas so information is inconsistent. The data from this study will add to the knowledge of the ON&LCN during development of healthy murine tibia between 4-38 weeks of age.

5.4.2   Assessment of CXEM

CXEM (i) exploits the advantages of µCT (large volume, 3D, non-destructive) and SBF SEM (high resolution, 3D, concurrent ON&LCN imaging), (ii) yields data across different length scales, (iii) sets the SBF SEM data in a larger context and (iv) facilitates choice of the sub-volume of interest by providing prior knowledge of 3D microstructure. CXEM facilitates imaging of both the ON and the LCN rather than the LCN alone, which has often been used as a proxy for the cell network (Vatsa et al., 2008, van Hove et al., 2009). 3D microstructural detail unobtainable by other imaging techniques such as PCS and cell process measures can be retrieved. CXEM also allows determination of lacunar occupancy, which is found to be high in healthy tissue (Núñez et al., 2018), but changes in which may be an interesting factor in ageing and in pathological conditions (Power et al., 2001) reflecting occurrence of osteocyte cell death, which is implicated in bone disease (Ru and Wang, 2020). The minimal

embedding technique used in this study (Schieber et al., 2017) was developed for FIB SEM imaging but is equally appropriate for SBF SEM and CXEM.

5.4.3   Anatomical area

The TFJ was selected as the region of interest in this study as it contains only cortical bone, provides a clear landmark allowing for consistent and reproducible imaging, while the size facilitates µCT imaging of the entire cross-section in a single field of view. Other researchers have studied the TFJ and comparable data for lacunar number density (but not osteocyte number density) exist. Values reported for lacunar density at the murine TFJ include 62,000 – 64,000 /mm^3 (15-week to 10-month-old) (Núñez et al., 2018); 64,000 (16-week-old) (Goring et al., 2019); and 45,000 - 63,000 (12-week-old) (Mosey et al., 2017). In the present study, the osteocyte number density (N.Ot/BV) ranges from 53,700 to 76,700 /mm^3, which compares well with previous results. As results for the ON in this study are consistent with those obtained for the LCN in previous research, high levels of lacunar occupancy in the murine samples can be assumed. This was confirmed by correlative SBF SEM imaging where no empty lacunae were observed (Figure 61).

The tibia adapts to mechanical loading. The mechanical strain environment of the tibia arises primarily due to bending. Inhomogeneity of strain has been demonstrated using FE modelling of axial compression of the tibia, although different peak strain locations have been reported. Studies have shown that peak compressive and tensile strains are experienced in the lateral and medial regions (Torcasio et al., 2012), posterior and anterior regions (Prasad et al., 2010), postero-lateral and antero-medial regions (Patel et al., 2014) and medial and lateral regions (Núñez et al., 2018) (Figure 64).
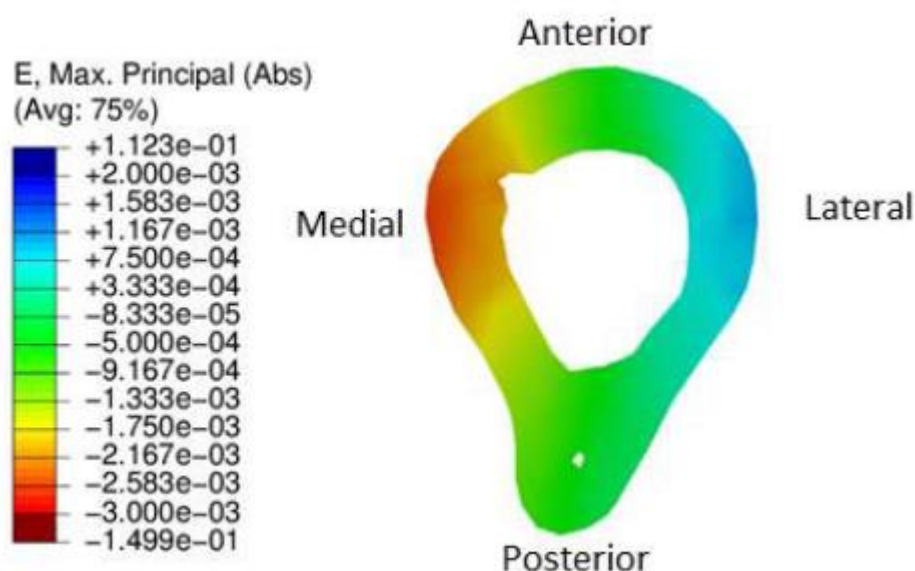
Figure 64   FE modelling of mechanical strain in mouse tibia

FE modelling results in 15 week old mouse tibia showing inhomogeneity of mechanical strain. Peak compressive strain is in the medial region and peak tensile strain in the lateral region. The anterior and posterior regions have lower compressive strain levels. (Núñez et al., 2018)

In the present study, osteocyte number density, porosity and volume in the posterior, anterior, lateral and medial volumes were compared in adult and juvenile animals to determine whether the differences which have been observed in mechanical strain in regions of the tibia are reflected in the structural properties of the ON. As the ON is mechanosensitive, changes in the structure may be related to the strain experienced in the region. No significant differences were found in ON measures between regions in this study, confirming previous results (Núñez et al., 2018). A study of rat bone investigated regional diversity from the endosteum, through the intra-cortical region to the periosteum (Tommasini et al., 2012). Future analysis of CXEM data, including the data produced in this study, in this way may be useful to investigate differences in cells and tissue formed at different times.

In summary, there are no significant differences in the ON measures analysed in the posterior, anterior, medial and lateral quadrants of the murine tibia and there are no

differences between the same measures in juvenile and adult bone tissue. It has been established that there are differences in the vascular network in regions of the tibia (Núñez et al., 2018). However, the inhomogeneous nature of compressive and tensile strain distribution are not reflected in the structure of the ON in the murine tibia.

5.4.4 **Discussion of results**

The results obtained in this study for osteocyte number density and porosity are comparable to the values obtained by other researchers for the respective lacunar measures produced using µCT and SR CT (Tiede-Lewis et al., 2017, Schneider et al., 2007, Tommasini et al., 2012, Hemmatian et al., 2017b). This, along with the observation from SBF SEM that lacunar occupancy in murine tibia bone tissue is high, confirms that LCN measures of healthy murine tissue reflect well the ON residing within it and adds confidence and validity to the use of LCN measures as a proxy for the ON in healthy murine tissue.

As discussed in section 2.5, in both human and murine bone, after an initial increase, osteocyte and lacunar number densities decrease with age (Bortel et al., 2015, Zimmermann et al., 2019). The animals studied (4-week-old and 38-week-old) represent juvenile and adult stages of development (Figure 47) (Dutta and Sengupta, 2016), and show neither the increase in osteocyte number density associated with early growth nor the decrease in osteocyte number density associated with ageing. The results of the present study suggest that osteocyte number density and porosity remain stable during this period.

There was no significant difference in <Ot.V> observed between adult and juvenile animals in this study. However, there was a decrease in the measured value of <Ot.V> as the voxel size of the imaging technique decreased (i.e., for higher spatial resolutions). <Ot.V> derived from µCT data acquired at 1.5 μm^3 voxel size was 163 ± 95 μm^3, using SBF SEM at 20 × 20

$\times$ 50 nm^3 voxel size was 136 ± 35 µm^3 and using SBF SEM at 10 $\times$ 10 $\times$ 50 nm^3 voxel size was

116 ± 22 µm^3. Studies of bone architecture using different voxel sizes have previously

illustrated the effects of resolution on structural parameters (Peyrin et al., 1998, Ritman,

2011, Jorgensen et al., 2008). A recent study carried out on idealised test data representing

lacunae found that volume measurements are sensitive to voxel size, with smaller voxel

sizes producing results closer to the ground truth (volume of idealised data) (Williams et

al., 2020). This is because a small number of large voxels represents an object less

accurately and the decrease in accuracy due to partial volume effects leads to errors in

thresholding and segmentation (Williams et al., 2020). This illustrates the value of using

SBF SEM when high-resolution 3D measures are required to address research questions,

such as understanding mechanobiology in the ON&LCN. It is important to note at the same

time that if data from large volumes or numbers of cells is required the high spatial

resolution and reduced volume imaged by SBF SEM may be a detriment.

The results obtained in this study for osteocyte dimensions (Ot.Le, Ot.Wi, Ot.Br and Ot.V)

compare well to osteocyte measures obtained by ssTEM (Palumbo, 1986) and CLSM

(Sharma et al., 2012, Sugawara et al., 2005, Vatsa et al., 2008) and lacunar measures

obtained using SR CT (Hannah et al., 2010) and AFM (Lin and Xu, 2011). There is extra value

in CXEM over µCT or SR CT because simultaneous 3D imaging of the ON and LCN produces

data unobtainable by µCT or SR CT such as volume and dimensions of the PCS. It is crucial

to quantify the spatial relationship between the cellular ON and the mineralised LCN in 3D

as changes in this relationship will affect interstitial fluid flow and direct matrix-cell

deformation, both proposed mechanisms for strain amplification in bone (Section 2.9.1).

The PCS volume data produced by SBF SEM in this study are unique and can play a valuable

role in understanding osteocyte mechanosensation. (Discussed later).

2D SEM studies found that infantile human bone has larger osteocyte lacunae than more developed bone (Jandl et al., 2020, Zimmermann et al., 2019). It is unclear from these studies whether this is reflective of an enlarged PCS or larger cells within the lacunae, or both. SBF SEM in the present work found that juvenile animals have a larger PCS than adults, suggesting that an increased PCS volume contributes to the lacunar enlargement. Larger PCS in infantile bone may be associated with less mineralised and less organised perilacunar bone (Nicolella et al., 2008), however, as bone tissue is decalcified in this study it is not possible to determine changes in bone matrix mineralisation.

A notable finding of this study is that PCS.V is smaller than has been previously determined. SBF SEM in the present study found that the mean lacunar volume occupied by an osteocyte is 87 ± 11%. A mathematical study which used TEM determined values for PCS.Wi (0.6 µm) (McNamara et al., 2009, Kerschnitzki et al., 2013) and SR CT derived values for lacunar surface area (336.2 µm^2) (Dong et al., 2014a) determined that the mean lacunar volume occupied by an osteocyte is 50% (Buenzli and Sims, 2015). If these calculations used the directly measured percentage occupancy data from CXEM, the total volume of fluid within the network calculated using the same equations would be reduced to a quarter of the estimated value (Table 21). Indeed this paper mentions the need for experimental studies such as the current study which can measure and compare Lc.V, Ot.V and PCS.V.

Table 21   Overestimation of the volume of extracellular fluid in human bone.

Column A shows calculations using the occupancy data in (Buenzli and Sims, 2015). Column B using the % occupancy determined by the current CXEM study.

Values and equations	A	B
<% Lc.V occupied by osteocyte> <Ot.V/Lc.V x 100>	50%	87%
Total volume of extracellular fluid in ON&LCN Lc.Ar $\times g \times$ Tt.N.Lc + π(Ca.Rd^2 – Pr.Rd^2)$\times$Tt.Pr.Le	24,207 mm^3	6,294 mm^3

Lc.Ar = lacunar surface area, g = gap, Tt.N.Lc = total number lacunae, Ca.Rd = canalicular radius, Pr.Rd = process radius, Tt.Pr.Le = total process length

The implications of changes in PCS.V and associated fluid volumes can be explored using the Hagen-Poiseuille formula, which describes the relationships between pressure, viscosity and flow rate. In a moving flow regime the point of greatest resistance is the point of maximum shear stress, which in the osteocyte would be the point of maximum mechanosensation. Making several simplifying assumptions: a uniform rigid hollow cylinder, Newtonian fluid behaviour, non-pulsatile flow and the presence of Poiseuille flow, the formula is used to calculate applied wall shear stress (WSS). The magnitude of WSS is proportional to the velocity gradient near the tube wall, thus low WSS values are associated with low local velocities and, thus, long residence times of fluid in the near-wall region.

Hagen-Poiseuille Formula $WSS = 4\mu Q / \pi R^3$

Where μ = dynamic fluid viscosity, Q = volumetric flow rate and R = cylinder radius (PCS.Wi/2). WSS is inversely proportional to the 'radius' (PCS.Wi/2) of the PCS and directly proportional to the flow rate. Thus, variation in PCS.Wi has substantial effects on the magnitude of shear stress at the osteocyte cell membrane. However, in a non-uniform

shape such as the osteocyte PCS, the situation is more complicated, shear stress is not simply inversely proportional to volume and large inhomogenous variations in shear stress are predicted.

In FE and FSI studies of idealised and realistic models, the simulated PCS is always of uniform width around the cell and values range from 0.05 to 0.75 μm (Verbruggen et al., 2016, Verbruggen et al., 2012, Vaughan et al., 2013, Vaughan et al., 2014, Wang et al., 2018, You et al., 2001). These values are determined from TEM images (You et al., 2004, McNamara et al., 2009), which as discussed in Chapter 2, provide 2D data from a small area of tissue. It is interesting to note from the SBF SEM results in the present study that PCS width varies considerably due to irregularities in both the cell shape and the lacunar wall from 0 μm where the cell is in contact with the lacunar wall to a maximum width of 4.45 μm. The inclusion of ECM projections in idealised osteocyte model resulted in an increase of 152% in shear stress stimulus to the cell (Verbruggen et al., 2014), so including realistic variations in minimum and maximum PCS.Wi would similarly increase shear stress predictions. Permeability scales with the porosity, PCS.Wi and the number of canaliculi (Fritton and Weinbaum, 2009) and this would also be affected by changing PCS values.

Studies have shown that maximum principal strains in realistic models are higher than in idealised models of the cell, lacuna and PCS (Verbruggen et al., 2012) and that progressive idealisation causes underestimation of flow magnitude and maximal shear stress and eliminates spikes in shear stress along the cell surface (Anderson and Knothe Tate, 2008). SBF SEM overcomes the experimental challenges mentioned in (Verbruggen et al., 2012) and obtains the precise size of the PCS gap, the use of which in future studies may serve to determine the significance of the PCM and projections of both cell and matrix in mechanical stimulation. According to the realistic cell and lacunar results, PCS is narrower in certain

regions and at these focal locations strain transfer to the osteocytes would be increased, as demonstrated by the increased levels of strain around idealised matrix projections (Verbruggen et al., 2012).

A recent study also highlights that changes in microstructural detail of the PCS affect mechanobiology (Lai et al., 2021). That study using idealised osteocyte and lacunar shapes showed that variations in lacunar dimensions during lactation affect behaviour of fluid flow and osteocyte sensation. Lacunar porosity and PCM density are major determinants of fluid flow in bone. Using 3D CXEM data in studies such as this would allow interrogation of the effects of ultrastructural changes in PCS dimensions.

In summary, quantitative hallmarks of bone tissue at the cell level in developing healthy murine tibia have been derived during this investigation. µCT imaging of decalcified and stained tissue produces osteocyte density and porosity data reflective of the data produced from analysis of lacunae in calcified bone tissue. Osteocyte number density, osteocyte porosity and osteocyte cell measures in juvenile and adult animals have been compared. No significant differences in osteocyte density and porosity were found between the anterior, posterior, medial and lateral regions of the tibia. No major significant differences in the ON&LCN measures were found between juvenile and adult animals in this study indicating that the period studied is not a time of microstructural change in tibial bone in male mice. Novel findings include the first 3D measurement of PCS dimensions and the number of osteocyte processes per cell determined over a number of cells by direct measurement. These geometries may contribute to the design of computational models for bone mechanobiology.

Chapter 6 CXEM study of osteoporosis and osteoarthritis in human bone tissue

6.1 Introduction and review

The optimised CXEM sample preparation, imaging, image processing and quantification techniques outlined in Chapters 3 and 4 are in this chapter applied to femoral head tissue from OP and osteoarthritic OA patients. Qualitative and quantitative results are compared to describe the ON&LCN in OP and OA and to discover features of disease which are relevant for changes in bone mechanobiology.

In this introductory section, the epidemiology of OP and OA are briefly recapped, their comorbidity discussed. A CXEM study of the ON&LCN in OP and OA in human femoral head tissue is presented.

6.1.1 Osteoporosis and osteoarthritis

Musculoskeletal disease is a major health burden both in the UK (Versus-Arthritis, 2019) and worldwide (WHO, 2019). Musculoskeletal conditions account for the third largest area of UK National Health Service (NHS) programme spending at £4.7 billion (Leal et al., 2016). OP and OA are two of the most common conditions implicated in the economic burden of musculoskeletal disease (WHO, 2019). Thus, there is an urgent need to understand more completely the processes underlying these bone pathologies.

6.1.2 Changes in bone with OP and OA

In Table 3 and Table 4 the changes observed in the ON&LCN of bone tissue during OP and OA are summarised. It is notable that no comprehensive 3D studies of the ON&LCN in OP bone have been carried out to date. Some of the changes in OP are similar to those

observed in ageing, namely a decrease in osteocyte and lacunar number densities and a decrease in connectivity. Lacunar occupancy decreases with age in human bone tissue, is found to decrease or remain unchanged in OP and has not been investigated in human OA tissue. Ageing is accompanied by both an increase in the number of empty lacunae and a change in lacunar shape, neither of which are observed in OP bone tissue. In OA, connectivity between osteocytes is also decreased (Knothe Tate et al., 2004) (Mazur et al., 2019) and apoptosis is increased in both OA and OP (Wong et al., 1987, Tomkinson et al., 1997). Any or all of these changes could affect signals perceived by osteocytes from strain or fluid flow which eventually trigger osteocyte biochemical outputs.

In summary, while differences in bone structure on the organ level in OA and OP have been shown, much evidence of the changes in the ON&LCN at cellular level in OA and OP is contradictory or missing (See Table 3 and Table 4). The CXEM study described in this chapter will attempt to increase the knowledge of the 3D structure of the ON&LCN in OA and OP.

6.1.3   **Comorbidity**

An inverse relationship between OA and OP had been accepted based on observations that fractured femoral heads showed a general absence of OA and that hip and spine fractures were rare in OA cases (Hart et al., 1994, Dequeker, 1999). It is suggested that alteration in bone tissue during OA, notably the increase in subchondral bone stiffness, predisposes individuals to cartilage loss but protects against OP (Dequeker et al., 2003). An SEM and TEM study of OA and OP bone supported this theory, finding significant differences in bone, collagen fibres, lacunae and osteoblasts (Shen et al., 2009). Interestingly, no osteocytes were seen in that study. Studies have shown that patients with OP suffer a deterioration in

trabecular bone architecture not seen in patients with OA (Blain et al., 2008, Boutroy et al., 2011, Tamimi et al., 2020, Zhang et al., 2010).

Studies of the sequence of changes occurring in the development of OA, however, suggest that the concept of an inverse relationship may be an overly simplistic approach (Baker-LePain and Lane, 2012, Hayami et al., 2004). Clinical experience shows that OP and OA may coexist (Rizou et al., 2018) and a cross-sectional analysis found that 20% of OP patients also suffered from OA (Puth et al., 2018). Osteoporotic OA (OP-OA) has been proposed as a defined phenotype of OA characterised by a significant decrease in subchondral bone density accompanied by other features (Bellido et al., 2010, Herrero-Beaumont and Roman-Blas, 2013). A review of the literature concluded that OA and OP are inversely related when studied cross-sectionally and systematically, however longitudinal studies report a more complex and circumstantial relationship, with individual variation (Im and Kim, 2014).

Risk factors for OA and OP and their relationships are illustrated in Figure 65. Several factors including age, sex and genetics contribute to the pathogenesis of both disorders. Inflammation and 'unfavourable body composition' are contributing factors to both – with low weight a risk for OP and obesity a risk for OA. Obesity contributes to mechanical overloading of joints, leading to the development of OA while reduction in loading through immobility is a factor in OP development (Bultink and Lems, 2013). As the osteocyte is a multifunctional cell that plays a key role in maintenance of bone mass through regulation of both osteoblast and osteoclast activity, it is likely to be a therapeutic target for the treatment of both OA and OP.

Ideally, the comparisons in this study would be between diseased and age- and sex-matched healthy human tissue. Cadaveric control material has been used in bone studies

(Jenkins et al., 2017), however preservation of cells is compromised by freezing and by delay in fixation. There are precedents for using OA and OP tissues in studies without healthy control tissue (Cınar et al., 2016, Zhang et al., 2009, Shen et al., 2009). In the current study, as fresh healthy human bone tissue is not available, bone samples from OP and OA patients are compared to each other. It is recognised that this is not a 'gold standard' comparison however, pragmatically, it is considered a reasonable compromise and results will be interpreted carefully considering the knowledge of co-morbidity outlined above.
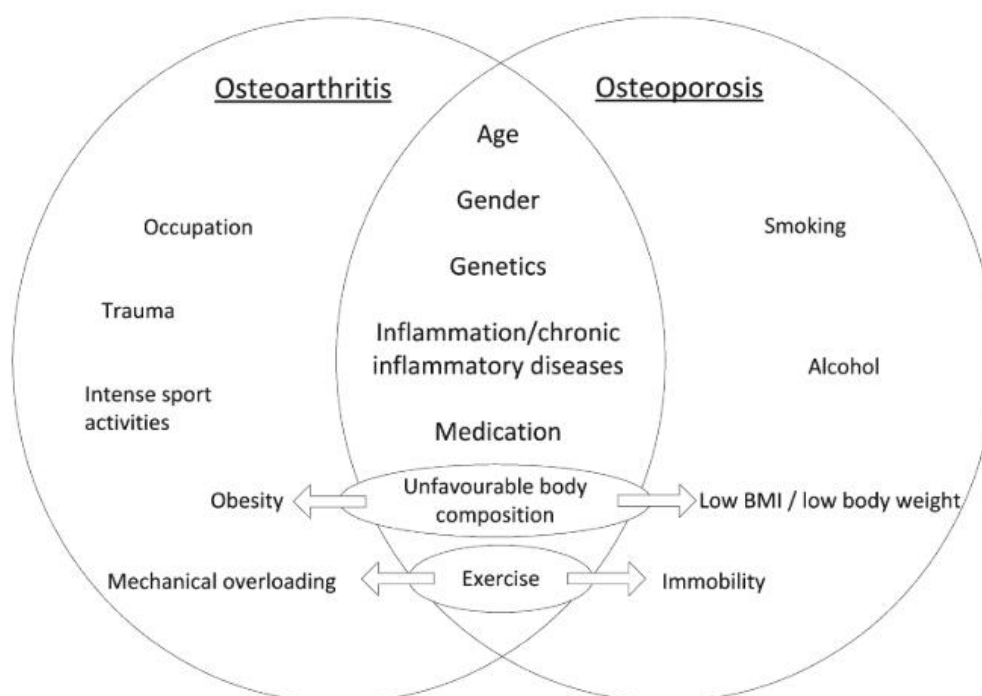
Figure 65   Risk factors for the osteoarthritis and osteoporosis.
              BMI - body mass index. From (Bultink and Lems, 2013).

6.1.4   **Summary**

Changes occur in bone microstructure in OA and OP (Section 2.6.2). CXEM can contribute to elucidating and understanding these changes by providing images and quantitative data on both osteocyte and lacunar measures, lacunar occupancy and degrees of cell health. Thus the remaining sections of the chapter present a study of OA and OP human femoral

head bone studied by CXEM with the intention of deriving quantitative hallmarks of both diseases.

6.2   Introduction to CXEM study

There is a dearth of comprehensive 3D imaging studies of changes in OP and OA at a cellular level. Also missing from previous studies are lacunar occupancy data, information about cell health and cell death, and a more detailed understanding of relationships between the osteocytes, lacunae and pericellular space. As the ON&LCN is involved with bone health and disease (Chapter 2), a fuller understanding of structure in diseased tissue will inform modelling approaches to bone mechanobiology and future therapeutic targets. CXEM can contribute by producing quantitative data on the ON&LCN and on lacunar occupancy. CXEM has the advantages of discovering the ultrastructural phenotype of cells, shedding light on cell health and thus the ability of the ON to function effectively.

In this chapter, CXEM is applied to femoral head tissue from human donors with osteoporosis (OP) and osteoarthritis (OA). This study aims to:

- Produce quantitative data on the 3D structure of the ON&LCN in OP and OA bone. The data will include osteocyte number density, porosity, volume, shape, lacunar occupancy, number of processes, process diameter and PCS volume.

- Identify differences if any, in the ON&LCN microstructure and ultrastructure in OP and OA human femoral head tissue. The results will shine a light on the mechanisms of mechanobiology and how they are affected during these conditions.

- Provide quantitative data which will enable improved computational modelling of mechanobiological processes in human bone diseases.

6.3   Materials and Methods

This section outlines the collection and sample preparation methods used to fix, stain and resin embed human femoral head tissue for CXEM. The imaging and quantification steps used to derive hallmark data on the ON&LCN are described. Fully detailed descriptions of the methods are included in Appendix A, Appendix B and (Goggin et al., 2020).

6.3.1   Sample collection

Collection of bone tissue was approved under the Southampton and South West Hampshire Local Research Ethics Committee (LREC 194/99). Human femoral head samples were collected from female OP (n=3, ages = 76, 51, 67 years) and OA (n=3, ages = 92, 95, 95 years) patients (Figure 66). OP samples were collected from patients undergoing hip arthroplasty at University Hospital Southampton NHS Foundation Trust. The indication for surgery in this group was intracapsular fracture of the femoral neck following a low trauma fall. This assumes that individuals suffering a fragility fracture of the femoral neck must be osteoporotic, however this does not incorporate fall risk or other factors related to fragility fractures. Patients in the OA group (collected from the Spire Hospital, Southampton) were undergoing elective total hip replacement (THR) for OA of the femoral head. Samples were collected and immersed in fixative (3% glutaraldehyde (GA), 4% formaldehyde (FA) in 0.1 M PIPES buffer) immediately after surgery.

6.3.2   Sample Preparation

Sub-volumes of bone with at least one dimension measuring less than 2 mm from the proximal surface of the femoral head were dissected while immersed in fixative (Figure 67). The sub-volumes were stored overnight in fixative at 4°C. Sample preparation for CXEM

including decalcification, staining and minimal resin embedding was carried out following

the protocol set out in Appendix A.
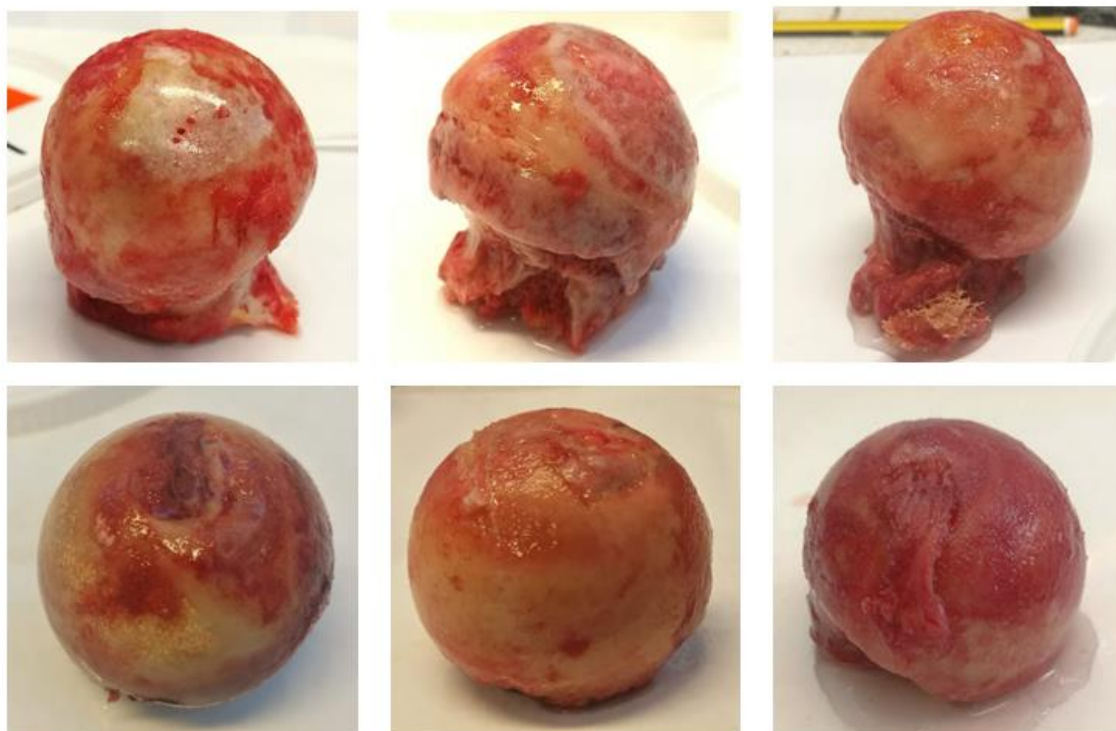
Figure 66   Femoral head samples collected after hip arthroplasty.

Top - OA samples, Bottom - OP samples
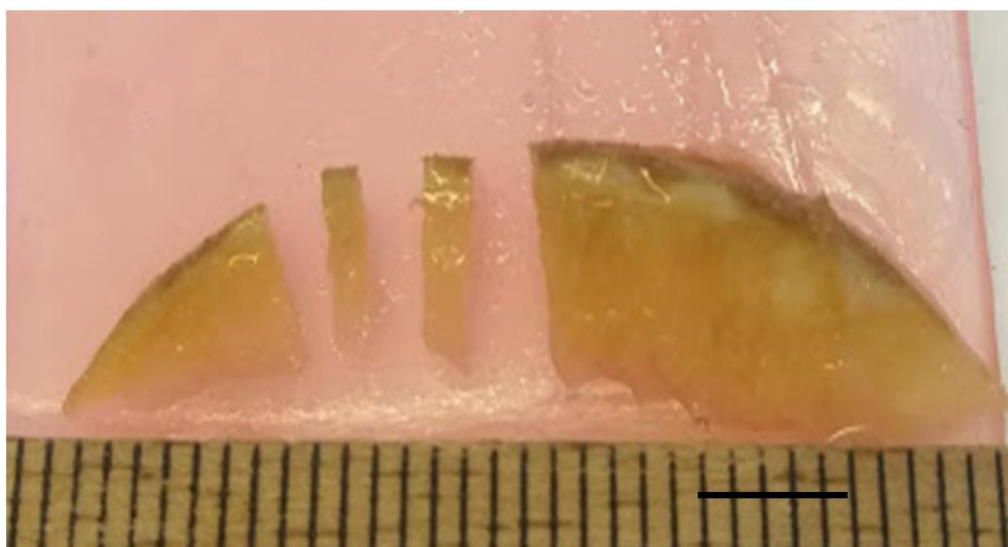
Figure 67   Dissection of fixed femoral head tissue

 Wedges of fixed bone tissue removed from the femoral head and cut into blocks (centre) for

further processing.

6.3.3   **µCT**

The first step of CXEM is µCT imaging of the entire stained tissue block. This produces images of the bone sample and quantitative data on the distribution, size and shape of osteocytes. µCT imaging facilitates choice of a sub-volume for subsequent SBF SEM imaging. µCT image acquisition, image processing and image analysis are described in this section.

Bone tissue blocks fixed, decalcified, stained and minimally embedded as described in Appendix A were mounted in a plastic straw and imaged by µCT using a Zeiss/Xradia Versa 510 scanner (Figure 68), which uses an 160 kVp source and a 2048 x 2048 pixel flat panel detector. Imaging settings were as follows: peak voltage 110 kVp, power 9.5 W, binning x 2, 1024 x 1024 pixel detector, x 4 objective lens, filter 0.34 mm of SiO_2, exposure time 5 s and sampling 4501 projections. Source-to-detector and source-to-object distances were set to 64.81 mm and -18.66 mm respectively, which along with the selected 4x objective resulted in a radiograph pixel size of 1.5 µm x 1.5 µm and a field of view of 1.5 mm x 1.5 mm.

The raw data (X-ray projections) were reconstructed using a standard filtered back projection (Zeiss reconstruction software), and an isotropic voxel with an edge size of 1.5 µm. The reconstructed data were exported as 16-bit tiff stacks for visualisation and analysis. Images from µCT scanning were reviewed by a consultant pathologist and rejected if they showed evidence of being a fracture site or other pathological features. For example, a sample which showed fibrous connective tissue reactive changes (Figure 69) was not used in this study. Data is available from DOI: 10.5258/SOTON/D2118
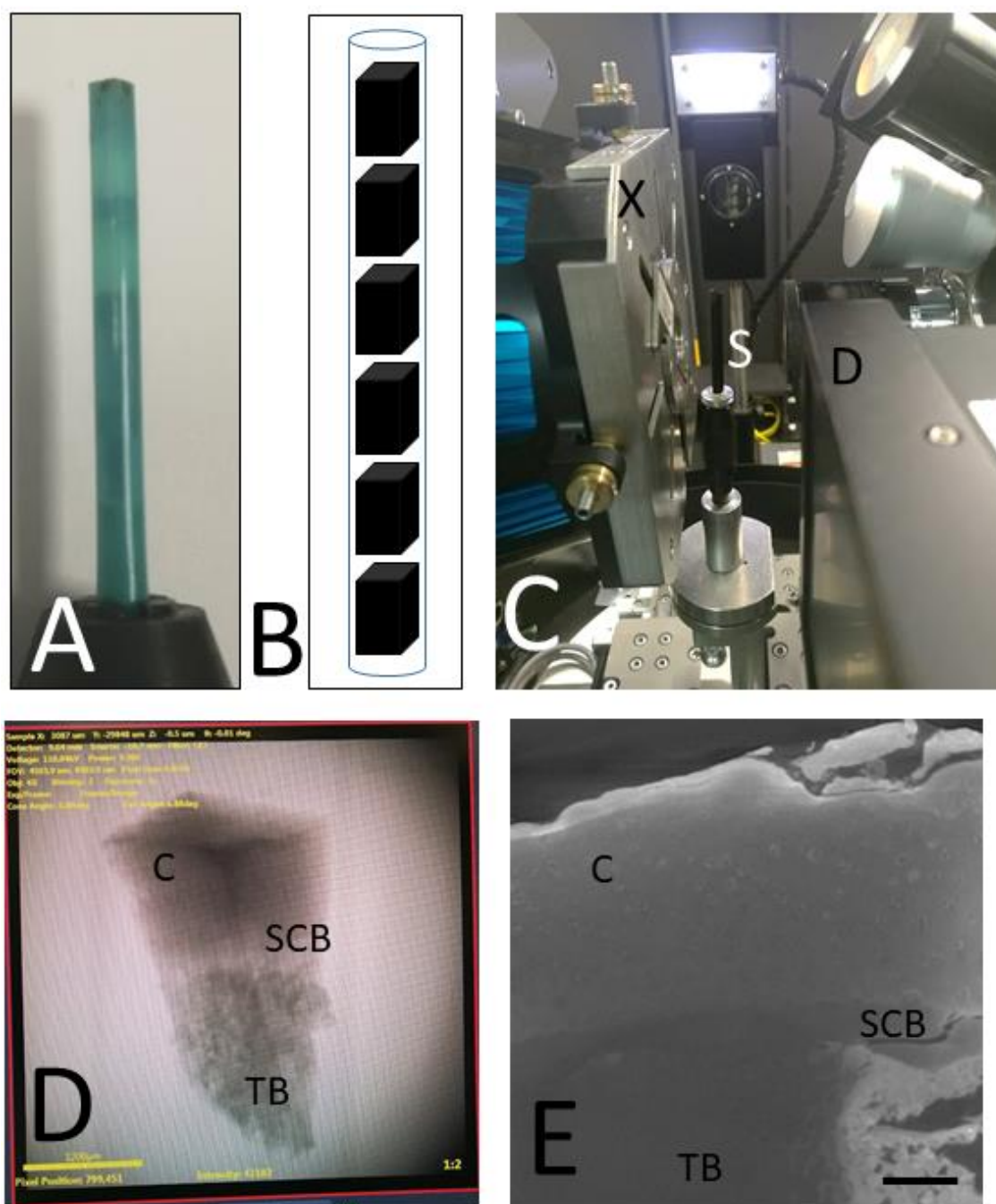
Figure 68   X-ray µCT imaging

A   Plastic tube containing samples for imaging.

B   Diagram showing the arrangement of samples inside the tube.

C   Tube mounted in Versa µCT scanner showing samples mounted in tube (S), detector (D) and X-ray source (X).

D   Radiograph showing the bone sample within the tube. C= cartilage, SCB = subchondral bone, TB = trabecular bone. Scale bar = 1200 µm

E   Image from scan showing cartilage (C), subchondral bone (SCB) and trabecular bone (TB). Scale bar = 400 µm
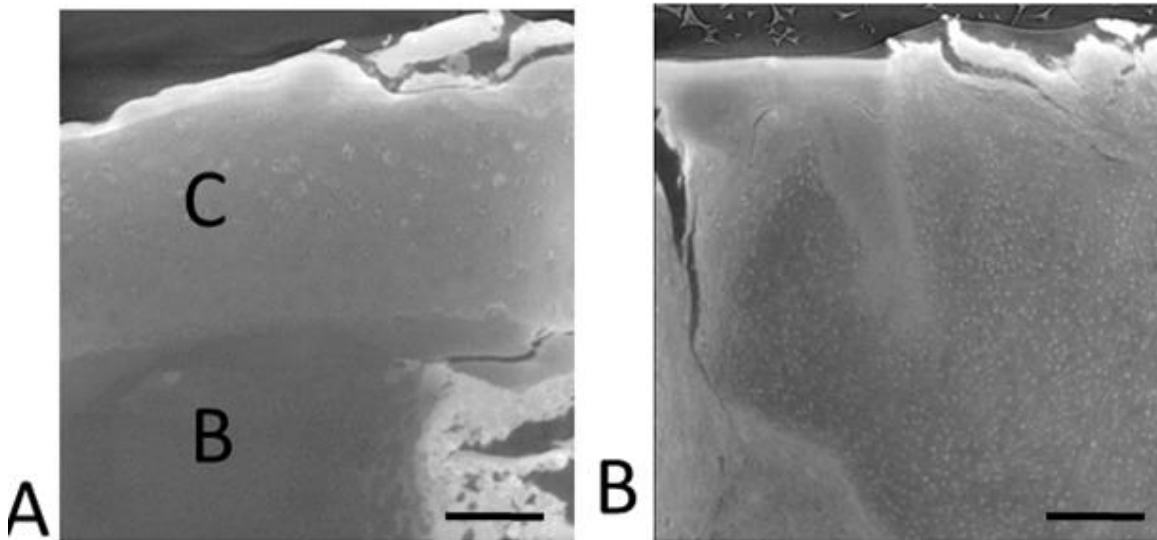
Figure 69   Selection of samples for inclusion in project

A   μCT image of a suitable bone tissue sample showing cartilage (C) and bone (B) layers.

B   μCT image of an unsuitable bone tissue sample showing fibrous connective tissue

               reactive changes. Scale bar = 300 μm

6.3.4   Image processing and analysis

Image processing of the μCT data was carried out using Avizo (version2019.4)

(ThermoFisher Scientific), and Fiji (Schindelin et al., 2012) as outlined in Appendix B.1.

Briefly, bone tissue was segmented, heavy metal stained elements comprising the

osteocytes and the vascular tissue were extracted, separated using a volume filter and the

osteocytes quantified as outlined in Appendix B.3.

6.3.5   SBFSEM

A single osteon was chosen from each tissue block as the volume of interest for SBF SEM

imaging. The sub-volume was prepared, imaged and analysed as described in A.4.6.

6.3.6   SBF SEM imaging

In each bone sample a frustum with face approximately 500 μm^2 centred on an osteon was

created by trimming the resin block. This sub-volume of interest was removed from the

block and mounted on an aluminium pin using conductive glue (Figure 38). Imaging was

carried out using a 3ViewXP2 system (Gatan Inc., Abingdon, UK) in a Quanta 250 FEGSEM

(ThermoFisher, Netherlands) as described in Appendix A.4.6 and set out in (Table 22).

Toluidine blue sections taken from the block at intervals were used to assist in area

selection and determining location within the block by comparison with the μCT images.

Data is available from DOI: 10.5258/SOTON/D2118

Table 22   Settings used for SBF SEM

Parameter	Value
kV	3 kV
Spot	3
Slice thickness	50 nm
Dwell time	4 μs
Vacuum	45 Pa
Number of pixels in x-y	8192 – 9000
Pixel size	20 nm
Number of slices	1101 - 1448

6.3.7   **Image processing and quantification**

The osteocyte cell bodies, processes and the PCS were segmented, visualised and

quantified using ImageJ (Schneider et al., 2012a), the Fiji plug-in Trainable Weka

Segmentation 3D (Arganda-Carreras et al., 2017) and Avizo (ThermoFisher) as described in

Appendix B.2. Weka segmentation is based on image features and as the cell contents and

condition vary so much in the human samples the Weka segmentation tool was less reliable

and some manual segmentation was performed to refine the results.

Table 23   Dimensions and volumes of tissue blocks imaged by SBF SEM

Patient	Condition	Number of pixels x	Number of pixels y	Pixel size (nm)	Number of slices z	Slice thickness (nm)	Volume (mm³)
F76	OA	8192	8192	20	1356	50	0.910
F51	OA	8192	8192	20	1416	50	0.950
F67	OA	8192	8192	20	1101	50	0.739
F92	OP	9000	9000	20	1448	50	1.173
F95A	OP	8192	8192	20	1218	50	0.817
F95B	OP	8192	8192	20	1107	50	0.743

6.4   Results

CXEM has been applied to OA and OP human bone tissue to visualise and to quantify the ON&LCN using existing quantitative measures and newly defined measures for processes and the PCS. Automatic segmentation was not as successful in the human samples as it was in the healthy murine bone samples (see below) because of the variations in cell contents and condition. Using SBF SEM, however, the ON&LCN were made visible concurrently at high resolution in 3D over a relatively large volume (Table 23) for the first time. This section firstly presents the results of the µCT imaging, followed by the SBF SEM imaging.

6.4.1   µCT

µCT imaging of decalcified, heavy metal stained, resin embedded human OA and OP tissue enabled visualisation of bone, bone marrow and cartilage (Figure 70 and Figure 68). Vascular components of the tissue were also stained and visualised. It was not possible to automatically visualise and quantify osteocyte cell bodies and osteocyte lacunae using the methods described in Chapter 3 as neither the cells nor lacunae showed sufficient contrast for segmentation using thresholding. Osteocytes and lacunae were identified in the images and could be manually segmented from the data stacks. The time required for manual segmentation prohibits its use over these volumes. Quantification of osteocyte and lacunar

density, porosity and distribution in the µCT images was not possible using the CXEM methods developed.
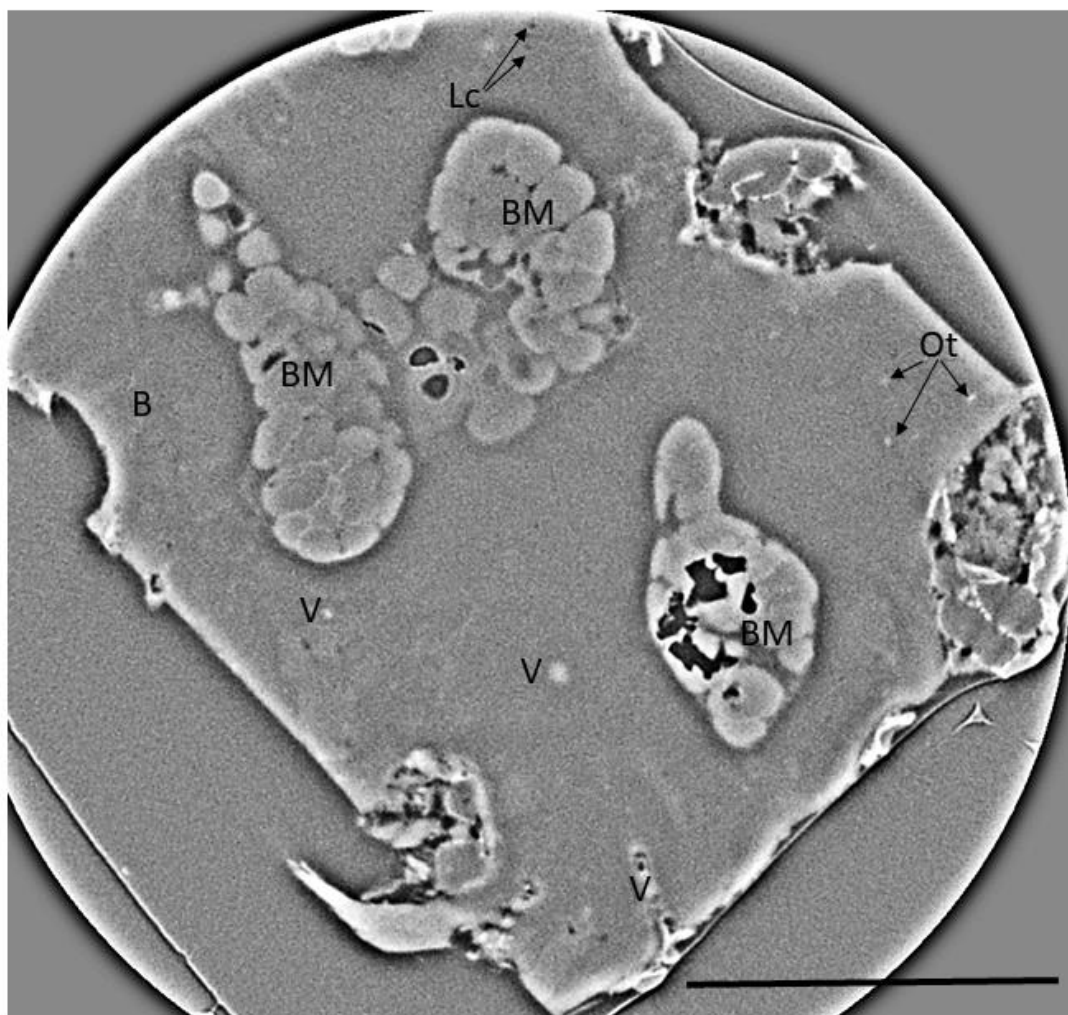
Figure 70   X-ray µCT of human bone tissue

An image of µCT scanned tissue (after application of a bandpass filter) showing bone tissue (B), bone marrow (BM), vascular tissue (V), osteocytes (Ot) and lacunae (Lc). Note that the osteonal structure is not seen because the tissue has been decalcified. Scale bar = 500 µm
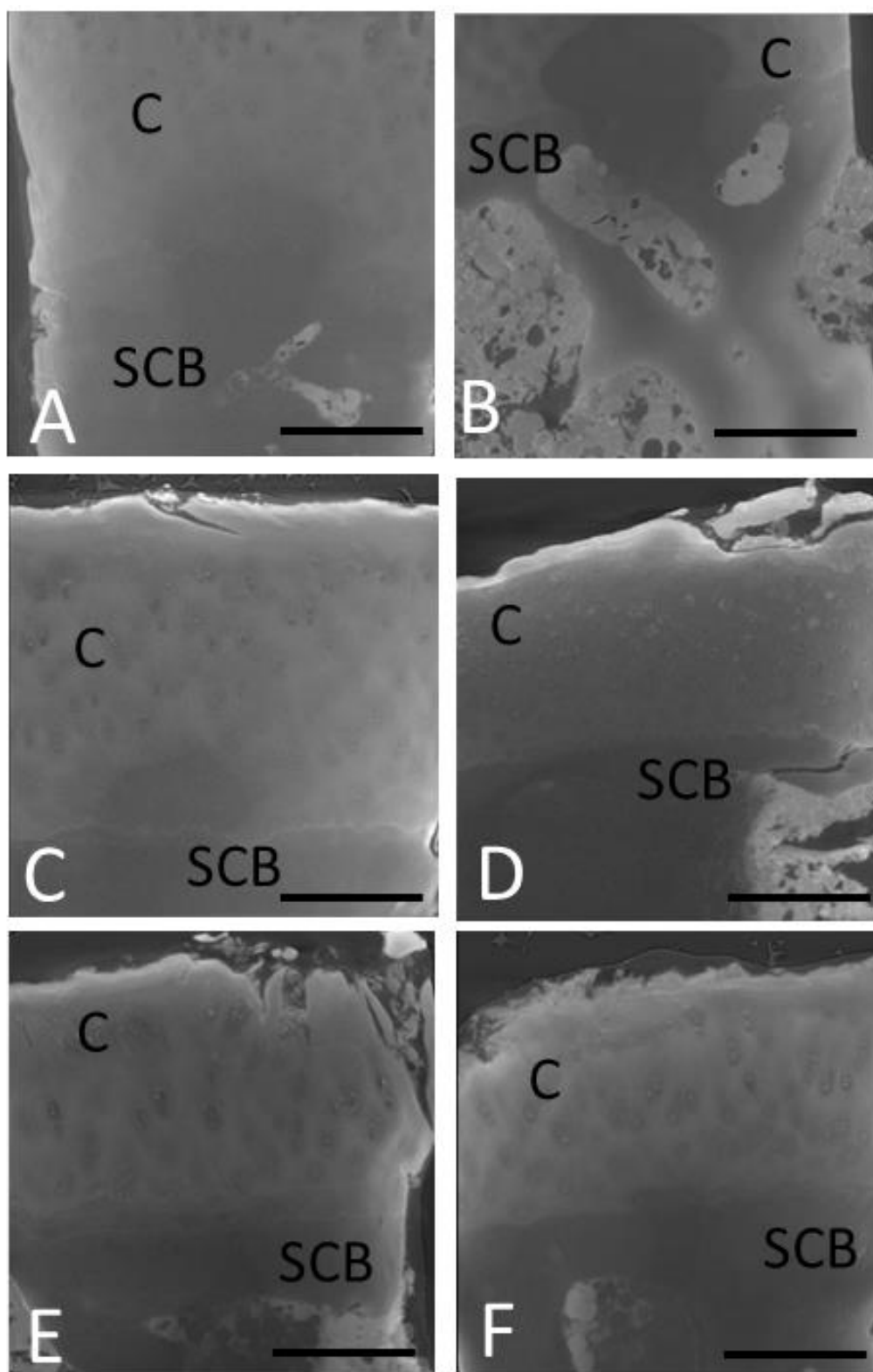
Figure 71   µCT images from OA and OP bone.

A – C   OA samples showing cartilage (C) and subchondral bone (SCB). Scale bars = 500 µm

D – F   OP samples showing cartilage (C) and subchondral bone (SCB). Scale bars = 500 µm

Note: B was scanned in a different position to minimise the volume of cartilage imaged and

maximise bone tissue imaged.

6.4.2   **SBF SEM**

Figure 72 shows the same osteon imaged with µCT and with SBFSEM. The improved resolution of SBFSEM is evident as detail of the tissue can be seen. It is possible to identify lacunae and cell structures. In the µCT image the same structures are discernible without the detail.
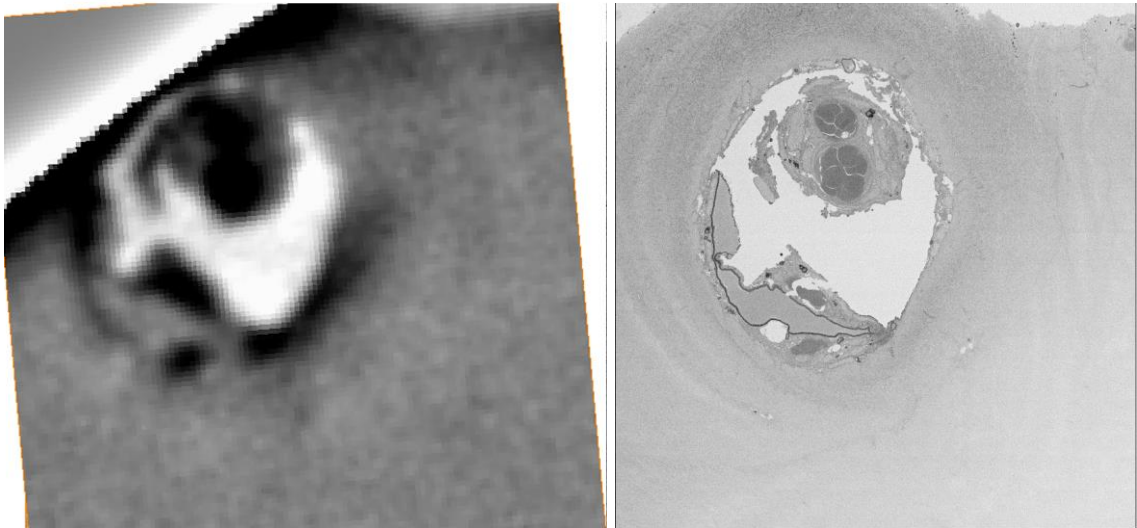
Figure 72   Correlative X-ray and SBFSEM images of an osteon in human bone tissue.

A   X-ray µCT image of an osteon

B   The same osteon imaged using SBF SEM.

Heavy metal stains taken up by cell components produced contrast in the SBF SEM images allowing visualisation of bone tissue, vascular canals, osteocytes and lacunae (Figure 73).
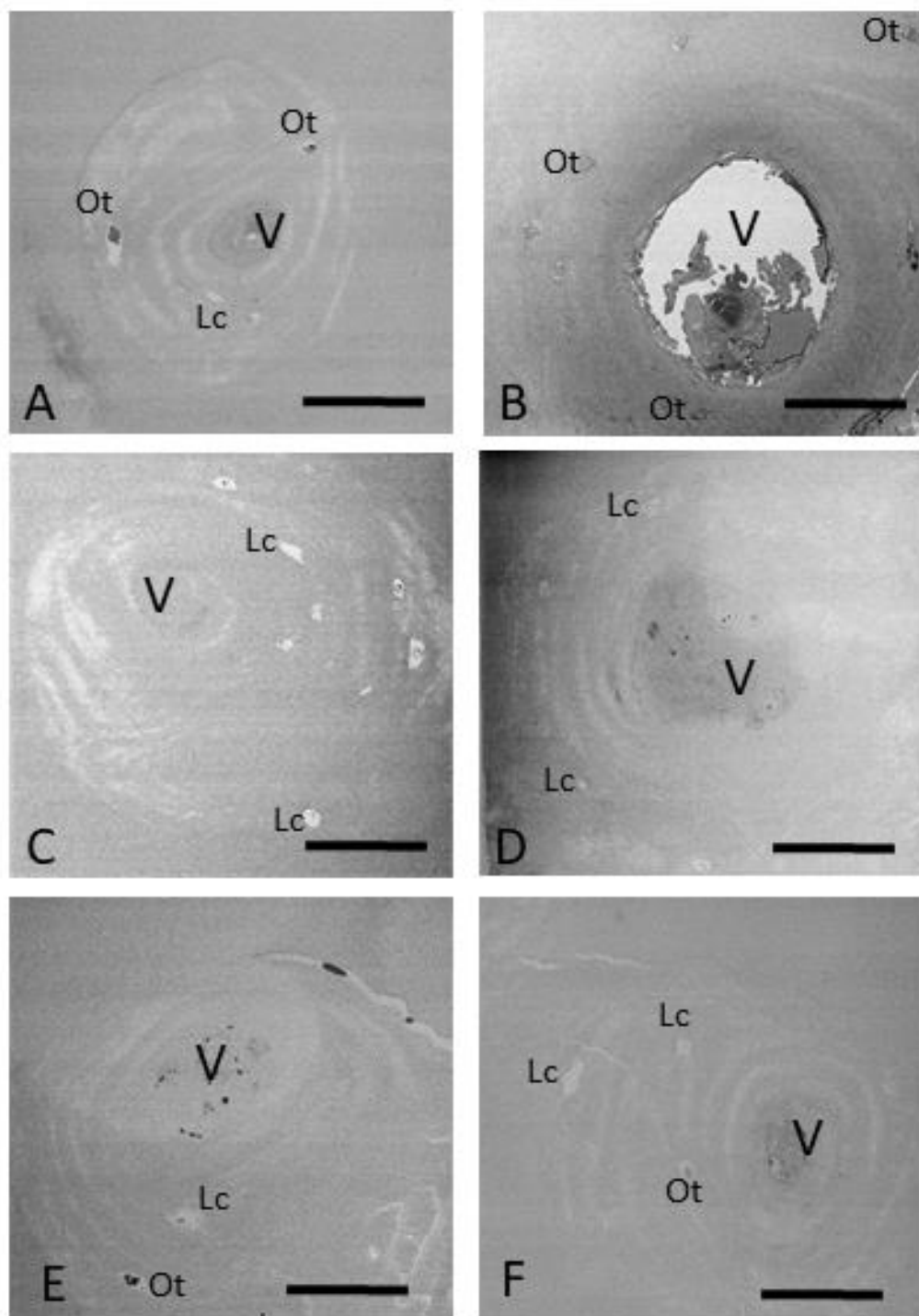
Figure 73   SBF SEM images from OA (A-C) and OP (D-F) tissue.

Images show vascular canals (V), osteocytes (Ot) and osteocyte lacunae (Lc). Scale bars = 50 μm

Osteocytes and lacunae were segmented using the Trainable Weka Segmentation plug-in as described in Appendix B2 (Figure 74).
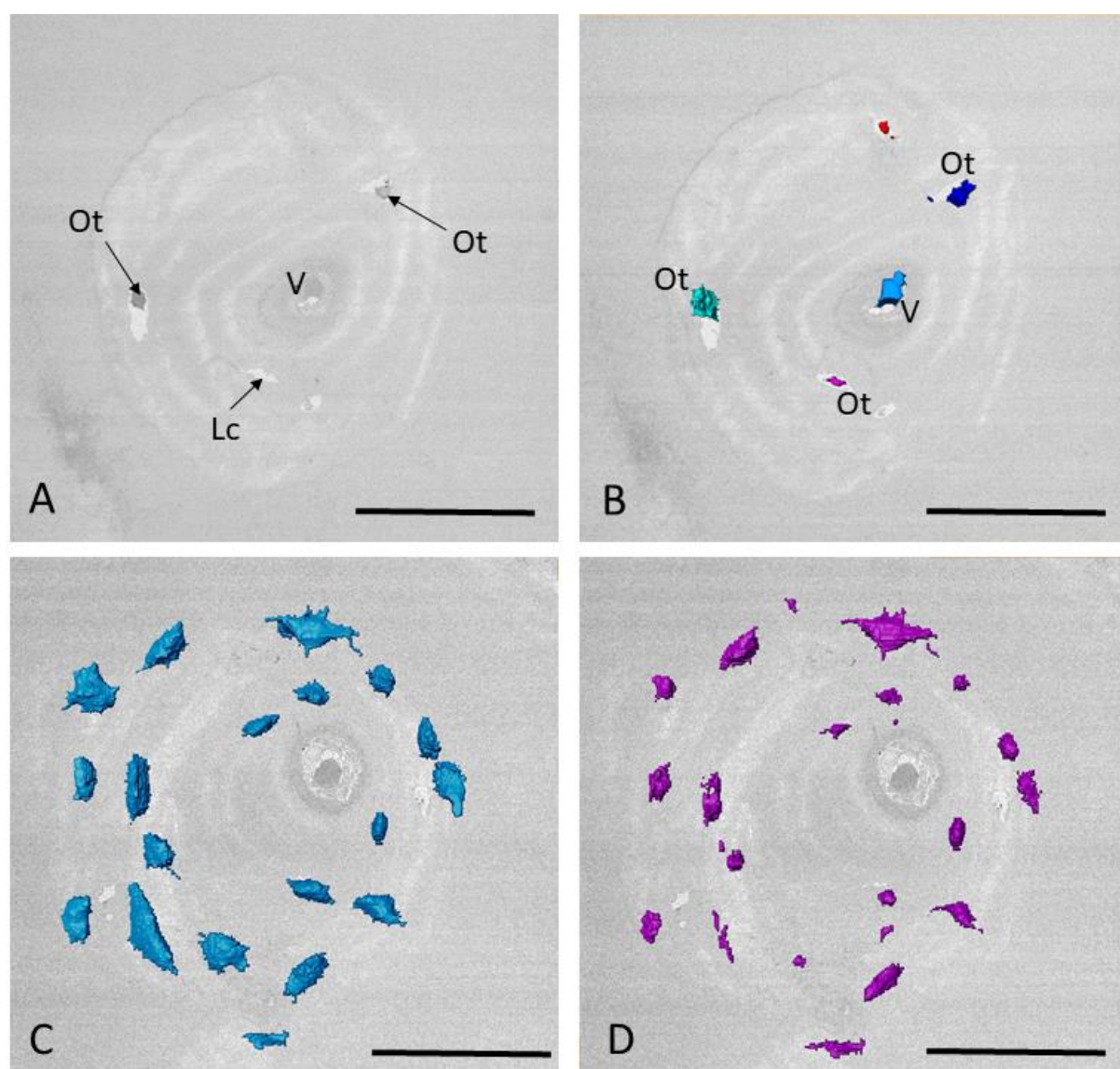
Figure 74   SBF SEM output and segmentation results

A   A single slice from an SBF SEM dataset showing lacunae occupied by osteocytes (Ot), apparently unoccupied lacunae (Lc) and a vascular canal (V).

B   Single slice showing reconstructions of the vascular tissue (V) at the centre of the osteon and osteocytes in the surrounding matrix (Ot).

C, D   Segmentation result of 1008 slices showing reconstructions of lacunae (blue) and cellular material (purple). Scale bars = 50 μm

SBF SEM images show that some lacunae are empty, some are occupied by healthy osteocytes, some by unhealthy cells and some by cell debris (Figure 76). Unhealthy cells show many of the same features as poorly fixed cells as both have started to undergo cell death. Thus, to quantify the numbers of healthy cells and the extent of 'ill health' or deterioration the cell descriptions in Table 10 are used. Varying states of cell health are

defined based on the state of ultrastructural preservation. Briefly, the morphology of the

cell membrane, lamina limitans, cytoplasm, nucleus and nuclear membrane are evaluated.

At the imaging conditions used here mitochondrial structure is not discernible and so the

mitochondrial criteria are not used (Table 24   Percentage of healthy cells, unhealthy cells

and cell debris in lacunae.Table 24 and Figure 75).

Table 24   Percentage of healthy cells, unhealthy cells and cell debris in lacunae.

Condition	% Healthy	% Unhealthy	% Debris
OA	0	21	79
OA	0	96	4
OA	6	9	85
OP	0	44	56
OP	0	100	0
OP	0	8	92
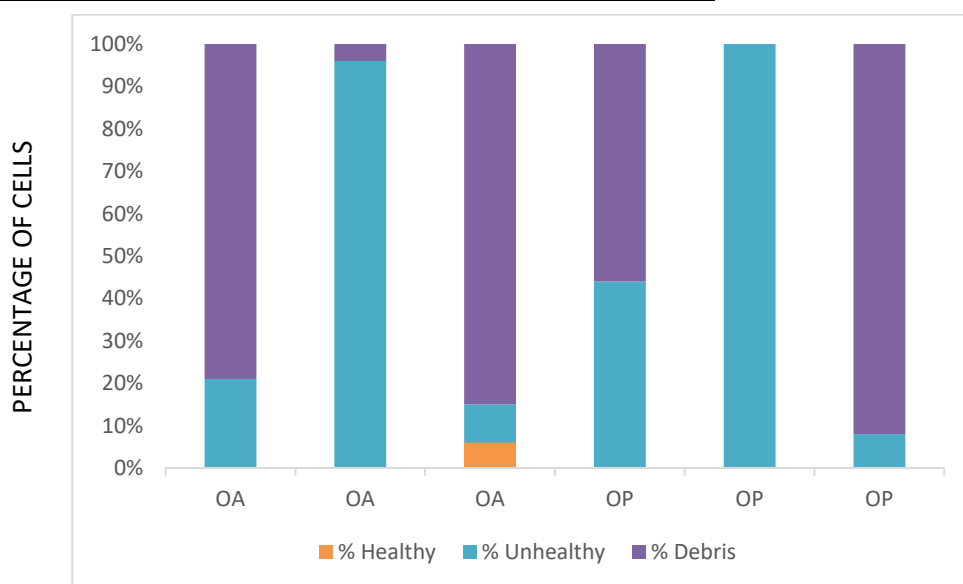
Figure 75   Effect of bone disease on cell health.

Graph showing the proportion of healthy cells, unhealthy cells and cell debris in lacunae from OA
and OP bone tissue.

Values for lacunar density in OA and OP bone samples range from 11,849 to 23,136 /mm^3

(Figure 77). Osteocyte density values calculated using cellular material, including cell

debris, are considerably lower, ranging from 1,505 to 22,634/mm^3. Mean osteocyte density

is 45 % of mean lacunar density in OA patients, 51 % of mean lacunar density in OP patients and 48% of mean lacunar density across all samples.

Values for lacunar porosity range from 0.3 to 0.5 % (Figure 77). Osteocyte porosity values calculated using Ot.V results, and excluding cell debris, are lower, ranging from 0.02 to 0.26 %. Mean osteocyte porosity is 30% of mean lacunar porosity in OA patients, 26% of lacunar porosity in OP patients and 28% of mean lacunar porosity across all samples.

Mean Ot.V (cellular material) is 107 μm^3 in OA, 102 μm^3 in OP and in 105 μm^3 across all samples. Mean Lc.V is 262 μm^3 in OA and 282 μm^3 in OP. Mean PCS.V is 155 μm^3 in OA and 180 μm^3 in OP. % lacunar volume occupied by cellular material ranged from 0- 100%. The mean % volume of the lacuna occupied by cellular material is 49% in OA and 44% in OP (Figure 78).
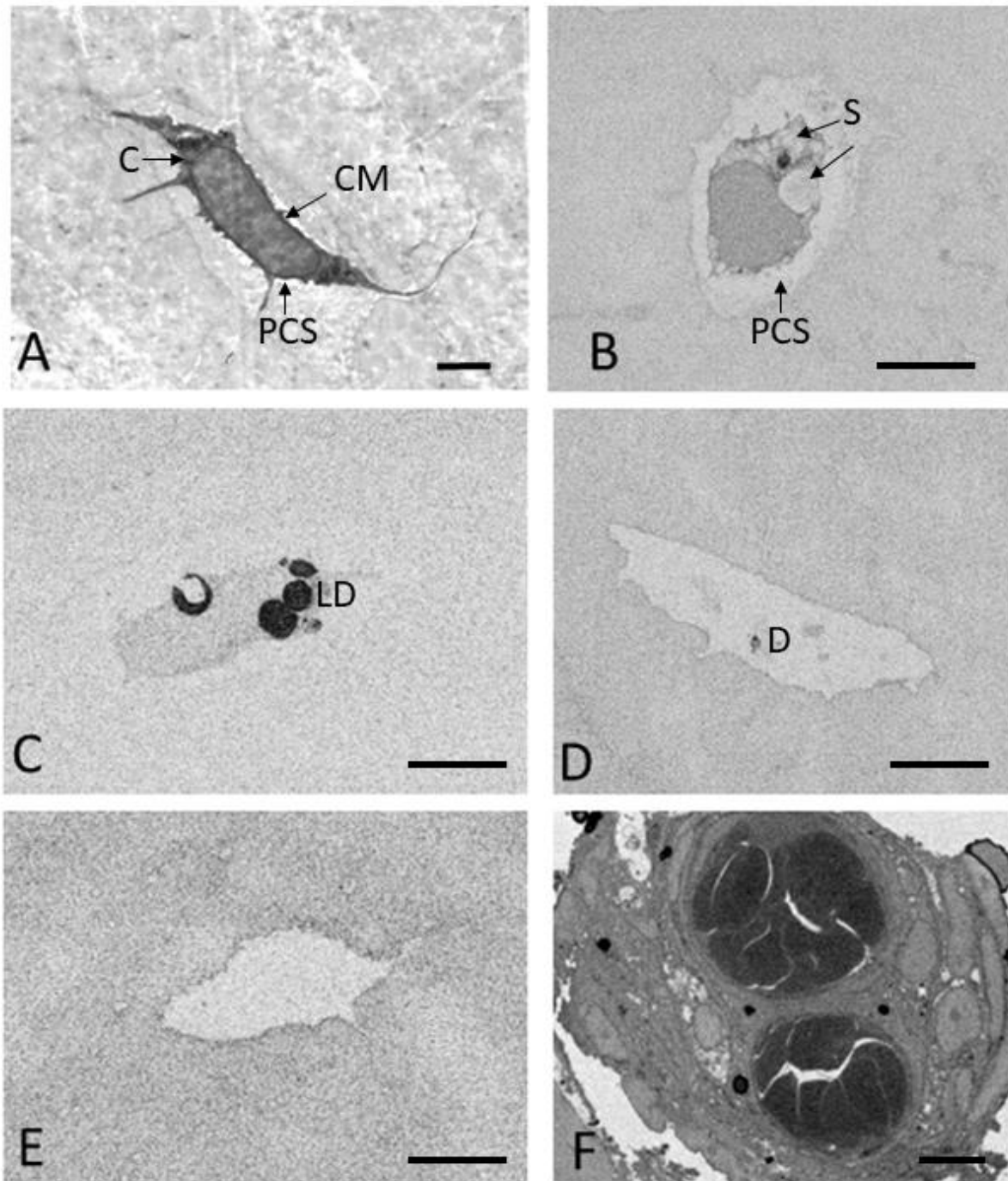
Figure 76   Varying states of cell health observed in human bone samples compared with healthy cell ultrastructure.

A   Osteocyte (murine bone, TEM) showing no obvious structural damage; continuous cell membrane (CM); pericellular space neither swollen nor empty (PCS); no empty spaces in the cytoplasm (C) or within organelles and no obvious cell shrinkage.

B   Osteocyte (human, SBFSEM) showing some changes including reduced cytoplasm volume, spaces in cytoplasm (S) and some shrinkage leading to an enlarged pericellular space (PCS).

C   Unhealthy osteocyte (human, SBFSEM) showing lipid droplets (LD).

D   Osteocyte lacuna (human, SBFSEM) containing unstructured material or debris (D).

E   Apparently empty lacuna (human, SBFSEM)

F   Endothelial cells of a vascular canal in human bone tissue (SBF SEM) showing good preservation of cells.

Scale bars A-E = 2 μm, scale bar F = 5 μm
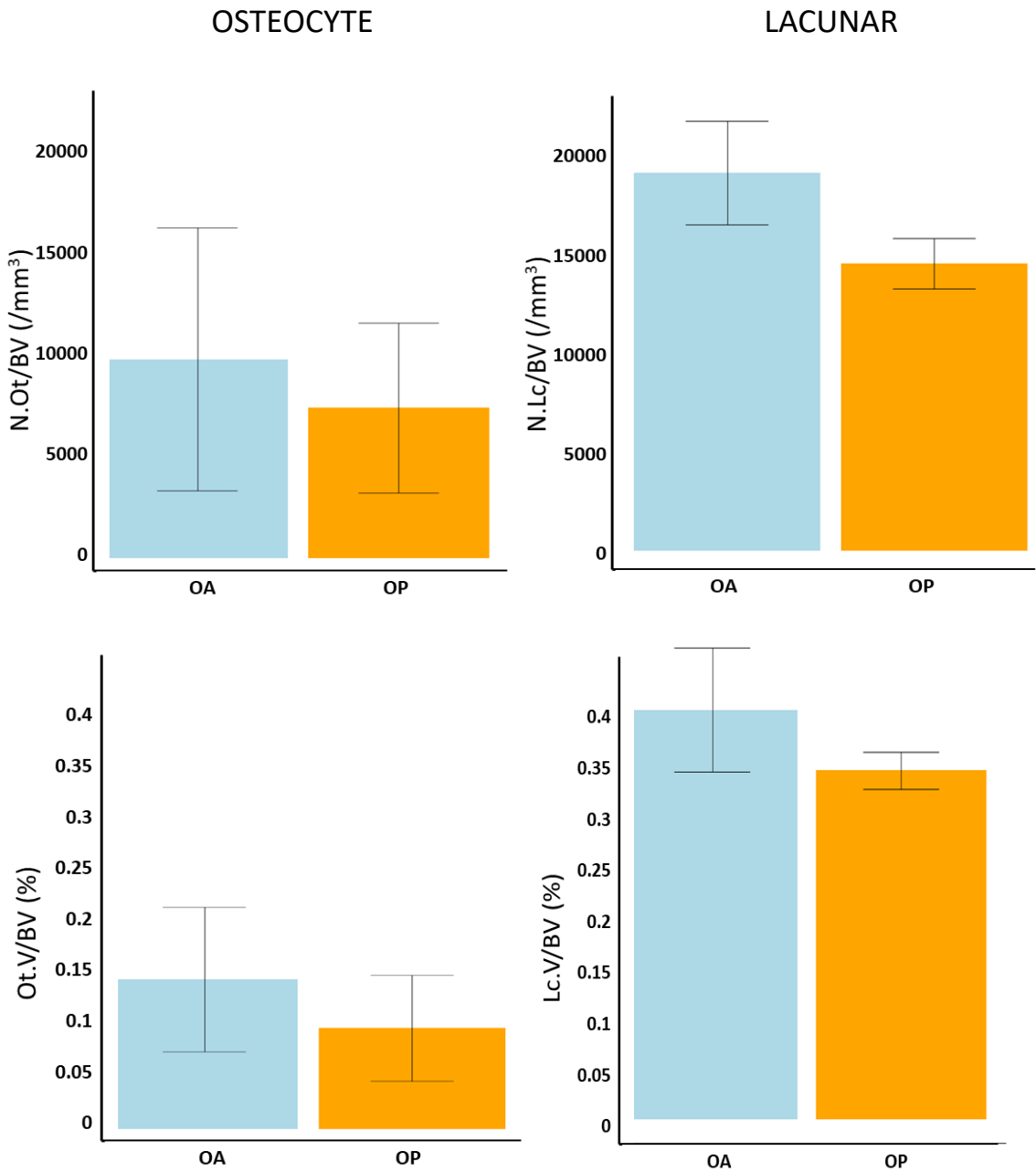
OSTEOCYTE   LACUNAR

Figure 77   Effect of disease condition on osteocyte and lacunar number density and porosity for OA and OP bone samples imaged using SBF SEM.

TOP   Mean osteocyte number density and lacunar number density in OA and OP tissue. No significant differences were observed. Values are mean ± SE, n=3 each group.

BOTTOM   Mean osteocyte porosity and lacunar porosity in OA and OP human tissue. No significant differences were observed. Values are mean ± SE, n=3 each group.
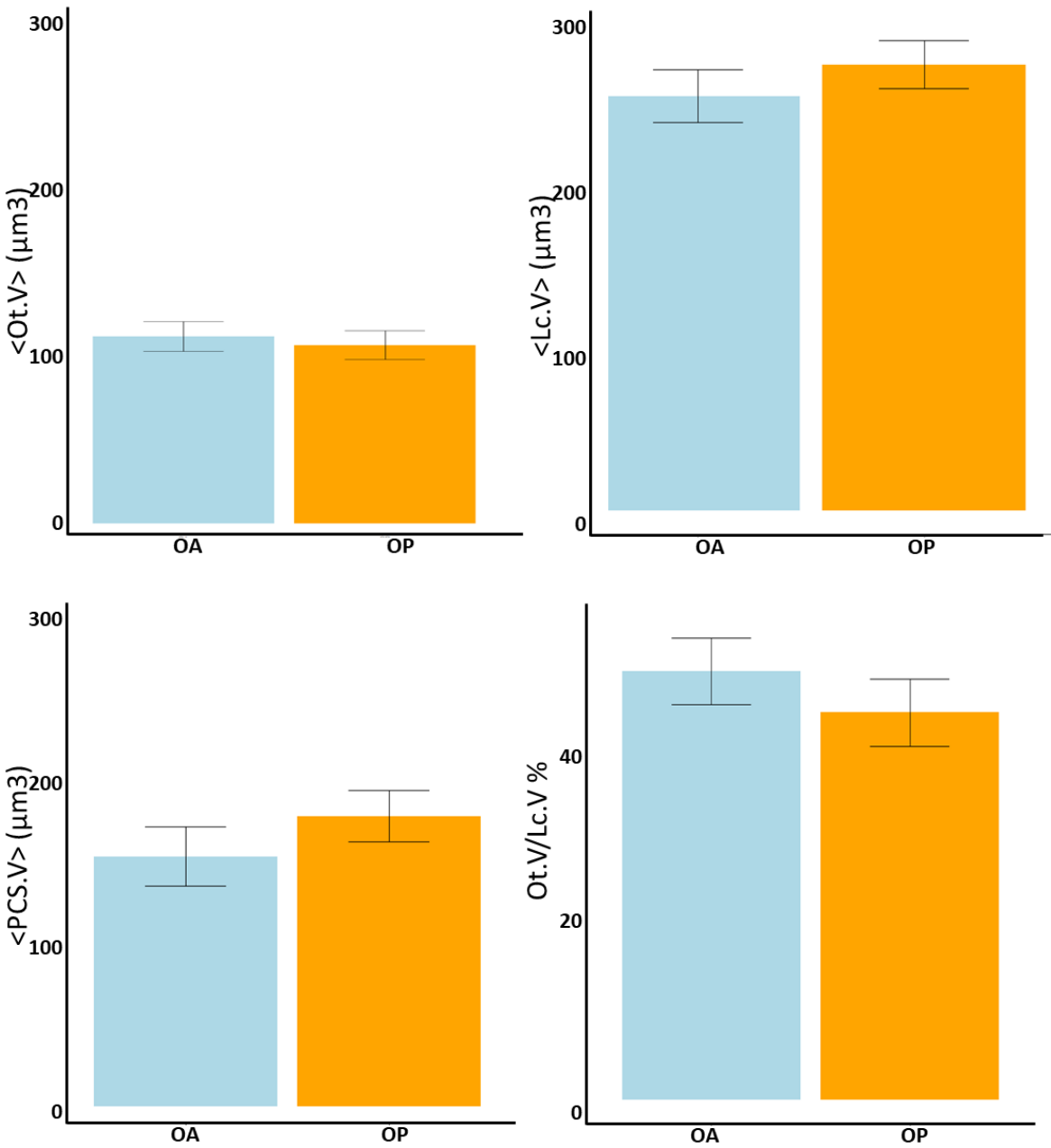
Figure 78   Effects of bone disease on osteocyte, lacunar and PCS volumes.

Mean osteocyte volume, lacunar volume, PCS volume and percentage lacunar volume occupied by cellular material. Includes all lacunae, whether they contain a healthy cell, unhealthy cell or cell debris. No significant differences were observed. Values are mean ± SE, n=3 each group.

6.4.3   **OA Samples (Figure 79)**

Cell ultrastructure and thus health, viability and ability to carry out physiological functions varies in OA samples. Individucal cell measures such as Ot.V cannot be interpreted without considering the associated cell ultrastructure. Thus, in addition to reporting quantitative cell measures in these samples, cell health, pertinent ultrastructural features and observations on distribution in individual samples are described in the following section.

R19_528 F51 : 79% of lacunae in this sample contain debris where no nucleus or organised ultrastructure is visible. The remaining 21% of lacunae contain unhealthy cells. No cell processes were observed on the cells. Most have large nuclei, little visible differentiation between euchromatin and heterochromatin and little surrounding cytoplasm. It appears that the cytoplasm has shrunk, increasing the PCS.V. Mean Ot.V/Lc.V is 37%. The remaining condensed cytoplasm contains multiple vesicles. The lamina limitans is well defined in all lacunae. These features indicate apoptosis apart from the nuclear appearance which in apoptosis features condensed chromatin.

R19_599 F67 : 96% of lacunae in this sample contain unhealthy cells while 4% contain cell debris. No cell processes were observed on the cells. The nuclei of most cells appear normal with euchromatin and heterochromatin visible. There are vesicles in the cytoplasm, some lipid droplets, cytoplasm with less structure and density than expected in a healthy cell and little apparent shrinkage. Mean Ot.V/Lc.V is 65%. Occasional cells have intact nuclei but partly or completely empty cytoplasm. Mean % lacunar volume occupied by a cell is 65 %.

R19_530 F76 : A small proportion of lacunae (15%) located close to the vasculature have no obvious PCS and contain cellular material including lipid droplets and cytoplasmic vesicles. Further away from the vascular canal lacunae 85% of lacunae contain debris which occupies 43% of the lacunar volume on average.
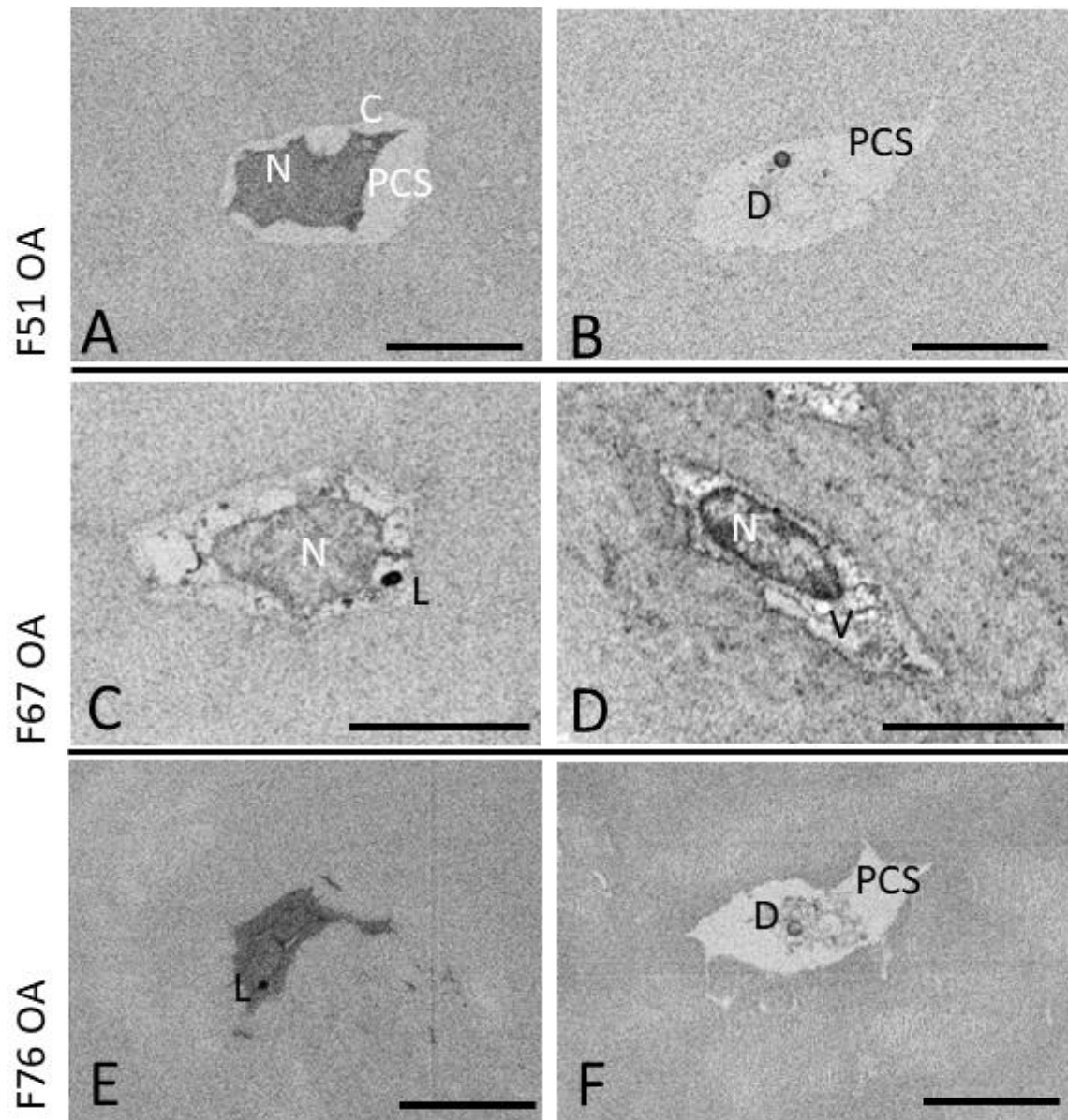
Figure 79   Osteocytes and lacunae in OA bone tissue.

A   Lacuna containing an osteocyte. The nucleus (N) has evenly dense chromatin, the cytoplasm (C) is condensed and shrunk, increasing the size of the PCS.

B   A lacuna containing debris (D).

C   A lacuna containing an osteocyte. The nucleus (N) is intact and contains euchromatin and heterochromatin. The cytoplasm has lost much of its structure and density and contains a lipid droplet (L).

D   A lacuna containing an osteocyte. The nucleus (N) is intact and contains euchromatin and heterochromatin. The cytoplasm has lost much of its structure and density and contains vesicles (V).

E   A lacuna containing an osteocyte with no visible PCS. A lipid droplet is present

F   A lacuna containing debris (D).

Scale bars = 5 μm

6.4.4   **OP samples (Figure 80)**

R19_531 F92 : In this sample 44% of lacunae are occupied by unhealthy osteocytes. No healthy osteocytes were seen. The cells show shrinkage and an increase in the volume of the PCS.   The mean Ot.V/Lc.V is 43%. The cytoplasm contains vesicles and appears condensed. The cell nuclei contain undifferentiated chromatin without definition of euchromatin and heterochromatin. The cells had no cell processes. The remaining lacunae (56%) contain cell debris.

R19_532 F95 : In this OP sample 100% of the lacunae are occupied by cells. All cells have lipid droplets in the cytoplasm including the endothelial cells in the vasculature. Nuclei are large and contain undifferentiated chromatin. The cells are flattened, especially those located near the vascular canal, and some evidence of shrinkage is observed. The cells had a reduced number of cell processes. The mean Ot.V/Lc.V is 47%. No cells are classified as unhealthy and no lacunae contain cell debris.

R19_533 F95 : 13% of the lacunae in the volume contain cellular material. The remaining 87% contain unstructured cell debris. Nuclei are large and contain undifferentiated chromatin. The cell cytoplasm is condensed. Electron dense droplets, likely lipid, are observed within some cells and the cell debris. No cell processes were observed in these cells. The mean percentage space occupied in the lacunae is 50 %.
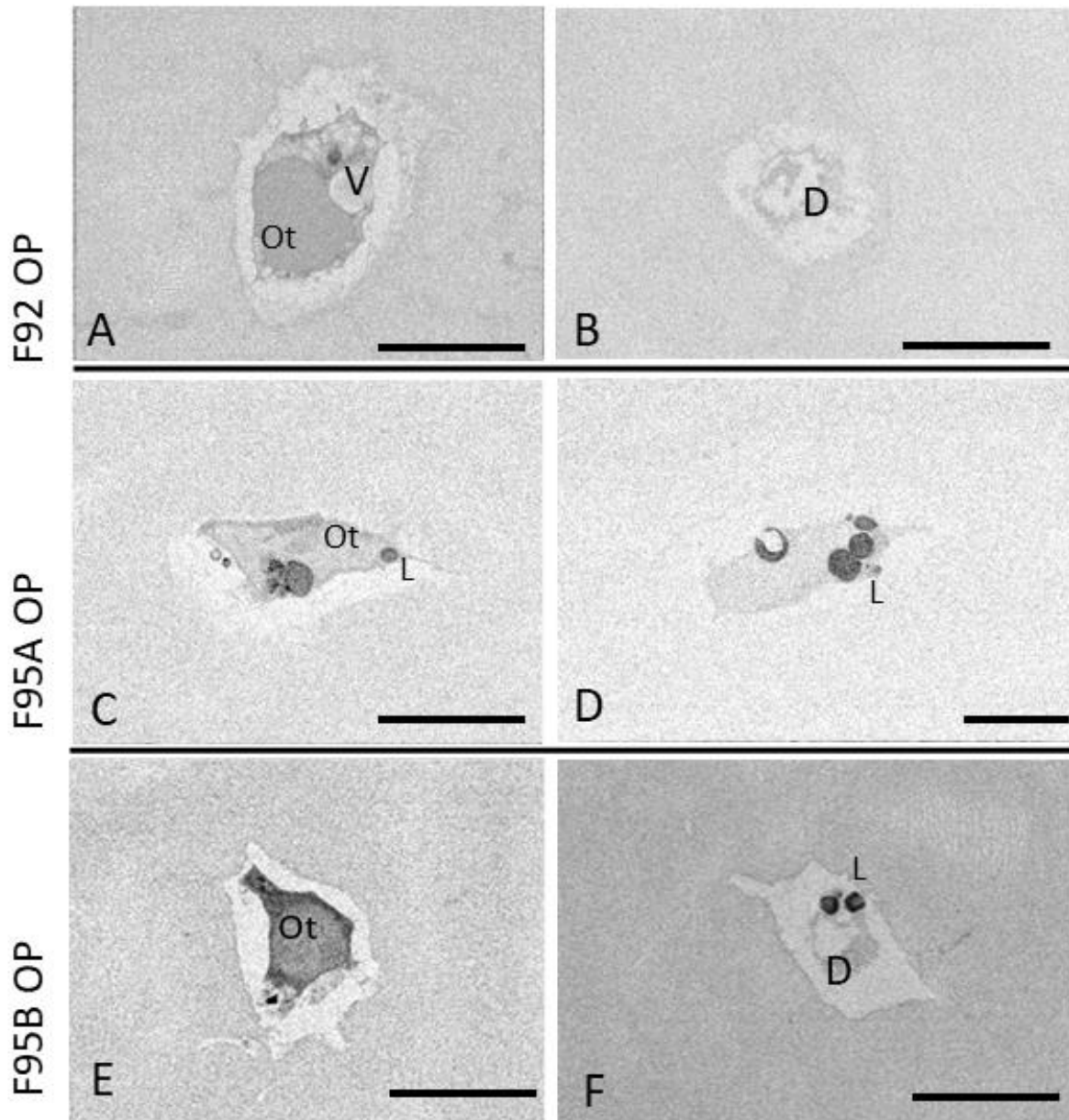
Figure 80   Osteocytes and lacunae in OP bone tissue.

A   Lacuna containing an osteocyte (Ot). The nucleus has evenly dense chromatin, the cytoplasm contains vesicles (V). Some cell shrinkage is seen.

B   A lacuna containing debris (D).

C   A lacuna containing an osteocyte. The cytoplasm has lost much of its structure and density and contains a lipid droplet (L).

D   A lacuna containing an osteocyte. The cytoplasm has lost much of its structure and density and contains lipid droplets (L).

E   A lacuna containing an osteocyte (Ot) with no visible PCS. The nucleus has evenly dense chromatin, the cytoplasm is dense and the cell appears to have shrunk, increasing the PCS volume.

F   A lacuna containing debris (D) and lipid droplets (L). Scale bars = 5 µm

6.5 Discussion

CXEM was applied to OA and OP human femoral head bone tissue with the intention of imaging and quantifying the ON&LCN within. As discussed in Chapter 2 there is a need to more fully understand the microstructural and ultrastructural changes occuring in bone disease in order to identify possible therapeutic targets. It is proposed that CXEM is a useful technique to investigate these structural changes and provide data which can feed into computational models of mechanobiology (Section 2.9.2).

This section will discuss:

- The suitability of CXEM as a technique for imaging and production of quantitative data on the 3D microstructure and ultrastructure of the ON&LCN in OP and OA bone.

- The implications of the CXEM results on knowledge of bone disease. In particular, how changes in the ON&LCN in OP and OA human femoral head tissue may affect mechanisms of mechanobiology. Additionally, how these results may be incorporated into computational modelling of mechanobiology in bone disease.

- How ultrastructure reflects cell health and how cell health may affect mechanobiology.

- Limitations of the work and possible improvements.

6.5.1 The suitability of CXEM as a technique for imaging diseased bone tissue.

SBF SEM imaging allows 3D visualisation of osteons, osteocytes, cell processes and empty lacunae. To the best knowledge of the author, all studies to date, where percentage lacunar occupancy has been estimated in human bone tissue, were performed in 2D using LM or

SEM. 2D imaging techniques can lead to osteocyte lacunae appearing empty when a cell is present deeper in the tissue block. An oblique view can be misinterpreted if the plane of section misses the cell within the lacuna and false negatives can be caused by cell shrinkage (Jilka et al., 2013). Therefore the application of 3D imaging techniques to the ON&LCN in bone tissue will provide accurate occupancy and cell volume data.

One of the advantages of using CXEM to investigate the ON&LCN is the direct visualisation of osteocytes and particularly the cell ultrastructure. As discussed in Chapter 3, perfusion fixation gives improved results over immersion fixation and is the ideal method for preservation of ultrastructure. As this is not possible, control of tissue before fixation is important so collection directly from theatre, avoiding refrigeration and immediate fixation ensures the best possible preservation.

Osteocyte phenotypes observed in this study could be reflective of either poor fixation or deteriorating cell health. The state of preservation and health of the endothelial cells in these samples demonstrates that the fixation is of good quality so changes in the cell appearance and thus health can be attributed to the bone pathology.

Using CXEM, the entire cross section of murine tibia could be imaged, however, in human femoral head only a small subsample can be imaged (Figure 5). Studies of large bones such as femur would benefit from a correlative technique incorporating an imaging method which covered a larger volume at as high a resolution as possible. Clinical imaging techniques such as quantitative CT (QCT), multidetector CT (MDCT) do not presently provide data at high enough resolution to image the ON&LCN but do provide data on structural measures such as bone fraction and trabecular number which would guide the application of further μCT and SBF SEM.

Using µCT can confirm the presence of cellular or mineral material within an osteocyte lacuna, but µCT data is not sufficient to distinguish between a healthy, fully functioning cell, an unhealthy or dying cell, a dead cell or cell debris. This distinction is relevant for the functioning of the ON&LCN as apoptotic or dead cells can neither contribute to communication within the network nor sense and transduce loading signals. EM or LM are required to distinguish this. Lactate dehydrogenase (LDH) staining in LM can demonstrate cell viability (Xia et al., 2010) and EM can provide evidence of cell health via the ultrastructural phenotype.

6.5.2   Implications of the CXEM results on knowledge of bone structure and bone disease

CXEM results from this study have produced data on osteocyte number density, osteocyte porosity and osteocyte volume from human OA and OP tissue in 3D for the first time. The results also show that in both OA and OP tissue lacunar occupancy is less than 50% and that cell health is compromised.

Results for human lacunar number density in the literature vary from 14,900 /mm^3 (Bach-Gansmo et al., 2016a) to 40,000 - 90,000 /mm^3 (Hannah et al., 2010). The variation may be dependent on some or all of the anatomical site, the disease state, the age of the individual and the species. Lacunar density values of 19,000 – 28,450/mm^3 based on (Dong et al., 2014a, Bromage et al., 2009, Carter et al., 2013b) were used as typical osteocyte density for human bone in a study which quantified the ON in the human skeleton (Buenzli and Sims, 2015). To the knowledge of the author, no comprehensive 3D studies of osteocyte number density in human bone tissue have been reported to date. The density of osteocytes is more significant than that of lacunae since cells are the active mechonsensors.

Lacunar density results in this study range from 13,329 to 27,160 /mm^3. Osteocyte density values are considerably lower ranging from 1,504 to 19,112/mm^3 (Figure 77). Mean

osteocyte density is 40% of mean lacunar density in OA patients and 35% of lacunar density in OP patients. Mean osteocyte porosity is 33% of lacunar porosity in OA and 26% of lacunar porosity in OP. These findings illustrate why using lacunar density and porosity measures to represent osteocyte measures in diseased human bone tissue can lead to inaccurate results. Most of the cells in the OP and OA samples lack cell processes, presumably lost as a consequence of declining cell health. Their loss has an impact on ON connectivity.

Osteocyte death is dependent on both patient age and tissue age, but can be caused by oestrogen deficiency, steroid excess and/or excessive strain (Milovanovic and Busse, 2020). Osteocyte death and subsequent lacunar mineralisation affect the functions of the ON, including intercellular communication, and thus, mechanosensation, targeted bone remodelling and repair, leading to damaged bone and accumulation of microcracks, ultimately decreasing bone quality.

Many of the changes in cell ultrastructure observed are indicative of deterioration in cell health and many cells show some, but not all the features of apoptosis. The nuclei of apoptotic cells are characterised by focally condensed chromatin and nuclear shrinkage, features which were not seen in this study. This suggests that other forms of cell death including necrosis, necroptosis or autophagy may be taking place.

Cell death and its inhibitors including necrostatin (Stolberg-Stolberg et al., 2020, Gilbert et al., 2009, Cui et al., 2016) and rapamycin (Yin et al., 2017), are under consideration as potential therapeutic agents for OP and OA. It is not possible to determine exactly which methods of cell death are taking place using EM. Combining CXEM with light microscopy stains for viability such as LDH or apoptotic labelling methods such as transferase mediated DNA nick end *labelling (*TUNEL) would enhance data in future studies.

Computer simulations which modelled osteocyte apoptosis and its effect on osteoblasts and osteoclasts, showed that only a 3% decrease in osteocyte number was needed to have a significant reduction in signalling to those cells (Jahani et al., 2012). This study sheds light on the importance of the interlinked, network between osteocytes, osteoclasts and osteoblasts and the effects which disruption of the network can have. Further studies using the data shown here will lead to more understanding of the consequences of cell death on overall bone function and pathology and perhaps determine where the critical levels of lacunar occupancy and cell health for bone lie, beyond which the tissue becomes non-viable.

No clear differences between the structure of the ON&LCN in OA and OP tissue were observed. A study investigating age and disease with reference to fracture toughness found that age but not disease led to compromise in the femoral neck and that neither OA nor OP further influence fracture toughness beyond natural ageing (Jenkins et al., 2017). No clear patterns are observed in the ON&LCN data from patients in this study when considered by age either. This may be due to the relatively small sample number.

Computational modelling which compares mechanobiology of the ON&LCN based on lacunar and canalicular data and ranges of osteocyte and process data (changing ON connectivity) would produce useful information on how lacunar and canalicular occupancy affect bone function. It would be interesting to compare these data in healthy bone tissue and tissue from different developmental stage of OA and OP.

While not the primary focus of this work, SBF SEM of decalcified tissue provides insights into the underlying organic structure of cement lines and interlamellar seams. The cement lines at the osteon boundary and the interlamellar seams within the osteons are not evident on CT but are visible in SBF SEM images (Figure 73 and Figure 74). The nature of

cement line composition is important for understanding crack growth and fracture resistance. It has been suggested that cement lines are hypermineralised, deficient in collagen, or both (Skedros et al., 2005, Milovanovic et al., 2018) .

In SBF SEM images the location of the cement lines is visible as a stained layer, indicating the presence of more dense organic material including collagen and non-collagenous material. The interlamellar seam lines however, are visible as electron lucent spaces, indicating a reduction in the density of organic material. The question of whether collagen fibres traverse the cement lines could be further investigated using SBF SEM data.

6.5.3   Limitations of the work

As heavy metal staining is used to contrast cellular content (osteocytes and vasculature) in these samples, where lacunae are less fully occupied there is less contrast. As the tissue has been decalcified and the spaces infiltrated with resin, the contrast generation method relied on in in conventional X-ray imaging is lost, the 'empty' lacunae have less contrast in µCT and are therefore more difficult to segment. Similarly, where cell shrinkage has occurred the number of stained voxels is lower and therefore more difficult to identify and thus segment. In the murine samples, as occupancy was high this difficulty was not encountered. Manual segmentation is possible in these cases but prohibitive for large scale studies considering the time involved.

Weka segmentation (Arganda-Carreras et al., 2017) is based on image features and as the cell contents and condition vary so much in the human samples the tool is less reliable and some manual segmentation has been required. Thus, in future, changes to the protocol such as carrying out µCT imaging before decalcification enabling segmentation of lacunae should be considered.

In this study OA and OP bone are compared to each other. There are few studies that directly compare OA or OP bone to non-diseased control tissue. Such studies have investigated properties including; bone hardness (Dall'Ara et al., 2011) , energy absorption (Dickenson et al., 1981), stiffness (Li and Aspden, 1997), microscopic appearance (LI et al., 1999) and reference point indentation properties (Jenkins et al., 2016). While not the ideal, the OPvOA comparison is considered the 'least worst' option and is a pragmatic approach considering the limited availability of freshly excised human tissue and controlled EM fixation. In the future biobanking may help with the supply of human tissue for research.

It is important to note that these findings may only be valid for the human femoral head. Bone is heterogeneous and strain is experienced differently in anatomical areas. Further investigation is required to determine if these results are representative of the entire femur and of other human bones.

In this study the age of the OA patients is significantly lower than the OP patients. OA (51, 67, 76, Average = 64.6), OP (92, 95, 95, Average = 94) (p= 0.016). As the structure of bone changes with ageing (Table 2) age could be a factor in the changes observed. There are confounding factors between the two groups as individuals who fracture are generally older with a somewhat reduced quality of life whereas patients undergoing elective hip arthroplasty are typically healthier and younger.

Information available on donor patients is limited by the ethics agreements in place. More detailed clinical histories would give access to data including BMD measurements, previous fractures, information on medication intake, history of smoking and alcohol consumption, general health status and the presence of other bone disease (osteomalacia, Paget's disease, primary bone tumours or bone metastasis), improving the robustness of results.

6.5.4   **Lacunar mineralisation**

The number of mineralized osteocyte lacunae per bone area is an indicator of former osteocyte death. It can be used to distinguish between healthy, aged, untreated osteoporotic and bisphosphonate-treated osteoporotic patients and is suggested as a marker of impaired bone quality (Milovanovic and Busse, 2020). CXEM as applied in this study cannot recognise mineralised lacunae as all mineral is removed during decalcification. Mineralised lacunae do not contain a collagen matrix like normal bone tissue (Milovanovic et al., 2017). It is possible that some of the lacunae which contain small amounts of debris have undergone micropetrosis and the decalcification process has re-opened them. CXEM cannot distinguish lacunae in this state. It would be interesting to CT scan bone tissue sample before subsequent decalcification and SBFSEM. This would allow measurement in 3D of micropetrosis, to date only carried out using 2D SEM.

6.6   Conclusion

In conclusion, 3D quantification of the ON&LCN number density, porosity and cell morphology from OA and OP human tissue has been achieved for the first time. SBF SEM allows determination of lacunar occupancy and additionally, allows the state of health of those osteocytes to be determined. Both OA and OP tissue show reduced lacunar occupancy compared to healthy bone tissue in other studies and healthy murine tissue studies in this project. CXEM imaging has limitations in diseased human bone tissue as less cellular material is present in the tissue, resulting in reduced contrast in µCT data.

Osteocyte number density is 40% of lacunar number density in OA patients and 35% of lacunar number density in OP patients. Osteocyte porosity is 33% of lacunar porosity in OA and 26% of lacunar porosity in OP. These findings illustrate why using lacunar number

density and porosity measures to represent osteocyte measures in diseased human bone tissue can lead to inaccurate results.

93% of osteocytes showed ultrastructural changes indicative of deteriorating health or cell death. This observation leads to the conclusion the cell network, crucial for mechanobiology, is compromised in OA and OP, although not in significantly different ways. It is hoped these insights will directly contribute to future computational modelling approaches by providing accurate geometries, occupancy data and features of diseased bone. The ON&LCN morphology and organisation can later be correlated with predictions from computational models in terms of disease-related differences in mechanotransduction.

Chapter 7 Discussion

7.1 Thesis summary

Mechanical loading is experienced at an organ level and induces stimuli which are transmitted through tissue architecture to individual osteocytes which respond by coordinating bone remodelling by osteoblasts and osteoclasts (Figure 2). Quantification of changes in hierarchical spatial organisation and the effects on cellular responses to loading is required. Computational models created using experimental data produced by imaging can help to unravel this transfer of loads from organ to cells and vice versa in health and in disease.

The goal of this thesis is to describe the development and application of a framework for correlative X-ray and electron microscopy (CXEM) which can characterise quantitatively 3D osteocyte microarchitecture in bone tissue. CXEM is a novel technique combining μCT and vEM which can, uniquely, image both the ON and the surrounding LCN in bone tissue at high spatial resolutions in 3D. As described in Chapter 2, high resolution 3D data is required to investigate mechanisms of bone mechanobiology, in particular the proposed mechanisms of sensation of loading by osteocytes (Section 2.9.1).

The completeness of study of osteocyte physiology and pathology in 3D has been restricted due to the location of the cells within the mineralised bone matrix. External force (loading) applied to the whole bone is sensed by individual osteocytes and the network arrangement of cells allow transmission of signals throughout the organ covering several length scales. Thus it is important both to observe the structural properties of the osteocyte networks within bone as well as the morphology of individual cells and the relationship of the cells to the matrix in 3D. Many studies investigating ON&LCN structure have been 2D in nature

and many have been carried out using X-ray based methods, which depict the bone matrix (LCN), without considering the cells residing within (ON). A crucial underlying assumption based on previous work ((Nicolella et al., 2006, Bonivtch et al., 2007, Ma et al., 2008)reviewed in (Hemmatian et al., 2017a)) is that the 3D ON&LCN structure controls bone mechanotransduction and that this structure is altered in disease.

This project proposes that CXEM is a useful technique to fill the knowledge gap existing around the ON&LCN structure in health and disease. The development of CXEM and the data produced on the ON&LCN in this work have provided new insights into healthy and diseased bone tissue. In this discussion chapter, the key findings of the work and the potential implications for bone imaging, bone mechanobiology and the wider field of biomedical imaging are summarised. The findings are set in context of the state of the art for bone imaging, conclusions summarised and an outlook provided on future work.

Optimisation of sample preparation and image acquisition for CXEM. Chapter 3 outlined the optimisation of sample preparation for CXEM. The individual requirements of µCT and SBFSEM are met and the advantages of both techniques exploited to provide 3D data on the ON&LCN across length scales.

Quantitative bone morphometric measures for the ON&LCN. Chapter 4 detailed workflows which allow meaningful and relevant quantification of CXEM data. Image processing and analysis frameworks used to semi-automatically reconstruct and quantify the ON&LCN according to existing metrics were described and novel metrics defined. Quantitative measures include osteocyte number density, porosity, volume, shape, number and diameter of processes and PCS dimensions.

Derivation of quantitative hallmarks of bone tissue at the cell level in health. The investigation of developing murine tibia outlined in Chapter 5 compared the ON&LCN in

juvenile and adult animals. Novel findings include the first 3D measurement of PCS dimensions and the number of osteocyte processes per cell determined over a number of cells by direct measurement. These geometries may contribute to the design of computational models for bone mechanobiology.

Derivation of quantitative hallmarks of bone tissue at the cell level in disease. The application of CXEM to bone from OA and OP patients, as described in Chapter 6, yielded quantitative data although there were challenges to using the semi-automatic workflow. Insights into lacunar occupancy, cell health and cell ultrastructure were gleaned. These observations have implications for the assumptions often made that relate LCN data to the ON residing within.

In summary, CXEM was successfully developed, protocols established (Goggin et al., 2020) and meaningful data produced.

7.2 Critical analysis of CXEM as a technique for imaging of the ON&LCN

CXEM considers the osteocyte network in 3D firstly using μCT, over large volumes compared to CLSM and TEM and secondly, using SBF SEM, produces high-resolution 3D correlative imaging of cells and matrix over relatively large volumes compared to TEM and FIB-SEM. This project has shown that μCT imaging of decalcified and stained tissue can produce osteocyte density and porosity data reflective of the data produced from analysis of lacunae in calcified bone tissue. Significantly, the 3D osteocyte data is produced by direct measurement of the cell network rather than the negative imprint, the LCN.

As direct observation of fluid flow around cells and processes in the ON&LCN is not technically feasible, computational studies are employed to predict behaviours. In these studies pericellular geometries are often idealised by ignoring irregularities of both the

osteocyte and lacunar surfaces, geometries are simplified to a few smooth straight channels and simplifying assumptions are made (Figure 21) (Anderson et al., 2005, Han et al., 2004, Weinbaum et al., 1994b, Knothe Tate et al., 1998). In reality, the ON&LCN is complex, coarse, tortuous and branched (Figure 44). Idealisation affects the magnitude and range of imparted forces predicted to occur at a subcellular level. Increasing numbers of canaliculi in a model increase the range of pressures and shear stress increases (Anderson et al., 2005), that increased canalicular tortuosity increases osteogenic strain stimulation (Verbruggen et al., 2016) and increasing complexity predicts greater strain amplification (Verbruggen et al., 2012). CXEM data produced in this and future studies can be used in models with more realistic geometry leading to improved outcomes. Further work continuing that in (Anderson et al., 2005) and (Verbruggen et al., 2016) comparing simplified models with increasingly complex geometry, assessing variation of results in pressure, stress and strain should be carried out. For example, increasing the number of processes and canaliculi in an osteocyte model from the typical 2-10 to a realistic value would increase the resulting range of pressures and shear stresses. Using a realistically varied instead of a uniform pericellular space width would show more variations in the level of focal shear stress experienced by the osteocyte. Determining how much idealisation is appropriate and compromising with the size, time and cost of computation will be important considerations.

CXEM in healthy murine tissue was more successful than in diseased human tissue as the uptake of heavy metal stains by cellular material (osteocytes and vasculature) provides contrast. In healthy tissue, where a high proportion of lacunae are occupied, stained cells produced contrast in both X-ray and EM imaging facilitating semi-automated segmentation. In diseased tissue, a larger proportion of lacunae are unoccupied and some contain very small remnants of cells. This reduction in cellular material to take up the heavy

metal stains led to a reduction in detectable X-ray signal. SBF SEM imaging was not affected as the difference in resolution allows detection of the cellular material. Reduced signal and contrast made semi-automatic segmentation of the cells and lacunae impossible. The blood vessels, larger structures which were well stained and detectable were used as landmark features for registration, realignment and volume location. Adaptation of the workflow could improve results, producing density, porosity and lacunar occupancy data from μCT.

Imaging decalcified and stained bone tissue in μCT is novel and there are opportunities to develop and improve this part of the technique and apply it more widely. It is recognised that there is a need for 3D histology in studies of tissue anatomy and pathology (Roberts et al., 2012, Pichat et al., 2018). Some work has been done using X-ray specific cellular stains for μCT which stain either the nucleus (Müller et al., 2018, Metscher, 2020) or cytoplasm (Busse et al., 2018), but not both. X-ray histology (XRH) for unstained tissue is also in development (Katsamenis et al., 2019). CXEM has the advantage of providing contrast for μCT and also contrast and conductivity for EM. The tissue has further uses after large volume scanning. If CXEM is to be applied more widely for ON imaging it needs further improvement to make segmentation easier. This would enable automatic analysis of distribution of occupied and unoccupied lacunae across large volumes.

To apply CXEM to diseased tissue in future the protocol might be adapted to use a smaller μCT voxel size, to include SR CT imaging or to carry out a μCT scan before decalcification and staining take place. XRH may enable imaging of the ON&LCN and may be incorporated into future CXEM workflows. Correlation with LM would allow labelling and co-localisation of proteins, cytoskeletal components and indicators of cell health and cell death. Combined with immunogold labelling or quantum dots, LM could provide much more information about integrins and tethering elements, which require further investigation.

Thus, the present CXEM workflows produce 3D data on the ON&LCN across length scales but can be further optimised to image a wider range of tissue states.

7.3   Animal study – critical analysis and implications of results for bone research, pathology and treatments

Using animal tissue allowed CXEM to be optimised before application to human tissue. In order to build up a more complete picture of bone development, identification of the normal variation of features in healthy bone tissue conditions (sex, age, tissue age, anatomical site, loading condition, etc.) is required, although this is beyond the scope of this thesis.

As previous standardisations of bone measures (Dempster et al., 2013, Parfitt et al., 1987, Bouxsein et al., 2010) were based on histology and μCT both ultrastructural and cellular measures are currently lacking from these frameworks. In this thesis, new measures for cells, cell processes and the PCS have been defined. As imaging methods further improve the range of measures should be increased in a process of constant review and update.

Other studies have used μCT and EM to investigate the structure of the ON&LCN but this is the first to combine both methods in a correlative 3D approach. The CXEM results agree broadly with findings from these other studies (μCT (Tiede-Lewis et al., 2017, Hemmatian et al., 2017b), EM (Palumbo, 1986)).

No significant differences in osteocyte density and porosity were found between the anterior, posterior, medial and lateral regions of the tibia. No major significant differences in the ON&LCN measures were found between juvenile and adult animals in this study indicating that the period studied is not a time of microstructural change in tibial bone in male mice. Ageing is known to induce changes in the ON&LCN (Section 2.6.1) and it is likely

that the age of onset of these changes is later than the age of the animals studied here. Future studies of a wider age range would help to determine the onset of these age-related changes.

PCS.V was larger in juvenile animals. This result is also found in cortical bone of 15 weeks compared to 32 week mice (2D TEM measurements) (Lai et al., 2015). Larger lacunae (no related osteocyte data), have been observed in >2 year old compared to 2-14 year old humans, a period of rapid bone growth (Zimmermann et al., 2019). The juvenile mice in this study are analogous to the juvenile human (Figure 47). The 3D PCS data is robust as it has been obtained by 3D measurement and considers both the osteocyte and lacuna. Differences in PCS and fluid volume around osteocytes could lead to changed patterns of permeability, fluid flow, shear stress, mechanosensation and osteolytic activity by osteocytes. Data from more extreme ages would be interesting to obtain and compare in the future. Dimensions of the PCS around processes are not reported here but are interesting and relevant for intercellular communication between cells and fluid flow in bone's response to mechanical forces. To the author's knowledge no modelling of different pericellular space volumes and thicknesses has been carried out. Modelling the changes to shear stress caused by changes in PCS.V would be an important investigation.

This project has succeeded in imaging and quantifying unique data such as 3D osteocyte density and porosity, osteocyte PCS dimensions in 3D and the number and thickness of cell processes obtained from a relevant number of cells.

In summary, the study described in Chapter 5 shows few changes in the developing male mouse tibial ON&LCN. However, the application of CXEM to the tissue has successfully enabled imaging and quantification of features of the healthy developing murine ON&LCN, providing data that can be used in computational models of bone mechanobiology.

7.4   Human study – critical analysis and Implications of results for bone research, pathology and treatments

In this thesis, the first 3D CXEM and SBF SEM studies of human bone are presented. As in the animal study, CXEM has allowed measurement of the osteocytes and their relationship to the lacunae in which they reside. Additionally, and relevant in the case of bone disease, it is possible to observe cell ultrastructure and thus infer cell health and viability. Many lacunae in OP and OA tissue did not contain a healthy and assumedly functioning osteocyte. Many lacunae contained an unhealthy osteocyte and more still, material assumed to be the remnants of a cell which has undergone cell death. Complete removal of cells was not always observed, likely due to the difficulty of transporting cell debris through the LCN. Cells observed in diseased human tissue (OA and OP) vary in appearance and ranged from normal through stages of unhealthiness. These changes in cell condition are not observable using μCT alone, and may not be observable by many light microscopy techniques.

In tissue where lacunae contain very small remnants of cells, staining and thus detectable X-ray signal are reduced. CXEM of diseased human tissue does not produce μCT data with sufficient contrast for semiautomatic segmentation using the protocols set out in this thesis. Therefore, the production of measures derived directly from μCT data has not been possible. SBF SEM imaging of the same tissue however, provided image data which have been semi-automatically segmented and quantified, producing unique and accurate measures which have not been possible to date.

Lacunar number density is reported to be between 20,000 and 37,000 /mm^3 in healthy human bone tissue (Carter et al., 2013b, Dong et al., 2014b). Values for lacunar density in OA and OP bone samples in this study are lower than these results, ranging from 11,849 to 23,136 /mm^3. Osteocyte number density is lower still, ranging from 1,505 to 22,634/mm^3.

Reduced osteocyte and lacunar number density in diseased tissue agree with previous studies of OP (Zarrinkalam et al., 2012, Mullender et al., 2005, Qiu et al., 2003) and OA (Knothe Tate et al., 2004) and disagree with (Mullender et al., 1996b, Power et al., 2002), which found higher lacunar and osteocyte densities in OP than in controls. All the previous studies are based on 2D histology extrapolated to 3D. To the knowledge of the author this is the first study which directly images and quantifies the ON in human tissue in 3D. Notably, no significant differences between density in OA and OP were found.

Mean osteocyte number density is 40% of mean lacunar number density in OA and 35% of lacunar density in OP patients. Mean osteocyte porosity is 33% of lacunar porosity in OA and 26% of lacunar porosity in OP. These findings show that using lacunar density and porosity measures to represent osteocyte measures, particularly in diseased tissue is inaccurate.

Histological studies of OP and control human tissue found occupancy rates vary significantly between subjects and region examined , but not between OP and control tissue (Power et al., 2001, Power et al., 2002). The studies do not distinguish between healthy and unhealthy osteocytes. This CXEM study produces a similar result and also shows that many of the osteocytes occupying lacunae are unhealthy or dead in OP and OA tissue (Figure 75 and Figure 76). Studies of lacunar occupancy and ageing have produced conflicting results. (Tomkinson et al., 1997) report that the percentage of dead osteocytes increases with age to 75% while (Mullender et al., 1996b) found no significant correlation between empty lacunae and age. Thus, it would be interesting to use CXEM to investigate lacunar occupancy and cell health in healthy human bone tissue across the lifecourse before further investigation of the changes in disease.

It has not been possible to determine the type of cell death undergone by osteocytes using CXEM in this study. As apoptosis regulates osteoclast activity (Verborgt et al., 2000) using RIPK3 and caspase in future work to show whether apoptosis, necrosis or nectroptosis is occurring could lead to possible therapeutic investigations (reviewed in (An et al., 2020). There remains an open question of a method to better evaluate occupancy and cell health in 3D over a large volume. The option of a cell viability marker used with CLSM or indeed, SBF SEM used at lower pixel size and greater number of pixels to increase the volume should be explored.

It is important to note that age may have impacted on results in this study. The OP group are older than the OA group and it is not possible to separate features of aged tissue from features of disease. It would be ideal to be able to investigate healthy and age matched human tissue; this is not possible under the tissue collection ethics agreements in place for this study, which also limits the clinical details obtainable.

7.5   Limitations of this work

There are some limitations to the work presented in this thesis. It would be ideal to be able to investigate healthy and age-matched human tissue; this is not possible under the ethics agreements in place. Cadaveric tissue is not used as it is not fixed in a manner suitable for EM and if frozen for storage will exhibit ice crystal artefacts (Taqi et al., 2018).

The sample preparation needed for CXEM is complex and moves the tissue away from its native state. As discussed in Section 2.7.1, the ideal imaging method does not exist and compromises must be made and accounted for. There is a lack of complete control over time to human tissue fixation, which has been minimised as much as possible. The necessity of fixation rules out the acquisition of dynamic and temporal data including fluid flow or

solute transport rates. As discussed in Section 2.7.2 AFM and time lapse LM could be used to obtain this data.

The number of samples in both the human and animal studies is n=3 in each group. Increasing the numbers would ensure better representation of the population. However, the numbers of osteocytes and lacunae studied were high (mean n= 35,350 per sample). In order to build up a complete picture of the ON&LCN in bone tissue, identification of the normal variation of features in the healthy condition (sex, age, tissue age, anatomical site, loading condition, etc.) is required, although that is beyond the scope of this project.

Poor contrast and compromised semi-automatic segmentation are features of μCT imaging of diseased human tissue samples, which relies on attenuation of the beam by heavy metal staining. This is a major limitation and needs to be solved before CXEM can be applied to larger numbers of pathological samples. The workflow could be improved by adding a step of an additional μCT scan before the tissue is decalcified. The use of SRCT with smaller voxel sizes will also be considered for future studies.

Sample preparation including fixation, decalcification and staining remove the potential for imaging, measuring and understanding better the properties of the organic-inorganic interface. Mineral information is removed along with the possibility of determining changes in hardness and other mechanical properties of the cell, PCM and ECM, which can affect magnitude and distribution of mechanical signals perceived by the cells. PCM density influences fluid flow and osteocyte mechanosensation (Lai et al., 2021). The stiffness of chondrocyte PCM decreases in OA cartilage (Alexopoulos et al., 2003) and osteocyte morphology changes according to the stiffness of the substrate (Zhang et al., 2018). These findings show the importance of obtaining experimental data on the material properties of the ON, PCM and ECM and including them in computational models with geometries

obtained from CXEM. AFM or time lapse LM (Section 2.7.2) could be used to acquire this data.

Decalcification also excludes the consideration of micropetrosis, or filling of empty lacunae with mineral by CXEM (Busse et al., 2010). After decalcification and staining, micropetrosed lacuna appear empty using EM and using μCT the lacuna will not be visible. In undecalcified tissue, μCT will not detect the occupied lacuna. A technique to study this in 3D along with the remaining cells is needed. It is possible to use SBF SEM on mineralised tissue (Section 3.2.1.2.2). SBF SEM is not as widely available as μCT, although recent moves toward establishing UK centres of excellence to make vEM resources more widely available are underway (https://www.volumeem.org/).

7.6   Future perspectives

7.6.1   Multiscale models

Computational models of mechanobiological processes in bone tissue range from studies of cell networks using idealised geometry (Vaughan et al., 2013) to detailed geometrically accurate models of a length of a canaliculus (Kamioka et al., 2012). The study of Vaughan et al. indicates that strain is felt inhomogenously throughout the network depending on location and only a subset of osteocytes may be sufficiently stimulated to act as mechanoreceptors. The second study also predicts inhomogeneity, but this time in the microscopic surface roughness of the canalicular wall. While both approaches have produced valuable insights, there remains a need for multiscale modelling approaches which combine more than one level of structural hierarchy and integrate levels of bone structure (Giorgi et al., 2016, Paul et al., 2018). CXEM is ideally placed to provide images and data to enable creation of these models, helping to understand better the relationships

between global organ loading and local cellular signalling. Indeed, improvements to CXEM by inclusion of further levels of imaging using larger volume/lower resolution clinical imaging scans and/or smaller volume/higher resolution electron tomography, would allow construction of multiscale models over organ, tissue, cell and molecular levels.

A multiscale study considering distribution of osteocytes, osteoblasts and osteoclasts includes lacunae but ignores canaliculi (Pastrama et al., 2018). CXEM data could enable the inclusion of the processes and canaliculi, expanding the model to another scale. A recent multiscale model spanning organ, tissue and cellular levels highlights the need for experimental data on the dimensions and density of the PCS, detail which SBF SEM can contribute (Lai et al., 2021). A recent study using CLSM images of human osteons provides a useful framework on which future studies could be based (van Tol et al., 2020). The study of healthy human bone uses image data from CLSM, existing values for the LCN, a description of bone based on poroelasticity and circuit theory based on Kirchoff's laws to calculate the fluid velocity in individual canaliculi. The study is limited by the imaging depth of CLSM and would be enhanced by the use of 3D high-resolution CXEM data on the ON and processes.

7.6.2 **Characterisation frameworks**

A framework has been proposed for the quantitative characterisation of osteocyte lacunae and their 3D spatial relationships (Mader et al., 2013), which included shape, orientation, number density, spatial distribution, and alignment. This thesis has expanded this valuable framework to encompass cell measures and finer cell detail such as cell processes. In a study, where the ON has been related to the surrounding bone mineral quality, measures related to connectivity and spatial distribution were compared for the ON, including canalicular details (Kerschnitzki et al., 2013). Dong and colleagues used automated

quantification to extract 3D shape descriptors from SR CT data (Dong et al., 2014). Combining the measures in these studies with CXEM data from this study and including ultrastructural detail would lead to a more comprehensive standard data set.

7.6.3   Improvements in imaging

Developments in BSE detector technology, correlative microscopy (Brama et al., 2016, Starborg et al., 2019), immuno-labelling (Vihinen, 2012), integration of EDX systems (Zankel, 2011) beam deceleration (Bouwer et al., 2017) in-chamber coating (Titze and Denk, 2013), software capabilities (Titze et al., 2018), focal gas injection (Deerinck et al., 2018) and multibeam SEM imaging (Tate et al., 2016) continue to improve the capabilities of SBF SEM. The development of conductive resins (Ellisman, 2015, Nguyen et al., 2016) will improve image quality and reduce the amount of heavy metal staining required. Workflows for automated segmentation and machine learning are being developed and improved leading to a more streamlined workflow (Perez et al., 2014, Wernitznig et al., 2016, Liu et al., 2014, Hussain et al., 2018, Hennies et al., 2020). These approaches will require sufficient reliable annotated ground truth datasets.

The overall impact of these technological improvements will be less costly and faster imaging, improved resolution, automated segmentation and a reduction in the amount of heavy metal stain required to provide tissue contrast. This will allow further expansion of the qualitative and quantitative CXEM data to the finer details of cell processes and mitochondria. Data presented in this thesis can be further investigated using new techniques, for example, characterisation based on geometry (Callens et al., 2020).

7.6.4   **Applications**

Other bone diseases and conditions such as vitamin D deficiency or Paget's disease can be investigated using CXEM. The changes known to occur in the LCN during lactation also could be usefully investigated using CXEM.

The sample preparation, imaging and analysis methods developed for bone tissue in this project have been adapted and applied to dentine (Mahmoodi et al., 2020) and are currently being used to image odontoblast tubules (personal communication R.Cook). Other fields where a correlative workflow for hard tissue may be exploited in the future include studies of biomineralised tissues such as enamel, mineralised mollusc radula, plants, calcified pathological inclusions in tissue, nacre/shell, radiolarians, diatoms, fossilised material and mixed materials such as scaffolds and cells.

7.7   Overall conclusions and major impact

CXEM has provided novel 3D data on the ON&LCN in murine and human tissue. The PCS dimensions, number and diameter of cell processes and direct osteocyte measures have been obtained for the first time in murine and human bone tissue over a relatively large number of cells. Defined measures of ON&LCN structure were found to be unchanged in the anatomical quadrants of the murine tibia. PCS.V is significantly smaller in juvenile animals compared to adults. Other measures of the ON&LCN were unchanged from juvenile and adult animals.

CXEM was unable to provide osteocyte and lacunar number density and porosity measures from μCT imaging. SBF SEM produced quantitative data on osteocyte, lacunar and PCS measures, lacunar occupancy and cell health. No significant changes were observed between OP and OA tissue.

As discussed, idealization affects the results and predictions of computational models. With the CXEM data produced in this and future studies, more realistic geometry and measures can be fed into models leading to improved outcomes.

These results confirm that using lacunar number density and porosity as indicators of the respective osteocyte measures is accurate in healthy tissue but may not be reliable in diseased tissue. Using more realistic data in computational models will likely increase the predicted shear stresses and increase the heterogeneity of those stresses on the cell surface.

7.7.1   Questions and challenges which remain to be addressed

The challenge of imaging successfully the ON&LCN in diseased human tissue at the CT level needs to be further addressed. The data need to be incorporated into models. This study leads on to further exploration of ON&LCN structure in a wider range of ages in mice, more bone diseases and conditions. Expansion of the CXEM workflow to include more imaging techniques and length scales will be explored.

7.7.2   The future role of high-resolution 3D imaging in osteocyte anatomy and pathology

It is necessary to clarify the role of structural, microstructural and ultrastructural differences between the cell process and the cell body of osteocytes, between healthy, ageing and diseased tissue in sensation of mechanical stimuli and in the initiation of cell signalling.

Improvements will help to validate theoretical and computational models for strain magnification as well as quantifying bone interstitial fluid movement in response to mechanical loading. Questions still to be addressed include:

i)   What is the 3D structure of the ON&LCN at different sites of an entire bone sample?

ii)   How are the ON and the LCN and thus, the interstitial fluid flow altered in disease?

To answer these questions, existing 3D imaging techniques including CXEM need refinement and further development, and wider application in the field of bone research.

CXEM assessment of the ON&LCN in health and disease paves the way for the study of mechanotransduction mechanisms by computational models based on accurate geometries. This will lead to the identification of relevant features of healthy and diseased bone at the cell level, which could serve as targets for the diagnosis and treatment of bone-related diseases, impacting significantly on public health.

Appendix A   Sample preparation protocols

The protocols for TEM and CXEM sample preparation used in this project are set out in this section along with reagent and equipment requirements. Parts of the work presented here are also contained in the paper *Development of protocols for the first serial block-face scanning electron microscopy (SBF SEM) studies of bone tissue*. Bone 2020 Feb;131:115107

A.1   Reagents

REAGENT	VOLUME
3% glutaraldehyde (GA) (TAAB Laboratories Equipment Ltd., Aldermaston, UK), 4% formaldehyde (FA) (Fisher Scientific, Loughborough, UK) in 0.1M piperazinediethane sulfonic acid (PIPES) buffer (Fisher Scientific, Loughborough, UK) pH7.2	
0.1M PIPES buffer pH7.2	
2% aqueous osmium tetroxide (Oxkem, Reading, UK)	
7% aqueous EDTA (Fisher Scientific, Loughborough, UK)	

Osmium/ferrocyanide (reduced osmium):
 	
• *Reagents:*
  3% potassium ferrocyanide (VWR, Lutterworth, UK) in 0.2M PIPES buffer pH7.2
  4% osmium tetroxide
• *Method:*
  Mix the two components together just before use to produce 1.5% potassium ferrocyanide plus 2% osmium tetroxide in 0.1M PIPES buffer pH7.2
	5 ml
	
	5 ml

Distilled water	

Thiocarbohydrazide solution:
 	
• *Reagents:*
  Thiocarbohydrazide (Acros Organics, ThermoFisher Scientific, Geel, Belgium)
  Distilled water
• *Method:*
  Mix the two components together and place in an oven at 60˚C for 1 h (agitate by swirling every 10 min). Filter through 0.22 µm Millipore filter before use.
	0.1 g
	
	10 ml

2% aqueous uranyl acetate (Agar Scientific, Stansted, UK)	
Walton's lead aspartate solution:	

• *Reagents:* *Lead nitrate (Agar Scientific, Stansted, UK)* *0.03 M aspartic acid (Acros Organics, ThermoFisher Scientific, Geel, Belgium)* • *Method:* *Mix the two components together and adjust to pH 5.5 with 1 M KOH. Place in oven for 30 min (no precipitate should form).*	*0.066 g* *10 ml*
Ethanol series 30%, 50%, 70%, 95%, absolute (Fisher Scientific, Loughborough, UK)	
Acetonitrile (Fisher Scientific, Loughborough, UK)	
Agar low viscosity resin (Spurr replacement) (Agar Scientific, Stansted, UK)	
Toluidine blue (Agar Scientific, Stansted, UK)	
Conductive glue (CircuitWorks Conductive Expoxy CW2400; ITW Chemtronics, GA, USA)	
Contact adhesive/glue (Pattex; Henkel, Düsseldorf, Germany)	

A.2   Equipment

Single-edged razor blades (Fisher Scientific, Loughborough, UK)
Fine toothed double bladed 'razor' saw (JLC, Czech Republic)
Fine forceps (No preferred supplier)
Glass knives (Agar, Scientific, Stansted, UK)
Cocktail sticks or fine paintbrush (No preferred supplier)
Glass vials (Fisher Scientific, Loughborough, UK)
EM grids(EM Resolutions, Sheffield, UK)
Glass slides (No preferred supplier)
Ultramicrotome (No preferred supplier)
Light microscope (No preferred supplier)
Rotator (No preferred supplier)
pH meter (No preferred supplier)
Plastic pipettes (Fisher Scientific, Loughborough, UK)
Oven at 60°C (No preferred supplier)
Embedding capsules (TAAB Laboratories Equipment Ltd., Aldermaston, UK)
Sputter coater (Quorum Technologies, Laughton, UK)
Aluminium pins (EM Resolutions, Sheffield, UK)

A.3 Protocol for TEM sample preparation

A.3.1 Bone tissue samples

This protocol has been developed for the preparation and imaging of murine and human bone. Collect tissue samples in accordance with the relevant local ethics regulations and legal guidelines. Fixation must be carried out as quickly as possible after excision, to preserve the ultrastructure and to arrest avoid autolytic changes in the osteocytes. Many of the reagents used in this protocol are hazardous. Appropriate risk assessments should be carried out and mitigation measures put in place.

A.3.2 Fixation

<u>It is important that the tissue is never allowed to dry during this protocol</u>. Unless otherwise indicated all stages are carried out at room temperature and solutions are rotated on a laboratory rotator during each stage.

1. Fix tissue by perfusion with 3% GA, 4% FA, in 0.1MPIPES buffer or if this is not possible, immerse in fixative immediately after excision.

2. Cut blocks of tissue < 2 x 2 x 2 mm with a single-edged razor blade, diamond saw or fine-toothed, double-blade razor saw from the selected area(s) without allowing the tissue to dry out. Immerse blocks in 3% GA, 4% FA, in 0.1M PIPES for at least 6 h. Tissue can be stored at 4°C for up to a week at this point. Rinse in 0.1M PIPES buffer (2 x 10 min) and place in 2% aqueous osmium tetroxide for 1 h.

A.3.3 Decalcification

Decalcify tissue blocks by immersing in 7% EDTA for 1 week, changing the solution daily.

A.3.4 Staining and resin embedding

Immerse tissue in each fluid as indicated below in a glass vial. Up to 6 pieces of tissue can be processed in each vial.

Solution	Temperature	Time
Main fixative	RT	6 h
Buffer rinse	RT	2 x 10 min
1% osmium tetroxide	RT	1 h
Buffer rinse	RT	2 x 10 min
2% uranyl acetate	RT	20 min
30% ethanol	RT	10 min
50% ethanol	RT	10 min
70% ethanol	RT	10 min
95% ethanol	RT	10 min
Absolute ethanol	RT	20 min
Absolute ethanol	RT	20 min
Acetonitrile	RT	20 min
50:50 Acetonitrile:ALV resin	RT	overnight
ALV resin	RT	6 h
Embed in capsules in fresh ALV resin	60 ˚C	20-24 h

A.3.5 Microtomy

Semi-thin (0.5-1 μm) sections may be taken, stained with toluidine blue and examined using a light microscope. Ultrathin (~90 nm) sections are taken, mounted on grids, stained with lead citrate for 5 minutes and examined using a TEM.

A.4 Protocol for SBF SEM sample preparation

A.4.1 Bone tissue samples

This protocol has been developed for the preparation and imaging of murine and human bone.

Collect tissue samples in accordance with the relevant local ethics regulations and legal guidelines.

Fixation must be carried out as quickly as possible after excision, to preserve the ultrastructure and

to arrest avoid autolytic changes in the osteocytes. Many of the reagents used in this protocol are

hazardous. Appropriate risk assessments should be carried out and mitigation measures put in

place.

A.4.2 Fixation

It is important that the tissue is never allowed to dry during this protocol. Unless otherwise

indicated all stages are carried out at room temperature and solutions are rotated on a laboratory

rotator during each stage.

1. Fix tissue by perfusion with 3% GA, 4% FA, in 0.1MPIPES buffer or if this is not possible,

    immerse in fixative immediately after excision.

2   Cut blocks of tissue < 2 x 2 x 2 mm with a single-edged razor blade, diamond saw or fine-

    toothed, double-blade razor saw from the selected area(s) without allowing the tissue to dry

    out. Immerse blocks in 3% GA, 4% FA, in 0.1M PIPES for at least 6 h. Tissue can be stored at

    4°C for up to a week at this point. Rinse in 0.1M PIPES buffer (2 x 10 min) and place in 2%

    aqueous osmium tetroxide for 1 h.

A.4.3 Decalcification

Decalcify tissue blocks by immersing in 7% EDTA for 1 week, changing the solution daily.

A.4.4 Staining and resin embedding

Immerse tissue in each fluid as indicated below in a glass vial. Up to 6 pieces of tissue can be processed in each vial. Blocks may be embedded in plastic capsules or minimally embedded. For minimal resin embedding, after resin infiltration place samples on absorbent paper and gently move around until excess resin is absorbed. Resin in the medullary cavity can be removed with a small piece of twisted tissue paper before resin polymerisation at 60 °C.

Solution	Temperature	Time
Osmium/ferrocyanide	On ice	1 h
Rinse in distilled water	RT	5 x 3 min
Thiocarbohydrazide solution	RT	20 min
Distilled water rinse	RT	5 x 3 min
2% osmium tetroxide	RT	30 min
Distilled water rinse	RT	5 x 3 min
2% uranyl acetate	4°C	1 h
Distilled water rinse	RT	5 x 3 min
Walton's lead aspartate solution	60 °C	30 min
Distilled water rinse	RT	5 x 3 min
30% ethanol	RT	10 min
50% ethanol	RT	10 min
70% ethanol	RT	10 min
95% ethanol	RT	10 min
Absolute ethanol	RT	20 min
Absolute ethanol	RT	20 min
Acetonitrile	RT	20 min
50:50 Acetonitrile:ALV resin	RT	overnight
ALV resin	RT	6 h
Embed in capsules in fresh ALV resin	RT	
ALV resin	60 °C	overnight

A.4.5   Light microscopy

Semi-thin (0.5-1 µm) sections may be taken, stained with toluidine blue and examined using a light microscope (Figure 36). Ultrathin (~90 nm) sections may be taken and examined using a TEM before proceeding to SBF SEM block preparation in order to confirm sample orientation, allow selection of an area of interest and confirm fixation quality.

A.4.6   Sample trimming, mounting and SBF SEM imaging (Figure 37 and Figure 38)

1. Trim the block-face with a single-edged razor blade or glass knife to a surface area of < 800 µm^2 with the region of interest (ROI) near the centre and remove it from the resin block using a sharp, single-edged razor blade. A piece of laboratory film, placed over the surface during removal, can protect against loss of the tissue sub-volume.

2. Attach the block to an aluminium pin using conductive adhesive to enhance conductivity and reduce the build-up of negative surface charge and its adverse effects, such as blurring and distortion of the image.

3. Trim the surface to produce a flat block-face using a glass knife or a diamond trimming knife.

4. Sputter-coat the mounted samples with a layer of metal (Au, Pt or Pd) to further reduce the build-up of surface charge.

5. Apply a thin layer of contact adhesive to the edge of the block which will be cut first by the diamond knife.

6. Place the pin in the SBF SEM system.

7. Adjust the height while observing the knife edge and block-face. Ensure the 'stroke-up' control is activated. This raises the sample by approx. 10 microns for cutting (so that it can drop again when the knife retracts, avoiding contact between knife and block)

8. Set the initial settings to 100 nm slice thickness, 100 slices.

9. Start approach and watch until the complete block-face is exposed.

10. Move the knife to the 'clear' position and clean debris from the block-face and knife edge using an air duster. Close door and pump down chamber.

11. Suggested settings for 3View® 2XP on a FEI Quanta 250 FEGSEM : accelerating voltage of 3 kV, spot size 3.5, chamber pressure 60 Pa, 4k × 4k image size at 5-50 nm pixel size (varies with desired field of view and time available).

12. Optimise focus and stigmator settings.

13. Set slice thickness, number of slices and autofocus.

14. Start data collection.

Appendix B   Workflows for image processing

B.1   Image processing and segmentation workflow for X-ray μCT data

Briefly: Bone tissue is prepared and imaged according to the protocols in Appendix A. Images are prepared for image processing and cortical bone is separated from the background and bone marrow. The heavy metal stained elements comprising the osteocytes and the vascular tissue are extracted, separated from each other using a volume filter and the osteocytes are quantified using measures defined in Section 4.4.

B.1.1   Preparation for image segmentation

Following image acquisition, raw data (X-ray projections) are reconstructed using standard filtered back-projection (Zeiss reconstruction software) and exported as a 16-bit tiff stacks for visualisation and analysis.

During scanning the bone tissue samples are held in a plastic tube. It is not always possible to orient the samples vertically resulting in some bones not being aligned with the image z-axis. Murine bone samples need to be aligned before separation into quadrant volumes. The Moments of inertia feature in the BoneJ plugin (Doube et al., 2010) in Fiji (Schindelin et al., 2012) is used to realign the bone with the z-axis of the stack (Appendix C.3). This plugin calculates the three principal orthogonal axes and moments of inertia around these axes before creating a new stack with the image centred and rotated so that the principal axes are parallel to the image stack's x, y and z axes (Figure 81). The new stack is saved.

Using the same macro, the aligned stack is split into 4 quadrants (posterior, anterior, medial and lateral) along the bone z-axis. These 4 quadrants are saved as individual stacks and analysed separately later in the workflow.
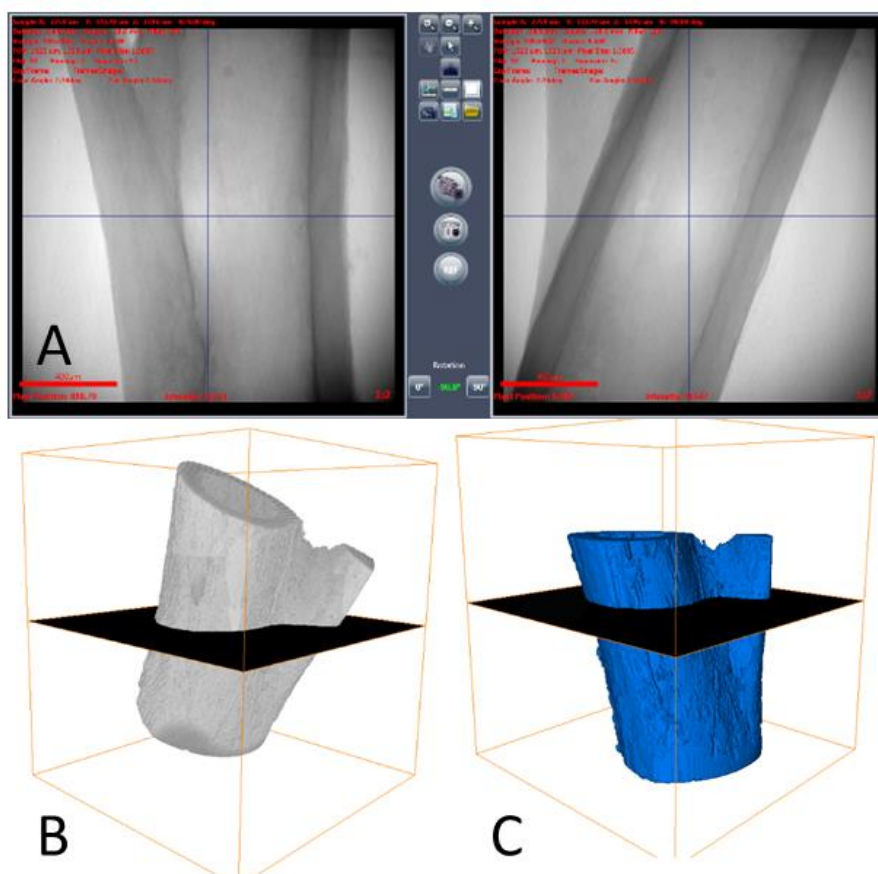
Figure 81   Alignment of data using Moments of Inertia plug-in

A   Radiographs taken of a bone sample during acquisition set-up with 90 degree rotation showing that the sample is not vertical during scanning.

B   Reconstructed data stack before realignment.

C   The same data after realignment with the imaging z-axis using Moments of Inertia plugin in BoneJ.

An intensity gradient from the periosteum to the endosteum was observed in the reconstructed stack (likely a stain penetration gradient). A custom bandpass filter (Appendix C.1) is used to enhance the edges and reduce the gradient's influence on the subsequent segmentation (Figure 82). Bandpass filters remove noise and bring edges (high frequency components) forward. Gradients are considered low frequency in the Fourier space and thus are excluded. Variation in the overall intensity per slice introduced by the bandpass filter is normalised using Fiji (Appendix C.2).
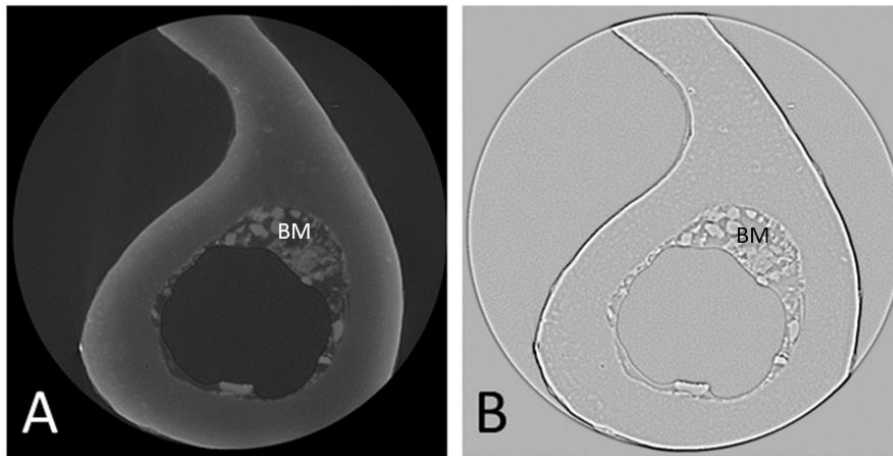
Figure 82   Bandpass filter

A   Raw data from Versa 510 µCT scanner showing decalcified and heavy metal stained tissue from murine tibia. Note the bone marrow (BM) remaining within the cortical bone.

 B   Image after application of a band pass filter used to remove the gradient.

B.1.2   Bone segmentation

Cortical bone tissue is segmented semi-automatically from the background and the bone marrow cavity using the 'blow' segmentation tool in Avizo. The blow tool allows the semi-automatic selection of areas with homogenous grey values and defined edges. Because some of the samples may have amounts of marrow remaining in the cavity (Figure 82), the blow tool may select the marrow as part of the tissue, thus producing an inaccurate result along the endosteal edge. To correct this, the brush tool in Avizo is used to modify the area defined with the blow tool by manually removing the marrow. The result of this segmentation is a binary label with two intensity values, 0 (black) for the background and the bone marrow cavity, and 1 (white) for the cortical bone (Figure 83). This binary label is then eroded (reduced in size) by three pixels and used as a mask on the greyscale images to select only the bone matrix excluding the bone marrow and the background. Using an eroded label ensures that the final masked image is entirely within the cortical bone volume.

B.1.3   Osteocyte and vascular tissue segmentation

The brightness value of the bone tissue was increased to enhance visualisation of the heavy metal stained soft tissue (osteocytes and vasculature) by adding an offset to the pixel values. The 'interactive threshold' feature in Avizo was used to select only the heavy metal stained tissue including osteocytes and vasculature (blood vessels), and convert that selection into a 3D binary label output (Figure 83). Interactive thresholding sorts greyscale pixels by changing them to black if they are within a certain greyscale range (threshold) and white if they are outside that range. As the heavy metal stain used during sample preparation is preferably taken up by soft tissue components in the bone (osteocytes and vasculature), they produce a stronger X-ray signal and thus appear brighter in the images. Interactive thresholding separates the cellular part of bone from the background matrix which is not as strongly stained.

B.1.4   Separation of osteocytes from vascular tissue

The 'Label analysis' feature, which computes pre-defined measures on each component of a binary image was used to measure the volume of all objects in the binary label. Based on knowledge of osteocyte dimensions from previous TEM and SBF SEM studies (Goggin et al., 2020, Goggin et al., 2016) using 50 and 400 μm^3 as upper and lower limits, the labels were sieved by volume to remove noise (< 50 μm^3) and vascular components (> 400 μm^3) of the bone, leaving the osteocytes.

The quadrant stacks (see Preparation for image segmentation above) were converted to binary labels and used as masks to select the osteocytes in each quadrant from the complete osteocyte binary label (Figure 84).
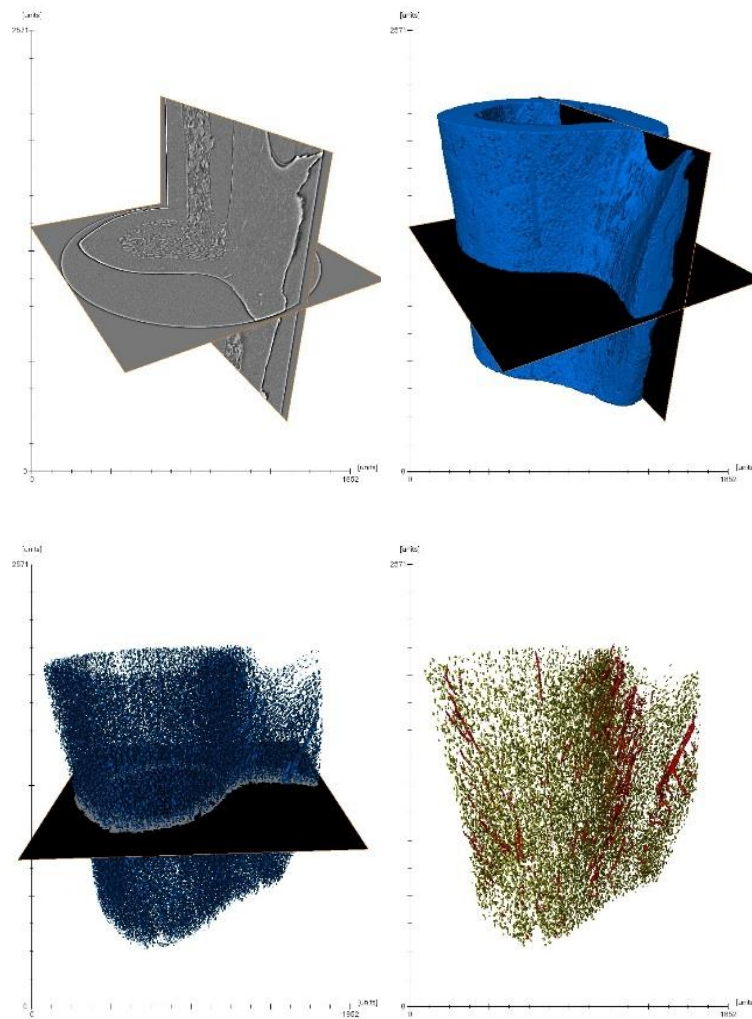
Figure 83   Stages of image processing shown on murine bone

A   Data which has been prepared for segmentation

B   Binary label of bone matrix

C   Stained cells and tissue selected from volume

D   Osteocytes (yellow) and vascular tissue (red) separated by volume and sieve

              analyses.
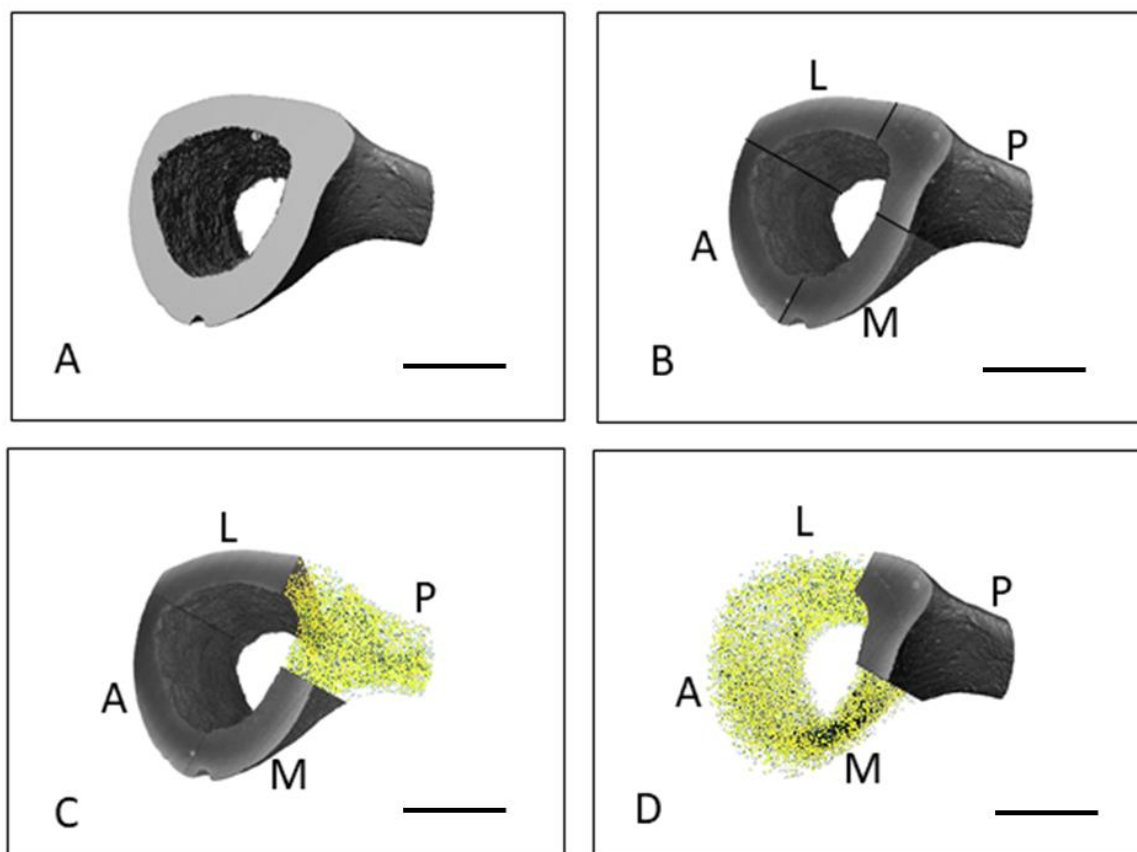
Figure 84   Division of tibia into quadrants and selection of osteocytes.

A   Binary label of total bone volume

B   Binary label divided into anterior (A), medial (M), posterior (P) and lateral (L)

             quadrants.

C   Osteocytes (yellow) located in posterior anatomical volume.

D   Osteocytes (yellow) located in medial, anterior and lateral volumes.

Scale bars = 200 µm

B.2   Image processing and segmentation workflow for SBF SEM data

Briefly: After selection and trimming of a sub-volume of interest the bone tissue is re-

imaged using SBF SEM according to the protocol in Appendix A.4.6. After preparation for

image processing, the osteocytes, pericellular space and bone matrix are segmented and

separated ready for quantification.

B.2.1   **Preparation for image segmentation**

SBF SEM images of the ON&LCN are acquired as .dm3 files using Digital Micrograph (DM) (Gatan, UK) software as described in Appendix A.4.6. The automated image alignment feature in DM is used to eliminate sample drift or 'jumps' which can be caused by charge build up on the sample during image collection. During this process lateral shift in an image stack is measured and removed, creating a newly aligned stack of images. Pieces of resin debris which have been removed from the block may result in occasional z slices having different (usually lower) image contrast. The Normalize Z Planes feature in DM analyses the grey levels and changes the range of pixel intensity values to match a defined calibration image, increasing the dynamic range to achieve consistency in the dataset. Images are then converted to .tiff format using the DM Batch Convert command.

B.2.2   **Segmentation using Trainable Weka Segmentation**

The osteocyte cell bodies, processes and the PCS space are segmented and visualised using the Trainable Weka Segmentation 3D plug-in (Arganda-Carreras et al., 2017) (Figure 43 and Figure 85) as described.

1. Open 20 consecutive slices from the stack as a representative 'training' dataset.

2. In the settings menu, select mean and variance as training features, minimum sigma = 1, maximum sigma = 8.

3. Create 3 classes and label them matrix, cell and pericellular space.

4. Trace lines on typical areas of each class over several slices and add to class.

5. Train classifier.

6. Assess classification result; retrain if needed by tracing more examples, save classifier.

7. Apply classifier to complete data stack using macro in Appendix C.4.

The result of the Weka segmentation is a series of labels, one per class, with separate grey values, making them easy to separate into the various compartments (cell, PCS, matrix) (Figure 85).
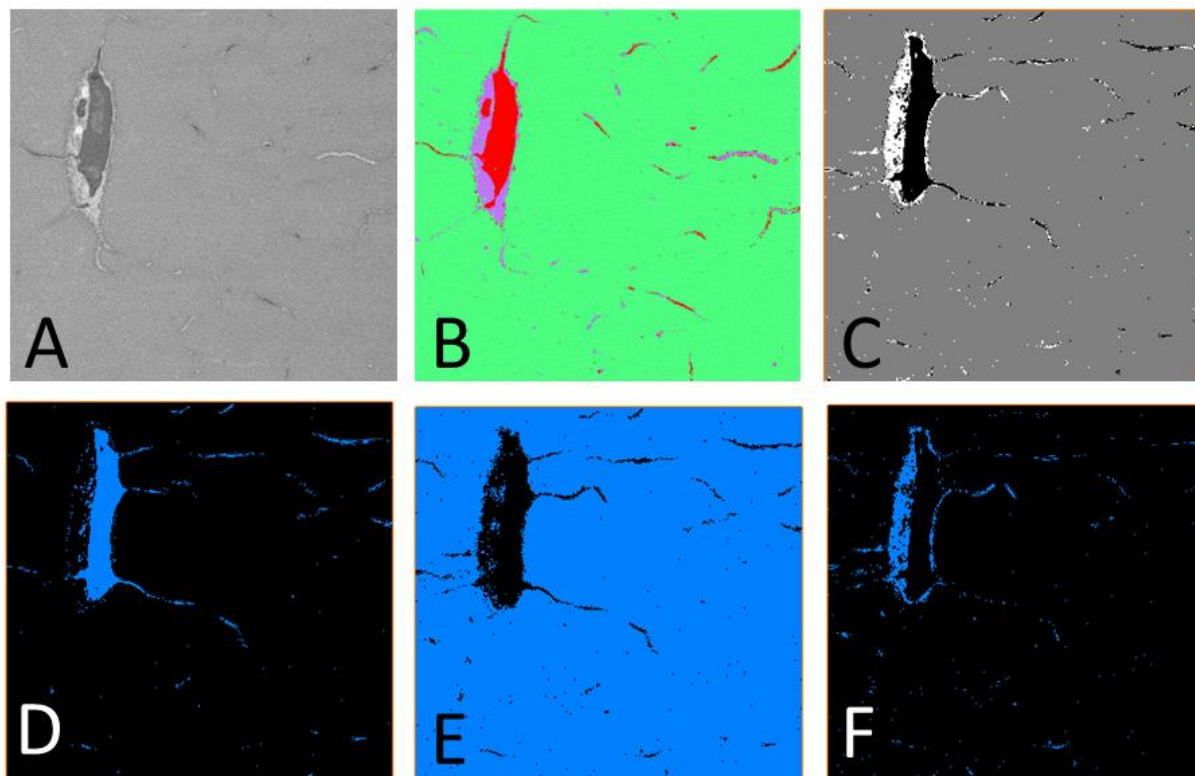
Figure 85   Trainable Weka segmentation results

A   Slice from SBF SEM stack

B   Result of Weka segmentation of slice in A, green – matrix, red - osteocyte, purple – pericellular space.

C   Weka segmentation result

D, E, F   Separation of C produces binary labels (blue) of the osteocyte (D), bone matrix (E), and PCS (F).

B.2.3   Separation of osteocytes, PCS and matrix

After segmentation, the data stack is opened in Avizo and the cell, matrix and PCS classes separated using thresholding. Osteocyte cell bodies and processes are separated into

individual labels by performing an opening operation (erosion followed by dilation) on the cell binary label.

B.3   Quantification of data from CXEM images

This section describes the outputs obtained and calculations used to determine the quantitative measures of the ON&LCN from CXEM data.

B.3.1   Quantification of osteocyte density and porosity from μCT data

Bone volume (BV) is obtained from a label analysis of the bone label in Avizo. The total number of osteocytes and the volume of each osteocyte are obtained from the osteocyte label using the label analysis module in Avizo and a custom measure group (Figure 86). Some measures correspond to direct quantitative outputs while others allow output measures such as density and porosity to be calculated. Calculations are listed in Table 25.

B.3.2   Quantification of osteocyte measures by anatomical area.

Division of tibial bone into anterior, posterior, medial and lateral quadrants for separate analysis is carried out in Avizo. Quantification is carried out using the label analysis module and the pre-defined set of measures.

Figure 86   Label analysis panel in Avizo

Label analysis panel shows individual osteocyte measures, mean osteocyte measures, osteocyte volume (Ot.V) and total number of osteocytes (N.Ot).

Table 25   Measures, direct outputs and equations used to calculate indirect outputs.

Measure	Abbreviation	Avizo output	Equation
Bone volume	BV	Volume3d	
Number of osteocytes	N.Ot	Max index	
Osteocyte number density	(N.Ot/BV)		(N.Ot/BV)
Osteocyte breadth	Ot.B	Breadth 3d	
Osteocyte length	Ot.Le	Length 3d	
Osteocyte width	Ot.Wi	Width 3d	
Osteocyte surface area	Ot.A	Area 3d	
Osteocyte volume	Ot.V	Volume 3d	
Total osteocyte volume	Tt.Ot.V		sum of Ot.V
Mean osteocyte volume	<Ot.V>		Tt.Ot.V/N.Ot
Osteocyte porosity	(Tt.Ot.V/BV)		(Tt.Ot.V/BV)
Shape factor		Shape_VA3d	$\dfrac{Area3d^3}{36\,\pi\,Vol3d^3}$
Osteocyte anisotropy	Ot.An*	Anisotropy*	
Osteocyte flatness	Ot.Fl*	Flatness*	
Osteocyte sphericity	Ot.Sph*		$(\dfrac{1}{ShapeVA3d})^{1/3}$
Pericellular space volume	PCS.V	Volume 3d	
PCS width	PCS.Wi	Distance map	
PCS thickness	PCS.Th		$PCS.Th = Ot.V/(4*\pi*Ot.r^2)$
Lacunar volume	Lc.V		Ot.V + PCS.V
Process diameter	Pr.Dm*		(sqrt(area/π) x 2
Process thickness	Pr.Th*	Distance map	

*Not standard measures in (Dempster et al., 2013, Bouxsein et al., 2010)

B.4 Quantification of data from SBF SEM images

The measures set out in Table 25 are obtained for SBF SEM data in a similar way to the quantification of µCT data using the label analysis feature in Avizo and the equations shown. Additionally, process and pericellular space data is obtained as follows.

B.4.1 Process measures

The number of cell processes per cell and the process diameter are determined using Avizo (Figure 87). An ellipsoid is fitted around each cell body using the Volume Edit feature. A new binary label consisting only of the voxels that are coincident with the ellipsoid is created. The number of these coincidences, determined using the Label Analysis feature gives the number of processes while the area of each coincidence is used to calculate the process diameter (Pr.Dm) at the point of coincidence using the equation in Table 25 which assumes that each process has a circular profile. A visual check is carried out to identify outliers, where the process crosses the ellipsoid far from perpendicular producing a large result, and these are removed.
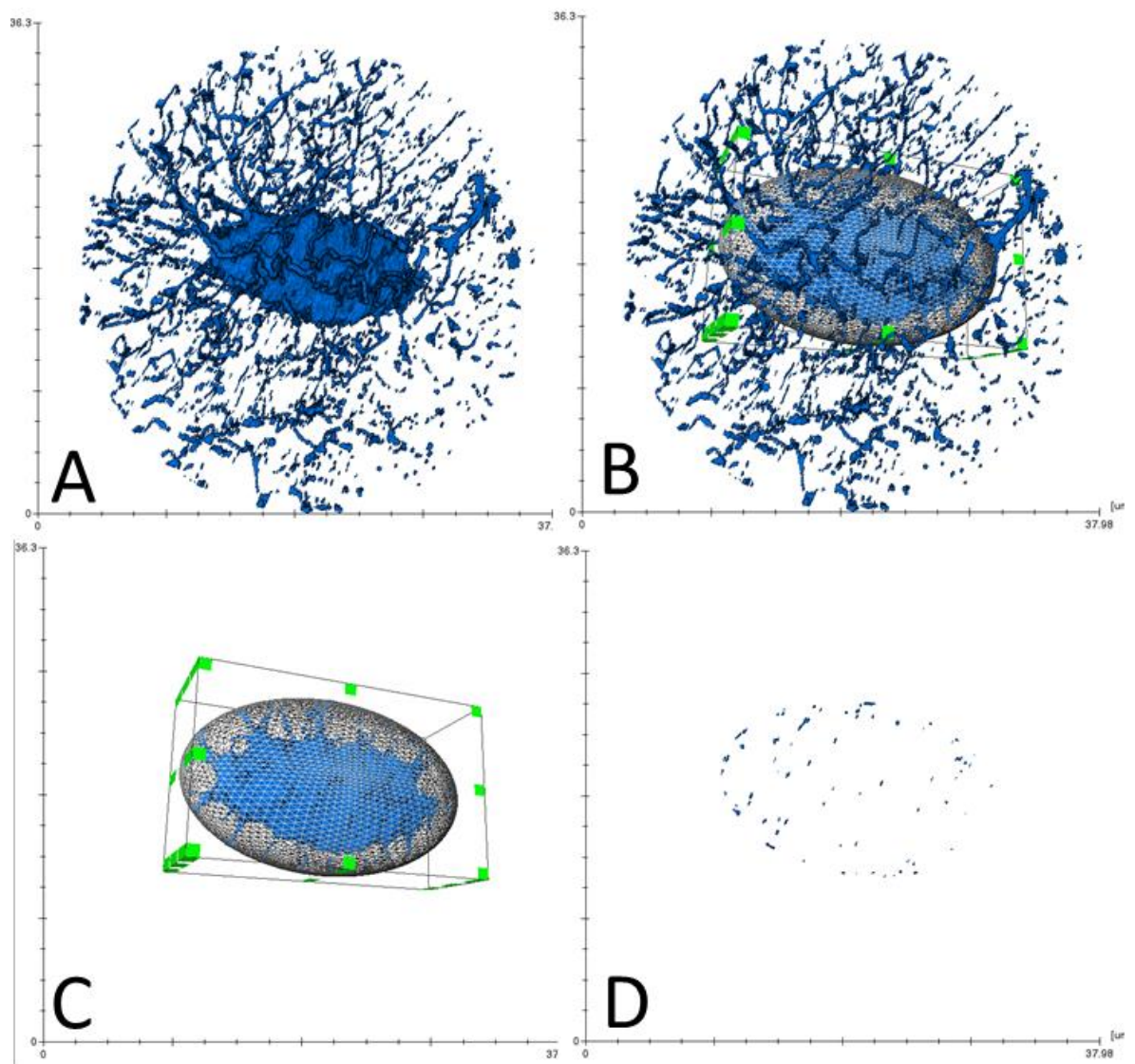
Figure 87   Obtaining process measures using Avizo

A   3D volume rendering of an osteocyte and processes

B   3D volume rendering of an osteocyte and processes with fitted ellipsoid

C   Fitted ellipsoid enclosing osteocyte cell body with external processes removed

D   Coincidence of processes and ellipsoid from which process diameter (Pr.Dm)

               measure is calculated.

B.4.2   Pericellular space

PCS.V is obtained from Volume3d results of the PCS label in the same way as the osteocyte

label (Figure 88). The pericellular space is not a uniform thickness around the cell (Figure

88). At some points the cell is in contact with the lacunar wall indicating a PCS.Wi = 0 and

at other points it is at a distance. To determine the PCS width around the cell, firstly Lc.V is

calculated by adding together Ot.V and PCS.V labels. A binary mesh one voxel thick defining the outline of the outer edge of the lacuna is created. A distance map is created from the edge of Ot.V outwards using the Distance Map feature (Figure 88 D). Multiplying that distance map by the binary outline produces PCS.Wi.

Pericellular space thickness is defined as the thickness of the PCS.V evened out around the cell assuming that both cell and lacuna are spheres. The volume of a spherical shell is the difference between the enclosed volume of the outer sphere and the enclosed volume of the inner sphere:

Where r is the radius of the inner sphere (osteocyte) and R is the radius of the outer sphere (lacuna). An approximation for the volume of a thin spherical shell is the surface area of the inner sphere multiplied by the thickness t of the shell: t V / 4 π r ^{2} when t is very small compared to r $(PCS.T = Ot.V/(4\pi\ Ot.r^2)$
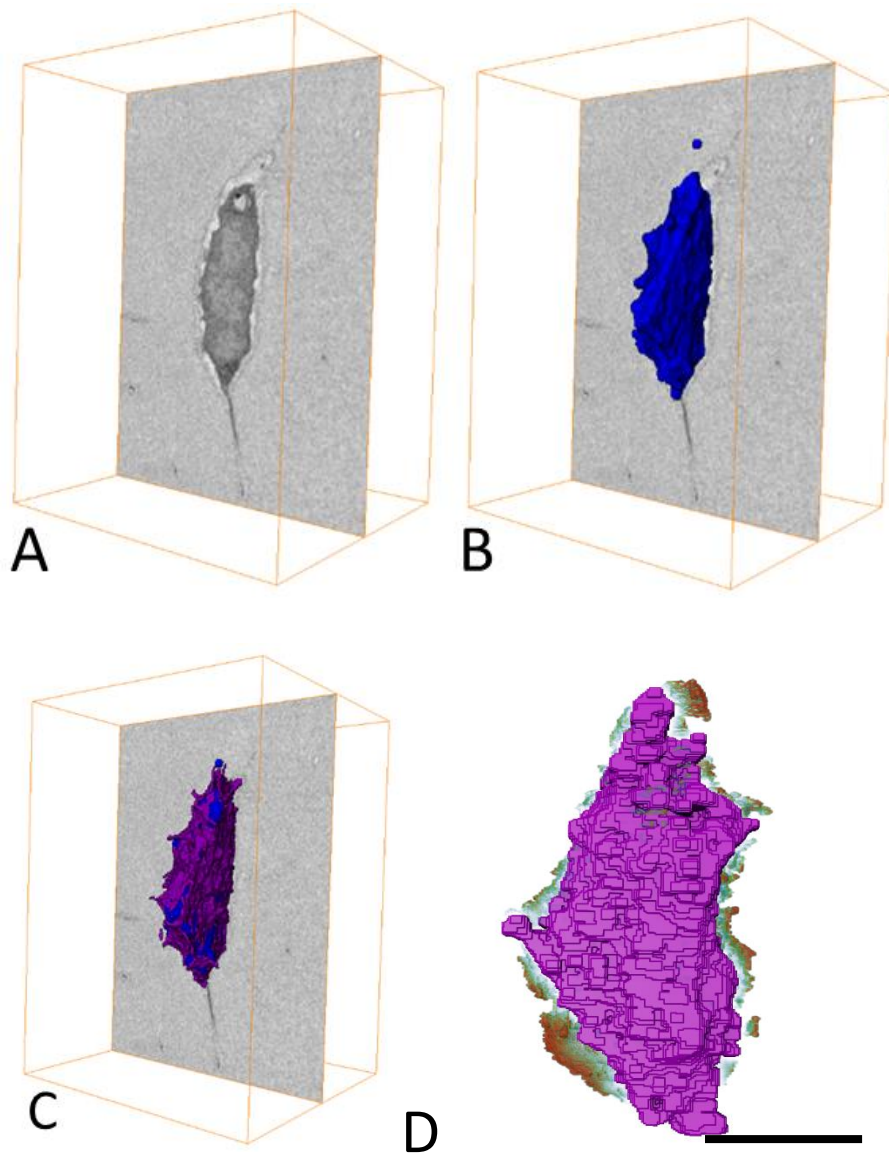
Figure 88   Pericellular space reconstruction and measurement of width

A   SBF SEM data showing an osteocyte and surrounding PCS

B   SBF SEM data showing 3D reconstruction of osteocyte cell body (blue)

C   SBF SEM data showing 3D reconstructions of osteocyte cell body (blue) and pericellular space (purple).

D   The width of the PCS surrounding the cell (purple) is calculated using a distance map. The widest PCS is shown in red. Scale bar = 5 μm

Appendix CMacros for image processing

C.1   Bandpass filter macro

```
dir = getDirectory("select image sequence folder");

files = getFileList(dir);

Array.sort(files);

setBatchMode(true);

for(i = 0;i<files.length;i++){

        open(files[i]);

        titleImage = getTitle();

        run("Duplicate...", "duplicate");

        rename("filter");

        // fiter params ___

        //run("Bandpass Filter...", "filter_large=15 filter_small=2 suppress=None tolerance=5 autoscale
saturate display process");

        run("Bandpass Filter...", "filter_large=10 filter_small=2 suppress=None tolerance=5 autoscale
saturate");

        resetMinAndMax();

        selectWindow("filter");

        run("32-bit");

        resetMinAndMax();

        run("Divide...", "value=65535 stack");

        setMinAndMax(0, 1);

        selectWindow("filter");

        saveAs("TIFF", dir + titleImage + "_BPF.tif");

        run("Close All");
```

```
}

exit("MACRO FINISHED");
```

C.2   Z-axis normalisation macro

```
*/

dir = getDirectory("Select the folder contaning the sequence of image");

list = getFileList(dir);

run("Image Sequence...", "open=["+dir+list[1]+"] sort");

titleImage = getTitle();

setTool("rectangle");

waitForUser("draw a rectangle in the background, then click OK");

run("Duplicate...", "title=background duplicate");

selectWindow(titleImage);

run("Select None");

rename("volume");

run("Clear Results"); run("Set Measurements...", "mean min redirect=None decimal=3");

negativeBckValueFlag =0; negativeBckValue =0;

selectWindow("background"); //run("32-bit");

greyBckCore = newArray(nSlices);

for (i=1;i<=nSlices;i++) {

        setSlice(i);

        run("Select All");

        run("Measure");

        greyBckCore[i-1] =getResult("Mean",i-1);

        // linear shift to positive values (in case of 32bit datasets)
```

```
        if (greyBckCore[i-1]<negativeBckValue){

                print ("negative Grey value fount!");

                negativeBckValueFlag =1;

                negativeBckValue =greyBckCore[i-1];

                }

}

selectWindow("volume"); run("32-bit");

//print(negativeBckValueFlag);

if (negativeBckValueFlag==1) {

        print ("Flag =1; Shifting to positive valuers");

        for (i=1;i<=nSlices;i++) {

                setSlice(i);

                corValueTemp = greyBckCore[i-1]-negativeBckValue;

                run("Subtract...", "value=corValueTemp slice");

                }

        }

else {

        for (i=1;i<=nSlices;i++) {

                setSlice(i);

                greyBckCoreTemp=greyBckCore[i-1];

                run("Subtract...", "value=greyBckCoreTemp slice");

        }

}

resetMinAndMax();
```

```
run("16-bit");

run("32-bit");

run("Divide...", "value=65535.000 stack");

setMinAndMax(0,1);

saveAs("TIFF", dir + titleImage + "_filteredZaxis.tif");

close();

selectWindow("Results");

run("Close");

selectWindow("background");

close();

exit("MACRO FINISHED");
```

C.3   Alignment and Quadrant Macro

Fiji Macro using IJ1Macro language

```
/*This macro splits the bone into quadrants (anterior, posterior, lateral

 * and medial) using the Moments of inertia function from the BoneJ plugin.

 * Inputs are tif image sequence of bone μCT and tif image sequence of bone

 * label, each in their own folder.

 * Output will be results from the boneJ plugin and tif image sequence of

 * the different quandrants.

 */

// Asking the user the locations of the different datasets

dir1 = getDirectory("Select the folder contaning the sequence of images");

dir2 = getDirectory("Select the folder contaning the sequence of image labels");

dir3 = getDirectory("Select the folder to save results");
```

Appendix

```
// Opening the µCT and label datasets

list1 = getFileList(dir1);

run("Image Sequence...", "open=["+dir1+list1[1]+"] sort");

titleImage = getTitle();

imageName = File.nameWithoutExtension;

list2 = getFileList(dir2);

run("Image Sequence...", "open=["+dir2+list2[1]+"] sort");

titleLabel = getTitle();

//Smoothing the label dataset with a median filter

selectWindow(titleLabel);

run("Median...", "radius=2 stack");

imageCalculator("Multiply create stack", titleImage,titleLabel);

titleResult = getTitle();

selectWindow(titleLabel);

close();

selectWindow(titleImage);

close();

// Calculate moments of inertia (boneJ plugin)

selectWindow(titleResult);

Stack.getDimensions(width, height, channels, slices, frames);

Stack.getStatistics(voxelCount, mean, min, max, stdDev);

//call("ij3d.ImageJ3DViewer.setCoordinateSystem", "false");

//run("Moments of Inertia", "start=1 end="+slices+" bone_min="+min+1+" bone_max="+max+"
slope=0.0000 y_intercept=1.8000 align show show_0");
```

```
run("Moments of Inertia", "start=1 end="+slices+" bone_min="+min+1+" bone_max="+max+"
slope=0.0000 y_intercept=1.8000 align");

selectWindow("Log");

saveAs("Text", dir3+imageName+"_MoI_Log.txt");

run("Close");

selectWindow("Results");

saveAs("Results", dir3+imageName+"_MoI_Results.csv");

run("Close");

selectWindow(titleResult);

close();

selectWindow("Aligned_"+titleResult);

run("8-bit");

run("Reslice [/]...", "output=1.000 start=Top avoid");

titleReslice = getTitle();

selectWindow("Aligned_"+titleResult);

close();

selectWindow(titleReslice);

run("Rotate... ", "angle=180 grid=1 interpolation=Bicubic stack");

Stack.getDimensions(width, height, channels, slices, frames);

if (width>height){

        run("Canvas Size...", "width="+width+" height="+width+" position=Center");

}

else {

        run("Canvas Size...", "width="+height+" height="+height+" position=Center");

}
```

Appendix

```
run("Rotate... ", "angle=-45 grid=1 interpolation=Bicubic stack");

run("Flip Horizontally", "stack");

Stack.getDimensions(width, height, channels, slices, frames);

setBatchMode(true);

run("Duplicate...", "title=temp duplicate");

run("Specify...", "width="+width/2+" height="+height/2+" x=0 y=0 slice="+slices);

run("Make Inverse");

run("Colors...", "foreground=black background=black selection=yellow");

run("Fill", "stack");

run("Select None");

stackName=imageName+"_ALLAB_M";

for(i=1; i<=slices; i++){

        print("Saving ALLAB_M - image "+i+" / "+slices);

        setSlice(i);

        run("Duplicate...", "title=image");

        saveAs("tif", dir3+stackName+"-"+pad(i-1));

        close();

}

close();

selectWindow(titleReslice);

run("Duplicate...", "title=temp duplicate");

run("Specify...", "width="+width/2+" height="+height/2+" x=0 y="+height/2+" slice="+slices);

run("Make Inverse");
```

```
run("Fill", "stack");

run("Select None");

stackName=imageName+"_ALLAB_A";

for(i=1; i<=slices; i++){

        print("Saving ALLAB_A - image "+i+" / "+slices);

        setSlice(i);

        run("Duplicate...", "title=image");

        saveAs("tif", dir3+stackName+"-"+pad(i-1));

        close();

}

close();

selectWindow(titleReslice);

run("Duplicate...", "title=temp duplicate");

run("Specify...", "width="+width/2+" height="+height/2+" x="+height/2+" y="+height/2+"
slice="+slices);

run("Make Inverse");

run("Fill", "stack");

run("Select None");

stackName=imageName+"_ALLAB_L";

for(i=1; i<=slices; i++){

        print("Saving ALLAB_L - image "+i+" / "+slices);

        setSlice(i);

        run("Duplicate...", "title=image");

        saveAs("tif", dir3+stackName+"-"+pad(i-1));

        close();
```

```
}

close();

selectWindow(titleReslice);

run("Specify...", "width="+width/2+" height="+height/2+" x="+height/2+" y=0 slice="+slices);

run("Make Inverse");

run("Fill", "stack");

run("Select None");

stackName=imageName+"_ALLAB_P";

for(i=1; i<=slices; i++){

        print("Saving ALLAB_P - image "+i+" / "+slices);

        setSlice(i);

        run("Duplicate...", "title=image");

        saveAs("tif", dir3+stackName+"-"+pad(i-1));

        close();

}

close();

exit("END OF MACRO");

function pad(n) {

    str = toString(n);

    while (lengthOf(str)<5)

      str = "0" + str;

    return str;

}
```

C.4   WekaSegmentation Macro

Fiji Macro using IJ1Macro language

```
// @File(label="Input directory", description="Select the directory with input images",
style="directory") inputDir

// @File(label="Output directory", description="Select the output directory", style="directory")
outputDir

// @File(label="Weka model", description="Select the Weka model to apply") modelPath

// @String(label="Result mode",choices={"Labels" , "Probabilities"}) resultMode

// @Integer(label="Number of tiles in X:", description="Number of image subdivisions in the X
direction", value=3) xTiles

// @Integer(label="Number of tiles in Y:", description="Number of image subdivisions in the Y
direction", value=3) yTiles

// @Integer(label="Number of tiles in Z (set to 0 for 2D processing):", description="Number of
image subdivisions in the Z direction (ignored when using 2D images)", value=3) zTiles

import trainableSegmentation.WekaSegmentation;

import trainableSegmentation.utils.Utils;

import ij.io.FileSaver;

import ij.IJ;

import ij.ImagePlus;

// starting time

startTime = System.currentTimeMillis();

// caculate probabilities?

getProbs = resultMode.equals( "Probabilities" );

// create segmentator

segmentator = new WekaSegmentation( zTiles > 0 );

// load classifier
```

Appendix

```java
segmentator.loadClassifier( modelPath.getCanonicalPath() );

// get list of input images

listOfFiles = inputDir.listFiles();

for ( i = 0; i < listOfFiles.length; i++ )

{

  // process only files (do not go into sub-folders)

  if( listOfFiles[ i ].isFile() )

  {

    // try to read file as image

    image = IJ.openImage( listOfFiles[i].getCanonicalPath() );

    if( image != null )

    {

      tilesPerDim = new int[ 2 ];

      if( image.getNSlices() > 1 )

      {

        tilesPerDim = new int[ 3 ];

        tilesPerDim[ 2 ] = zTiles;

      }

      tilesPerDim[ 0 ] = xTiles;

      tilesPerDim[ 1 ] = yTiles

      // apply classifier and get results (0 indicates number of threads is auto-detected)

      result = segmentator.applyClassifier( image, tilesPerDim, 0, getProbs );

      if( !getProbs )

        // assign same LUT as in GUI
```

```
        result.setLut( Utils.getGoldenAngleLUT() );


      // save result as TIFF in output folder

      outputFileName = listOfFiles[ i ].getName().replaceFirst("[.][^.]+$", "") + ".tif";

      new FileSaver( result ).saveAsTiff( outputDir.getPath() + File.separator + outputFileName );

      // force garbage collection (important for large images)

      result = null;

      image = null;

      System.gc();

    }

  }

}

// print elapsed time

estimatedTime = System.currentTimeMillis() - startTime;

IJ.log( "** Finished processing folder in " + estimatedTime + " ms **" );

System.gc();
```

Appendix D   Publications

High-resolution 3D imaging of osteocytes and computational modelling in mechanobiology: Insights on bone development, ageing, health and disease.

European Cells and Materials, Vol. 31 2016 (pages 264-295)

P.M. Goggin, K.C. Zygalakis, R.O.C. Oreffo, P. Schneider.

Development of protocols for the first serial block-face scanning electron microscopy (SBF SEM) studies of bone tissue.

Bone 2020 Feb;131:115107. doi: 10.1016/j.bone.2019.11510

Patricia Goggin, Elaine M.L. Ho, Helmut Gnaegi, Stuart Searle, Richard O.C. Oreffo, Philipp Schneider

List of References

AARDEN, E. M., BURGER, E. H. & NIJWEIDE, P. J. 1994. Function of osteocytes in bone. *J Cell Biochem,* 55**,** 287-99.

ACHIOU, Z., TOUMI, H., TOUVIER, J., BOUDENOT, A., UZBEKOV, R., OMINSKY, M. S., PALLU, S. & LESPESSAILLES, E. 2015. Sclerostin antibody and interval treadmill training effects in a rodent model of glucocorticoid-induced osteopenia. *Bone,* 81**,** 691-701.

ADACHI, T., AONUMA, Y., TANAKA, M., HOJO, M., TAKANO-YAMAMOTO, T. & KAMIOKA, H. 2009. Calcium response in single osteocytes to locally applied mechanical stimulus: differences in cell process and cell body. *J Biomech,* 42**,** 1989-95.

AFFATATO, S. 2014. 4 - Contemporary designs in total hip arthroplasty (THA). *In:* AFFATATO, S. (ed.) *Perspectives in Total Hip Arthroplasty.* Woodhead Publishing.

ALEXOPOULOS, L. G., HAIDER, M. A., VAIL, T. P. & GUILAK, F. 2003. Alterations in the mechanical properties of the human chondrocyte pericellular matrix with osteoarthritis. *J Biomech Eng,* 125**,** 323-33.

ALMEIDA, M., HAN, L., MARTIN-MILLAN, M., PLOTKIN, L. I., STEWART, S. A., ROBERSON, P. K., KOUSTENI, S., O'BRIEN, C. A., BELLIDO, T., PARFITT, A. M., WEINSTEIN, R. S., JILKA, R. L. & MANOLAGAS, S. C. 2007. Skeletal involution by age-associated oxidative stress and its acceleration by loss of sex steroids. *J Biol Chem,* 282**,** 27285-97.

ALMEIDA, M. & O'BRIEN, C. A. 2013. Basic biology of skeletal aging: role of stress response pathways. *J Gerontol A Biol Sci Med Sci,* 68**,** 1197-208.

AN, S., HU, H., LI, Y. & HU, Y. 2020. Pyroptosis Plays a Role in Osteoarthritis. *Aging Dis,* 11**,** 1146-1157.

AN, Y. H. & MARTIN, K. 2003. *Handbook of Histology Methods for Bone and Cartilage,* Totowa, New Jersey, Humana Press.

ANDERSON, E. J., KALIYAMOORTHY, S., IWAN, J., ALEXANDER, D. & KNOTHE TATE, M. L. 2005. Nano-microscale models of periosteocytic flow show differences in stresses imparted to cell body and processes. *Ann Biomed Eng,* 33**,** 52-62.

ANDERSON, E. J. & KNOTHE TATE, M. L. 2008. Idealization of pericellular fluid space geometry and dimension results in a profound underprediction of nano-microscale stresses imparted by fluid drag on osteocytes. *J Biomech,* 41**,** 1736-46.

ANDREWS, J. C., ALMEIDA, E., VAN DER MEULEN, M. C. H., ALWOOD, J. S., LEE, C., LIU, Y., CHEN, J., MEIRER, F., FESER, M., GELB, J., RUDATI, J., TKACHUK, A., YUN, W. & PIANETTA, P. 2010. Nanoscale X-Ray Microscopic Imaging of Mammalian Mineralized Tissue. *Microscopy and microanalysis,* 16**,** 327-336.

ARGANDA-CARRERAS, I., KAYNIG, V., RUEDEN, C., ELICEIRI, K. W., SCHINDELIN, J., CARDONA, A. & SEUNG, H. S. 2017. Trainable Weka Segmentation: a machine learning tool for microscopy pixel classification. *Bioinformatics,* 33**,** 2424-2426.

ARKILL, K. P., QVORTRUP, K., STARBORG, T., MANTELL, J. M., KNUPP, C., MICHEL, C. C., HARPER, S. J., SALMON, A. H., SQUIRE, J. M., BATES, D. O. & NEAL, C. R. 2014. Resolution of the three dimensional structure of components of the glomerular filtration barrier. *BMC Nephrol,* 15**,** 24.

Appendix

ARMER, H. E., MARIGGI, G., PNG, K. M., GENOUD, C., MONTEITH, A. G., BUSHBY, A. J., GERHARDT, H. & COLLINSON, L. M. 2009. Imaging transient blood vessel fusion events in zebrafish by correlative volume electron microscopy. *PLoS One,* 4**,** e7716.

ARNETT, T. R. 2013. Chapter 8 - Osteoclast Biology. *In:* MARCUS, R., FELDMAN, D., DEMPSTER, D. W., LUCKEY, M. & CAULEY, J. A. (eds.) *Osteoporosis (Fourth Edition).* San Diego: Academic Press.

ARNETT, T. R. & ORRISS, I. R. 2018. Metabolic properties of the osteoclast. *Bone,* 115**,** 25-30.

ASCENZI, M. G., GILL, J. & LOMOVTSEV, A. 2008. Orientation of collagen at the osteocyte lacunae in human secondary osteons. *J Biomech,* 41**,** 3426-35.

ASHIQUE, A. M., HART, L. S., THOMAS, C. D. L., CLEMENT, J. G., PIVONKA, P., CARTER, Y., MOUSSEAU, D. D. & COOPER, D. M. L. 2017. Lacunar-canalicular network in femoral cortical bone is reduced in aged women and is predominantly due to a loss of canalicular porosity. *Bone Reports,* 7**,** 9-16.

ATKINSON, E. G. & DELGADO-CALLE, J. 2019. The Emerging Role of Osteocytes in Cancer in Bone. *JBMR Plus,* 3**,** e10186.

BAANDRUP, U., FLORIO, R. A., ROTERS, F. & OLSEN, E. G. 1981. Electron microscopic investigation of endomyocardial biopsy samples in hypertrophy and cardiomyopathy. A semiquantitative study in 48 patients. *Circulation,* 63**,** 1289-98.

BACH-GANSMO, F. L., BRUEL, A., JENSEN, M. V., EBBESEN, E. N., BIRKEDAL, H. & THOMSEN, J. S. 2016a. Osteocyte lacunar properties and cortical microstructure in human iliac crest as a function of age and sex. *Bone,* 91**,** 11-19.

BACH-GANSMO, F. L., WEAVER, J. C., JENSEN, M. H., LEEMREIZE, H., MADER, K. S., STAMPANONI, M., BRUEL, A., THOMSEN, J. S. & BIRKEDAL, H. 2015. Osteocyte lacunar properties in rat cortical bone: Differences between lamellar and central bone. *J Struct Biol,* 191**,** 59-67.

BACH-GANSMO, F. L., WITTIG, N. K., BRUEL, A., THOMSEN, J. S. & BIRKEDAL, H. 2016b. Immobilization and long-term recovery results in large changes in bone structure and strength but no corresponding alterations of osteocyte lacunar properties. *Bone*.

BAE, J. A., MU, S., KIM, J. S., TURNER, N. L., TARTAVULL, I., KEMNITZ, N., JORDAN, C. S., NORTON, A. D., SILVERSMITH, W. M., PRENTKI, R., SOREK, M., DAVID, C., JONES, D. L., BLAND, D., STERLING, A. L. R., PARK, J., BRIGGMAN, K. L. & SEUNG, H. S. 2018. Digital Museum of Retinal Ganglion Cells with Dense Anatomy and Physiology. *Cell,* 173**,** 1293-1306.e19.

BAKER-LEPAIN, J. C. & LANE, N. E. 2012. Role of bone architecture and anatomy in osteoarthritis. *Bone,* 51**,** 197-203.

BAKHSH, T. A. 2016. Ultrastructural features of dentinoenamel junction revealed by focused gallium ion beam milling. *J Microsc,* 264**,** 14-21.

BAKHSH, T. A., SADR, A., MANDURAH, M. M., SHIMADA, Y., ZAKARIA, O. & TAGAMI, J. 2015. In situ characterization of resin-dentin interfaces using conventional vs. cryofocused ion-beam milling. *Dent Mater,* 31**,** 833-44.

BARRAGAN-ADJEMIAN, C., NICOLELLA, D., DUSEVICH, V., DALLAS, M. R., EICK, J. D. & BONEWALD, L. F. 2006. Mechanism by which MLO-A5 late osteoblasts/early osteocytes mineralize in culture: similarities with mineralization of lamellar bone. *Calcif Tissue Int,* 79**,** 340-53.

BELEVICH, I., JOENSUU, M., KUMAR, D., VIHINEN, H. & JOKITALO, E. 2016. Microscopy Image Browser: A Platform for Segmentation and Analysis of Multidimensional Datasets. *PLoS Biol,* 14**,** e1002340.

BELL, A. 2008. The pipe and the pinwheel: is pressure an effective stimulus for the 9+0 primary cilium? *Cell Biol Int,* 32**,** 462-8.

BELLIDO, M., LUGO, L., ROMAN-BLAS, J. A., CASTAÑEDA, S., CAEIRO, J. R., DAPIA, S., CALVO, E., LARGO, R. & HERRERO-BEAUMONT, G. 2010. Subchondral bone microstructural damage by increased remodelling aggravates experimental osteoarthritis preceded by osteoporosis. *Arthritis Research & Therapy,* 12**,** R152.

BENO, T., YOON, Y. J., COWIN, S. C. & FRITTON, S. P. 2006. Estimation of bone permeability using accurate microstructural measurements. *J Biomech,* 39**,** 2378-87.

BETTS, J. G., YOUNG, K.A., WISE, J.A., JOHNSON E., POE, B., KRUSE, D.H., KOROL, O.,JOHNSON, J.E., WOMBLE, M., DESAIX, P. 2013. *Anatomy and Physiology,* Houston, Texas, OpenStax.

BLAIN, H., CHAVASSIEUX, P., PORTERO-MUZY, N., BONNEL, F., CANOVAS, F., CHAMMAS, M., MAURY, P. & DELMAS, P. D. 2008. Cortical and trabecular bone distribution in the femoral neck in osteoporosis and osteoarthritis. *Bone,* 43**,** 862-8.

BONEWALD, L. F. 2006. Mechanosensation and Transduction in Osteocytes. *Bonekey Osteovision,* 3**,** 7-15.

BONEWALD, L. F. 2007. Osteocytes as dynamic multifunctional cells. *Ann N Y Acad Sci,* 1116**,** 281-90.

BONEWALD, L. F. 2021. Chapter 7 - Osteocytes. *In:* DEMPSTER, D. W., CAULEY, J. A., BOUXSEIN, M. L. & COSMAN, F. (eds.) *Marcus and Feldman's Osteoporosis (Fifth Edition).* Content Repository Only!

BONIVTCH, A. R., BONEWALD, L. F. & NICOLELLA, D. P. 2007. Tissue strain amplification at the osteocyte lacuna: A microstructural finite element analysis. *Journal of Biomechanics,* 40**,** 2199-2206.

BORRETT, S. & HUGHES, L. 2016. Reporting methods for processing and analysis of data from serial block face scanning electron microscopy. *Journal of Microscopy***,** n/a-n/a.

BORTEL, E. L., DUDA, G. N., MUNDLOS, S., WILLIE, B. M., FRATZL, P. & ZASLANSKY, P. 2015. Long bone maturation is driven by pore closing: A quantitative tomography investigation of structural formation in young C57BL/6 mice. *Acta Biomater,* 22**,** 92-102.

BOULOGNE, C., GILLET, C., HUGHES, L., LE BARS, R., CANETTE, A., HAWES, C. R. & SATIAT-JEUNEMAITRE, B. 2020. Functional organisation of the endomembrane network in the digestive gland of the Venus flytrap: revisiting an old story with a new microscopy toolbox. *Journal of Microscopy,* 280**,** 86-103.

BOUTROY, S., VILAYPHIOU, N., ROUX, J. P., DELMAS, P. D., BLAIN, H., CHAPURLAT, R. D. & CHAVASSIEUX, P. 2011. Comparison of 2D and 3D bone microarchitecture evaluation at the femoral neck, among postmenopausal women with hip fracture or hip osteoarthritis. *Bone,* 49**,** 1055-61.

BOUWER, J. C., DEERINCK, T. J., BUSHONG, E., ASTAKHOV, V., RAMACHANDRA, R., PELTIER, S. T. & ELLISMAN, M. H. 2017. Deceleration of probe beam by stage bias potential improves resolution of serial block-face scanning electron microscopic images. *Adv Struct Chem Imaging,* 2**,** 11.

BOUXSEIN, M. L., BOYD, S. K., CHRISTIANSEN, B. A., GULDBERG, R. E., JEPSEN, K. J. & MULLER, R. 2010. Guidelines for assessment of bone microstructure in rodents using micro-computed tomography. *J Bone Miner Res,* 25**,** 1468-86.

BRAET, F. & GEERTS, W. J. 2009. Foreword to the themed issue on correlative microscopy. *J Microsc,* 235**,** 239-40.

BRAMA, E., PEDDIE, C. J., WILKES, G., GU, Y., COLLINSON, L. M. & JONES, M. L. 2016. ultraLM and miniLM: Locator tools for smart tracking of fluorescent cells in correlative light and electron microscopy. *Wellcome Open Res,* 1**,** 26.

BRELJE, T. C., SORENSON, R.L. 2019. *Histology Guide* [Online]. Minnesota, USA: Univeristy of Minnesota. [Accessed 02/12/2020 2020].

BRENNAN, M. A., GLEESON, J. P., O'BRIEN, F. J. & MCNAMARA, L. M. 2014a. Effects of ageing, prolonged estrogen deficiency and zoledronate on bone tissue mineral distribution. *Journal of the Mechanical Behavior of Biomedical Materials,* 29**,** 161-170.

BRENNAN, M. A., HAUGH, M. G., O'BRIEN, F. J. & MCNAMARA, L. M. 2014b. Estrogen withdrawal from osteoblasts and osteocytes causes increased mineralization and apoptosis. *Horm Metab Res,* 46**,** 537-45.

BRITZ, H. M., CARTER, Y., JOKIHAARA, J., LEPPANEN, O. V., JARVINEN, T. L., BELEV, G. & COOPER, D. M. 2012a. Prolonged unloading in growing rats reduces cortical osteocyte lacunar density and volume in the distal tibia. *Bone,* 51**,** 913-9.

BRITZ, H. M., CARTER, Y., JOKIHAARA, J., LEPPÄNEN, O. V., JÄRVINEN, T. L. N., BELEV, G. & COOPER, D. M. L. 2012b. Prolonged unloading in growing rats reduces cortical osteocyte lacunar density and volume in the distal tibia. *Bone,* 51**,** 913-919.

BRODT, M. D., ELLIS, C. B. & SILVA, M. J. 1999. Growing C57Bl/6 mice increase whole bone mechanical properties by increasing geometric and material properties. *J Bone Miner Res,* 14**,** 2159-66.

BROMAGE, T. G., LACRUZ, R. S., HOGG, R., GOLDMAN, H. M., MCFARLIN, S. C., WARSHAW, J., DIRKS, W., PEREZ-OCHOA, A., SMOLYAR, I., ENLOW, D. H. & BOYDE, A. 2009. Lamellar bone is an incremental tissue reconciling enamel rhythms, body size, and organismal life history. *Calcif Tissue Int,* 84**,** 388-404.

BROWN, J. L., KUMBAR, S. G. & LAURENCIN, C. T. 2013. Chapter II.6.7 - Bone Tissue Engineering. *In:* RATNER, B. D., HOFFMAN, A. S., SCHOEN, F. J. & LEMONS, J. E. (eds.) *Biomaterials Science (Third Edition).* Academic Press.

BUENZLI, P. R. & SIMS, N. A. 2015. Quantifying the osteocyte network in the human skeleton. *Bone,* 75**,** 144-150.

BUIE, H. R., MOORE, C. P. & BOYD, S. K. 2008. Postpubertal architectural developmental patterns differ between the L3 vertebra and proximal tibia in three inbred strains of mice. *J Bone Miner Res,* 23**,** 2048-59.

BULLMORE, E. & SPORNS, O. 2009. Complex brain networks: graph theoretical analysis of structural and functional systems. *Nat Rev Neurosci,* 10**,** 186-198.

BULTINK, I. E. & LEMS, W. F. 2013. Osteoarthritis and osteoporosis: what is the overlap? *Curr Rheumatol Rep,* 15**,** 328.

BURRA, S., NICOLELLA, D. P., FRANCIS, W. L., FREITAS, C. J., MUESCHKE, N. J., POOLE, K. & JIANG, J. X. 2010. Dendritic processes of osteocytes are mechanotransducers that induce the opening of hemichannels. *Proc Natl Acad Sci U S A,* 107**,** 13648-53.

BUSHBY, A. J., MARIGGI, G., ARMER, H. E. & COLLINSON, L. M. 2012. Correlative light and volume electron microscopy: using focused ion beam scanning electron microscopy to image transient events in model organisms. *Methods Cell Biol,* 111**,** 357-82.

BUSSE, B., DJONIC, D., MILOVANOVIC, P., HAHN, M., PUSCHEL, K., RITCHIE, R. O., DJURIC, M. & AMLING, M. 2010. Decrease in the osteocyte lacunar density accompanied by hypermineralized lacunar occlusion reveals failure and delay of remodeling in aged human bone. *Aging Cell,* 9**,** 1065-75.

BUSSE, M., MÜLLER, M., KIMM, M. A., FERSTL, S., ALLNER, S., ACHTERHOLD, K., HERZEN, J. & PFEIFFER, F. 2018. Three-dimensional virtual histology enabled through cytoplasm-specific X-ray stain for microscopic and nanoscopic computed tomography. *Proc Natl Acad Sci U S A,* 115**,** 2293-2298.

CABAHUG-ZUCKERMAN, P., STOUT, R. F., JR., MAJESKA, R. J., THI, M. M., SPRAY, D. C., WEINBAUM, S. & SCHAFFLER, M. B. 2018. Potential role for a specialized beta3 integrin-based structure on osteocyte processes in bone mechanosensation. *J Orthop Res,* 36**,** 642-652.

CALLENS, S. J. P., TOUROLLE NÉ BETTS, D. C., MÜLLER, R. & ZADPOOR, A. A. 2020. The local and global geometry of trabecular bone. *bioRxiv***,** 2020.12.02.408377.

CALLIS, G. & STERCHI, D. 1998. Decalcification of Bone: Literature Review and Practical Study of Various Decalcifying Agents. Methods, and Their Effects on Bone Histology. *Journal of Histotechnology,* 21**,** 49-58.

CAPLAN, J., NIETHAMMER, M., TAYLOR, R. M., 2ND & CZYMMEK, K. J. 2011. The power of correlative microscopy: multi-modal, multi-scale, multi-dimensional. *Curr Opin Struct Biol,* 21**,** 686-93.

CARDINALI, M. A., DALLARI, D., GOVONI, M., STAGNI, C., MARMI, F., TSCHON, M., BROGINI, S., FIORETTO, D. & MORRESI, A. 2019. Brillouin micro-spectroscopy of subchondral, trabecular bone and articular cartilage of the human femoral head. *Biomed Opt Express,* 10**,** 2606-2611.

CARDONA, A., SAALFELD, S., SCHINDELIN, J., ARGANDA-CARRERAS, I., PREIBISCH, S., LONGAIR, M., TOMANCAK, P., HARTENSTEIN, V. & DOUGLAS, R. J. 2012. TrakEM2 software for neural circuit reconstruction. *PLoS One,* 7**,** e38011.

CARDOSO, L., FRITTON, S. P., GAILANI, G., BENALLA, M. & COWIN, S. C. 2013. Advances in assessment of bone porosity, permeability and interstitial fluid flow. *Journal of biomechanics,* 46**,** 253-265.

CARDOSO, L., HERMAN, B. C., VERBORGT, O., LAUDIER, D., MAJESKA, R. J. & SCHAFFLER, M. B. 2009. Osteocyte apoptosis controls activation of intracortical resorption in response to bone fatigue. *J Bone Miner Res,* 24**,** 597-605.

CARTER, Y., THOMAS, C. D., CLEMENT, J. G. & COOPER, D. M. 2013a. Femoral osteocyte lacunar density, volume and morphology in women across the lifespan. *J Struct Biol,* 183**,** 519-26.

CARTER, Y., THOMAS, C. D., CLEMENT, J. G., PEELE, A. G., HANNAH, K. & COOPER, D. M. 2013b. Variation in osteocyte lacunar morphology and density in the human femur--a synchrotron radiation micro-CT study. *Bone,* 52**,** 126-32.

CARZANIGA, R., DOMART, M. C., DUKE, E. & COLLINSON, L. M. 2014. Correlative cryo-fluorescence and cryo-soft X-ray tomography of adherent cells at European synchrotrons. *Methods Cell Biol,* 124**,** 151-78.

CHEN, D., SHEN, J., ZHAO, W., WANG, T., HAN, L., HAMILTON, J. L. & IM, H.-J. 2017. Osteoarthritis: toward a comprehensive understanding of pathological mechanism. *Bone research,* 5**,** 16044-16044.

CHENG, B., ZHAO, S., LUO, J., SPRAGUE, E., BONEWALD, L. F. & JIANG, J. X. 2001. Expression of functional gap junctions and regulation by fluid flow in osteocyte-like MLO-Y4 cells. *J Bone Miner Res,* 16**,** 249-59.

CIANI, A., TOUMI, H., PALLU, S., TSAI, E. H. R., DIAZ, A., GUIZAR-SICAIROS, M., HOLLER, M., LESPESSAILLES, E. & KEWISH, C. M. 2018. Ptychographic X-ray CT characterization of the osteocyte lacuno-canalicular network in a male rat's glucocorticoid induced osteoporosis model. *Bone Rep,* 9**,** 122-131.

CIANI, C., SHARMA, D., DOTY, S. B. & FRITTON, S. P. 2014. Ovariectomy enhances mechanical load-induced solute transport around osteocytes in rat cancellous bone. *Bone,* 59**,** 229-34.

CıNAR, Y., ATAMAZ, F. C., KIRAZLI, Y., DOGANAVSARGIL, B., SEZAK, M., OZKAYIN, N., AKTUGLU, K. & AYDOGDU, S. 2016. A comparison of the femur heads histomorphometrically regarding trabecular bone properties in the patients with osteoporosis and osteoarthritis. *Aging Clin Exp Res,* 28**,** 997-1001.

CLINIC, C. 2021. *Arthritis advisor* [Online]. Belvoir Media Group. [Accessed 01/02/21 2021].

COCKS, E., TAGGART, M., RIND, F. C. & WHITE, K. 2018. A guide to analysis and reconstruction of serial block face scanning electron microscopy data. *Journal of microscopy,* 270**,** 217-234.

COLLMAN, F., BUCHANAN, J., PHEND, K. D., MICHEVA, K. D., WEINBERG, R. J. & SMITH, S. J. 2015. Mapping Synapses by Conjugate Light-Electron Array Tomography. *The Journal of Neuroscience,* 35**,** 5792-5807.

COOPER, D. M., TURINSKY, A. L., SENSEN, C. W. & HALLGRIMSSON, B. 2003. Quantitative 3D analysis of the canal network in cortical bone by micro-computed tomography. *Anat Rec B New Anat,* 274**,** 169-79.

COUGHLIN, T. R., VOISIN, M., SCHAFFLER, M. B., NIEBUR, G. L. & MCNAMARA, L. M. 2015. Primary Cilia Exist in a Small Fraction of Cells in Trabecular Bone and Marrow. *Calcif Tissue Int,* 96**,** 65-72.

COWIN, S. C., MOSS-SALENTIJN, L. & MOSS, M. L. 1991. Candidates for the mechanosensory system in bone. *J Biomech Eng,* 113**,** 191-7.

COWIN, S. C. & WEINBAUM, S. 1998. Strain amplification in the bone mechanosensory system. *Am J Med Sci,* 316**,** 184-8.

COWIN, S. C., WEINBAUM, S. & ZENG, Y. 1995. A case for bone canaliculi as the anatomical site of strain generated potentials. *J Biomech,* 28**,** 1281-97.

CUI, H., ZHU, Y., YANG, Q., ZHAO, W., ZHANG, S., ZHOU, A. & JIANG, D. 2016. Necrostatin-1 treatment inhibits osteocyte necroptosis and trabecular deterioration in ovariectomized rats. *Scientific Reports,* 6**,** 33803.

CUMMINGS, S. R. & MELTON, L. J. 2002. Epidemiology and outcomes of osteoporotic fractures. *The Lancet,* 359**,** 1761-1767.

DALL'ARA, E., OHMAN, C., BALEANI, M. & VICECONTI, M. 2011. Reduced tissue hardness of trabecular bone is associated with severe osteoarthritis. *J Biomech,* 44**,** 1593-8.

DALLAS, S. L. & BONEWALD, L. F. 2010. Dynamics of the transition from osteoblast to osteocyte. *Ann N Y Acad Sci,* 1192**,** 437-43.

DALLAS, S. L. & MOORE, D. S. 2020. Using confocal imaging approaches to understand the structure and function of osteocytes and the lacunocanalicular network. *Bone***,** 115463.

DALLAS, S. L., VENO, P. A., ROSSER, J. L., BARRAGAN-ADJEMIAN, C., ROWE, D. W., KALAJZIC, I. & BONEWALD, L. F. 2009. Time lapse imaging techniques for comparison of mineralization dynamics in primary murine osteoblasts and the late osteoblast/early osteocyte-like cell line MLO-A5. *Cells Tissues Organs,* 189**,** 6-11.

DEERINCK, T., BUSHONG, E., LEV-RAM, V., SHU, X., TSIEN, R. & ELLISMAN, M. 2010. Enhancing Serial Block-Face Scanning Electron Microscopy to Enable High Resolution 3-D Nanohistology of Cells and Tissues. *Microscopy and Microanalysis,* 16**,** 1138-1139.

DEERINCK, T. J., BUSHONG, E.A., THOR, A, ELLISMAN, M.H. 2010. *NCMIR METHODS FOR 3D EM: A NEW PROTOCOL FOR PREPARATION OF BIOLOGICAL SPECIMENS FOR SERIAL BLOCKFACE SCANNING ELECTRON MICROSCOPY* [Online]. https://ncmir.ucsd.edu/sbem-protocol. [Accessed 2014].

DEERINCK, T. J., SHONE, T. M., BUSHONG, E. A., RAMACHANDRA, R., PELTIER, S. T. & ELLISMAN, M. H. 2018. High-performance serial block-face SEM of nonconductive biological samples enabled by focal gas injection-based charge compensation. *J Microsc,* 270**,** 142-149.

DELIGIANNI, D. D. & APOSTOLOPOULOS, C. A. 2008. Multilevel finite element modeling for the prediction of local cellular deformation in bone. *Biomech Model Mechanobiol,* 7**,** 151-9.

DEMETRIUS, L. 2006. Aging in Mouse and Human Systems. *Annals of the New York Academy of Sciences,* 1067**,** 66-82.

DEMPSTER, D. W., COMPSTON, J. E., DREZNER, M. K., GLORIEUX, F. H., KANIS, J. A., MALLUCHE, H., MEUNIER, P. J., OTT, S. M., RECKER, R. R. & PARFITT, A. M. 2013. Standardized Nomenclature, Symbols, and Units for Bone Histomorphometry: A 2012 Update of the Report of the ASBMR Histomorphometry Nomenclature Committee. *Journal of bone and mineral research : the official journal of the American Society for Bone and Mineral Research,* 28**,** 2-17.

DENK, W. & HORSTMANN, H. 2004. Serial block-face scanning electron microscopy to reconstruct three-dimensional tissue nanostructure. *PLoS Biol,* 2**,** 1900-1909.

DEQUEKER, J. 1999. The inverse relationship between osteoporosis and osteoarthritis. *Adv Exp Med Biol,* 455**,** 419-22.

DEQUEKER, J., AERSSENS, J. & LUYTEN, F. P. 2003. Osteoarthritis and osteoporosis: clinical and research evidence of inverse relationship. *Aging Clin Exp Res,* 15**,** 426-39.

DICKENSON, R. P., HUTTON, W. C. & STOTT, J. R. 1981. The mechanical properties of bone in osteoporosis. *J Bone Joint Surg Br,* 63-b**,** 233-8.

DIEROLF, M., MENZEL, A., THIBAULT, P., SCHNEIDER, P., KEWISH, C. M., WEPF, R., BUNK, O. & PFEIFFER, F. 2010. Ptychographic X-ray computed tomography at the nanoscale. *Nature,* 467**,** 436-9.

DIVIETI PAJEVIC, P. & KRAUSE, D. S. 2019. Osteocyte regulation of bone and blood. *Bone,* 119**,** 13-18.

DONG, P., HAUPERT, S., HESSE, B., LANGER, M., GOUTTENOIRE, P. J., BOUSSON, V. & PEYRIN, F. 2014a. 3D osteocyte lacunar morphometric properties and distributions in human femoral cortical bone using synchrotron radiation micro-CT images. *Bone,* 60**,** 172-85.

DONG, P., PACUREANU, A., ZULUAGA, M. A., OLIVIER, C., GRIMAL, Q. & PEYRIN, F. 2014b. Quantification of the 3d Morphology of the Bone Cell Network from Synchrotron Micro-Ct Images. *Image Analysis & Stereology,* 33**,** 157.

DOTY, S. B. 1981. Morphological evidence of gap junctions between bone cells. *Calcif Tissue Int,* 33**,** 509-12.

DOUBE, M., KLOSOWSKI, M. M., ARGANDA-CARRERAS, I., CORDELIERES, F. P., DOUGHERTY, R. P., JACKSON, J. S., SCHMID, B., HUTCHINSON, J. R. & SHEFELBINE, S. J. 2010. BoneJ: Free and extensible bone image analysis in ImageJ. *Bone,* 47**,** 1076-9.

DRAENERT, M. E., DRAENERT, A. I., FORRIOL, F., CERLER, M., KUNZELMANN, K. H., HICKEL, R. & DRAENERT, K. 2012. Value and limits of mu-CT for nondemineralized bone tissue processing. *Microsc Res Tech,* 75**,** 416-24.

DUKE, E. M. H., RAZI, M., WESTON, A., GUTTMANN, P., WERNER, S., HENZLER, K., SCHNEIDER, G., TOOZE, S. A. & COLLINSON, L. M. 2014. Imaging endosomes and autophagosomes in whole mammalian cells using correlative cryo-fluorescence and cryo-soft X-ray microscopy (cryo-CLXM). *Ultramicroscopy,* 143**,** 77-87.

DUNSTAN, C. R., EVANS, R. A., HILLS, E., WONG, S. Y. & HIGGS, R. J. 1990. Bone death in hip fracture in the elderly. *Calcif Tissue Int,* 47**,** 270-5.

DUTTA, S. & SENGUPTA, P. 2016. Men and mice: Relating their ages. *Life Sci,* 152**,** 244-8.

ELLIOTT, J. C. & DOVER, S. D. 1982. X-ray microtomography. *Journal of Microscopy,* 126**,** 211-213.

ELLISMAN, M. H., JOHNSON J.R., DEERINCK T.J., BUSHONG E.A., BOUWER J., RUMACHANDRA, R., SIEGEL J.S. 2015. *Highly conductive nanocomposite, biological and small molecule materials for enhanced resin conductivilty.* USA patent application PCT/US2014/047046.

FABRE, S., FUNCK-BRENTANO, T. & COHEN-SOLAL, M. 2020. Anti-Sclerostin Antibodies in Osteoporosis and Other Bone Diseases. *Journal of Clinical Medicine,* 9**,** 3439.

FANTNER, G. & LAFONT, F. 2019. Correlative Microscopy Using Scanning Probe Microscopes. *Correlative Imaging.*

FAZZALARI, N. L., FORWOOD, M. R., SMITH, K., MANTHEY, B. A. & HERREEN, P. 1998. Assessment of cancellous bone quality in severe osteoarthrosis: bone mineral density, mechanics, and microdamage. *Bone,* 22**,** 381-8.

FELDKAMP, L. A., GOLDSTEIN, S. A., PARFITT, A. M., JESION, G. & KLEEREKOPER, M. 1989. The direct examination of three-dimensional bone architecture in vitro by computed tomography. *J Bone Miner Res,* 4**,** 3-11.

FERGUSON, V. L., AYERS, R. A., BATEMAN, T. A. & SIMSKE, S. J. 2003. Bone development and age-related bone loss in male C57BL/6J mice. *Bone,* 33**,** 387-98.

FERNANDEZ-MORAN, V. H. 1965. *METHOD OFMAKINGDIAMOND KNIVES*. USA patent application.

FERRETTI, M., MUGLIA, M. A., REMAGGI, F., CANE, V. & PALUMBO, C. 1999. Histomorphometric study on the osteocyte lacuno-canalicular network in animals of different species. II. Parallel-fibered and lamellar bones. *Ital J Anat Embryol,* 104**,** 121-31.

FIALA, J. C. 2005. Reconstruct: a free editor for serial section microscopy. *J Microsc,* 218**,** 52-61.

FLURKEY, K., CURRER, J.M., HARRISON, D.E. 2007. Mouse models in Aging Research. *In:* FOX, J. G., BARTHOLD, S.W., DAVISSON, M.T. ET AL (ed.) *The Mouse in Biomedical Research.* 2 ed. Burlington: Academic Press.

FRITTON, S. P. & WEINBAUM, S. 2009. Fluid and Solute Transport in Bone: Flow-Induced Mechanotransduction. *Annu Rev Fluid Mech,* 41**,** 347-374.

FROST, H. M. 1960. In vivo osteocyte death. *J Bone Joint Surg Am,* 42-a**,** 138-43.

FROST, H. M. & JEE, W. S. 1992. On the rat model of human osteopenias and osteoporoses. *Bone Miner,* 18**,** 227-36.

GARDINIER, J. D., ROSTAMI, N., JULIANO, L. & ZHANG, C. 2018. Bone adaptation in response to treadmill exercise in young and adult mice. *Bone reports,* 8**,** 29-37.

GAUTHIER, R., LANGER, M., FOLLET, H., OLIVIER, C., GOUTTENOIRE, P.-J., HELFEN, L., RONGIÉRAS, F., MITTON, D. & PEYRIN, F. 2018. 3D micro structural analysis of human cortical bone in paired femoral diaphysis, femoral neck and radial diaphysis. *Journal of Structural Biology,* 204**,** 182-190.

GAYTAN, F., MORALES, C., REYMUNDO, C. & TENA-SEMPERE, M. 2020. A novel RGB-trichrome staining method for routine histological analysis of musculoskeletal tissues. *Scientific Reports,* 10**,** 16659.

GENOUD, C., TITZE, B., GRAFF-MEYER, A. & FRIEDRICH, R. W. 2018. Fast Homogeneous En Bloc Staining of Large Tissue Samples for Volume Electron Microscopy. *Frontiers in Neuroanatomy,* 12.

GEOGHEGAN, I. P., HOEY, D. A. & MCNAMARA, L. M. 2019. Integrins in Osteocyte Biology and Mechanotransduction. *Current Osteoporosis Reports*.

GILBERT, S. J., SINGHRAO, S. K., KHAN, I. M., GONZALEZ, L. G., THOMSON, B. M., BURDON, D., DUANCE, V. C. & ARCHER, C. W. 2009. Enhanced tissue integration during cartilage repair in vitro can be achieved by inhibiting chondrocyte death at the wound edge. *Tissue Eng Part A,* 15**,** 1739-49.

GIORGI, M., VERBRUGGEN, S. W. & LACROIX, D. 2016. In silico bone mechanobiology: modeling a multifaceted biological system. *Wiley Interdiscip Rev Syst Biol Med,* 8**,** 485-505.

GKIATAS, I., LYKISSAS, M., KOSTAS-AGNANTIS, I., KOROMPILIAS, A., BATISTATOU, A. & BERIS, A. 2015. Factors affecting bone growth. *Am J Orthop (Belle Mead NJ),* 44**,** 61-7.

GLATT, V., CANALIS, E., STADMEYER, L. & BOUXSEIN, M. L. 2007. Age-related changes in trabecular architecture differ in female and male C57BL/6J mice. *J Bone Miner Res,* 22**,** 1197-207.

GLAUERT, A. M. 1975. *Fixation, dehydration and embedding of biological specimens.*, Elsevier North- Holland, New York.

GOGGIN, P., HO, E. M. L., GNAEGI, H., SEARLE, S., OREFFO, R. O. C. & SCHNEIDER, P. 2020. Development of protocols for the first serial block-face scanning electron microscopy (SBF SEM) studies of bone tissue. *Bone,* 131**,** 115107.

GOGGIN, P. M., ZYGALAKIS, K. C., OREFFO, R. O. & SCHNEIDER, P. 2016. High-resolution 3D imaging of osteocytes and computational modelling in mechanobiology: insights on bone development, ageing, health and disease. *Eur Cell Mater,* 31**,** 264-95.

GOLDMAN, H. M., BLAYVAS, A., BOYDE, A., HOWELL, P. G., CLEMENT, J. G. & BROMAGE, T. G. 2000. Correlative light and backscattered electron microscopy of bone--part II: automated image analysis. *Scanning,* 22**,** 337-44.

GOLDMAN, H. M., KINDSVATER, J. & BROMAGE, T. G. 1999. Correlative light and backscattered electron microscopy of bone--Part I: Specimen preparation methods. *Scanning,* 21**,** 40-3.

GORING, A., SHARMA, A., JAVAHERI, B., SMITH, R. C., KANCZLER, J. M., BOYDE, A., HESSE, E., MAHAJAN, S., OLSEN, B. R., PITSILLIDES, A. A., SCHNEIDER, P., OREFFO, R. O. & CLARKIN, C. E. 2019. Regulation of the bone vascular network is sexually dimorphic. *J Bone Miner Res*.

GRAB, D., THIERAUF, S., ROSENBUSCH, B. & STERZIK, K. 1993. Scanning electron microscopy of human sperms after preparation of semen for in-vitro fertilization. *Arch Gynecol Obstet,* 252**,** 137-41.

GRAHAM, B. J., HILDEBRAND, D. G. C., KUAN, A. T., MANIATES-SELVIN, J. T., THOMAS, L. A., SHANNY, B. L. & LEE, W.-C. A. 2019. High-throughput transmission electron microscopy with automated serial sectioning. *bioRxiv***,** 657346.

GUAY, M., EMAM, Z. & LEAPMAN, R. 2018. Problems and Progress in Automating Electron Microscopy Segmentation. *Microscopy and Microanalysis,* 24**,** 508-509.

GUENOUN, D., FOURE, A., PITHIOUX, M., GUIS, S., LE CORROLLER, T., MATTEI, J. P., PAULY, V., GUYE, M., BERNARD, M., CHABRAND, P., CHAMPSAUR, P. & BENDAHAN, D. 2017. Correlative Analysis Of Vertebral Trabecular Bone Microarchitecture and Mechanical Properties: A Combined Ultra-High Field (7 Tesla) MRI and Biomechanical Investigation. *Spine (Phila Pa 1976)*.

HAN, Y., COWIN, S. C., SCHAFFLER, M. B. & WEINBAUM, S. 2004. Mechanotransduction and strain amplification in osteocyte cell processes. *Proc Natl Acad Sci U S A,* 101**,** 16689-94.

HANDSCHUH, S., BAEUMLER, N., SCHWAHA, T. & RUTHENSTEINER, B. 2013. A correlative approach for combining microCT, light and transmission electron microscopy in a single 3D scenario. *Front Zool,* 10**,** 44.

HANNAH, K. M., THOMAS, C. D., CLEMENT, J. G., DE CARLO, F. & PEELE, A. G. 2010. Bimodal distribution of osteocyte lacunar size in the human femoral cortex as revealed by micro-CT. *Bone,* 47**,** 866-71.

HART, D. J., MOOTOOSAMY, I., DOYLE, D. V. & SPECTOR, T. D. 1994. The relationship between osteoarthritis and osteoporosis in the general population: the Chingford Study. *Ann Rheum Dis,* 53**,** 158-62.

HASEGAWA, T., YAMAMOTO, T., HONGO, H., QIU, Z., ABE, M., KANESAKI, T., TANAKA, K., ENDO, T., DE FREITAS, P. H. L., LI, M. & AMIZUKA, N. 2018. Three-dimensional ultrastructure of osteocytes assessed by focused ion beam-scanning electron microscopy (FIB-SEM). *Histochem Cell Biol,* 149**,** 423-432.

HASHIMOTO, T., THOMPSON, G. E., ZHOU, X. & WITHERS, P. J. 2016. 3D imaging by serial block face scanning electron microscopy for materials science using ultramicrotomy. *Ultramicroscopy,* 163**,** 6-18.

HAUGH, M. G., VAUGHAN, T. J. & MCNAMARA, L. M. 2015. The role of integrin alpha(V)beta(3) in osteocyte mechanotransduction. *J Mech Behav Biomed Mater,* 42**,** 67-75.

HAYAMI, T., PICKARSKI, M., WESOLOWSKI, G. A., MCLANE, J., BONE, A., DESTEFANO, J., RODAN, G. A. & DUONG, L. T. 2004. The role of subchondral bone remodeling in osteoarthritis: reduction of cartilage degeneration and prevention of osteophyte formation by alendronate in the rat anterior cruciate ligament transection model. *Arthritis Rheum,* 50**,** 1193-206.

HAYAT, M. A. 1989. *Principles and techniques of electron microscopy : biological applications,* Basingstoke, Basingstoke : Macmillan.

HEILIGENSTEIN, X., PAUL-GILLOTEAUX, P., RAPOSO, G. & SALAMERO, J. 2017. eC-CLEM: A multidimension, multimodel software to correlate intermodal images with a focus on light and electron microscopy. *Methods Cell Biol,* 140**,** 335-352.

HEINO, T. J., KURATA, K., HIGAKI, H. & VAANANEN, H. K. 2009. Evidence for the role of osteocytes in the initiation of targeted remodeling. *Technol Health Care,* 17**,** 49-56.

HELMSTAEDTER, M., BRIGGMAN, K. L. & DENK, W. 2011. High-accuracy neurite reconstruction for high-throughput neuroanatomy. *Nat Neurosci,* 14**,** 1081-8.

HEMMATIAN, H., BAKKER, A. D., KLEIN-NULEND, J. & VAN LENTHE, G. H. 2017a. Aging, Osteocytes, and Mechanotransduction. *Current osteoporosis reports,* 15**,** 401-411.

HEMMATIAN, H., LAURENT, M. R., BAKKER, A. D., VANDERSCHUEREN, D., KLEIN-NULEND, J. & VAN LENTHE, G. H. 2018. Age-related changes in female mouse cortical bone microporosity. *Bone,* 113**,** 1-8.

HEMMATIAN, H., LAURENT, M. R., GHAZANFARI, S., VANDERSCHUEREN, D., BAKKER, A. D., KLEIN-NULEND, J. & VAN LENTHE, G. H. 2017b. Accuracy and reproducibility of mouse cortical bone microporosity as quantified by desktop microcomputed tomography. *PloS one,* 12**,** e0182996-e0182996.

HENNIES, J., LLETI, J. M. S., SCHIEBER, N. L., TEMPLIN, R. M., STEYER, A. M. & SCHWAB, Y. 2020. AMST: Alignment to Median Smoothed Template for Focused Ion Beam Scanning Electron Microscopy Image Stacks. *Scientific Reports,* 10**,** 2004.

HERNLUND, E., SVEDBOM, A., IVERGÅRD, M., COMPSTON, J., COOPER, C., STENMARK, J., MCCLOSKEY, E. V., JÖNSSON, B. & KANIS, J. A. 2013. Osteoporosis in the European Union: medical management, epidemiology and economic burden. A report prepared in collaboration with the International Osteoporosis Foundation (IOF) and the European Federation of Pharmaceutical Industry Associations (EFPIA). *Archives of osteoporosis,* 8**,** 136-136.

HERRERO-BEAUMONT, G. & ROMAN-BLAS, J. A. 2013. Osteoarthritis: Osteoporotic OA: a reasonable target for bone-acting agents. *Nat Rev Rheumatol,* 9**,** 448-50.

HESSE, B., VARGA, P., LANGER, M., PACUREANU, A., SCHROF, S., MANNICKE, N., SUHONEN, H., MAURER, P., CLOETENS, P., PEYRIN, F. & RAUM, K. 2015. Canalicular network morphology is the major determinant of the spatial distribution of mass density in human bone tissue: evidence by means of synchrotron radiation phase-contrast nano-CT. *J Bone Miner Res,* 30**,** 346-56.

HEVERAN, C. M., RAUFF, A., KING, K. B., CARPENTER, R. D. & FERGUSON, V. L. 2018. A new open-source tool for measuring 3D osteocyte lacunar geometries from confocal laser scanning

microscopy reveals age-related changes to lacunar size and shape in cortical mouse bone. *Bone,* 110**,** 115-127.

HIROSE, S., LI, M., KOJIMA, T., DE FREITAS, P. H., UBAIDUS, S., ODA, K., SAITO, C. & AMIZUKA, N. 2007. A histological assessment on the distribution of the osteocytic lacunar canalicular system using silver staining. *J Bone Miner Metab,* 25**,** 374-82.

HOLMBECK, K., BIANCO, P., PIDOUX, I., INOUE, S., BILLINGHURST, R. C., WU, W., CHRYSOVERGIS, K., YAMADA, S., BIRKEDAL-HANSEN, H. & POOLE, A. R. 2005. The metalloproteinase MT1-MMP is required for normal development and maintenance of osteocyte processes in bone. *J Cell Sci,* 118**,** 147-56.

HONDOW, N., BROWN, M. R., STARBORG, T., MONTEITH, A. G., BRYDSON, R., SUMMERS, H. D., REES, P. & BROWN, A. 2016. Quantifying the cellular uptake of semiconductor quantum dot nanoparticles by analytical electron microscopy. *Journal of Microscopy,* 261**,** 167-176.

HONGO, H., HASEGAWA, T., SAITO, M., TSUBOI, K., YAMAMOTO, T., SASAKI, M., ABE, M., HENRIQUE LUIZ DE FREITAS, P., YURIMOTO, H., UDAGAWA, N., LI, M. & AMIZUKA, N. 2020. Osteocytic Osteolysis in PTH-treated Wild-type and Rankl(-/-) Mice Examined by Transmission Electron Microscopy, Atomic Force Microscopy, and Isotope Microscopy. *J Histochem Cytochem,* 68**,** 651-668.

HOSHAW, S. J., FYHRIE, D. P., TAKANO, Y., BURR, D. B. & MILGROM, C. 1997. A method suitable for in vivo measurement of bone strain in humans. *J Biomech,* 30**,** 521-4.

HUA, Y., LASERSTEIN, P. & HELMSTAEDTER, M. 2015. Large-volume en-bloc staining for electron microscopy-based connectomics. *Nat Commun,* 6**,** 7923.

HUGHES, L., TOWERS, K., STARBORG, T., GULL, K. & VAUGHAN, S. 2013. A cell-body groove housing the new flagellum tip suggests an adaptation of cellular morphogenesis for parasitism in the bloodstream form of Trypanosoma brucei. *J Cell Sci,* 126**,** 5748-57.

HUSSAIN, A., GHOSH, S., KALKHORAN, S. B., HAUSENLOY, D. J., HANSSEN, E. & RAJAGOPAL, V. 2018. An automated workflow for segmenting single adult cardiac cells from large-volume serial block-face scanning electron microscopy data. *J Struct Biol,* 202**,** 275-285.

IM, G. I. & KIM, M. K. 2014. The relationship between osteoarthritis and osteoporosis. *J Bone Miner Metab,* 32**,** 101-9.

IWAMOTO, J., MATSUMOTO, H., TAKEDA, T., SATO, Y. & YEH, J. K. 2010. Effects of Vitamin K2 on Cortical and Cancellous Bone Mass, Cortical Osteocyte and Lacunar System, and Porosity in Sciatic Neurectomized Rats. *Calcified Tissue International,* 87**,** 254-262.

JACOBS, C. R., TEMIYASATHIT, S. & CASTILLO, A. B. 2010. Osteocyte mechanobiology and pericellular mechanics. *Annu Rev Biomed Eng,* 12**,** 369-400.

JAHANI, M., GENEVER, P. G., PATTON, R. J., AHWAL, F. & FAGAN, M. J. 2012. The effect of osteocyte apoptosis on signalling in the osteocyte and bone lining cell network: a computer simulation. *J Biomech,* 45**,** 2876-83.

JAIPRAKASH, A., PRASADAM, I., FENG, J. Q., LIU, Y., CRAWFORD, R. & XIAO, Y. 2012. Phenotypic Characterization of Osteoarthritic Osteocytes from the Sclerotic Zones: A Possible Pathological Role in Subchondral Bone Sclerosis. *International Journal of Biological Sciences,* 8**,** 406-417.

JANDL, N. M., VON KROGE, S., STÜRZNICKEL, J., BARANOWSKY, A., STOCKHAUSEN, K. E., MUSHUMBA, H., BEIL, F. T., PÜSCHEL, K., AMLING, M. & ROLVIEN, T. 2020. Large

osteocyte lacunae in iliac crest infantile bone are not associated with impaired mineral distribution or signs of osteocytic osteolysis. *Bone,* 135**,** 115324.

JANEL, S., WERKMEISTER, E., BONGIOVANNI, A., LAFONT, F. & BAROIS, N. 2017. CLAFEM: Correlative light atomic force electron microscopy. *Methods Cell Biol,* 140**,** 165-185.

JANG, A., PREVOST, R. & HO, S. P. 2016. Strain mapping and correlative microscopy of the alveolar bone in a bone-periodontal ligament-tooth fibrous joint. *Proc Inst Mech Eng H*.

JENKINS, T., COUTTS, L. V., D'ANGELO, S., DUNLOP, D. G., OREFFO, R. O., COOPER, C., HARVEY, N. C. & THURNER, P. J. 2016. Site-Dependent Reference Point Microindentation Complements Clinical Measures for Improved Fracture Risk Assessment at the Human Femoral Neck. *J Bone Miner Res,* 31**,** 196-203.

JENKINS, T., KATSAMENIS, O. L., ANDRIOTIS, O. G., COUTTS, L. V., CARTER, B., DUNLOP, D. G., OREFFO, R. O. C., COOPER, C., HARVEY, N. C., THURNER, P. J. & THE, O. G. 2017. The inferomedial femoral neck is compromised by age but not disease: Fracture toughness and the multifactorial mechanisms comprising reference point microindentation. *J Mech Behav Biomed Mater,* 75**,** 399-412.

JI, M.-X. & YU, Q. 2015. Primary osteoporosis in postmenopausal women. *Chronic diseases and translational medicine,* 1**,** 9-13.

JILKA, R. L. 2013. The relevance of mouse models for investigating age-related bone loss in humans. *The journals of gerontology. Series A, Biological sciences and medical sciences,* 68**,** 1209-1217.

JILKA, R. L., NOBLE, B. & WEINSTEIN, R. S. 2013. Osteocyte apoptosis. *Bone,* 54**,** 264-71.

JOENG, K. S., LEE, Y. C., LIM, J., CHEN, Y., JIANG, M. M., MUNIVEZ, E., AMBROSE, C. & LEE, B. H. 2017. Osteocyte-specific WNT1 regulates osteoblast function during bone homeostasis. *J Clin Invest,* 127**,** 2678-2688.

JONES, M. G., FABRE, A., SCHNEIDER, P., CINETTO, F., SGALLA, G., MAVROGORDATO, M., JOGAI, S., ALZETANI, A., MARSHALL, B. G., O'REILLY, K. M., WARNER, J. A., LACKIE, P. M., DAVIES, D. E., HANSELL, D. M., NICHOLSON, A. G., SINCLAIR, I., BROWN, K. K. & RICHELDI, L. 2016. Three-dimensional characterization of fibroblast foci in idiopathic pulmonary fibrosis. *JCI Insight,* 1.

JONES, M. L. & SPIERS, H. 2018. The crowd storms the ivory tower. *Nat Methods,* 15**,** 579-580.

JORDAN, G. R., LOVERIDGE, N., POWER, J., CLARKE, M. T., PARKER, M. & REEVE, J. 2003. The ratio of osteocytic incorporation to bone matrix formation in femoral neck cancellous bone: an enhanced osteoblast work rate in the vicinity of hip osteoarthritis. *Calcif Tissue Int,* 72**,** 190-6.

JORGENSEN, S. M., EAKER, D. R., VERCNOCKE, A. J. & RITMAN, E. L. 2008. Reproducibility of global and local reconstruction of three-dimensional micro-computed tomography of iliac crest biopsies. *IEEE Trans Med Imaging,* 27**,** 569-75.

JURRUS, E., HARDY, M., TASDIZEN, T., FLETCHER, P. T., KOSHEVOY, P., CHIEN, C. B., DENK, W. & WHITAKER, R. 2009. Axon tracking in serial block-face scanning electron microscopy. *Med Image Anal,* 13**,** 180-8.

KAMEL-ELSAYED, S. A., TIEDE-LEWIS, L. M., LU, Y., VENO, P. A. & DALLAS, S. L. 2015. Novel approaches for two and three dimensional multiplexed imaging of osteocytes. *Bone,* 76**,** 129-40.

Appendix

KAMIOKA, H., HONJO, T. & TAKANO-YAMAMOTO, T. 2001. A three-dimensional distribution of osteocyte processes revealed by the combination of confocal laser scanning microscopy and differential interference contrast microscopy. *Bone,* 28**,** 145-9.

KAMIOKA, H., KAMEO, Y., IMAI, Y., BAKKER, A. D., BACABAC, R. G., YAMADA, N., TAKAOKA, A., YAMASHIRO, T., ADACHI, T. & KLEIN-NULEND, J. 2012. Microscale fluid flow analysis in a human osteocyte canaliculus using a realistic high-resolution image-based three-dimensional model. *Integr Biol (Camb),* 4**,** 1198-206.

KAMIOKA, H., MURSHID, S. A., ISHIHARA, Y., KAJIMURA, N., HASEGAWA, T., ANDO, R., SUGAWARA, Y., YAMASHIRO, T., TAKAOKA, A. & TAKANO-YAMAMOTO, T. 2009. A method for observing silver-stained osteocytes in situ in 3-microm sections using ultra-high voltage electron microscopy tomography. *Microsc Microanal,* 15**,** 377-83.

KANIS, J. A., MELTON, L. J., 3RD, CHRISTIANSEN, C., JOHNSTON, C. C. & KHALTAEV, N. 1994. The diagnosis of osteoporosis. *J Bone Miner Res,* 9**,** 1137-41.

KAPISHNIKOV, S., GROLIMUND, D., SCHNEIDER, G., PEREIRO, E., MCNALLY, J. G., ALS-NIELSEN, J. & LEISEROWITZ, L. 2017. Unraveling heme detoxification in the malaria parasite by in situ correlative X-ray fluorescence microscopy and soft X-ray tomography. *Sci Rep,* 7**,** 7610.

KARNOVSKY, M. J. 1971. Use of ferrocyanide-reduced osmium in electron microscopy. *Proc 14th Annual Meeting Amer Soc Cell Biol*.

KARREMAN, M. A., RUTHENSTEINER, B., MERCIER, L., SCHIEBER, N. L., SOLECKI, G., WINKLER, F., GOETZ, J. G. & SCHWAB, Y. 2017. Find your way with X-Ray. *Methods in Cell Biology,* 140**,** 277-301.

KATSAMENIS, O. L., CHONG, H. M. H., ANDRIOTIS, O. G. & THURNER, P. J. 2013. Load-bearing in cortical bone microstructure: Selective stiffening and heterogeneous strain distribution at the lamellar level. *Journal of the Mechanical Behavior of Biomedical Materials,* 17**,** 152-165.

KATSAMENIS, O. L., OLDING, M., WARNER, J. A., CHATELET, D. S., JONES, M. G., SGALLA, G., SMIT, B., LARKIN, O. J., HAIG, I., RICHELDI, L., SINCLAIR, I., LACKIE, P. M. & SCHNEIDER, P. 2019. X-ray Micro-Computed Tomography for Nondestructive Three-Dimensional (3D) X-ray Histology. *Am J Pathol,* 189**,** 1608-1620.

KEENE, D. R., TUFA, S. F., WONG, M. H., SMITH, N. R., SAKAI, L. Y. & HORTON, W. A. 2014. Chapter 18 - Correlation of the Same Fields Imaged in the TEM, Confocal, LM, and MicroCT by Image Registration: From Specimen Preparation to Displaying a Final Composite Image. *In:* THOMAS, M.-R. & PAUL, V. (eds.) *Methods in Cell Biology.* Academic Press.

KERSCHNITZKI, M., KOLLMANNSBERGER, P., BURGHAMMER, M., DUDA, G. N., WEINKAMER, R., WAGERMAIER, W. & FRATZL, P. 2013. Architecture of the osteocyte network correlates with bone material quality. *J Bone Miner Res,* 28**,** 1837-45.

KERSCHNITZKI, M., WAGERMAIER, W., ROSCHGER, P., SETO, J., SHAHAR, R., DUDA, G. N., MUNDLOS, S. & FRATZL, P. 2011. The organization of the osteocyte network mirrors the extracellular matrix orientation in bone. *J Struct Biol,* 173**,** 303-11.

KITTELMANN, M., HAWES, C. & HUGHES, L. 2016. Serial block face scanning electron microscopy and the reconstruction of plant cell membrane systems. *J Microsc,* 263**,** 200-11.

KIZILYAPRAK, C., LONGO, G., DARASPE, J. & HUMBEL, B. M. 2015. Investigation of resins suitable for the preparation of biological sample for 3-D electron microscopy. *J Struct Biol,* 189**,** 135-46.

KLEIN-NULEND, J., BAKKER, A. D., BACABAC, R. G., VATSA, A. & WEINBAUM, S. 2013. Mechanosensation and transduction in osteocytes. *Bone,* 54**,** 182-190.

KLEIN-NULEND, J., VAN DER PLAS, A., SEMEINS, C. M., AJUBI, N. E., FRANGOS, J. A., NIJWEIDE, P. J. & BURGER, E. H. 1995. Sensitivity of osteocytes to biomechanical stress in vitro. *Faseb j,* 9**,** 441-5.

KNOTHE TATE, M. L., ADAMSON, J. R., TAMI, A. E. & BAUER, T. W. 2004. The osteocyte. *Int J Biochem Cell Biol,* 36**,** 1-8.

KNOTHE TATE, M. L., NIEDERER, P. & KNOTHE, U. 1998. In vivo tracer transport through the lacunocanalicular system of rat bone in an environment devoid of mechanical loading. *Bone,* 22**,** 107-17.

KOBAYASHI, K., NOJIRI, H., SAITA, Y., MORIKAWA, D., OZAWA, Y., WATANABE, K., KOIKE, M., ASOU, Y., SHIRASAWA, T., YOKOTE, K., KANEKO, K. & SHIMIZU, T. 2015. Mitochondrial superoxide in osteocytes perturbs canalicular networks in the setting of age-related osteoporosis. *Sci Rep,* 5**,** 9148.

KOLLET, O., DAR, A., SHIVTIEL, S., KALINKOVICH, A., LAPID, K., SZTAINBERG, Y., TESIO, M., SAMSTEIN, R. M., GOICHBERG, P., SPIEGEL, A., ELSON, A. & LAPIDOT, T. 2006. Osteoclasts degrade endosteal components and promote mobilization of hematopoietic progenitor cells. *Nature Medicine,* 12**,** 657-664.

KOLLMANNSBERGER, P., KERSCHNITZKI, M., REPP, F., WAGERMAIER, W., WEINKAMER, R. & FRATZL, P. 2017. The small world of osteocytes: connectomics of the lacuno-canalicular network in bone. *New Journal of Physics,* 19**,** 073019.

KONG, Y. Y., YOSHIDA, H., SAROSI, I., TAN, H. L., TIMMS, E., CAPPARELLI, C., MORONY, S., OLIVEIRA-DOS-SANTOS, A. J., VAN, G., ITIE, A., KHOO, W., WAKEHAM, A., DUNSTAN, C. R., LACEY, D. L., MAK, T. W., BOYLE, W. J. & PENNINGER, J. M. 1999. OPGL is a key regulator of osteoclastogenesis, lymphocyte development and lymph-node organogenesis. *Nature,* 397**,** 315-23.

KORKMAZ, E. 2016. New approach to 3-D imaging of biological materials provides isotropic resolution down to a few nanometers. *Am. Lab.* [Online], 48.

KREMER, A., LIPPENS, S., BARTUNKOVA, S., ASSELBERGH, B., BLANPAIN, C., FENDRYCH, M., GOOSSENS, A., HOLT, M., JANSSENS, S., KROLS, M., LARSIMONT, J. C., MC GUIRE, C., NOWACK, M. K., SAELENS, X., SCHERTEL, A., SCHEPENS, B., SLEZAK, M., TIMMERMAN, V., THEUNIS, C., VAN BREMPT, R., VISSER, Y. & GUÉRIN, C. J. 2015. Developing 3D SEM in a broad biological context. *Journal of Microscopy,* 259**,** 80-96.

KREMER, J. R., MASTRONARDE, D. N. & MCINTOSH, J. R. 1996. Computer visualization of three-dimensional image data using IMOD. *J Struct Biol,* 116**,** 71-6.

KRESHUK, A., STRAEHLE, C. N., SOMMER, C., KOETHE, U., CANTONI, M., KNOTT, G. & HAMPRECHT, F. A. 2011. Automated detection and segmentation of synaptic contacts in nearly isotropic serial electron microscopy images. *PLoS One,* 6**,** e24899.

KUBOTA, Y. 2015. New developments in electron microscopy for serial image acquisition of neuronal profiles. *Microscopy (Oxf),* 64**,** 27-36.

KUFAHL, R. H. & SAHA, S. 1990. A theoretical model for stress-generated fluid flow in the canaliculi-lacunae network in bone tissue. *J Biomech,* 23**,** 171-80.

Appendix

KUHN, H., BREITHARDT, G., KNIERIEM, H. J., LOOGEN, F., BOTH, A., SCHMIDT, W. A., STROOBANDT, R. & GLEICHMANN, U. 1975. [[Diagnostic and prognostic value of endomyocardial biopsy in patients with congestive cardiomyopathy (author's transl)]rdiomyopathy(author]. *Dtsch Med Wochenschr,* 100**,** 717.

LAI, X., CHUNG, R., LI, Y., LIU, X. S. & WANG, L. 2021. Lactation alters fluid flow and solute transport in maternal skeleton: A multiscale modeling study on the effects of microstructural changes and loading frequency. *Bone***,** 116033.

LAI, X., PRICE, C., MODLA, S., THOMPSON, W. R., CAPLAN, J., KIRN-SAFRAN, C. B. & WANG, L. 2015. The dependences of osteocyte network on bone compartment, age, and disease. *Bone Research,* 3**,** 15009.

LANDIS, E. N. & KEANE, D. T. 2010. X-ray microtomography. *Materials Characterization,* 61**,** 1305-1316.

LANE, N. E., YAO, W., BALOOCH, M., NALLA, R. K., BALOOCH, G., HABELITZ, S., KINNEY, J. H. & BONEWALD, L. F. 2006. Glucocorticoid-treated mice have localized changes in trabecular bone material properties and osteocyte lacunar size that are not observed in placebo-treated or estrogen-deficient mice. *J Bone Miner Res,* 21**,** 466-76.

LANGER, M., PACUREANU, A., SUHONEN, H., GRIMAL, Q., CLOETENS, P. & PEYRIN, F. 2012. X-Ray Phase Nanotomography Resolves the 3D Human Bone Ultrastructure. *PLoS ONE,* 7**,** e35691.

LEAL, J., GRAY, A. M., PRIETO-ALHAMBRA, D., ARDEN, N. K., COOPER, C., JAVAID, M. K. & JUDGE, A. 2016. Impact of hip fracture on hospital care costs: a population-based study. *Osteoporos Int,* 27**,** 549-58.

LEE, K. L., GUEVARRA, M. D., NGUYEN, A. M., CHUA, M. C., WANG, Y. & JACOBS, C. R. 2015. The primary cilium functions as a mechanical and calcium signaling nexus. *Cilia,* 4**,** 7.

LEES, R. M., PEDDIE, C. J., COLLINSON, L. M., ASHBY, M. C. & VERKADE, P. 2017. Correlative two-photon and serial block face scanning electron microscopy in neuronal tissue using 3D near-infrared branding maps. *Methods Cell Biol,* 140**,** 245-276.

LEIGHTON, S. B. 1981. SEM IMAGES OF BLOCK FACES, CUT BY A MINIATURE MICROTOME WITHIN THE SEM - A TECHNICAL NOTE. *Scanning Electron Microscopy***,** 73-76.

LEIGHTON, S. B. & KUZIRIAN, A. M. 1987. SECTIONLESS SECTIONING - A SYSTEMATIC METHOD FOR SCANNING ELECTRON-MICROSCOPIC EXAMINATION OF EMBEDDED TISSUE. *Biological Bulletin,* 173**,** 444-445.

LI, B. & ASPDEN, R. M. 1997. Composition and mechanical properties of cancellous bone from the femoral head of patients with osteoporosis or osteoarthritis. *J Bone Miner Res,* 12**,** 641-51.

LI, B., MARSHALL, D., ROE, M. & ASPDEN, R. M. 1999. The electron microscope appearance of the subchondral bone plate in the human femoral head in osteoarthritis and osteoporosis. *Journal of Anatomy,* 195**,** 101-110.

LI, X., OMINSKY, M. S., WARMINGTON, K. S., MORONY, S., GONG, J., CAO, J., GAO, Y., SHALHOUB, V., TIPTON, B., HALDANKAR, R., CHEN, Q., WINTERS, A., BOONE, T., GENG, Z., NIU, Q. T., KE, H. Z., KOSTENUIK, P. J., SIMONET, W. S., LACEY, D. L. & PASZTY, C. 2009. Sclerostin antibody treatment increases bone formation, bone mass, and bone strength in a rat model of postmenopausal osteoporosis. *J Bone Miner Res,* 24**,** 578-88.

LIN, Y. & XU, S. 2011. AFM analysis of the lacunar-canalicular network in demineralized compact bone. *J Microsc,* 241**,** 291-302.

LIU, J., LI, L., YANG, Y., HONG, B., CHEN, X., XIE, Q. & HAN, H. 2020. Automatic Reconstruction of Mitochondria and Endoplasmic Reticulum in Electron Microscopy Volumes by Deep Learning. *Front Neurosci,* 14**,** 599.

LIU, T., JONES, C., SEYEDHOSSEINI, M. & TASDIZEN, T. 2014. A modular hierarchical approach to 3D electron microscopy image segmentation. *J Neurosci Methods,* 226**,** 88-102.

LUCAS, M., GUENTHERT, M., GASSER, P., LUCAS, F. & WEPF, R. 2014. Correlative 3D Imaging: CLSM and FIB-SEM Tomography Using High-Pressure Frozen, Freeze-Substituted Biological Samples. *In:* KUO, J. (ed.) *Electron Microscopy.* Humana Press.

LUCAS, M. S., GÜNTHERT, M., BITTERMANN, A. G., DE MARCO, A. & WEPF, R. 2017. Correlation of live-cell imaging with volume scanning electron microscopy. *Methods in Cell Biology,* 140**,** 123-148.

LUCAS, M. S., GUNTHERT, M., GASSER, P., LUCAS, F. & WEPF, R. 2012. Bridging microscopes: 3D correlative light and scanning electron microscopy of complex biological structures. *Methods Cell Biol.* 2012/08/04 ed.

MA, Y. L., DAI, R. C., SHENG, Z. F., JIN, Y., ZHANG, Y. H., FANG, L. N., FAN, H. J. & LIAO, E. Y. 2008. Quantitative associations between osteocyte density and biomechanics, microcrack and microstructure in OVX rats vertebral trabeculae. *J Biomech,* 41**,** 1324-32.

MADER, K. S., DONAHUE, L. R., MULLER, R. & STAMPANONI, M. 2015. High-throughput phenotyping and genetic linkage of cortical bone microstructure in the mouse. *BMC Genomics,* 16**,** 493.

MADER, K. S., SCHNEIDER, P., MULLER, R. & STAMPANONI, M. 2013. A quantitative framework for the 3D characterization of the osteocyte lacunar system. *Bone,* 57**,** 142-54.

MAHAMID, J., SHARIR, A., GUR, D., ZELZER, E., ADDADI, L. & WEINER, S. 2011. Bone mineralization proceeds through intracellular calcium phosphate loaded vesicles: A cryo-electron microscopy study. *Journal of Structural Biology,* 174**,** 527-535.

MAHMOODI, B., GOGGIN, P., FOWLER, C. & COOK, R. B. 2020. Quantitative assessment of dentine mineralization and tubule occlusion by NovaMin and stannous fluoride using serial block face scanning electron microscopy. *Journal of Biomedical Materials Research Part B: Applied Biomaterials,* n/a.

MALICK, L. E. & WILSON, R. B. 1975. Modified thiocarbohydrazide procedure for scanning electron microscopy: routine use for normal, pathological, or experimental tissues. *Stain Technol,* 50**,** 265-9.

MALONE, A. M., ANDERSON, C. T., TUMMALA, P., KWON, R. Y., JOHNSTON, T. R., STEARNS, T. & JACOBS, C. R. 2007. Primary cilia mediate mechanosensing in bone cells by a calcium-independent mechanism. *Proc Natl Acad Sci U S A,* 104**,** 13325-30.

MARIE, P. J. & COHEN-SOLAL, M. 2018. The Expanding Life and Functions of Osteogenic Cells: From Simple Bone-Making Cells to Multifunctional Cells and Beyond. *Journal of Bone and Mineral Research,* 33**,** 199-210.

MARIEB, E. N. & KELLER, S. M. 2017. *Essentials of Human Anatomy & Physiology, Global Edition,* Harlow, United Kingdom, UNITED KINGDOM, Pearson Education Limited.

MARKERT, S. M., BAUER, V., MUENZ, T. S., JONES, N. G., HELMPROBST, F., BRITZ, S., SAUER, M., RÖSSLER, W., ENGSTLER, M. & STIGLOHER, C. 2017. 3D subcellular localization with superresolution array tomography on ultrathin sections of various species. *Methods Cell Biol,* 140**,** 21-47.

MAROTTI, G., FERRETTI, M., REMAGGI, F. & PALUMBO, C. 1995. Quantitative evaluation on osteocyte canalicular density in human secondary osteons. *Bone,* 16**,** 125-8.

MARTIN, R. B. 2000. Toward a unifying theory of bone remodeling. *Bone,* 26**,** 1-6.

MARTIN, R. B. 2002. Is all cortical bone remodeling initiated by microdamage? *Bone,* 30**,** 8-13.

MAZUR, C. M., WOO, J. J., YEE, C. S., FIELDS, A. J., ACEVEDO, C., BAILEY, K. N., KAYA, S., FOWLER, T. W., LOTZ, J. C., DANG, A., KUO, A. C., VAIL, T. P. & ALLISTON, T. 2019. Osteocyte dysfunction promotes osteoarthritis through MMP13-dependent suppression of subchondral bone homeostasis. *Bone Research,* 7**,** 34.

MCCREADIE, B. R., HOLLISTER, S. J., SCHAFFLER, M. B. & GOLDSTEIN, S. A. 2004. Osteocyte lacuna size and shape in women with and without osteoporotic fracture. *Journal of Biomechanics,* 37**,** 563-572.

MCNAMARA, L., MAJESKA, RJ, WEINBAUM, S, FRIEDRICH, V, SCHAFFLER, MB 2006. Attachment Of Osteocyte Cell Processes To The Bone Matrix. *Trans. Orthop. Res. Soc.,* 31**,** 393.

MCNAMARA, L., MAJESKA, RJ, WEINBAUM, S, FRIEDRICH, V, SCHAFFLER, MB 2009. ATTACHMENT OF OSTEOCYTE CELL PROCESSES TO THE BONE MATRIX *52nd Annual Meeting of the Orthopaedic Research Society*.

MCNAMARA, L. M., MAJESKA, R. J., WEINBAUM, S., FRIEDRICH, V. & SCHAFFLER, M. B. 2009. Attachment of osteocyte cell processes to the bone matrix. *Anat Rec (Hoboken),* 292**,** 355-63.

MCNAMARA, L. M. & PRENDERGAST, P. J. 2007. Bone remodelling algorithms incorporating both strain and microdamage stimuli. *J Biomech,* 40**,** 1381-91.

MELTON III, L. J. 2003. Adverse Outcomes of Osteoporotic Fractures in the General Population. *Journal of Bone and Mineral Research,* 18**,** 1139-1141.

METSCHER, B. 2020. A simple nuclear contrast staining method for microCT-based 3D histology using lead(II) acetate. *J Anat*.

METSCHER, B. D. 2009. MicroCT for comparative morphology: simple staining methods allow high-contrast 3D imaging of diverse non-mineralized animal tissues. *BMC Physiol,* 9**,** 11.

MIKULA, S. & DENK, W. 2015. High-resolution whole-brain staining for electron microscopic circuit reconstruction. *Nat Methods,* 12**,** 541-6.

MILGROM, C., FINESTONE, A., HAMEL, A., MANDES, V., BURR, D. & SHARKEY, N. 2004. A comparison of bone strain measurements at anatomically relevant sites using surface gauges versus strain gauged bone staples. *J Biomech,* 37**,** 947-52.

MILOVANOVIC, P. & BUSSE, B. 2020. Phenomenon of osteocyte lacunar mineralization: indicator of former osteocyte death and a novel marker of impaired bone quality? *Endocr Connect,* 9**,** R70-80.

MILOVANOVIC, P., VOM SCHEIDT, A., MLETZKO, K., SARAU, G., PÜSCHEL, K., DJURIC, M., AMLING, M., CHRISTIANSEN, S. & BUSSE, B. 2018. Bone tissue aging affects mineralization of cement lines. *Bone,* 110**,** 187-193.

MILOVANOVIC, P., ZIMMERMANN, E. A., HAHN, M., DJONIC, D., PUSCHEL, K., DJURIC, M., AMLING, M. & BUSSE, B. 2013. Osteocytic canalicular networks: morphological implications for altered mechanosensitivity. *ACS Nano,* 7**,** 7542-51.

MILOVANOVIC, P., ZIMMERMANN, E. A., VOM SCHEIDT, A., HOFFMANN, B., SARAU, G., YORGAN, T., SCHWEIZER, M., AMLING, M., CHRISTIANSEN, S. & BUSSE, B. 2017. The Formation of Calcified Nanospherites during Micropetrosis Represents a Unique Mineralization Mechanism in Aged Human Bone. *Small,* 13.

MOHUN, T. J. & WENINGER, W. J. 2012. Generation of volume data by episcopic three-dimensional imaging of embryos. *Cold Spring Harb Protoc,* 2012**,** 681-2.

MOLLENHAUER, H. H. 1993. Artifacts caused by dehydration and epoxy embedding in transmission electron microscopy. *Microscopy Research and Technique,* 26**,** 496-512.

MOSEY, H., NÚÑEZ, J. A., GORING, A., CLARKIN, C. E., STAINES, K. A., LEE, P. D., PITSILLIDES, A. A. & JAVAHERI, B. 2017. Sost Deficiency does not Alter Bone's Lacunar or Vascular Porosity in Mice. *Front Mater,* 4**,** 27.

MULLENDER, M. G., HUISKES, R., VERSLEYEN, H. & BUMA, P. 1996a. Osteocyte density and histomorphometric parameters in cancellous bone of the proximal femur in five mammalian species. *J Orthop Res,* 14**,** 972-9.

MULLENDER, M. G., TAN, S. D., VICO, L., ALEXANDRE, C. & KLEIN-NULEND, J. 2005. Differences in osteocyte density and bone histomorphometry between men and women and between healthy and osteoporotic subjects. *Calcif Tissue Int,* 77**,** 291-6.

MULLENDER, M. G., VAN DER MEER, D. D., HUISKES, R. & LIPS, P. 1996b. Osteocyte density changes in aging and osteoporosis. *Bone,* 18**,** 109-113.

MULLER-REICHERT, T. V., P. 2012. Introduction to correlative light and electron microscopy. *In:* MULLER-REICHERT, T. V., P. (ed.) *Correlative light and electron microsopy.* Academic Press.

MÜLLER, M., KIMM, M. A., FERSTL, S., ALLNER, S., ACHTERHOLD, K., HERZEN, J., PFEIFFER, F. & BUSSE, M. 2018. Nucleus-specific X-ray stain for 3D virtual histology. *Sci Rep,* 8**,** 17855.

MULLER, R. 2009. Hierarchical microimaging of bone structure and function. *Nat Rev Rheumatol,* 5**,** 373-81.

NAKASHIMA, T., HAYASHI, M., FUKUNAGA, T., KURATA, K., OH-HORA, M., FENG, J. Q., BONEWALD, L. F., KODAMA, T., WUTZ, A., WAGNER, E. F., PENNINGER, J. M. & TAKAYANAGI, H. 2011. Evidence for osteocyte regulation of bone homeostasis through RANKL expression. *Nat Med,* 17**,** 1231-4.

NANGO, N., KUBOTA, S., HASEGAWA, T., YASHIRO, W., MOMOSE, A. & MATSUO, K. 2016. Osteocyte-directed bone demineralization along canaliculi. *Bone,* 84**,** 279-88.

NEVE, A., CORRADO, A. & CANTATORE, F. P. 2012. Osteocytes: central conductors of bone biology in normal and pathological conditions. *Acta Physiologica,* 204**,** 317-330.

NGUYEN, H. B., THAI, T. Q., SAITOH, S., WU, B., SAITOH, Y., SHIMO, S., FUJITANI, H., OTOBE, H. & OHNO, N. 2016. Conductive resins improve charging and resolution of acquired images in electron microscopic volume imaging. *Scientific Reports,* 6**,** 23721.

NGUYEN, V. H., LEMAIRE, T. & NAILI, S. 2011. Influence of interstitial bone microcracks on strain-induced fluid flow. *Biomech Model Mechanobiol,* 10**,** 963-72.

NICOLELLA, D. P., BONEWALD, L. F., MORAVITS, D. E. & LANKFORD, J. 2005. Measurement of microstructural strain in cortical bone. *Eur J Morphol,* 42**,** 23-9.

NICOLELLA, D. P., FENG, J. Q., MORAVITS, D. E., BONIVITCH, A. R., WANG, Y., DUSECICH, V., YAO, W., LANE, N. & BONEWALD, L. F. 2008. Effects of nanomechanical bone tissue properties on bone tissue strain: implications for osteocyte mechanotransduction. *J Musculoskelet Neuronal Interact,* 8**,** 330-1.

NICOLELLA, D. P., MORAVITS, D. E., GALE, A. M., BONEWALD, L. F. & LANKFORD, J. 2006. Osteocyte lacunae tissue strain in cortical bone. *J Biomech,* 39**,** 1735-43.

NOBLE, B. S., PEET, N., STEVENS, H. Y., BRABBS, A., MOSLEY, J. R., REILLY, G. C., REEVE, J., SKERRY, T. M. & LANYON, L. E. 2003. Mechanical loading: biphasic osteocyte survival and targeting of osteoclasts for bone destruction in rat cortical bone. *Am J Physiol Cell Physiol,* 284**,** C934-43.

NÚÑEZ, J. A., GORING, A., JAVAHERI, B., RAZI, H., GOMEZ-NICOLA, D., PITSILLIDES, A. A., THURNER, P. J., GOMEZ-NICOLA, D., SCHNEIDER, P. & CLARKIN, C. E. 2018. Regional diversity in the murine cortical vascular network is revealed by synchrotron X-ray tomography and is amplified with age. *Eur Cell Mater,* 35**,** 281-299.

OBATA, Y., BALE, H. A., BARNARD, H. S., PARKINSON, D. Y., ALLISTON, T. & ACEVEDO, C. 2020. Quantitative and qualitative bone imaging: A review of synchrotron radiation microtomography analysis in bone research. *Journal of the Mechanical Behavior of Biomedical Materials,* 110**,** 103887.

OKADA, S., YOSHIDA, S., ASHRAFI, S. H. & SCHRAUFNAGEL, D. E. 2002. The canalicular structure of compact bone in the rat at different ages. *Microsc Microanal,* 8**,** 104-15.

OMINSKY, M. S., NIU, Q. T., LI, C., LI, X. & KE, H. Z. 2014. Tissue-level mechanisms responsible for the increase in bone formation and bone volume by sclerostin antibody. *J Bone Miner Res,* 29**,** 1424-30.

ONG, A. C. & WHEATLEY, D. N. 2003. Polycystic kidney disease--the ciliary connection. *Lancet,* 361**,** 774-6.

OZCIVICI, E., LUU, Y. K., ADLER, B., QIN, Y. X., RUBIN, J., JUDEX, S. & RUBIN, C. T. 2010. Mechanical signals as anabolic agents in bone. *Nat Rev Rheumatol,* 6**,** 50-9.

PADHI, D., JANG, G., STOUCH, B., FANG, L. & POSVAR, E. 2011. Single-dose, placebo-controlled, randomized study of AMG 785, a sclerostin monoclonal antibody. *J Bone Miner Res,* 26**,** 19-26.

PALADE, G. E. 1952. A study of fixation for electron microscopy. *J Exp Med,* 95**,** 285-98.

PALAMARA, J., PHAKEY, P. P., RACHINGER, W. A. & ORAMS, H. J. 1981. Electron-microscope study of the dentine-enamel junction of kangaroo (Macropus giganteus) teeth using selected-area argon-ion-beam thinning. *Cell Tissue Res,* 221**,** 405-19.

PALUMBO, C. 1986. A three-dimensional ultrastructural study of osteoid-osteocytes in the tibia of chick embryos. *Cell and Tissue Research,* 246**,** 125-131.

PALUMBO, C., FERRETTI, M. & MAROTTI, G. 2004. Osteocyte dendrogenesis in static and dynamic bone formation: an ultrastructural study. *Anat Rec A Discov Mol Cell Evol Biol,* 278**,** 474-80.

PALUMBO, C., PALAZZINI, S., ZAFFE, D. & MAROTTI, G. 1990. Osteocyte differentiation in the tibia of newborn rabbit: an ultrastructural study of the formation of cytoplasmic processes. *Acta Anat (Basel),* 137**,** 350-8.

PARFITT, A. M. 1983. The physiologic and clinical significance of bone histomorphometric data. *Bone Histomorphometry : Techniques and Interpretation***,** 143-223.

PARFITT, A. M. 1994a. Osteonal and hemi-osteonal remodeling: the spatial and temporal framework for signal traffic in adult human bone. *J Cell Biochem,* 55**,** 273-86.

PARFITT, A. M. 1994b. The two faces of growth: benefits and risks to bone integrity. *Osteoporos Int,* 4**,** 382-98.

PARFITT, A. M., DREZNER, M. K., GLORIEUX, F. H., KANIS, J. A., MALLUCHE, H., MEUNIER, P. J., OTT, S. M. & RECKER, R. R. 1987. Bone histomorphometry: Standardization of nomenclature, symbols, and units: Report of the asbmr histomorphometry nomenclature committee. *Journal of Bone and Mineral Research,* 2**,** 595-610.

PASTRAMA, M. I., SCHEINER, S., PIVONKA, P. & HELLMICH, C. 2018. A mathematical multiscale model of bone remodeling, accounting for pore space-specific mechanosensation. *Bone,* 107**,** 208-221.

PATEL, T. K., BRODT, M. D. & SILVA, M. J. 2014. Experimental and finite element analysis of strains induced by axial tibial compression in young-adult and old female C57Bl/6 mice. *J Biomech,* 47**,** 451-7.

PAUL-GILLOTEAUX, P., HEILIGENSTEIN, X., BELLE, M., DOMART, M.-C., LARIJANI, B., COLLINSON, L., RAPOSO, G. & SALAMERO, J. 2017. eC-CLEM: flexible multidimensional registration software for correlative microscopies. *Nature Methods,* 14**,** 102-103.

PAUL, G. R., MALHOTRA, A. & MULLER, R. 2018. Mechanical Stimuli in the Local In Vivo Environment in Bone: Computational Approaches Linking Organ-Scale Loads to Cellular Signals. *Curr Osteoporos Rep,* 16**,** 395-403.

PECKHAM, M. 2003. *The Histology Guide* [Online]. Leeds: University of Leeds. Available: https://www.histology.leeds.ac.uk/bone/bone_cell_types.php [Accessed 01/12 2020].

PEDDIE, C. J. & COLLINSON, L. M. 2014. Exploring the third dimension: Volume electron microscopy comes of age. *Micron,* 61**,** 9-19.

PEDDIE, C. J., DOMART, M. C., SNETKOV, X., O'TOOLE, P., LARIJANI, B., WAY, M., COX, S. & COLLINSON, L. M. 2017. Correlative super-resolution fluorescence and electron microscopy using conventional fluorescent proteins in vacuo. *J Struct Biol,* 199**,** 120-131.

PEDDIE, C. J., LIV, N., HOOGENBOOM, J. P. & COLLINSON, L. M. 2014. Integrated light and scanning electron microscopy of GFP-expressing cells. *Methods Cell Biol,* 124**,** 363-89.

PEDDIE, C. J., SCHIEBER, N.L. 2019. The Importance of Sample Processing for Correlative Imaging (or, Rubbish In, Rubbish Out). *In:* VERKADE, P., COLLINSON, L.M. (ed.) *Correlative Imaging.* John Wiley and Sons Ltd.

PEREZ, A. J., SEYEDHOSSEINI, M., DEERINCK, T. J., BUSHONG, E. A., PANDA, S., TASDIZEN, T. & ELLISMAN, M. H. 2014. A workflow for the automatic segmentation of organelles in electron microscopy image stacks. *Front Neuroanat,* 8**,** 126.

PEYRIN, F., DONG, P., PACUREANU, A. & LANGER, M. 2014. Micro- and nano-CT for the study of bone ultrastructure. *Curr Osteoporos Rep,* 12**,** 465-74.

Appendix

PEYRIN, F., SALOME, M., CLOETENS, P., LAVAL-JEANTET, A. M., RITMAN, E. & RUEGSEGGER, P. 1998. Micro-CT examinations of trabecular bone samples at different resolutions: 14, 7 and 2 micron level. *Technol Health Care,* 6**,** 391-401.

PICHAT, J., IGLESIAS, J. E., YOUSRY, T., OURSELIN, S. & MODAT, M. 2018. A Survey of Methods for 3D Histology Reconstruction. *Med Image Anal,* 46**,** 73-105.

PIEKARSKI, K. & MUNRO, M. 1977. Transport mechanism operating between blood supply and osteocytes in long bones. *Nature,* 269**,** 80-2.

PIEMONTESE, M., ALMEIDA, M., ROBLING, A. G., KIM, H. N., XIONG, J., THOSTENSON, J. D., WEINSTEIN, R. S., MANOLAGAS, S. C., O'BRIEN, C. A. & JILKA, R. L. 2017. Old age causes de novo intracortical bone remodeling and porosity in mice. *JCI Insight,* 2.

PITOL, D. L., CAETANO, F. H. & LUNARDI, L. O. 2007. Microwave-induced fast decalcification of rat bone for electron microscopic analysis: an ultrastructural and cytochemical study. *Brazilian Dental Journal,* 18**,** 153-157.

POWER, J., LOVERIDGE, N., RUSHTON, N., PARKER, M. & REEVE, J. 2002. Osteocyte density in aging subjects is enhanced in bone adjacent to remodeling haversian systems. *Bone,* 30**,** 859-65.

POWER, J., NOBLE, B. S., LOVERIDGE, N., BELL, K. L., RUSHTON, N. & REEVE, J. 2001. Osteocyte lacunar occupancy in the femoral neck cortex: an association with cortical remodeling in hip fracture cases and controls. *Calcif Tissue Int,* 69**,** 13-9.

POWER, J., POOLE, K. E., VAN BEZOOIJEN, R., DOUBE, M., CABALLERO-ALIAS, A. M., LOWIK, C., PAPAPOULOS, S., REEVE, J. & LOVERIDGE, N. 2010. Sclerostin and the regulation of bone formation: Effects in hip osteoarthritis and femoral neck fracture. *J Bone Miner Res,* 25**,** 1867-76.

PRASAD, J., WIATER, B. P., NORK, S. E., BAIN, S. D. & GROSS, T. S. 2010. Characterizing gait induced normal strains in a murine tibia cortical bone defect model. *J Biomech,* 43**,** 2765-70.

PRASADAM, I., FARNAGHI, S., FENG, J. Q., GU, W., PERRY, S., CRAWFORD, R. & XIAO, Y. 2013. Impact of extracellular matrix derived from osteoarthritis subchondral bone osteoblasts on osteocytes: role of integrinbeta1 and focal adhesion kinase signaling cues. *Arthritis Res Ther,* 15**,** R150.

PUTH, M.-T., KLASCHIK, M., SCHMID, M., WECKBECKER, K. & MÜNSTER, E. 2018. Prevalence and comorbidity of osteoporosis– a cross-sectional analysis on 10,660 adults aged 50 years and older in Germany. *BMC Musculoskeletal Disorders,* 19**,** 144.

QING, H., ARDESHIRPOUR, L., PAJEVIC, P. D., DUSEVICH, V., JAHN, K., KATO, S., WYSOLMERSKI, J. & BONEWALD, L. F. 2012. Demonstration of osteocytic perilacunar/canalicular remodeling in mice during lactation. *J Bone Miner Res,* 27**,** 1018-29.

QIU, N., XIAO, Z., CAO, L., BUECHEL, M. M., DAVID, V., ROAN, E. & QUARLES, L. D. 2012. Disruption of Kif3a in osteoblasts results in defective bone formation and osteopenia. *J Cell Sci,* 125**,** 1945-57.

QIU, S., RAO, D. S., PALNITKAR, S. & PARFITT, A. M. 2002a. Age and distance from the surface but not menopause reduce osteocyte density in human cancellous bone. *Bone,* 31**,** 313-8.

QIU, S., RAO, D. S., PALNITKAR, S. & PARFITT, A. M. 2002b. Relationships between osteocyte density and bone formation rate in human cancellous bone. *Bone,* 31**,** 709-11.

QIU, S., RAO, D. S., PALNITKAR, S. & PARFITT, A. M. 2003. Reduced iliac cancellous osteocyte density in patients with osteoporotic vertebral fracture. *J Bone Miner Res,* 18**,** 1657-63.

QIU, S., RAO, D. S., PALNITKAR, S. & PARFITT, A. M. 2006. Differences in osteocyte and lacunar density between Black and White American women. *Bone,* 38**,** 130-5.

RABELO, G. D., VOM SCHEIDT, A., KLEBIG, F., HEMMATIAN, H., CITAK, M., AMLING, M., BUSSE, B. & JAHN, K. 2020. Multiscale bone quality analysis in osteoarthritic knee joints reveal a role of the mechanosensory osteocyte network in osteophytes. *Sci Rep,* 10**,** 673.

REILLY, G. C., HAUT, T. R., YELLOWLEY, C. E., DONAHUE, H. J. & JACOBS, C. R. 2003. Fluid flow induced PGE2 release by bone cells is reduced by glycocalyx degradation whereas calcium signals are not. *Biorheology,* 40**,** 591-603.

REILLY, G. C., KNAPP, H. F., STEMMER, A., NIEDERER, P. & KNOTHE TATE, M. L. 2001. Investigation of the morphology of the lacunocanalicular system of cortical bone using atomic force microscopy. *Ann Biomed Eng,* 29**,** 1074-81.

REMAGGI, F., CANE, V., PALUMBO, C. & FERRETTI, M. 1998. Histomorphometric study on the osteocyte lacuno-canalicular network in animals of different species. I. Woven-fibered and parallel-fibered bones. *Ital J Anat Embryol,* 103**,** 145-55.

REPP, F., KOLLMANNSBERGER, P., ROSCHGER, A., KERSCHNITZKI, M., BERZLANOVICH, A., GRUBER, G. M., ROSCHGER, P., WAGERMAIER, W. & WEINKAMER, R. 2017. Spatial heterogeneity in the canalicular density of the osteocyte network in human osteons. *Bone Rep,* 6**,** 101-108.

RESS, D. B., HARLOW, M. L., MARSHALL, R. M. & MCMAHAN, U. J. 2004. Methods for generating high-resolution structural models from electron microscope tomography data. *Structure (London, England : 1993),* 12**,** 1763-1774.

RIDHA, H., ALMITANI, K. H., CHAMEKH, A., TOUMI, H. & TAVARES, J. M. R. S. 2015. A theory for bone resorption based on the local rupture of osteocytes cells connections: A finite element study. *Mathematical Biosciences,* 262**,** 46-55.

RITMAN, E. L. 2011. Current Status of Developments and Applications of Micro-CT. *Annual Review of Biomedical Engineering,* 13**,** 531-552.

RIZOU, S., CHRONOPOULOS, E., BALLAS, M. & LYRITIS, G. P. 2018. Clinical manifestations of osteoarthritis in osteoporotic and osteopenic postmenopausal women. *J Musculoskelet Neuronal Interact,* 18**,** 208-214.

ROBERTS, N., MAGEE, D., SONG, Y., BRABAZON, K., SHIRES, M., CRELLIN, D., ORSI, N. M., QUIRKE, R., QUIRKE, P. & TREANOR, D. 2012. Toward routine use of 3D histopathology as a research tool. *Am J Pathol,* 180**,** 1835-42.

ROBLING, A. G. & BONEWALD, L. F. 2020. The Osteocyte: New Insights. *Annu Rev Physiol,* 82**,** 485-506.

ROELS, J., AELTERMAN, J.,LUONG, H.Q., LIPPENS, S., PIZURICA, A., SAEYS, Y.,PHILIPS, W. 2018. An overview of state-of-the-art image restoration in electron microscopy. *Journal of Microscopy,* 271**,** 239-254.

ROLVIEN, T., SCHMIDT, F. N., MILOVANOVIC, P., JAHN, K., RIEDEL, C., BUTSCHEIDT, S., PUSCHEL, K., JESCHKE, A., AMLING, M. & BUSSE, B. 2018. Early bone tissue aging in human auditory ossicles is accompanied by excessive hypermineralization, osteocyte death and micropetrosis. *Sci Rep,* 8**,** 1920.

ROSS, T. D., COON, B. G., YUN, S., BAEYENS, N., TANAKA, K., OUYANG, M. & SCHWARTZ, M. A. 2013. Integrins in mechanotransduction. *Curr Opin Cell Biol,* 25**,** 613-8.

RSTUDIO TEAM 2016. RStudio: Integrated Development Environment for R. Boston, MA: RStudio, Inc.

RU, J.-Y. & WANG, Y.-F. 2020. Osteocyte apoptosis: the roles and key molecular mechanisms in resorption-related bone diseases. *Cell Death & Disease,* 11**,** 846.

RUBINACCI, A., COVINI, M., BISOGNI, C., VILLA, I., GALLI, M., PALUMBO, C., FERRETTI, M., MUGLIA, M. A. & MAROTTI, G. 2002. Bone as an ion exchange system: evidence for a link between mechanotransduction and metabolic needs. *American Journal of Physiology-Endocrinology and Metabolism,* 282**,** E851-E864.

RÜEGSEGGER, P., KOLLER, B. & MÜLLER, R. 1996. A microtomographic system for the nondestructive evaluation of bone architecture. *Calcif Tissue Int,* 58**,** 24-9.

RUSSELL, M. R. G., LERNER, T. R., BURDEN, J. J., NKWE, D. O., PELCHEN-MATTHEWS, A., DOMART, M.-C., DURGAN, J., WESTON, A., JONES, M. L., PEDDIE, C. J., CARZANIGA, R., FLOREY, O., MARSH, M., GUTIERREZ, M. G. & COLLINSON, L. M. 2016. 3D correlative light and electron microscopy of cultured cells using serial blockface scanning electron microscopy. *Journal of Cell Science*.

SALTER, D. M., ROBB, J. E. & WRIGHT, M. O. 1997. Electrophysiological responses of human bone cells to mechanical stimulation: evidence for specific integrin function in mechanotransduction. *J Bone Miner Res,* 12**,** 1133-41.

SANGEETHA, R., UMA, K. & CHANDAVARKAR, V. 2013. Comparison of routine decalcification methods with microwave decalcification of bone and teeth. *Journal of oral and maxillofacial pathology : JOMFP,* 17**,** 386-391.

SANJAI, K., KUMARSWAMY, J., PATIL, A., PAPAIAH, L., JAYARAM, S. & KRISHNAN, L. 2012. Evaluation and comparison of decalcification agents on the human teeth. *J Oral Maxillofac Pathol,* 16**,** 222-7.

SANSALONE, V., KAISER, J., NAILI, S. & LEMAIRE, T. 2013. Interstitial fluid flow within bone canaliculi and electro-chemo-mechanical features of the canalicular milieu: a multi-parametric sensitivity analysis. *Biomech Model Mechanobiol,* 12**,** 533-53.

SCHAFFLER, M. B., CHEUNG, W. Y., MAJESKA, R. & KENNEDY, O. 2014. Osteocytes: master orchestrators of bone. *Calcif Tissue Int,* 94**,** 5-24.

SCHIEBER, N. L., MACHADO, P., MARKERT, S. M., STIGLOHER, C., SCHWAB, Y. & STEYER, A. M. 2017. Minimal resin embedding of multicellular specimens for targeted FIB-SEM imaging. *Methods Cell Biol,* 140**,** 69-83.

SCHINDELIN, J., ARGANDA-CARRERAS, I., FRISE, E., KAYNIG, V., LONGAIR, M., PIETZSCH, T., PREIBISCH, S., RUEDEN, C., SAALFELD, S., SCHMID, B., TINEVEZ, J. Y., WHITE, D. J., HARTENSTEIN, V., ELICEIRI, K., TOMANCAK, P. & CARDONA, A. 2012. Fiji: an open-source platform for biological-image analysis. *Nat Methods,* 9**,** 676-82.

SCHNEIDER, C. A., RASBAND, W. S. & ELICEIRI, K. W. 2012a. NIH Image to ImageJ: 25 years of image analysis. *Nature Methods,* 9**,** 671-675.

SCHNEIDER, P., MEIER, M., WEPF, R. & MULLER, R. 2010. Towards quantitative 3D imaging of the osteocyte lacuno-canalicular network. *Bone,* 47**,** 848-58.

SCHNEIDER, P., MEIER, M., WEPF, R. & MÜLLER, R. 2011. Serial FIB/SEM imaging for quantitative 3D assessment of the osteocyte lacuno-canalicular network. *Bone,* 49**,** 304-311.

SCHNEIDER, P., RUFFONI, D., LARSSON, D., CHIAPPARINI, I. & MÜLLER, R. 2012b. Image-based finite element models for the inestigation of osteocyte mechanotransduction. *Journal of Biomechanics,* 45, Supplement 1**,** S436.

SCHNEIDER, P., STAUBER, M., VOIDE, R., STAMPANONI, M., DONAHUE, L. R. & MULLER, R. 2007. Ultrastructural properties in cortical bone vary greatly in two inbred strains of mice as assessed by synchrotron light based micro- and nano-CT. *J Bone Miner Res,* 22**,** 1557-70.

SCHNEIDER, P., VOIDE, R., STAMPANONI, M., DONAHUE, L. R. & MULLER, R. 2013. The importance of the intracortical canal network for murine bone mechanics. *Bone,* 53**,** 120-8.

SCOTT, A. E., VASILESCU, D. M., SEAL, K. A., KEYES, S. D., MAVROGORDATO, M. N., HOGG, J. C., SINCLAIR, I., WARNER, J. A., HACKETT, T. L. & LACKIE, P. M. 2015. Three dimensional imaging of paraffin embedded human lung tissue samples by micro-computed tomography. *PLoS One,* 10**,** e0126230.

SEEMAN, E. 2013. Age- and menopause-related bone loss compromise cortical and trabecular microstructure. *J Gerontol A Biol Sci Med Sci,* 68**,** 1218-25.

SELA, J. & BAB, I. A. 1979. Correlative transmission and scanning electron microscopy of the initial mineralization of healing alveolar bone in rats. *Acta Anat (Basel),* 105**,** 401-8.

SELIGMAN, A. M., WASSERKRUG, H. L. & HANKER, J. S. 1966. A new staining method (OTO) for enhancing contrast of lipid--containing membranes and droplets in osmium tetroxide--fixed tissue with osmiophilic thiocarbohydrazide(TCH). *J Cell Biol,* 30**,** 424-32.

SENGLE, G., TUFA, S. F., SAKAI, L. Y., ZULLIGER, M. A. & KEENE, D. R. 2013. A correlative method for imaging identical regions of samples by micro-CT, light microscopy, and electron microscopy: imaging adipose tissue in a model system. *J Histochem Cytochem,* 61**,** 263-71.

SHAH, F. A., JOHANSSON, B. R., THOMSEN, P. & PALMQUIST, A. 2015. Ultrastructural evaluation of shrinkage artefacts induced by fixatives and embedding resins on osteocyte processes and pericellular space dimensions. *J Biomed Mater Res A,* 103**,** 1565-76.

SHAH, F. A., RUSCSÁK, K. & PALMQUIST, A. 2019. 50 years of scanning electron microscopy of bone—a comprehensive overview of the important discoveries made and insights gained into bone material properties in health, disease, and taphonomy. *Bone Research,* 7**,** 15.

SHAMI, G., CHENG, D., HENRIQUEZ, J. & BRAET, F. 2014. Assessment of different fixation protocols on the presence of membrane-bound vesicles in Caco-2 cells: a multidimensional view by means of correlative light and 3-D transmission electron microscopy. *Micron,* 67**,** 20-9.

SHARMA, D., CIANI, C., MARIN, P. A., LEVY, J. D., DOTY, S. B. & FRITTON, S. P. 2012. Alterations in the osteocyte lacunar-canalicular microenvironment due to estrogen deficiency. *Bone,* 51**,** 488-97.

SHARMA, U., MIKOS, A. G. & COWIN, S. C. 2007. Chapter Sixty-One - Mechanosensory Mechanisms in Bone. *In:* LANZA, R., LANGER, R. & VACANTI, J. (eds.) *Principles of Tissue Engineering (Third Edition).* Burlington: Academic Press.

SHEARER, T., BRADLEY, R. S., HIDALGO-BASTIDA, L. A., SHERRATT, M. J. & CARTMELL, S. H. 2016. Three-dimensional visualisation of soft biological structures by X-ray computed micro-tomography. *Journal of Cell Science,* 129**,** 2483-2492.

SHEMESH, M., ADDADI, S., MILSTEIN, Y., GEIGER, B. & ADDADI, L. 2016. Study of Osteoclast Adhesion to Cortical Bone Surfaces: A Correlative Microscopy Approach for Concomitant Imaging of Cellular Dynamics and Surface Modifications. *ACS Applied Materials & Interfaces,* 8**,** 14932-14943.

SHEN, Y., ZHANG, Z. M., JIANG, S. D., JIANG, L. S. & DAI, L. Y. 2009. Postmenopausal women with osteoarthritis and osteoporosis show different ultrastructural characteristics of trabecular bone of the femoral head. *BMC Musculoskelet Disord,* 10**,** 35.

SHIFLETT, L. A., TIEDE-LEWIS, L. M., XIE, Y., LU, Y., RAY, E. C. & DALLAS, S. L. 2019. Collagen Dynamics During the Process of Osteocyte Embedding and Mineralization. *Frontiers in Cell and Developmental Biology,* 7.

SKEDROS, J. G., HOLMES, J. L., VAJDA, E. G. & BLOEBAUM, R. D. 2005. Cement lines of secondary osteons in human bone are not mineral-deficient: New data in a historical perspective. *The Anatomical Record Part A: Discoveries in Molecular, Cellular, and Evolutionary Biology,* 286A**,** 781-803.

SKERRY, T. M., BITENSKY, L., CHAYEN, J. & LANYON, L. E. 1989. Early strain-related changes in enzyme activity in osteocytes following bone loading in vivo. *J Bone Miner Res,* 4**,** 783-8.

SMITH, D. & STARBORG, T. 2019. Serial block face scanning electron microscopy in cell biology: Applications and technology. *Tissue Cell,* 57**,** 111-122.

SPIERS, H., SONGHURST, H., NIGHTINGALE, L., DE FOLTER, J., HUTCHINGS, R., PEDDIE, C. J., WESTON, A., STRANGE, A., HINDMARSH, S., LINTOTT, C., COLLINSON, L. M. & JONES, M. L. 2020. Citizen science, cells and CNNs – deep learning for automatic segmentation of the nuclear envelope in electron microscopy data, trained with volunteer segmentations. *bioRxiv***,** 2020.07.28.223024.

STACHNIK, K., WARMER, M., MOHACSI, I., HENNICKE, V., FISCHER, P., MEYER, J., SPITZBART, T., BARTHELMESS, M., EICH, J., DAVID, C., FELDMANN, C., BUSSE, B., JAHN, K., SCHAIBLE, U. E. & MEENTS, A. 2020. Multimodal X-ray imaging of nanocontainer-treated macrophages and calcium distribution in the perilacunar bone matrix. *Scientific Reports,* 10**,** 9.

STARBORG, T., KALSON, N. S., LU, Y., MIRONOV, A., COOTES, T. F., HOLMES, D. F. & KADLER, K. E. 2013. Using transmission electron microscopy and 3View to determine collagen fibril size and three-dimensional organization. *Nature Protocols,* 8**,** 1433-1448.

STARBORG, T., MARTINS CARNEIRO, C., BEHENSEN, J., O'SULLIVAN, J., ELSE, K.J., WITHERS P.J., GRENCIS, R. 2017. Using X-ray micro CT to direct serial block face imaging. *Microscience Microscopy Congress.* Manchester.

STARBORG, T., O'SULLIVAN, J. D. B., CARNEIRO, C. M., BEHNSEN, J., ELSE, K. J., GRENCIS, R. K. & WITHERS, P. J. 2019. Experimental steering of electron microscopy studies using prior X-ray computed tomography. *Ultramicroscopy,* 201**,** 58-67.

STERCK, J. G., KLEIN-NULEND, J., LIPS, P. & BURGER, E. H. 1998. Response of normal and osteoporotic human bone cells to mechanical stress in vitro. *Am J Physiol,* 274**,** E1113-20.

STOLBERG-STOLBERG, J., SAMBALE, M., HANSEN, U., RASCHKE, A. S. M., BERTRAND, J., PAP, T. & SHERWOOD, J. 2020. Cartilage Trauma Induces Necroptotic Chondrocyte Death and Expulsion of Cellular Contents. *Int J Mol Sci,* 21.

SUGAWARA, Y., ANDO, R., KAMIOKA, H., ISHIHARA, Y., HONJO, T., KAWANABE, N., KUROSAKA, H., TAKANO-YAMAMOTO, T. & YAMASHIRO, T. 2011. The three-dimensional morphometry

and cell-cell communication of the osteocyte network in chick and mouse embryonic calvaria. *Calcif Tissue Int,* 88**,** 416-24.

SUGAWARA, Y., KAMIOKA, H., HONJO, T., TEZUKA, K. & TAKANO-YAMAMOTO, T. 2005. Three-dimensional reconstruction of chick calvarial osteocytes and their cell processes using confocal microscopy. *Bone,* 36**,** 877-83.

SUGAWARA, Y., KAMIOKA, H., ISHIHARA, Y., FUJISAWA, N., KAWANABE, N. & YAMASHIRO, T. 2013. The early mouse 3D osteocyte network in the presence and absence of mechanical loading. *Bone,* 52**,** 189-196.

TAMIMI, I., CORTES, A. R. G., SÁNCHEZ-SILES, J.-M., ACKERMAN, J. L., GONZÁLEZ-QUEVEDO, D., GARCÍA, Á., YAGHOUBI, F., ABDULLAH, M. N., EIMAR, H., ALSHEGHRI, A., LAURENTI, M., AL-SUBAEI, A., GUERADO, E., GARCÍA-DE-QUEVEDO, D. & TAMIMI, F. 2020. Composition and characteristics of trabecular bone in osteoporosis and osteoarthritis. *Bone***,** 115558.

TANAKA-KAMIOKA, K., KAMIOKA, H., RIS, H. & LIM, S. S. 1998. Osteocyte shape is dependent on actin filaments and osteocyte processes are unique actin-rich projections. *J Bone Miner Res,* 13**,** 1555-68.

TANOUE, R., OHTA, K., MIYAZONO, Y., IWANAGA, J., KOBA, A., NATORI, T., IWAMOTO, O., NAKAMURA, K.-I. & KUSUKAWA, J. 2018. Three-dimensional ultrastructural analysis of the interface between an implanted demineralised dentin matrix and the surrounding newly formed bone. *Scientific reports,* 8**,** 2858-2858.

TAPIA, J. C., KASTHURI, N., HAYWORTH, K. J., SCHALEK, R., LICHTMAN, J. W., SMITH, S. J. & BUCHANAN, J. 2012. High-contrast en bloc staining of neuronal tissue for field emission scanning electron microscopy. *Nat Protoc,* 7**,** 193-206.

TAQI, S. A., SAMI, S. A., SAMI, L. B. & ZAKI, S. A. 2018. A review of artifacts in histopathology. *Journal of oral and maxillofacial pathology : JOMFP,* 22**,** 279-279.

TATE, M. L. K., ZEIDLER, D., PEREIRA, A. F., HAGEMAN, D., GARBOWSKI, T., MISHRA, S., GARDNER, L. & KNOTHE, U. R. 2016. Organ-to-Cell-Scale Health Assessment Using Geographical Information System Approaches with Multibeam Scanning Electron Microscopy. *Advanced Healthcare Materials,* 5**,** 1581-1587.

TATSUMI, S., ISHII, K., AMIZUKA, N., LI, M., KOBAYASHI, T., KOHNO, K., ITO, M., TAKESHITA, S. & IKEDA, K. 2007. Targeted ablation of osteocytes induces osteoporosis with defective mechanotransduction. *Cell Metab,* 5**,** 464-75.

TEMIYASATHIT, S. & JACOBS, C. R. 2010. Osteocyte primary cilium and its role in bone mechanotransduction. *Ann N Y Acad Sci,* 1192**,** 422-8.

THI, M. M., SUADICANI, S. O., SCHAFFLER, M. B., WEINBAUM, S. & SPRAY, D. C. 2013. Mechanosensory responses of osteocytes to physiological forces occur along processes and not cell body and require alphaVbeta3 integrin. *Proc Natl Acad Sci U S A,* 110**,** 21012-7.

TIEDE-LEWIS, L. M., XIE, Y., HULBERT, M. A., CAMPOS, R., DALLAS, M. R., DUSEVICH, V., BONEWALD, L. F. & DALLAS, S. L. 2017. Degeneration of the osteocyte network in the C57BL/6 mouse model of aging. *Aging (Albany NY),* 9**,** 2190-2208.

TIMMERMANS, F. J., LISZKA, B., LENFERINK, A. T. M., VAN WOLFEREN, H. A. G. M. & OTTO, C. 2016. Integration of correlative Raman microscopy in a dualbeam FIB SEM. *Journal of Raman Spectroscopy,* 47**,** 956-962.

TITZE, B. & DENK, W. 2013. Automated in-chamber specimen coating for serial block-face electron microscopy. *Journal of Microscopy,* 250**,** 101-110.

TITZE, B., GENOUD, C. & FRIEDRICH, R. W. 2018. SBEMimage: Versatile Acquisition Control Software for Serial Block-Face Electron Microscopy. *Frontiers in neural circuits,* 12**,** 54-54.

TOMKINSON, A., REEVE, J., SHAW, R. W. & NOBLE, B. S. 1997. The death of osteocytes via apoptosis accompanies estrogen withdrawal in human bone. *J Clin Endocrinol Metab,* 82**,** 3128-35.

TOMMASINI, S. M., TRINWARD, A., ACERBO, A. S., DE CARLO, F., MILLER, L. M. & JUDEX, S. 2012. Changes in intracortical microporosities induced by pharmaceutical treatment of osteoporosis as detected by high resolution micro-CT. *Bone,* 50**,** 596-604.

TORCASIO, A., ZHANG, X., DUYCK, J. & VAN LENTHE, G. H. 2012. 3D characterization of bone strains in the rat tibia loading model. *Biomech Model Mechanobiol,* 11**,** 403-10.

TRIRÈ, A., MARTINI, D., ORSINI, E., FRANCHI, M., DE PASQUALE, V., BACCHELLI, B., RASPANTI, M., RUGGERI, A. & OTTANI, V. 2010. Correlative microscopy of bone in implant osteointegration studies. *ScientificWorldJournal,* 10**,** 2238-47.

TROUILLE, L., LINTOTT, C. J. & FORTSON, L. F. 2019. Citizen science frontiers: Efficiency, engagement, and serendipitous discovery with human-machine systems. *Proc Natl Acad Sci U S A,* 116**,** 1902-1909.

TSAI, W. T., HASSAN, A., SARKAR, P., CORREA, J., METLAGEL, Z., JORGENS, D. M. & AUER, M. 2014. From voxels to knowledge: a practical guide to the segmentation of complex electron microscopy 3D-data. *J Vis Exp***,** e51673.

TSOURDI, E., JAHN, K., RAUNER, M., BUSSE, B. & BONEWALD, L. F. 2018. Physiological and pathological osteocytic osteolysis. *J Musculoskelet Neuronal Interact,* 18**,** 292-303.

TURNER, A. S. 2001. Animal models of osteoporosis--necessity and limitations. *Eur Cell Mater,* 1**,** 66-81.

UDA, Y., AZAB, E., SUN, N., SHI, C. & PAJEVIC, P. D. 2017. Osteocyte Mechanobiology. *Curr Osteoporos Rep,* 15**,** 318-325.

UZBEKOV, R. E., MAUREL, D. B., AVELINE, P. C., PALLU, S., BENHAMOU, C. L. & ROCHEFORT, G. Y. 2012. Centrosome fine ultrastructure of the osteocyte mechanosensitive primary cilium. *Microsc Microanal,* 18**,** Am J Med GenetAnat Embryol (Berl)1430-41.

VAN DEN BERGH WEERMAN MA, C.-B., J., VEDDER, A.C., WIJBURG, F.A. HOLLAK, C.E.M., FLORQUIN. S. 2008. *Ultrastructural analysis of lysosomal storage diseases: effects of therapy*, Springer.

VAN HOVE, R. P., NOLTE, P. A., VATSA, A., SEMEINS, C. M., SALMON, P. L., SMIT, T. H. & KLEIN-NULEND, J. 2009. Osteocyte morphology in human tibiae of different bone pathologies with different bone mineral density--is there a role for mechanosensing? *Bone,* 45**,** 321-9.

VAN TOL, A. F., ROSCHGER, A., REPP, F., CHEN, J., ROSCHGER, P., BERZLANOVICH, A., GRUBER, G. M., FRATZL, P. & WEINKAMER, R. 2020. Network architecture strongly influences the fluid flow pattern through the lacunocanalicular network in human osteons. *Biomechanics and Modeling in Mechanobiology,* 19**,** 823-840.

VARGA, P., HESSE, B., LANGER, M., SCHROF, S., MÄNNICKE, N., SUHONEN, H., PACUREANU, A., PAHR, D., PEYRIN, F. & RAUM, K. 2014. Synchrotron X-ray phase nano-tomography-based

analysis of the lacunar–canalicular network morphology and its relation to the strains experienced by osteocytes in situ as predicted by case-specific finite element analysis. *Biomechanics and Modeling in Mechanobiology,* 14**,** 267-82.

VASHISHTH, D., VERBORGT, O., DIVINE, G., SCHAFFLER, M. B. & FYHRIE, D. P. 2000. Decline in osteocyte lacunar density in human cortical bone is associated with accumulation of microcracks with age. *Bone,* 26**,** 375-380.

VATSA, A., BREULS, R. G., SEMEINS, C. M., SALMON, P. L., SMIT, T. H. & KLEIN-NULEND, J. 2008. Osteocyte morphology in fibula and calvaria --- is there a role for mechanosensing? *Bone,* 43**,** 452-8.

VAUGHAN, T. J., MULLEN, C. A., VERBRUGGEN, S. W. & MCNAMARA, L. M. 2014. Bone cell mechanosensation of fluid flow stimulation: a fluid-structure interaction model characterising the role integrin attachments and primary cilia. *Biomech Model Mechanobiol,* 14**,** 703-18.

VAUGHAN, T. J., VERBRUGGEN, S. W. & MCNAMARA, L. M. 2013. Are all osteocytes equal? Multiscale modelling of cortical bone to characterise the mechanical stimulation of osteocytes. *Int J Numer Method Biomed Eng,* 29**,** 1361-72.

VENO P.A., N. D. P., KALAJZIC I., ROWE D.W., BONEWALD .LF., DALLAS S.L. 2007. Dynamic imagin of living calvaria reveals the motile prperties of osteoblasts and osteocytes and suggests heterogeneity of osteoblasts in bone. ASBMR 29th Annual Meeting. *Journal of Bone and Mineral Research,* 22**,** S13.

VERBORGT, O., GIBSON, G. J. & SCHAFFLER, M. B. 2000. Loss of osteocyte integrity in association with microdamage and bone remodeling after fatigue in vivo. *J Bone Miner Res,* 15**,** 60-7.

VERBRUGGEN, S. W., VAUGHAN, T. J. & MCNAMARA, L. M. 2012. Strain amplification in bone mechanobiology: a computational investigation of the in vivo mechanics of osteocytes. *J R Soc Interface,* 9**,** 2735-44.

VERBRUGGEN, S. W., VAUGHAN, T. J. & MCNAMARA, L. M. 2014. Fluid flow in the osteocyte mechanical environment: a fluid-structure interaction approach. *Biomech Model Mechanobiol,* 13**,** 85-97.

VERBRUGGEN, S. W., VAUGHAN, T. J. & MCNAMARA, L. M. 2016. Mechanisms of osteocyte stimulation in osteoporosis. *J Mech Behav Biomed Mater,* 62**,** 158-168.

VERKADE, P. 2013. Webinar: Correlative Light Electron Microscopy: 1 + 1 = 3.

VERSUS-ARTHRITIS 2019. The state of musculoskeletal health report.

VIHINEN, H., BELEVICH, I., JOKITALO, E. 2012. Electron tomography and serial block face scanning electron microscopy complement each other in 3D morphological characterization of cell organelles. *EMC 2012.* Manchester.

WANG, L., CIANI, C., DOTY, S. B. & FRITTON, S. P. 2004. Delineating bone's interstitial fluid pathway in vivo. *Bone,* 34**,** 499-509.

WANG, L., DONG, J. & XIAN, C. J. 2015a. Strain Amplification Analysis of an Osteocyte under Static and Cyclic Loading: A Finite Element Study. *Biomed Research International,* 2015**,** 376474.

WANG, L., DONG, J. & XIAN, C. J. 2015b. Strain amplification analysis of an osteocyte under static and cyclic loading: a finite element study. *BioMed research international,* 2015**,** 376474-376474.

WANG, L., DONG, J. & XIAN, C. J. 2018. Computational Investigation on the Biomechanical Responses of the Osteocytes to the Compressive Stimulus: A Poroelastic Model. *BioMed research international,* 2018**,** 4071356-4071356.

WANG, Y., MCNAMARA, L. M., SCHAFFLER, M. B. & WEINBAUM, S. 2007. A model for the role of integrins in flow induced mechanotransduction in osteocytes. *Proc Natl Acad Sci U S A,* 104**,** 15941-6.

WANG, Z., ODAGAKI, N., TANAKA, T., HASHIMOTO, M., NAKAMURA, M., HAYANO, S., ISHIHARA, Y., KAWANABE, N. & KAMIOKA, H. 2016. Alternation in the gap-junctional intercellular communication capacity during the maturation of osteocytes in the embryonic chick calvaria. *Bone,* 91**,** 20-9.

WEBER, M., MICKOLEIT, M. & HUISKEN, J. 2014. Chapter 11 - Light sheet microscopy. *In:* JENNIFER, C. W. & TORSTEN, W. (eds.) *Methods in Cell Biology.* Academic Press.

WEBSTER, D. & MULLER, R. 2011. In silico models of bone remodeling from macro to nano--from organ to cell. *Wiley Interdiscip Rev Syst Biol Med,* 3**,** 241-51.

WEBSTER, K. 1994. Osteoporosis: A Multifactorial Disease. *Nutrition & Food Science,* 94**,** 11-16.

WEINBAUM, S., COWIN, S. C. & ZENG, Y. 1994a. A model for the excitation of osteocytes by mechanical loading-induced bone fluid shear stresses. *J Biomech,* 27**,** 339-60.

WEINBAUM, S., COWIN, S. C. & ZENG, Y. 1994b. A model for the excitation of osteocytes by mechanical loading-induced bone fluid shear stresses. *Journal of Biomechanics,* 27**,** 339-360.

WEINKAMER, R., KOLLMANNSBERGER, P. & FRATZL, P. 2019. Towards a Connectomic Description of the Osteocyte Lacunocanalicular Network in Bone. *Curr Osteoporos Rep,* 17**,** 186-194.

WERNITZNIG, S., SELE, M., URSCHLER, M., ZANKEL, A., POLT, P., RIND, F. C. & LEITINGER, G. 2016. Optimizing the 3D-reconstruction technique for serial block-face scanning electron microscopy. *J Neurosci Methods,* 264**,** 16-24.

WESTON, A. E., ARMER, H. E. J. & COLLINSON, L. M. 2010. Towards native-state imaging in biological context in the electron microscope. *Journal of Chemical Biology,* 3**,** 101-112.

WHITFIELD, J. F. 2004. The neuronal primary cilium--an extrasynaptic signaling device. *Cell Signal,* 16**,** 763-7.

WHO 1994. Assessment of fracture risk and its application to screening for postmenopausal osteoporosis : report of a WHO study group [meeting held in Rome from 22 to 25 June 1992]. Geneva: World Health Organization.

WHO. 2019. *Musculoskeletal conditions* [Online]. Available: https://www.who.int/news-room/fact-sheets/detail/musculoskeletal-conditions [Accessed 08/12/20 2020].

WILLIAMS, K. A., GOSTLING, N. J., STEER, J. W., OREFFO, R. O. C. & SCHNEIDER, P. 2020. Quantifying intracortical bone microstructure: A critical appraisal of 2D and 3D approaches for assessing vascular canals and osteocyte lacunae. *J Anat,* 238**,** 653-68.

WILLINGHAM, M. C. & RUTHERFORD, A. V. 1984. The use of osmium-thiocarbohydrazide-osmium (OTO) and ferrocyanide-reduced osmium methods to enhance membrane contrast and preservation in cultured cells. *J Histochem Cytochem,* 32**,** 455-60.

WITTIG, N. K., BACH-GANSMO, F. L., BIRKBAK, M. E., LAUGESEN, M., BRUEL, A., THOMSEN, J. S. & BIRKEDAL, H. 2016. Organ and tissue level properties are more sensitive to age than osteocyte lacunar characteristics in rat cortical bone. *Bone Rep,* 4**,** 28-34.

WITTKOWSKE, C., REILLY, G. C., LACROIX, D. & PERRAULT, C. M. 2016. In Vitro Bone Cell Models: Impact of Fluid Shear Stress on Bone Formation. *Frontiers in bioengineering and biotechnology,* 4**,** 87-87.

WONG, S. Y., EVANS, R. A., NEEDS, C., DUNSTAN, C. R., HILLS, E. & GARVAN, J. 1987. The pathogenesis of osteoarthritis of the hip. Evidence for primary osteocyte death. *Clin Orthop Relat Res***,** 305-12.

WONG, S. Y., KARIKS, J., EVANS, R. A., DUNSTAN, C. R. & HILLS, E. 1985. The effect of age on bone composition and viability in the femoral head. *J Bone Joint Surg Am,* 67**,** 274-83.

WRONSKI, T. J., LOWRY, P. L., WALSH, C. C. & IGNASZEWSKI, L. A. 1985. Skeletal alterations in ovariectomized rats. *Calcif Tissue Int,* 37**,** 324-8.

WU, X. T., SUN, L. W., YANG, X., DING, D., HAN, D. & FAN, Y. B. 2017. The potential role of spectrin network in the mechanotransduction of MLO-Y4 osteocytes. *Sci Rep,* 7**,** 40940.

WYSOLMERSKI, J. J. 2013. Osteocytes remove and replace perilacunar mineral during reproductive cycles. *Bone,* 54**,** 230-6.

XIA, X., KAR, R., GLUHAK-HEINRICH, J., YAO, W., LANE, N. E., BONEWALD, L. F., BISWAS, S. K., LO, W.-K. & JIANG, J. X. 2010. Glucocorticoid-induced autophagy in osteocytes. *Journal of bone and mineral research : the official journal of the American Society for Bone and Mineral Research,* 25**,** 2479-2488.

XIAO, Z., DALLAS, M., QIU, N., NICOLELLA, D., CAO, L., JOHNSON, M., BONEWALD, L. & QUARLES, L. D. 2011. Conditional deletion of Pkd1 in osteocytes disrupts skeletal mechanosensing in mice. *Faseb j,* 25**,** 2418-32.

XIPELL, J. M. & GLADWIN, R. C. 1972. The use of a low-viscosity epoxy resin in the preparation of undecalcified bone sections for light microscopy. *J Microsc,* 96**,** 125-9.

YIN, Z. Y., YIN, J., HUO, Y. F., YU, J., SHENG, L. X. & DONG, Y. F. 2017. Rapamycin facilitates fracture healing through inducing cell autophagy and suppressing cell apoptosis in bone tissues. *Eur Rev Med Pharmacol Sci,* 21**,** 4989-4998.

YOU, L.-D., WEINBAUM, S., COWIN, S. C. & SCHAFFLER, M. B. 2004. Ultrastructure of the osteocyte process and its pericellular matrix. *The Anatomical Record Part A: Discoveries in Molecular, Cellular, and Evolutionary Biology,* 278A**,** 505-513.

YOU, L., COWIN, S. C., SCHAFFLER, M. B. & WEINBAUM, S. 2001. A model for strain amplification in the actin cytoskeleton of osteocytes due to fluid drag on pericellular matrix. *J Biomech,* 34**,** 1375-86.

YUAN, R., TSAIH, S. W., PETKOVA, S. B., MARIN DE EVSIKOVA, C., XING, S., MARION, M. A., BOGUE, M. A., MILLS, K. D., PETERS, L. L., BULT, C. J., ROSEN, C. J., SUNDBERG, J. P., HARRISON, D. E., CHURCHILL, G. A. & PAIGEN, B. 2009. Aging in inbred strains of mice: study design and interim report on median lifespans and circulating IGF1 levels. *Aging Cell,* 8**,** 277-87.

YUSHKEVICH, P. A., PIVEN, J., HAZLETT, H. C., SMITH, R. G., HO, S., GEE, J. C. & GERIG, G. 2006. User-guided 3D active contour segmentation of anatomical structures: significantly improved efficiency and reliability. *Neuroimage,* 31**,** 1116-28.

ZANKEL, A. 2011. 3D Elemental Mapping in the ESEM- A Combination of Serial Block FAce SEM and EDS. *Imaging and Microscopy*.

ZARRINKALAM, M. R., MULAIBRAHIMOVIC, A., ATKINS, G. J. & MOORE, R. J. 2012. Changes in osteocyte density correspond with changes in osteoblast and osteoclast activity in an osteoporotic sheep model. *Osteoporos Int,* 23**,** 1329-36.

ZENG, Y., COWIN, S. C. & WEINBAUM, S. 1994. A fiber matrix model for fluid flow and streaming potentials in the canaliculi of an osteon. *Ann Biomed Eng,* 22**,** 280-92.

ŽEROVNIK MEKUČ, M., BOHAK, C., HUDOKLIN, S., KIM, B. H., ROMIH, R., KIM, M. Y. & MAROLT, M. 2020. Automatic segmentation of mitochondria and endolysosomes in volumetric electron microscopy data. *Comput Biol Med,* 119**,** 103693.

ZHANG, C., XU, S., ZHANG, S., LIU, M., DU, H., SUN, R., JING, B. & SUN, Y. 2019. Ageing characteristics of bone indicated by transcriptomic and exosomal proteomic analysis of cortical bone cells. *Journal of Orthopaedic Surgery and Research,* 14**,** 129.

ZHANG, D., ZHOU, C., WANG, Q., CAI, L., DU, W., LI, X., ZHOU, X. & XIE, J. 2018. Extracellular Matrix Elasticity Regulates Osteocyte Gap Junction Elongation: Involvement of Paxillin in Intracellular Signal Transduction. *Cell Physiol Biochem,* 51**,** 1013-1026.

ZHANG, K., BARRAGAN-ADJEMIAN, C., YE, L., KOTHA, S., DALLAS, M., LU, Y., ZHAO, S., HARRIS, M., HARRIS, S. E., FENG, J. Q. & BONEWALD, L. F. 2006. E11/gp38 selective expression in osteocytes: regulation by mechanical strain and role in dendrite elongation. *Mol Cell Biol,* 26**,** 4539-52.

ZHANG, Z. M., JIANG, L. S., JIANG, S. D. & DAI, L. Y. 2009. Differential articular calcified cartilage and subchondral bone in postmenopausal women with osteoarthritis and osteoporosis: two-dimensional analysis. *Joint Bone Spine,* 76**,** 674-9.

ZHANG, Z. M., LI, Z. C., JIANG, L. S., JIANG, S. D. & DAI, L. Y. 2010. Micro-CT and mechanical evaluation of subchondral trabecular bone structure between postmenopausal women with osteoarthritis and osteoporosis. *Osteoporos Int,* 21**,** 1383-90.

ZHOU, M., LI, S. & PATHAK, J. L. 2019. Pro-inflammatory Cytokines and Osteocytes. *Curr Osteoporos Rep,* 17**,** 97-104.

ZIMMERMANN, E. A., RIEDEL, C., SCHMIDT, F. N., STOCKHAUSEN, K. E., CHUSHKIN, Y., SCHAIBLE, E., GLUDOVATZ, B., VETTORAZZI, E., ZONTONE, F., PUSCHEL, K., AMLING, M., RITCHIE, R. O. & BUSSE, B. 2019. Mechanical Competence and Bone Quality Develop During Skeletal Growth. *J Bone Miner Res,* 34**,** 1461-1472.